

Electronic Thesis and Dissertation Repository

6-7-2011 12:00 AM

Magnetic diffusion in star formation: From clouds to cores to stars to disks

Wolfgang B. Dapp, *The University of Western Ontario*

Supervisor: Shantanu Basu, *The University of Western Ontario*

A thesis submitted in partial fulfillment of the requirements for the Doctor of Philosophy degree in Astronomy

© Wolfgang B. Dapp 2011

Follow this and additional works at: <https://ir.lib.uwo.ca/etd>



Part of the [Stars, Interstellar Medium and the Galaxy Commons](#)

Recommended Citation

Dapp, Wolfgang B., "Magnetic diffusion in star formation: From clouds to cores to stars to disks" (2011). *Electronic Thesis and Dissertation Repository*. 173.
<https://ir.lib.uwo.ca/etd/173>

This Dissertation/Thesis is brought to you for free and open access by Scholarship@Western. It has been accepted for inclusion in Electronic Thesis and Dissertation Repository by an authorized administrator of Scholarship@Western. For more information, please contact wlsadmin@uwo.ca.

MAGNETIC DIFFUSION IN STAR FORMATION:
FROM CLOUDS TO CORES TO STARS TO DISKS
(Spine title: Magnetic Diffusion in Star Formation)
(Thesis format: Integrated Article)

by

Wolfgang Dapp

Graduate Program in Physics and Astronomy

A thesis submitted in partial fulfillment
of the requirements for the degree of
Doctor of Philosophy

The School of Graduate and Postdoctoral Studies
The University of Western Ontario
London, Ontario, Canada

© Wolfgang Benjamin Dapp 2011

THE UNIVERSITY OF WESTERN ONTARIO
School of Graduate and Postdoctoral Studies
CERTIFICATE OF EXAMINATION

Supervisor:

.....
Dr. Shantanu Basu

Examiners:

.....
Dr. T. A. A. Sigut

Supervisory Committee:

.....
Dr. T. A. A. Sigut

.....
Dr. P. Wiegert

.....
Dr. P. Wiegert

.....
Dr. M. Karttunen

.....
Dr. D. Balsara

The thesis by

Wolfgang Benjamin Dapp

entitled:

**Magnetic Diffusion in Star Formation:
From Clouds to Cores to Stars to Disks**

is accepted in partial fulfillment of the
requirements for the degree of
Doctor of Philosophy

.....
Date

.....
Chair of the Thesis Examination Board

Co-Authorship Statement

The four papers that make up this Thesis were co-authored with various collaborators.

For the work described in Chapter 2, I am second author. My task was modifying the numerical code written by Shantanu Basu, running simulations, and analyzing the resulting data. Serendipitously, I discovered the long-lasting oscillations, but it was Dr. Basu who recognized the significance of that phenomenon. He also did the analytical work shown in that work, and wrote most of the paper, with my input.

The idea for the work presented in Chapter 3 again originates from Shantanu Basu, but I did the analytical and numerical work, and wrote the paper, for which I am the principal author. This happened under guidance and supervision of Shantanu Basu who is second author.

I was also the principal author for the paper presented in Chapter 4. I wrote the numerical code for my M.Sc. work, ran the simulations and performed the data analysis. I also wrote the paper. Again, Dr. Basu suggested the project and provided comments, ideas and guidance throughout the process, and helped troubleshoot when there were problems. He is second author.

The final paper, presented in Chapter 5 has three authors. It is a continuation of the work in the previous chapter, and sparked by an idea originating with Shantanu Basu, who is co-author. I implemented methods and code written by Matthew Kunz, the other co-author, to determine the abundances of the various species, and calculate the non-ideal MHD effects into my simulation code. Dr. Kunz helped me understand the details of his additions, and also with troubleshooting. I ran the code (partly with computer time kindly provided by Dr. Jan Cami), and analyzed the data. I wrote the paper.

حدیث از مطرب و می گو و راز دهر کمتر جو
که کس نگشود و مگشاید به حکمت این معما را

خواجه شمس الدین محمد حافظ شیرازی
Khwāja Šamsu d-Dīn Muḥammad Hāfez-e Šīrāzī
(1325 - 1389)

Von Wein und Musikanten singe! Der Welt Geheimnis lasse ruhn!
Dies Rätsel löste nicht, noch löst es ein philosophischer Verstand.

Of minstrels and of wine discourse; care little how the skies revolve:
By wisdom no one has solved yet - and shall not this enigma solve.

Acknowledgements

I am pleased to acknowledge a number of people without whom the completion of this Thesis would not have been possible.

- ... first and foremost, I am grateful to Shantanu Basu, who guided and encouraged me every step of the way, who challenged me and put great trust in me. I learned a tremendous amount from his deep physical and astronomical insight. I also thank you for your good advice over all these years.
- ... Martin Houde for taking an interest in my work and his strong support in academic matters, and for being the same to Talayeh as Shantanu was to me.
- ... Igor Khavkine for help with countless larger and smaller problems in numerics and maths, for being the best Badminton partner I ever had, and for being a great friend
- ... Jan Cami for allowing me to use his group's computers when it came to crunching time, and I needed to run many models fast.
- ... Matt Kunz for his advice, his scientific rigor and his honesty. I value him as a collaborator and friend, and greatly appreciate his help in completing our joint project.
- ... mine and also Talayeh's family for gentle encouragement, for visits, for unconditional support and for always believing in me. Special thanks goes to my brother Götz for thoroughly proof-reading my introduction.
- ... my various recreational pastimes that helped me keep my work-life balance. Notably, those include the Badminton Club and our Squash group, but also the three D&D groups I was fortunate enough to be part of over the years. I also thank the Doppelkopf group for giving me my weekly fix of German culture and company.
- ... those who brought music to my life. Thanks to the UWO choir, and later Amabile Primus for letting me sing with them. Nothing challenges one quite the same way as making music does. Also I'm grateful to my singing teachers Jackie Wolting née Nelson, Rachel Wood, and Jeff Boyd from each of whom I learnt a lot. Thanks for coaching me and putting up with my lack of self-study and practice.

- ... our many great friends whom we spent countless hours with. Thank you for good times of fun and laughter, games, BBQs, movies, and discussions. Among them are Els & Jan, Parisa & Steve, Armin, and Draco & Dina (along with many others whom I apologize to for not naming them directly).
- ... everyone who came to my public PhD lecture. I feel privileged to have been allowed to speak in front of such a large audience who all came to support me.
- ... my Schatz Talayeh for always being there for me, even across 8,000 km of ocean, for listening to my rants, for putting up with me, for pushing me when I need pushing, for your unwavering love, for making me a better person. I couldn't have done this without you. I love you.

Dedication

*Für meine Großeltern,
Karl und Ingeborg Umbach,
Eugen und Anneliese Dapp.*

Abstract

We investigate magnetic diffusion on scales from molecular clouds over prestellar and protostellar cores down to young stellar objects (YSOs) and their surrounding protoplanetary disk.

In Chapter 2, we present thin-sheet simulations that exhibit long-lived magnetic-tension-driven oscillations, founded in the interaction of the cloud’s magnetic field with that anchored in an external medium. In contrast with “local” simulations in a periodic box, where turbulence decays away in approximately a sound crossing time, and needs to be continually replenished by driving, our simulation has “global” aspects, and retains some kinetic energy indefinitely. We provide an analytical explanation for these modes, that occur in the flux-freezing limit, as may be applicable to photoionized molecular cloud envelopes. The motions decay rapidly if ambipolar diffusion is introduced.

Chapter 3 introduces a new analytical three-parameter column density profile to fit prestellar cores. It is a replacement for the Bonnor-Ebert sphere model which has severe drawbacks, not the least of which is that fitting it often produces unrealistic temperatures. Our model instead fits the size of the flat region of both collapsing cores and those in equilibrium. It uses temperature as an input parameter. It can also be used to fit flattened cores, as well as cores with rotation and magnetic fields. Finally, our model provides a quantitative measure to judge whether a core is collapsing or in equilibrium. We apply it to B68 and L1689B.

In Chapters 4 and 5, we present numerical simulations that show that catastrophic magnetic braking can be avoided in the collapse of a prestellar core. Non-ideal MHD effects (ambipolar diffusion and Ohmic dissipation) weaken the magnetic field in the first core, inactivate magnetic braking there, and allow a disk to form close to the protostar. The formation of a small disk is consistent with observations that do not show evidence of a large centrifugal disk around Class 0 and I protostars. We propose a scenario where over time, a small but initially massive disk can expand to sizes of ≈ 100 AU, as commonly observed around Class II protostars.

Keywords: diffusion – ISM: clouds – ISM: kinematics and dynamics – ISM: magnetic fields – magnetohydrodynamics (MHD) – protoplanetary disks – stars: formation – stars: low-mass – stars: magnetic field – stars: protostars – turbulence

Contents

Certificate of Examination	ii
Co-Authorship Statement	iii
Acknowledgements	v
Dedication	vii
Abstract	viii
List of Figures	xiii
List of Tables	xv
List of Appendices	xvi
List of Abbreviations	xvii
List of Symbols	xix
1 Introduction	1
1.1 Preliminaries and overview	1
1.2 From clouds to cores	2
1.2.1 Lifetimes of molecular clouds	2
1.2.2 Constituents of the ISM	5
1.2.3 Non-thermal motions in the ISM	8
1.2.4 Initial conditions of star formation	10
1.3 From cores to stars	10
1.3.1 Angular momentum problem	14
1.3.2 Magnetic flux problem	18
1.3.3 Accretion rates	23
Bibliography	27

2	Long-lived Modes in a Molecular Cloud	36
2.1	Introduction	36
2.2	Method	37
2.3	Results	38
	2.3.1 Canonical models	38
	2.3.2 Connection to Linear Analysis	40
	2.3.3 Further modeling	42
2.4	Discussion	45
2.5	Summary	48
	Bibliography	48
3	Column density profile for prestellar cores	51
3.1	Introduction	51
3.2	Spherical Geometry	53
	3.2.1 Basic model	53
	3.2.2 Model parameters	55
	3.2.3 Total mass	59
3.3	Disc geometry	61
	3.3.1 Basic model	61
	3.3.2 Model parameters	62
	Effect of magnetic fields	63
	Effect of rotation	64
3.4	Applications	64
	3.4.1 B68	64
	3.4.2 L1689B	65
3.5	Summary and conclusions	67
	Bibliography	69
4	Disk formation due to Ohmic dissipation	71
4.1	Introduction	71
4.2	Method	72
4.3	Initial conditions and normalization	74
4.4	Results	74
	4.4.1 Prestellar phase and formation of the second core	74
	4.4.2 Evolution after second core formation	76
4.5	Discussion and conclusions	78
	Bibliography	80

5	Disk formation due to AD and OD	83
5.1	Introduction	83
5.2	Method	85
5.3	Magnetic braking	88
5.4	Non-ideal MHD treatment	90
5.5	Chemistry	94
5.5.1	Ionization rate	94
5.5.2	Fractional abundances	96
5.6	Initial Conditions and Normalization	97
5.7	Results	99
5.7.1	Collapse phase	99
5.7.2	Disk formation	112
5.8	Discussion	115
5.9	Summary and conclusions	118
	Bibliography	119
6	Summary and outlook	123
	Bibliography	125
A	Rate Coefficients and Collision time scales	127
A.1	Rate Coefficients	127
A.2	Collision time scales	128
	Bibliography	129
B	Derivation of the thin-disk equations	131
B.1	Applicability	131
B.2	Continuity equation in the thin-disk approximation	132
B.3	Equations of motion	136
B.3.1	Radial momentum equation in the thin disk model	138
B.3.2	Angular momentum equation in the thin disk model	139
B.4	Forces in the momentum equation	140
B.4.1	Normal vector	140
B.4.2	Thermal pressure	142
B.4.3	Magnetic Force	143
B.4.4	Gravity	145
B.5	Induction equation	146
B.6	Radial magnetic field component $B_{r,Z}$	147

Bibliography	148
C Implementation into the code	149
C.1 Continuity equation and mass conservation	149
C.2 Momentum equation	150
C.2.1 Barotropic energy equation	150
C.2.2 Stability	150
C.2.3 Implementation of the pressure force	152
C.2.4 Implemented momentum equation	154
C.3 Gravity	154
C.3.1 Gravity correction due to the disk's finite thickness	155
C.3.2 Gravity correction due to the disk's finite extent	159
C.3.3 Gravity correction for a central point mass	159
C.4 Angular momentum equation	161
C.5 Induction Equation	161
C.6 Calculation of magnetic field lines	162
C.7 Normalization and full system of equations	166
C.8 Numerical Code	168
C.8.1 Programming Language	168
C.8.2 Code description	168
C.8.3 Code structure	169
Bibliography	170
D The Bonnor-Ebert Sphere	174
Bibliography	179
Curriculum Vitae	180

List of Figures

1.1	Line-of-sight magnetic field vs. column density	20
1.2	Accretion rate evolution for spherical cloud	25
2.1	Kinetic energy for $\tilde{\tau}_{\text{ni},0} = 0$ and $\tilde{\tau}_{\text{ni},0} = 0.2$ models	39
2.2	Gas column density images for $\tilde{\tau}_{\text{ni},0} = 0.0$ and $\tilde{\tau}_{\text{ni},0} = 0.2$ models	40
2.3	Surface map of column density and field lines for $\tilde{\tau}_{\text{ni},0} = 0.0$ model	41
2.4	Kinetic energy decay with different power spectra and turbulent velocity amplitudes	44
2.5	Periods of kinetic energy oscillations	46
3.1	Schematic illustration of a cut through a spherical cloud	55
3.2	Plots of equation (3.5)	56
3.3	Comparison between the BE sphere and Dapp & Basu's model	58
3.4	Fit of column density of BE spheres with Dapp & Basus' model	60
3.5	Fits to B68	66
3.6	Fits to L1689B	68
4.1	Spatial profiles after second collapse	77
4.2	Disk formation close to the protostar with Ohmic Dissipation	79
4.3	Magnetic field lines on 10 and 100 AU scales	80
5.1	Column number density vs. radius over time	101
5.2	Volume number density vs. radius over time	103
5.3	Diffusion coefficient vs. central density for different grain sizes	105
5.4	Contributions to the effective resistivity	106
5.5	Ionization fraction vs. central density for different grain sizes	107
5.6	Fractional abundances of species for three smaller grain sizes	108
5.7	Fractional abundances for two larger grain sizes	109
5.8	Mass-to-flux ratio vs. radius for different grain sizes.	110
5.9	Evolution of B_z vs. radius over time	111
5.10	Evolution of B_r vs. radius over time	112

5.11	Evolution of Ω vs. radius over time	113
5.12	Evolution of v_r vs. radius over time	113
5.13	Disk formation	114
5.14	Magnetic field lines on 10 and 100 AU scales	115
5.15	Magnetic braking condition	116
5.16	Specific centrifugal radius	117
B.1	Core flattening	133
B.2	Evolution of Z vs. radius over time	133
B.3	Evolution of $f(r) \partial f / \partial r ^{-1}$ vs. Z over time	134
B.4	Definitions for the normal vector.	141
C.1	Barotropic pressure-density relation	151
C.2	Gravitational Field of a thin disk with finite thickness	157
C.3	Relative effect of thickness on gravitational field	158
C.4	Schematic diagram of pressure correction due to point mass	160
C.5	Flow chart: Code initialization	171
C.6	Flow chart: Main Loop	172
C.7	Flow chart: Numerical Step	173
D.1	Exponent k in $\rho \propto r^{-k}$ for the Lane-Emden equation	176
D.2	Mass vs. pressure for a Bonnor-Ebert Sphere	178

List of Tables

2.1	Velocity amplitude results for selected models.	45
5.1	Simulation model overview.	99
5.2	Output times in the evolution plots.	102

List of Appendices

Appendix A Rate Coefficients and Collision time scales	127
Appendix B Derivation of the thin-disk equations	131
Appendix C Implementation into the code	149
Appendix D The Bonnor-Ebert Sphere	174

List of Abbreviations

ACA	Atacama Compact Array
AD	Ambipolar Diffusion
ALMA	Atacama Large Millimeter Array
AMR	Adaptive Mesh refinement
AU	Astronomical Unit
BE	Bonnor-Ebert (Sphere, Model)
CMF	Core Mass Function
COBE	Cosmic Background Explorer
CR	Cosmic Ray
CSO	Caltech Submillimeter Observatory
ESA	European Space Agency
FIR	far-infrared
GMC	Giant Molecular Cloud
HD	Hydrodynamics, hydrodynamical
HST	Hubble Space Telescope
IMF	Initial Mass Function
IR	Infrared
IRAM	Institut de Radioastronomie Millimtrique
IRAS	Infrared Astronomical Satellite
ISM	Interstellar Medium
ISO	Infrared Space Observatory
IVP	Initial Value Problem
JCMT	James Clerk Maxwell Telescope
JWST	James Webb Space Telescope
LE	Lane-Emden (equation)
LHS	Left-Hand-Side
LOS	Line-Of-Sight

LP	Larson-Penston (Model, Solution)
MHD	Magnetohydrodynamics, magnetohydrodynamical
MRI	Magnetorotational Instability
MRN	distribution of grain sizes, named after Mathis, Rumpl, and Nordsieck
NSERC	National Science and Engineering Research Council
NIR	near infrared
OD	Ohmic Dissipation
ODE	Ordinary Differential Equation
PAH	Polycyclic Aromatic Hydrocarbon
PDE	Partial Differential Equation
POS	Plane-Of-the-Sky
RHD	Radiation Hydrodynamics, radiation hydrodynamical
RHS	Right-Hand-Side
RMHD	Radiation Magnetohydrodynamics, radiation magnetohydrodynamical
RMS	Root Mean Square
SCUBA	Submillimetre Common-User Bolometer Array
SF	Star Formation
SFE	Star Formation Efficiency
SIS	Singular Isothermal Sphere
SKA	Square Kilometer Array
SMA	SubMillimeter Array
SPH	Smoothed Particle Hydrodynamics
TVD	Total Variation Diminishing
UV	Ultra Violet
UWO	The University of Western Ontario
YSO	Young Stellar Object

List of Symbols

Symbol	Description	(Value and) Units
Σ	mass column density	g cm^{-2}
N	number column density	cm^{-2}
Ω	angular velocity	s^{-2}
ρ	mass volume density	g cm^{-3}
n	number volume density	cm^{-3}
T	temperature	K
$B_{z,\text{eq}}$	mid-plane vertical magnetic field component	G
$B_{\varphi,Z}$	azimuthal magnetic field component at $z = Z$	G
$B_{r,Z}$	radial magnetic field component at $z = Z$	G
L	angular momentum column density	g s^{-1}
μ	mass-to-flux ratio in critical units	dimensionless
c_s	sound speed	cm s^{-1}
v_A	Alfvén speed	cm s^{-1}
v_n	gas velocity of neutral species	cm s^{-1}
v_r	radial infall velocity	cm s^{-1}
v_φ	azimuthal velocity	cm s^{-1}
a_{gr}	grain radius	cm
M	mass	g
P	radial momentum	g cm s^{-1}
J	angular momentum	$\text{g cm}^2 \text{s}^{-1}$
Φ	magnetic flux	G cm^2
\dot{M}	mass accretion rate	$M_\odot \text{yr}^{-1}$
α	empirical viscosity coefficient	dimensionless
M_\odot	Solar mass	$1.989 \times 10^{33} \text{ g}$
R_\odot	Solar radius	$6.957 \times 10^{10} \text{ cm}$
A_V	visual extinction	mag
pc	parsec	$3.086 \times 10^{18} \text{ cm}$
AU	astronomical unit	$1.496 \times 10^{13} \text{ cm}$

Symbol	Description	(Value and) Units
g_r	radial gravitational acceleration	cm s^{-2}
M_\star	mass of protostar	g
W_\star	added weight of gas column due to extra squeezing of protostar	$\text{g cm}^{-1} \text{s}^{-2}$
m_H	mass of atomic hydrogen	$1.6738 \times 10^{-24} \text{ g}$
r	radial coordinate	
φ	azimuthal coordinate	
z	vertical coordinate	
k_B	Boltzmann's constant	$8.6173 \times 10^{-5} \text{ eV K}^{-1}$ $1.3806 \times 10^{-16} \text{ erg K}^{-1}$
G	gravitational constant	$6.6743 \times 10^{-8} \text{ cm}^3 \text{ g}^{-1} \text{ s}^{-2}$
q	electrical charge	ESU = $3.335 \times 10^{-10} \text{ C}$
γ	ratio of specific heats	dimensionless
C_P	heat capacity for an isobaric process	J K^{-1}
C_V	heat capacity for an isochoric process	J K^{-1}
Ψ	gravitational potential	$\text{g}^3 \text{ s}^{-2}$
Θ	magnetic scalar potential	$\text{g}^{1/2} \text{ cm}^{1/2} \text{ s}^{-1}$
\mathcal{M}	integral kernel appearing the thin-disk Poisson equation	
$K(k)$	Complete Elliptic Integral of the first kind	
$E(k)$	Complete Elliptic Integral of the second kind	

Chapter 1

Introduction

1.1 Preliminaries and overview

Star formation (SF) research is a young and very active field of study. There are still many open questions of great importance, some of which will be briefly described in the following sections. This Thesis starts with a discussion of molecular gas clouds and structures therein. It will then focus on prestellar cores and their properties, and subsequently turn to their evolution to the next stage, class 0 protostars, and conclude with prospects of theoretical star formation research for the future.

All discussion will be about low-mass star formation ($\lesssim 3 M_{\odot}$). High-mass star formation was thought to be conceptually different only two decades ago (Shu et al., 1987; Lizano and Shu, 1989), after Herbig (1962) introduced the idea of *bimodal star formation*. Today, it is essentially believed that high-mass SF is mostly based on the same processes as its lower-mass counterpart, scaled up, with the help of geometrical factors such as non-spherical accretion (e.g., Keto and Wood, 2006). In order to assemble much greater masses in the same time frame, the accretion rate must be greater by a factor of up to $\approx 10^3$. All gravitational energy released during the accretion must escape as radiation, and radiation pressure on dust and gas becomes significant. Additionally, the high-energy photons emitted by high-mass protostars will create a compact HII region opposing further accretion. Both effects necessitate a detailed treatment of radiative transfer, which greatly complicates the study. From an observational point of view, the general scarcity and short lifetimes of high-mass stars compared to their low-mass siblings brings about the problem that high-mass star formation sites are generally located much

¹The ghazal in the epigraph and its translations are taken from the book “Divan-e Hafiz”, Deluxe Edition, 2nd edition, 2006, Kalhor Publishing House, Tehran, Iran. The German translation is by Johann Christoph Bürgel; no author is given for the English translation.

further away from our solar system. Furthermore, the rapid evolution of high-mass protostars causes them to ignite the hydrogen fusion while still being obscured by a thick envelope. It is thus very difficult to observe very young massive stars. To date, the detection of high-mass analogues of prestellar cores remains controversial (Motte et al., 2007, 2010).

In this Thesis, we study processes most likely occurring in *all* stars, but focus on the formation of low-mass stars since there exists a great abundance of observations with which to test our models.

1.2 From clouds to cores

1.2.1 Lifetimes of molecular clouds

It has been well established that the conversion rate of gas contained in the Galaxy’s spiral arms into stars must be only a few percent per free-fall time. If the gas was to collapse into stars in a free-fall time, the Galaxy would have been depleted of gas long ago. However, we observe large amounts of gas in the interstellar medium (ISM). In fact, the largest coherent structures in the Galaxy are dense clouds of molecular gas, called Giant molecular gas clouds (GMCs), and each containing $\approx 10^6 M_{\odot}$ of predominantly H_2 .

In the “standard” picture of the onset of star formation, those clouds originally have a subcritical mass-to-flux ratio (i.e., are magnetically dominated, see Section 1.3.2) and evolve in $\approx 10 t_{\text{dyn}}$, the ambipolar diffusion timescale (ambipolar diffusion is explained in Section 1.2.2 below) until enough flux has been dissipated so that they become supercritical and they can collapse under self-gravity in $\approx 1 t_{\text{dyn}}$ (e.g., Mestel, 1965; Mouschovias, 1976; Shu et al., 1987). Here, $t_{\text{dyn}} \propto (G\rho)^{-1/2}$ is the free-fall time at the density ρ . In recent years, this picture has been challenged by various observations. Firstly, all known GMCs harbor star formation. If the time to form cores really was 10 times longer than the time for collapse of the cores, one would expect a number of clouds in a dormant state, devoid of star formation. Furthermore, Tafalla et al. (e.g. 1998) and Walsh et al. (2006) found evidence in cores for infall motions at large radii, consistent with supercritical core collapse (e.g., Basu and Ciolek, 2004). Also, the ages of pre-main-sequence stars within clouds (≈ 1 Myr) are presumed to be too small (Hartmann, 2001) to be explained by the standard model, which proposes that GMCs live for at least several t_{dyn} (≈ 10 Myr). These points suggest the picture of cloud evolution through slow contraction moderated by strong magnetic fields may need to be modified to fit most GMCs. However, there

are notable exceptions. One is Taurus molecular cloud, which Elmegreen (2007) suggests as a possible example where the “standard” picture indeed could apply. Goldsmith et al. (2008) and Heyer et al. (2008) show striations in Taurus’ envelope that seem to be aligned perfectly with optical polarization measurements of the magnetic field. This could indicate that motions parallel to the field lines are in progress, consistent with a magnetically-dominated envelope.

An alternative picture is that of short-lived molecular clouds, in which rapid star formation takes place. This view is promoted by supporters of turbulence-regulated star formation (Elmegreen, 2000; Palla and Stahler, 2000; Hartmann, 2001; Hartmann et al., 2001; Padoan and Nordlund, 2002; Klessen et al., 2005). The ISM is pervaded by supersonic motions, possibly on a large scale. As a collective, these motions are commonly referred to as “turbulence”, even though they probably have not much in common with the familiar “eddy-like” turbulence of incompressible fluids. If not replenished, those motions decay in $\lesssim 1 t_{\text{dyn}}$ (Mac Low et al., 1998). Potential “small-scale” driving sources could be supernovae, HII regions, stellar winds, or jets. Galactic sources could include effects such as instance spiral density waves, and galactic shear. Cloud formation in this paradigm is thought to be triggered by the collision of large-scale flows in the diffuse (atomic) ISM (e.g., Hartmann, 2001), as opposed to assemblage by flows along magnetic field lines (e.g., by the Parker instability, Parker, 1966; Mouschovias, 1974). Critics cite the fact that GMCs do not show any large-scale expansion or dispersal motions, which would be required to explain the destruction of clouds after stars have formed. Also, quiescent regions such as the Taurus molecular cloud do not fit this picture. In the following Sections the initial conditions of star formation are discussed in greater detail.

Magnetic field measurements help little in deciding between the long- and short-lived GMC picture. Core envelopes, highly ionized by incident UV light, are found to be subcritical (Cortes et al., 2005; Heyer et al., 2008), while cores themselves, shielded by their high column density, are not (Crutcher and Troland, 2007). In fact, direct measurements of the magnetic field strength in cores (e.g., Troland et al., 1996; Crutcher, 1999) and magnetic field morphology around cores (e.g., Cortes and Crutcher, 2006) seem to indicate that they are supercritical. It is not well established what value the average mass-to-flux ratio in a whole cloud takes (see, e.g., Mouschovias et al., 2006). Opponents of the standard model cite the fact that no stable, subcritical core is known. Such condensations should exist for a long time during which they slowly increase the mass-to-magnetic-flux ratio. Proponents of the standard model on the other hand point out that cores are always expected to be supercritical and need not exist in a subcritical state for a long time (Mouschovias et al., 2006) since clouds as a whole are thought to have

mass-to-flux-ratios fairly close to critical (e.g. Elmegreen, 2007).

In a more general argument, Elmegreen (2007) proposes that all processes from the formation of GMCs down to core collapse work on close to a *local* dynamical time scale. Processes further down the line, at greater local density, happen faster than the ones preceding them, since $t_{\text{dyn}} \propto (G\rho)^{-1/2}$. Galactic star formation takes place over times set by the total mass in molecular form divided by the Galactic star formation rate ($\approx 10^8 - 10^9$ yr for CO — Zuckerman and Evans, 1974). Core evolution and star formation as the last step, in turn, proceeds very fast (several 10^5 yr — Onishi et al., 2002) because of higher densities. In this picture, star formation (especially high-mass) is so disruptive to its surroundings that the core envelope is dispersed (but not destroyed) in only a fraction of the dynamical time appropriate for that envelope. Elmegreen (2007) posits that, after a certain time lag, this dispersal triggers a second generation of star formation in a different location. This embraces the paradigm of slow envelope evolution under the influence of ambipolar diffusion (e.g., Mouschovias, 1991), but rejects the conclusion that molecular clouds are old. Elmegreen (2007) and Huff and Stahler (2006) refute the interpretation of observations to the contrary (see, e.g., Mouschovias et al., 2006) and claim for instance that the presence of older stars in star forming regions does not indicate that clouds as seen today are long-lived, but instead suggests that clouds have been contracting as a whole after the decay of their turbulent support. This would have caused the density to increase over time, and made the dynamical time for later generations of stars much shorter than for the first. Accordingly, Palla and Stahler (2000) call this “accelerating star formation” (but see Hartmann, 2001, for various caveats). The old stars observed are then remnants from a previous star formation episode. This model would require neither magnetic fields nor sustained turbulence, as all processes take place essentially on the time scale set by self-gravity (Elmegreen, 2000).

The resolution to the question about the formation of cores will be found in a combination of both ambipolar diffusion and turbulence (e.g., Smith and Mac Low, 1998; Balsara et al., 2001). Their fusion leads to “turbulence-enhanced ambipolar diffusion” (e.g., Heitsch et al., 2004; Li and Nakamura, 2004; Nakamura and Li, 2005; Kudoh and Basu, 2008; Basu et al., 2009a,b). Here, turbulent motions compress the gas and, while not able to overcome magnetic forces in a subcritical cloud unless they are super-Alfvénic (Basu et al., 2009a), increase the local rate of ambipolar diffusion dramatically, and hence decrease the time for the core to become supercritical and collapse due to self-gravity. In that case, collapse is not delayed much beyond t_{dyn} . This is also discussed in Section 1.3.2.

In any case, a reasonable theory for cloud life times and star formation must explain

the observed low efficiency of star formation (e.g., Williams and McKee, 1997). The “turbulence-dominated” scenario claims that cores form by turbulent compression, at which point gravity takes over (see, e.g., Klessen et al., 2005). The remaining material is moving about too quickly to be accreted, has too little self-gravity (Elmegreen, 2000), or is dispersed by stellar feedback mechanisms. The “standard model” on the other hand invokes magnetic forces to hold up the core envelope and keep it from accreting onto the protostar (see, e.g., Basu and Mouschovias, 1994). Future observations and refined models considering both contributions will have to settle this dispute.

Recently, observational and theoretical indications have been put forward that the effect of ambipolar diffusion may soon come into reach of being observed directly (Li and Houde, 2008; Tilley and Balsara, 2010). The authors link the ambipolar diffusion length scale $L_{AD} = v_A \tau_{in} \rho_n / \rho_i$ with the scale of turbulent dissipation. Here, v_A is the Alfvén velocity, τ_{in} is the ion-neutral collision time, and ρ_i and ρ_n are the ion and neutral density, respectively. Below this scale, Alfvén waves (and other magnetohydrodynamical waves as well) suffer strong damping (see Balsara, 1996). Li and Houde (2008) find an ambipolar diffusion scale of ≈ 360 AU. ALMA will make this scale observable, so one can hope for new insights into the relative importance of magnetic fields and turbulence in not too distant a future.

1.2.2 Constituents of the ISM

The four constituents matter and radiation, gravity and magnetic fields make up the ISM. Each can play a bigger or smaller role in a given region, depending on various conditions.

The gravitational field depends on the amount of matter present, and there is a consensus that it is the main driver of all star formation (Mestel, 1965; Larson, 2003; Bonnell et al., 2007; McKee and Ostriker, 2007; André et al., 2009). There is some argument that molecular gas clouds as a whole (e.g., Hartmann et al., 2001) and some prestellar cores may be transient and not be gravitationally bound (e.g., André et al., 2009), but even most advocates of the turbulent star formation paradigm concede that gravity takes over once a dense core is formed (e.g., Ballesteros-Paredes et al., 2003; Mac Low and Klessen, 2004, but see also for instance Padoan and Nordlund, 2002 for a different view).

The matter making up the ISM can be split into three parts again, in particular gas, dust, and electrons. The most abundant elements in the gas are, in descending order, hydrogen ($\approx 90\%$ in number), helium ($\approx 10\%$), and carbon and other “metals” (traces), a term which encompasses all elements heavier than helium. These higher elements are

of great importance. Not only do they provide the building material for what is called “dust”, which accounts for $\approx 1\%$ of the total mass in the ISM due to their high specific mass, they also are the source of most of the free electrons in the ISM because they are comparatively easy to ionize.

In regions where the density is high enough and the temperature is sufficiently low, most of the gas is in molecular form. Over 160 molecules have been identified in the ISM by their spectrum to date. The simplest and most abundant molecule is H_2 , even though its emission lines are not found in molecular clouds. The temperature in those very cold regions typically is not high enough to excite those transitions, as they lie in the optical and UV range. Furthermore, H_2 is a symmetric molecule and does not have any rotational transitions observable at submillimeter (submm) wavelengths for which molecular clouds are transmissive. The second-most abundant molecule is CO, which is important for instance for its strong dipole moment. However, observed molecules can be made of more, even dozens, atoms (e.g., Methanol, CH_3OH , or the Fullerenes C_{60} and C_{70} , Cami et al., 2010). From their collective emission behavior, so-called polycyclic aromatic hydrocarbon (PAH) molecules have been identified, which might have hundreds of carbon atoms in dozens or even hundreds of benzene rings (see, e.g., the reviews by Puget and Léger, 1989; Tielens, 2008).

The term “dust” includes all collections of molecules loosely bound to each other. They form grains that can range in size from mere nanometers to millimeter sizes and greater. Dust is of pivotal influence for the interstellar radiation field. As opposed to individual molecules, dust is not destroyed by hard UV radiation (for instance from OB associations) but instead absorbs these photons and re-radiates them in longer wavelengths. Even though there are comparatively few dust particles in the ISM, their emission provides effective cooling to the densest regions of molecular clouds, even more so than atomic and molecular line emissions, which tend to be reabsorbed if the density is sufficiently high. This cooling is so efficient that GMCs are the coldest objects known, and temperatures reach as low as 6 K in the densest cores (Galli et al., 2002). The average temperature in molecular clouds where stars are forming range between 10 – 20 K (e.g., see the review by Larson, 2003).

Free electrons and ions play an important role for the magnetic field, as they (particularly the electrons) gyrate around the field lines and re-induce the field. A tiny drift between electrons and the positively-charged ions suffices to set up large-scale magnetic fields. Whether they are produced by the enhancement of a primordial magnetic field in the protogalaxy or a large-scale Galactic dynamo, magnetic fields are omnipresent the Galaxy. They are predominantly oriented along the Galactic spiral arms (see, e.g., Han

and Zhang, 2007) and can have a strong impact on molecular cloud dynamics. In regions with a sufficiently high ionization fraction, frequent collisions between neutrals and charged species couple the magnetic field effectively to the neutral matter, that drags the field along. Vice-versa, the neutrals feel the influence of the field through collisions, even though the Lorentz force does not affect them directly. If the magnetic force dominates self-gravity, cores are supported against gravitational collapse. Evolution then happens on a diffusive time scale, with neutrals slowly drifting past the ions held in place by the magnetic field. This process is called *ambipolar diffusion* in an astrophysical context¹ (Mestel and Spitzer, 1956; Mestel, 1965; Mouschovias, 1977). When sufficient magnetic diffusion has taken place and the mass-to-flux ratio has surpassed the critical value (e.g., Nakano and Nakamura, 1978) collapse ensues, albeit slower than under free-fall conditions. This retardation also occurs when the field is significant but does not suffice to balance gravity. In regions with too few ions to couple to the neutrals effectively by collisions, or with a very weak magnetic field, other phenomena such as turbulence dominate the dynamics.

Finally, as the fourth constituent of the ISM, the interstellar radiation field comprises of photons, their wavelengths ranging from Radio to hard X-rays, and charged particles that constitute the so-called cosmic rays. Cosmic rays (CRs) are mainly electrons and protons that are accelerated (the mechanisms of which are still controversial) to very high energies, and pervade the ISM. They can penetrate into even the densest molecular cloud cores, where they maintain a low background ionization fraction ($\approx 10^{-8}$ at $n \approx 10^5 \text{ cm}^{-3}$ — Hezareh et al., 2008). X-Rays are emitted by radioactive processes in the ISM, but also by nearly all main-sequence stars (Güdel and Nazé, 2009), especially high-mass stars. Additionally, T-Tauri stars produce X-rays in their surrounding disks. X-rays do not have energies quite high enough, nor are they common enough, to play a major role in ISM dynamics. More important are UV photons that young stars and high-mass stars emit in large quantities. Hard UV radiation can ionize hydrogen, while less-energetic UV photons still carry significant momentum. They exert pressure on the surrounding gas and drive stellar winds, which in turn can influence the ISM dynamics, in particular close to OB associations. UV and optical photons also get absorbed and reprocessed by dust particles and large molecules such as PAHs, i.e., are re-emitted at longer wavelengths. Vibrational and – at still lower energies and also for smaller molecules – rotational modes are excited. This means that molecular clouds are opaque to optical radiation. They appear as dark “holes in the sky” against a backdrop of stars. However, the extinction

¹in plasma physics, the term refers to a situation where ions and electrons are tethered electrostatically, rather than magnetically (Chen, 1984)

decreases with increasing wavelength of radiation, and indeed, the clouds are transmissive to submillimeter radiation (Stahler and Palla, 2005). In fact, the peak of blackbody emission at the temperatures prevalent there (20 – 30 K) occurs at $\approx 100 - 150 \mu\text{m}$. Much of star formation research therefore relies on observations in the submillimeter and millimeter regime. Finally, the radio regime contains one of astronomy’s most famous spectral lines, the hyperfine transition of HI gas at 21 cm. With it, the temperature and density distribution of neutral hydrogen gas can be traced in the Galaxy and beyond. Lastly, the Cosmic Microwave Background (CMB) is remnant emission from the surface of last scattering in the early universe.

1.2.3 Non-thermal motions in the ISM

Linewidths suggesting supersonic motions have been measured in the ISM and GMCs early on (see the review by Zuckerman and Palmer, 1974). They can be described by the famous “linewidth-size relation”. Larson (1981) showed that the velocity dispersion increases as one studies larger and larger structures. His scaling law of $\sigma_v \propto L^{0.38}$, reminiscent of Kolmogorov turbulence, was later updated to be closer to $\propto L^{0.5}$ (Myers, 1983; Solomon et al., 1987). This power-law relationship between the two quantities is consistent with virial equilibrium, rather than with a turbulent cascade as in the eddy-like incompressible Kolmogorov turbulence. Since the ISM instead is a strongly compressible medium, the nature of the supersonic motions probably more closely resembles Burgers turbulence (see the review by McKee and Ostriker, 2007), where energy is dissipated in strong shocks and by excitation of waves. If a magnetic field is present, its capacity to be the host of various waves is crucial to this process. The observable effect of this “turbulence” is a broadening of spectral lines.

It was suggested that the observed supersonic motions could be long-lived magneto-hydrodynamical (MHD) waves, in particular Alfvén waves, as those are non-compressive and therefore not dissipated in shocks (e.g., Arons and Max, 1975). In contrast, Stone et al. (1998) argue that interaction of Alfvén waves would still excite compressive MHD motions and dissipate at least part of their energy. Another possible magnetic-field-related explanation is explored in Chapter 2 of this Thesis, namely that of magnetic-tension-driven modes induced by the interaction of the cloud’s magnetic field with that anchored in an external low-density and environment. Some simulations include super-Alfvénic turbulence (e.g., Padoan and Nordlund, 2002; Mac Low and Klessen, 2004, and references therein) in which case, the magnetic field would not play a major role in the dynamics no matter what its strength was until the turbulence had dissipated.

Whatever their source, the turbulent motions need steady kinetic energy input on both large scales and small scales, as they decay on time scales roughly comparable to a sound crossing time of the system Stone et al. (1998); Mac Low et al. (1998); Mac Low (1999); Ostriker et al. (2001). It is not clear what this input is precisely. Hartmann (2001) suspects large-scale flows in the ISM, while Klessen et al. (2005) favor supernovae, but there might also be other contributors such as Galactic shear and flows due to the Parker instability on large scales, or stellar feedback on a smaller scale. Recent models, such as Nakamura and Li (2008) include ad-hoc feedback effects from jets and outflows to simulate small-scale driving, while other authors such as Heitsch and Hartmann (2008) start with the assumption of large-scale colliding flows. Most of the turbulent energy is contained in the largest modes (Heyer and Brunt, 2007), possibly hinting at a driving mechanism on large rather than smaller scales.

In order to rule out or confirm the applicability of the magnetic theory or the turbulent paradigm for the early phase of star formation, decisive tests need to be devised. One possibility is to examine in detail column density profiles that the various models produce. Unfortunately these are not very strong discriminators between models, because only column density is observable, and thus any density distribution a theoretical model produces needs to be integrated along a line of sight in order to be compared with observations. Observational smoothing and averaging additionally smears out details. Many models produce approximately comparable column density profiles matching observed features. In fact, Ballesteros-Paredes et al. (2003) even arrived at BE sphere-like cores without any gravity, even though no a-priori physical reason explains this. In any case, the radial core structure does not necessarily discriminate clearly between the two extreme scenarios.

Chemistry is another way to select the most appropriate model. If one puts in a sophisticated chemical model, and evolves the model of the cloud all the way from purely atomic gas (e.g., Heitsch and Hartmann, 2008) all the way until core formation including a detailed treatment of radiation, observationally testable predictions of the chemical composition and the spatial distribution of molecules might be possible. This avenue must be pursued in future simulations.

Another approach lies in the velocity structure the different theories predict. André et al. (2009) review observational evidence that cores in Taurus and other regions that predominantly form low-mass stars are essentially non-turbulent (they feature spectral lines not broadened much beyond their thermal linewidths), and their immediate surroundings exhibit small velocity dispersions. This goes to show that those cores form in a quiescent environment, while “massive-star-forming regions” such as Orion and other

cluster-forming clouds show larger velocity dispersions, i.e. more “turbulence”. It seems that turbulent simulations (Padoan and Nordlund, 2002; Klessen et al., 2005, e.g.) produce motions too fast to be reconcilable with quiescent modes of star formation. Purely magnetic models in turn produce cores that take a long time to evolve and are too large to explain observations in some star forming regions (Bacmann et al., 2000). On the other hand, the hybrid simulations presented in Kirk et al. (2009), which include both supersonic initial velocities and subcritical to transcritical magnetic fields, show that sufficiently subsonic velocities within cores can be achieved with this approach. However, the core-to-core velocities are still larger than observed. These recent advances make it seem plausible that this major source of controversy around the detailed initial conditions of star formation can be settled in the coming years with new observations and new sophisticated simulations that include more of the relevant physics. As already stated in Section 1.2.1, a successful model for low-mass star formation (and possibly for high-mass star formation as well) will most likely involve both magnetic fields *and* turbulence.

1.2.4 Initial conditions of star formation

The general (and uncontroversial) initial conditions of star formation include a cold (≈ 10 K) molecular cloud, made up of about 90% hydrogen and 10% helium in number. This gas is assembled in a prestellar core, with clearly subsonic internal velocities. The core is about 0.1 pc in size, and contains a few solar masses of gas. It will be centrally condensed, with a central volume density of $\approx 10^6$ cm $^{-3}$, which has a profile resembling that of a Bonnor-Ebert Sphere (see Appendix D). The mass-to-flux ratio, even if it was subcritical ($\mu \lesssim 1$) or transcritical ($\mu \approx 1$) in the envelope, is supercritical in the interior of the core ($\mu \approx 2 - 3$). However, it is still far from the values found in main-sequence stars ($\mu \approx 10^6 - 10^8$ — McKee and Ostriker, 2007). This mass-to-flux ratio will have to be achieved in the collapse process (see Section 1.3.2). The cores most likely rotate slightly (at ≈ 1 km/s/pc) and thus will have to shed some angular momentum also, to collapse to stellar dimensions (see Section 1.3.1).

1.3 From cores to stars

This section is concerned with the formation of Class 0 protostars from prestellar cores and their evolution towards YSOs of Class I and higher.

In principle, a “realistic” simulation of the protostellar collapse problem should be radiation-magneto-hydrodynamical (RMHD) in nature and cover all three spatial di-

mensions. It should include non-ideal MHD effects such as ambipolar diffusion, Ohmic dissipation and the Hall effect, since without the first two, fragmentation and collapse can be (possibly spuriously) inhibited altogether (e.g., Hennebelle and Fromang, 2008). The simulation should also treat the thermodynamical effects of the collapse carefully, ideally with full wavelength-dependent radiative transfer. However currently, these requirements cannot yet all be fulfilled in one simulation, for computational reasons. The main limiting factor is resolution. Starting from GMCs (with average number density $n \approx 10^2 \text{ cm}^{-3}$) and going all the way to stars ($n > 10^{23} \text{ cm}^{-3}$), over 20 orders of magnitude in density are spanned. Similarly, linear scales extend from tens of pc to R_{\odot} (9 orders of magnitude), not accounting for possible effects of turbulence on even smaller scales. Velocities range from subsonic speeds of a core contracting potentially quasi-statically under the influence of ambipolar diffusion ($\lesssim 0.1 \text{ km/s}$) up to the high-speed jets that are launched with several hundreds of km/s. Finally, time resolution requirements also change dramatically. At least 7 orders of magnitude are covered from the dynamical time scale in GMCs (10^7 yr) down to mere months for the entire “second collapse” to happen (e.g., Larson, 2003; Machida et al., 2006), and jets to be launched. In cluster-forming environments, it is conceivable that extreme ends of the spectrum of these scales need to be monitored simultaneously, and the history of rapidly-evolving objects needs to be followed for a Myr or longer.

This makes reasonable approximations in various forms an inevitable necessity. One possibility is to restrict the model to fewer than three dimensions. Indeed, early models of cloud collapse were spherically symmetric. In the first half of the 20th century there were no computers available to solve the hydrodynamic equations in more complicated geometries. Hayashi (1966) hence relied on timescale arguments to make some statements about the nature of the collapse, which he suggested to proceed homologously and in free-fall. Early collapse computer models were presented by Bodenheimer and Sweigart (1968), Larson (1969) and Penston (1969). The so-called Larson-Penston (LP) solution started with a homogeneous initial state, which soon became quite non-uniform. They included a simple radiation treatment and also self-similar solutions for the spherically symmetric isothermal prestellar phase ($t < 0$). Hunter (1977) extended the LP solution to $t > 0$, i.e., after the formation of a central protostellar object.

Shu (1977) presented the self-similar “standard” model of star formation, starting with an analytical model called the Singular Isothermal Sphere model (SIS). He started from a static setting with a density profile $\rho_{\text{SIS}} = c_s^2 (2\pi Gr^2)^{-1}$ at $t = 0$ (the formation of the protostar) and calculated its collapse for $t > 0$. Terebey et al. (1984) extended the self-similar SIS model, adding rotation, while Galli and Shu (1993) included magnetic

fields (without rotation).

In spherical symmetry, as employed in the early computational models, rotation and magnetic fields cannot be taken into consideration, since these effects require a preferred direction (i.e., that of the rotation axis, and the mean field direction, respectively). Fiedler and Mouschovias (1993) showed in an axisymmetric numerical model that an initially spherical cloud quickly flattens under the influence of a magnetic field and assumes a disk-like geometry. The reason is that magnetic tension and magnetic pressure provide support against motions perpendicular to the field lines, but not parallel to them (see Appendix B). Similarly, when a rotating sphere contracts, it flattens along the axis of rotation, since the centrifugal force counteracts gravity perpendicular to it. This flattening motivates the use of yet another simplified geometry, the thin disk (see, e.g., Mouschovias and Morton, 1991; Ciolek and Mouschovias, 1993, 1994; Li and Nakamura, 2004; Basu and Ciolek, 2004; Ciolek and Basu, 2006). Here, all equations of hydrodynamics are integrated vertically over the z -direction. This approximation is valid as long as all quantities do not vary much in the z -direction. Regarding its applicability, e.g. Tassis and Mouschovias (2007) argue that thermal pressure smears out all density contrasts over a thermal scale length, and that the thickness of the sheet is always comparable in size to this scale length (see also Mouschovias, 1991).

Other models invoked axisymmetric cylindrical geometries; and some of those included magnetic fields and ambipolar diffusion (see, e.g., Nakano, 1979; Lizano and Shu, 1989).

Recent advances in computational facilities have seen the advent of large three-dimensional simulations. As recent examples, Bonnell et al. (2008) present hydrodynamical simulations using the “Smoothed Particle Hydrodynamics” (SPH) technique with 4.5×10^7 Lagrangian particles. This approach is intrinsically three-dimensional, naturally achieves high resolution in high-density regions, and can be integrated for a long time since it does not suffer much from time-step restrictions. These advantages come at the cost of being able to add the effect of magnetic fields with great difficulty only, as well as reduced resolution in low-density regions. Additionally, SPH modelers have to take care to capture shocks properly, while avoiding to introduce too much diffusivity into the system. In contrast, Machida et al. (2006) and Hennebelle and Fromang (2008) show MHD simulations on adaptive-mesh Eulerian grids with up to 21 levels of refinement (each a factor of 2 higher resolution than the previous), the former including Ohmic dissipation as a non-ideal MHD effect². An Eulerian grid-based simulation technique buys

²It may be noted that the first fully three-dimensional simulation including ambipolar diffusion and self-gravity (albeit not for the collapse problem but for studying the fragmentation of molecular clouds)

the extremely high resolution at any point of interest at the cost of only being able to integrate the solution for a severely limited time. It allows for an accurate treatment of most relevant physics, but is difficult to implement. The fact that both schemes still suffer from significant drawbacks make simulations with reduced dimensionality useful to focus on special problems (e.g., Basu et al., 2009a,b).

At low densities, clouds achieve very low temperatures (≈ 6 K — Galli et al., 2002) by atomic and molecular line cooling. A possibility for computational simplification came with the realization that the gas couples very closely to the dust at higher densities, and thus dust emission provides effective radiative cooling as long as the cloud stays optically thin. This means that dense cores are very nearly isothermal over a large range of densities (Hayashi, 1966; Larson, 1969; Narita et al., 1970; Winkler and Newman, 1980a,b). Masunaga and Inutsuka (2000) performed detailed RHD simulations in spherical symmetry which confirmed the results calculated earlier using a gray-approximation (see the review by André et al., 2009). In agreement with Tohline (1982) they found a density-temperature relation well approximated by a barotropic pressure-density relation with piecewise-constant ratios of specific heat γ instead of a sophisticated heat equation. This result is now widely used in hydrodynamical and MHD calculations to simplify the calculation of the temperature evolution of a collapsing core (e.g., Bate, 1998; Vorobyov and Basu, 2005; Machida et al., 2006; Bonnell et al., 2008). More recently, Stamatellos et al. (2007) and Krumholz et al. (2007) present fully three-dimensional RHD simulations, and criticize the use of the simple barotropic pressure-density relation. In the future it would be desirable to marry RHD calculations with non-ideal MHD calculations in one three-dimensional simulation code. However, this goal seems still unattainable in the next few years.

Regardless of which geometry was used and which physical effects were included (e.g., Larson, 1969; Narita et al., 1984; Ciolek and Mouschovias, 1993; Basu and Mouschovias, 1994), all models find a non-uniform dynamical collapse phase during which a r^{-2} density profile (e.g., Bodenheimer and Sweigart, 1968) develops in the nearly scale-free collapse for $t < 0$ (i.e., before protostar formation). This power law profile is also seen in equilibrium calculations such as the BE sphere (discussed in Section 3 and Appendix D).

In the following sections, two predominant problems of the theory of gravitational collapse will be discussed, which have been the focus of much attention over the last decades (see, e.g., the reviews by Hayashi, 1966; Shu et al., 1987; Larson, 2003). They are called the angular momentum problem and the magnetic flux problem.

was presented by Kudoh and Basu (2008).

1.3.1 Angular momentum problem

When a rotating sphere contracts, it flattens along the axis of rotation, since the centrifugal force counteracts gravity only perpendicular to this axis. If there is sufficient angular momentum present a centrifugally-supported, nearly Keplerian disk forms. Disks have played a major role in astronomy ever since it was discovered that the rotation of the planets in our Solar System takes place in co-planar orbits. Rotation was known to also play a role in the formation of Saturn's rings, as well as in the shape of spiral galaxies, and it was included in many simulations of star formation early-on (Larson, 1972; Bodenheimer, 1981, and references therein).

Rotation introduces the problem of *angular momentum transfer*. An average molecular gas cloud rotates at a rate of about 1 km/s/pc (see, e.g., Goldsmith and Arquilla, 1985; Goodman et al., 1993; Caselli et al., 2002). This rotation rate would increase significantly during collapse if angular momentum was conserved. The Sun as an example of a typical main-sequence star rotates with an average rotation frequency of about one revolution per month (at about $4.5 \times 10^{-7} \text{ s}^{-1}$), which is about 6 orders of magnitude smaller than if a cloud collapsed under the assumption of strict angular momentum conservation (as shown below). Note that even for large high-mass stars rotating close to break-up speed (e.g, Be-stars) all but 5% of the initial angular momentum must be removed during the star's formation process. The question is why stars rotate comparatively slowly, and therefore how angular momentum present in the parent clouds is dissipated.

The angular momentum per unit mass of a molecular cloud core can be calculated with the expression $j_{\text{core}} = \Omega_{\text{core}} r_0^2$. The average angular velocity of a core is $\Omega_{\text{core}} \approx 1 \text{ km/s/pc} \approx 3.3 \times 10^{-14} \text{ s}^{-1}$ (e.g., Caselli et al., 2002), while the average radius containing about $1 M_{\odot}$ is $r_0 \approx 0.1 \text{ pc}$. This yields

$$j_{\text{core}} \approx 3.3 \times 10^{-14} \text{ s}^{-1} (3 \times 10^{17} \text{ cm})^2 = 3.0 \times 10^{21} \text{ cm}^2 \text{ s}^{-1}, \quad (1.1)$$

whereas

$$j_{\text{star}} \approx \Omega_{\odot} r_{\odot}^2 = 4.5 \times 10^{-7} \text{ s}^{-1} (7 \times 10^{10} \text{ cm})^2 = 2.2 \times 10^{15} \text{ cm}^2 \text{ s}^{-1}. \quad (1.2)$$

Thus

$$j_{\text{core}} \approx 1.4 \times 10^6 j_{\odot}. \quad (1.3)$$

Hence, only a fraction of less than 10^{-6} of the angular momentum originally present in the core is retained in the star, while the rest has to be shed in some way.

After about all but 1% of the angular momentum of a cloud is dissipated, multiple

star systems or even planetary systems can account for the rest of the excess to observed typical stellar angular momenta. In fact, Lada (2006) showed that the probability for stars to form in multiples increases with mass and therefore greater angular momenta in the parent clouds (as they are larger). Planetary systems can also take up some of the excess angular momentum. In our Solar System, the Sun contains 99% of the mass, but 99% of the angular momentum is held in Jupiter and Saturn. Note that both of their orbits are presumably within the centrifugal barrier of the Solar System's parent core, which can be estimated to be ≈ 15 AU (Basu, 1998). This means that the material making up the planets could not have reached its present location unless it had lost most of its angular momentum during the formation of the Solar System.

Many mechanisms have been proposed for angular momentum transfer in collapsing cloud cores, as well as at later stages of the evolution, once protostars and surrounding protoplanetary disks have been formed. One of the most generic descriptions for this effect was proposed by Shakura and Sunyaev (1973) and Lynden-Bell and Pringle (1974). They suggested viscous dissipation in a differentially-rotating disk to cause angular momentum to be redistributed. However, the microphysical origin of this drag is unknown. The classical mechanical viscosity is orders of magnitude too small to account for the observed mass accretion rates. In absence of a physical model, an empirical quantity called α -viscosity was introduced. Its value was chosen to explain the deduced accretion rates, and it represents a generic source of viscous drag but it is not indisputably identified with any specific physical phenomenon. One of the most promising candidates is the so-called *magnetorotational instability* (MRI, Balbus and Hawley, 1991), an instability in a differentially-rotating disk threaded by a weak magnetic field. However, any of the other mechanisms described below can also be parametrized by an α -viscosity. The basic mechanism of the MRI is as follows: a parcel of gas is displaced outwards and slowed down from its equilibrium orbit. However, it is tethered magnetically to another parcel which still rotates at the initial speed. This second parcel is slowed down by the link, loses centrifugal support, and drops to a lower orbit. At the same time, the originally-displaced parcel is pulled to accelerate, whereby it increases its angular velocity and moves to an orbit further out. Since the disk rotates differentially, this exacerbates the problem and leads to angular momentum transport from the inner parcel to the outer one. This effectively constitutes a torque on the cloud.

Magnetic fields (which are omnipresent in the Galaxy and the ISM) are responsible for some spin-down in collapsing cores and disks. Magnetic field lines twist if they are dragged along with the matter rotating about a central object. This twisting causes torsional waves to propagate along the magnetic field lines (e.g., Mestel and Spitzer,

1956; Basu and Mouschovias, 1994), taking some angular momentum with them. The net result of this effect, termed *magnetic braking* is that the disk spins down while envelope material above the disk gains the excess angular momentum. This phenomenon requires coupling between the ions and the neutral species both in the disk (in order to achieve a significant twist and thus magnetic tension) as well as in the extended and tenuous envelope (in order to provide a sink to absorb the angular momentum removed from the disk). The latter is not a matter of great debate since the low-density regions of the ISM are relatively well ionized due to their transparency to UV radiation. In addition, the rarefied envelopes that can absorb excess angular momentum contain more matter than the dense regions. The former requirement depends on the ionization fraction within the dense parts of the disk, as well as on magnetic field strengths. Observations currently do not constrain either stringently. Magnetic braking is discussed further in Chapters 4 and 5.

Pudritz and Norman (1983) proposed that excess angular momentum is shed through outflows launched from the protostellar disk as another mechanism. As frozen-in magnetic field lines are tightly wound up around the rotation axis of a spinning protostar, an outflow or jet is launched. Material might be flung out on spiraling trails and carry away some angular momentum.

There is yet another idea of angular momentum transport which does not require magnetic fields, but relies on gravity alone. Disks are not perfectly axisymmetric but rather contain nonaxisymmetries such as spiral structure (e.g., Fukagawa et al., 2004; Vorobyov and Basu, 2006) that gives rise to gravitational torques (Larson, 1984; Vorobyov and Basu, 2006). The concept behind these torques is relatively simple, and resembles that of the MRI discussed above: in a centrifugally-supported disk, material closer to the axis of rotation moves faster than material further out. This differential rotation has the effect that a clump of gas on a close orbit is slowed down by the gravitational pull of a clump further out. The clump further out is accelerated slightly by the tug of the fast, inner clump; it receives additional centrifugal support and expands its orbit. The inner clump on the other hand is decelerated, cannot maintain its orbit due to the reduced centrifugal support and has to move further in. Vorobyov and Basu (2006) demonstrated that this phenomenon can be quite effective in transporting angular momentum and may in fact give rise to FU Ori-like outbursts when clumps that form in the disk are sufficiently decelerated to fall onto the protostar.

Over the last three decades, many authors have published simulations that included rotation. One of the first was Larson (1972), who had already pioneered the spherical collapse calculations. In his axisymmetric model he found the formation of rings, which

he hypothesized to fragment into a binary or multiple system later on. Later, however, Norman et al. (1980) attributed this ring formation to insufficient resolution and diffusive numerical schemes and showed that no ring instability developed with their more accurate and less diffusive algorithm for advecting the angular momentum. Toomre (1981) showed that axisymmetric disks indeed *are* generally susceptible to ring formation if the dimensionless parameter $Q = c_s \Omega / (\pi G \Sigma)$, now called Toomre parameter, fell below a certain value. In this definition, c_s is the sound speed (representing the effect of thermal pressure), Ω is the angular velocity (signifying rotational support), and Σ the column density (gravity working to contract the disk). The exact number for the critical value of Q depends on the exact conditions, geometry and equation of state among other things. As a general guideline it can be stated that a disk is unstable if $Q \lesssim 1$ (Vorobyov and Basu, 2006). Hayashi et al. (1982) and Toomre (1982) independently published a family of analytical solutions for rotating disks, that both led to a column density profile now called the *singular isothermal disk* (SID). This state with infinite density at the center is expected to be reached for fast rotation, and results in a very thin disk. However, Narita et al. (1984) and Saigo and Hanawa (1998) presented numerical simulations and self-similar solutions showing that rotation is unimportant for support of realistic prestellar cores against collapse. Basu and Mouschovias (1995a,b) demonstrated that, in fact, a centrifugally-supported disk (i.e., rotational acceleration balancing gravitational acceleration) cannot form at all in a core unless there is a central object that effectively provides a point-mass-like gravitational potential. This means that a gravitationally unstable prestellar core will always collapse to form a star, even if it has some finite rotation. After point-mass formation most of the mass ends up in a disk rather than the central object, when matter hits its *centrifugal radius* $r_{\text{cf}} = j^2 / GM_\star$. Here $j = \Omega r^2$ is the specific angular momentum of the gas parcel, and M_\star is the central object's mass.

Rotation is also responsible for the formation of binaries and systems of multiple stars. For instance, Durisen et al. (1986) calculated the conditions for protostellar disks to succumb to dynamic instabilities as a consequence of nonaxisymmetric perturbations. This can cause fragmentation during the collapse, and fission into binary systems.

In fully three-dimensional simulations (e.g., Bate, 1998; Bonnell et al., 2008), and particularly in turbulent ones (see, e.g., Klessen et al., 2005), rotation is usually not introduced explicitly but occurs naturally because of random motions.

Shu et al. (1987) hypothesize that self-regulating mechanisms are at work in astrophysics that ensure that certain phenomena function the way they do. Lack of such self-consistent means of regulation would make significant fine-tuning seem necessary, which is generally unsatisfactory. They give the example relating to the thermonuclear

fusion processes in the center of stars. They suppose that a process exists that stops accretion once the star has obtained sufficient mass to burn hydrogen in its core. This problem is very important for the formation of massive stars, and may be connected with radiation pressure. However, the concept of self-regulation is more general and can easily be extended to other phenomena. The evolution of angular momentum in prestellar cores, protostars, and YSOs is certainly one of them. Lin and Pringle (1987) for instance presented a self-similar solution for disk evolution in which Q is regulated to be always close to the critical value of unity.

In recent years, a problem diametrically-opposing the angular momentum problem has been pointed out. It was shown that, when flux freezing is assumed, magnetic braking is so effective in removing angular momentum from the core that large-scale ($\approx 10^2$ AU) centrifugally-supported protoplanetary disks — ubiquitously observed around YSOs — can no longer form (Allen et al., 2003; Mellon and Li, 2008; Hennebelle and Fromang, 2008). This remained a problem even when ambipolar diffusion was included (Mellon and Li, 2009), and the effect has been labelled “catastrophic magnetic braking”. Hennebelle and Ciardi (2009) demonstrated that inclination effects can modify the efficiency of magnetic braking, but a supercritical mass-to-flux ratio by a factor $> 3 - 5$ (i.e., a weak magnetic field) was still required to form a large-scale disk. Dapp and Basu (2010) (see Chapter 4, and also Chapter 5) show that Ohmic dissipation can annul magnetic braking so that a disk can still form, albeit at small scales.

It is evident that the angular momentum problem is closely interconnected with the issue of magnetic flux discussed in Section 1.3.2. The decisive resolution to the angular momentum problem remains elusive even though a combination of all the above mechanisms is likely.

1.3.2 Magnetic flux problem

Magnetic fields have direct effects only on charged species (electrons, and ionized grains, molecules, and atoms) and make them gyrate around the field lines. However, if the neutral and ionized portions of the gas are sufficiently well coupled through collisions, magnetic forces are effectively exerted on all constituents of the gas. This is the case for ionization fractions as low as 10^{-7} ($n_n/10^4 \text{ cm}^{-3}$) $^{-1/2}$ (assuming ionization primarily due to cosmic rays). The reason why such a low ionization fraction still makes for good coupling lies in the fact that H_2 is a highly-polarizable molecule. This raises its effective collision cross section with ions by a factor of $\approx 10^2$ over the geometric cross section (Osterbrock, 1961; Mestel, 1999).

If this coupling is very efficient, the magnetic field is said to be “frozen into the gas”, because it is dragged along as the gas moves about. The magnetic flux per unit area stays constant even though it is still possible to move matter parallel to the field lines. In the case of poor coupling, neutral particles are only mildly impeded by collisions with ions tied to the field and can drift past them. This phenomenon is referred to as *ambipolar diffusion* (Mestel and Spitzer, 1956; Mouschovias, 1976; Shu et al., 1987, see also Section 1.2.2).

Similar to the angular momentum, there is a lot less magnetic flux observed in main sequence stars than could be expected if a gas cloud collapsed under magnetic flux conservation (“flux freezing”). A well-known relation exists between the line-of-sight magnetic field strength and the column density. It holds over several orders of magnitude in both quantities and is found in almost all clouds (see Basu, 2005). It is consistent with the relation

$$\frac{\Sigma}{B} = \mu (2\pi G^{1/2})^{-1}, \quad (1.4)$$

where Σ is the column mass density and B is the magnitude of the magnetic field. The gravitational constant has its usual symbol G , and μ is the dimensionless *mass-to-flux ratio* in units of the critical value required for collapse $(2\pi G^{1/2})^{-1}$ (Nakano and Nakamura, 1978). If $\mu < 1$ the object is said to have a *subcritical* mass-to-flux ratio, and the influence of the magnetic field is stronger than gravity. Such a cloud core is supported against collapse by magnetic restoring forces (see, e.g., Kudoh and Basu, 2008; Basu et al., 2009a). Conversely, conditions are said to be *supercritical* if $\mu > 1$. In this case, gravity will overwhelm magnetic pressure and tension, and a cloud core will collapse, even though the non-vanishing influence of the magnetic field will still retard the collapse (e.g., Ciolek and Mouschovias, 1993).

On average, μ is found to be close to unity (cf. Fig. 1.1) in molecular clouds, which means that the magnetic field almost balances the gravitational field over significant portions of the clouds and a large range of scales. Thus, for an average cloud core (which needs to be at least critical to collapse), the following integrated relation approximately holds for the mass M and the magnetic flux Φ (where the mass and magnetic flux are obtained by integrating over a surface element):

$$\frac{M}{\Phi} \approx (2\pi G^{1/2})^{-1}. \quad (1.5)$$

For a $1 M_{\odot}$ cloud core we find

$$\Phi_{\text{core}} \approx 2\pi M_{\odot} G^{1/2}. \quad (1.6)$$

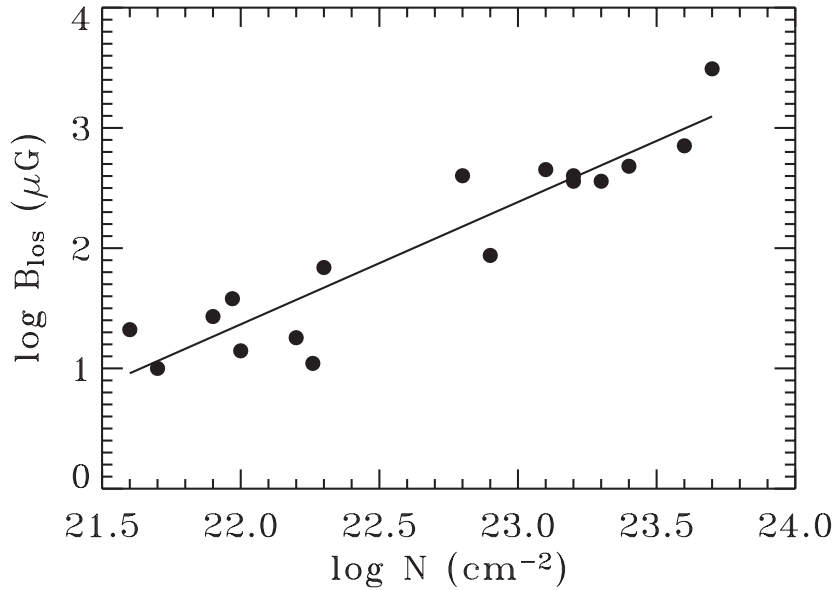


Figure 1.1: Observed relation between line-of-sight magnetic field strength and column number density (Basu, 2005, with data from Crutcher, 1999). The best fit to the data (solid line) is consistent with $\mu \approx 1$.

For our Sun, the magnetic flux is given by

$$\Phi_{\odot} \approx \pi B_{\odot} R_{\odot}^2, \quad (1.7)$$

where B_{\odot} is the mean solar magnetic field (≈ 1 Gauss), and R_{\odot} is the solar radius. Then the ratio between the two is

$$\frac{\Phi_{\text{core}}}{\Phi_{\odot}} \approx \frac{2M_{\odot}G^{1/2}}{B_{\odot}R_{\odot}^2} \approx 3 \times 10^8. \quad (1.8)$$

This order-of-magnitude calculation shows that all but a very small fraction of the magnetic flux has to be dissipated during the collapse in order to arrive at conditions typical for stars. Even for peculiar magnetic stars with mean fields of order 10^5 Gauss (e.g., Borra and Landstreet, 1978) only 0.1% of the flux is retained. The question why so little magnetic flux is observed in main sequence stars remains unanswered in detail. The following discussion will highlight some possible mechanisms of flux loss.

One mechanism for removing magnetic flux is Ohmic dissipation (e.g., Li and McKee, 1996; Mohanty et al., 2002). It has been shown to operate effectively in the density range of $n \approx 10^{12} - 10^{16} \text{ cm}^{-3}$ (e.g., Nakano et al., 2002). This process considers the decay of the magnetic field by collisions between charged particles and neutrals which may knock

the charged particles off their gyration path around the magnetic field lines (Mohanty et al., 2002). Without further self-induction, the magnetic field is weakened. It effectively introduces a finite effective electrical resistance, which is why the theory is called resistive non-ideal magnetohydrodynamics. Machida et al. (2006) quote a reduction in magnetic flux by a factor of 10^3 in a resistive collapse compared to flux-frozen collapse. This process is independent of magnetic field strength and may be one of the contributing factors to the solution of the magnetic flux problem. Chapter 4, published as Dapp and Basu (2010) also studies this problem.

The most prominent mechanism of flux loss, ambipolar diffusion, was proposed by Mestel and Spitzer (1956). It received much attention between the late 1970s and the late 1990s. Mouschovias (1977) demonstrated ambipolar diffusion to be important between 10^4 and 10^{11} cm^{-3} . He proposed a long-lasting quasi-static phase of core contraction on the ambipolar-diffusion time scale (Nakano, 1984; Shu et al., 1987; Mouschovias, 1991), while magnetic forces support the core against gravity. After the core became critical dynamical and rapid collapse would ensue. The idea of quasi-static contraction is somewhat controversial today, and probably more applicable to core formation rather than core collapse. However, ambipolar diffusion is indeed credited for initiating collapse from an initially magnetically-supported state (Mouschovias, 1979; Shu et al., 1987; Basu and Mouschovias, 1994; Kunz and Mouschovias, 2009, 2010). If conditions in the parent clump are initially subcritical, contraction can only occur as a consequence of ambipolar diffusion, and collapse only begins once the core has reached supercriticality. Recent simulations of fragmentation indeed find collapsing supercritical cores embedded in subcritical ambient clouds (e.g., Basu and Ciolek, 2004; Ciolek and Basu, 2006).

Later work showed that a substantial amount of flux loss occurs not only during prestellar collapse (Nakano and Umebayashi, 1986; Fiedler and Mouschovias, 1993; Basu and Mouschovias, 1994, 1995a,b), but also during the later phase of star formation and close to an already-formed protostar (e.g., Ciolek and Königl, 1998). The preceding collapse with densities beyond 10^5 cm^{-3} occurs on time scales close to free-fall and thus can be well approximated by flux freezing, i.e., the neutrals effectively drag in the ions that are coupled to the magnetic field lines. Prestellar cores remain mildly supercritical (with a mass-to-flux ratio $1 \lesssim \mu < 10$) during most of their collapse. This causes a massive build-up of magnetic field strength with increasing density. Magnetic braking then operates at such a high efficiency so that it inhibits the formation of a protoplanetary disk (e.g., Allen et al., 2003; Mellon and Li, 2008, 2009). Chapters 4 and 5 investigate this “magnetic braking catastrophe.” In the dense and poorly-ionized accretion disk and the remnant of the first core, non-ideal MHD effects regain importance (e.g., Ciolek

and Königl, 1998; Contopoulos et al., 1998; Tassis and Mouschovias, 2005; Kunz and Mouschovias, 2009, 2010; Dapp and Basu, 2010) and disable magnetic braking. This is possible since, at that stage, the length scales involved are quite small so that even a diffusive process can happen rapidly. Also, the diffusion constant is nonlinearly dependent on the magnetic field strength (Mohanty et al., 2002), which speeds up the diffusion additionally.

Note that very close to a YSO (< 1 AU — Li and McKee, 1996; Shu et al., 2006) a recoupling between gas and the field is expected. The reason is that radiation from the star increases the ionization fraction (see also Chapter 5), mainly by ionizing alkali metals (Li and McKee, 1996). This recoupling is part of the reason why the magnetic flux problem can still not be considered to be solved completely.

There might be a self-regulation mechanism at work that allows for a balance between magnetic flux loss that is required to form a disk and sufficient magnetic braking to ensure ample angular momentum redistribution. Details have to be investigated using simulations with high central resolution that are also capable of following the evolution of a magnetized rotating prestellar core all the way to stellar densities, and after that for a long duration of the accretion phase (see also Section 1.3.3). Currently, the computational costs for such an endeavor are prohibitive in three dimensions. However, in a dimensionally-reduced model, such as presented in Vorobyov and Basu (2006) and used in Dapp and Basu (2010), it might be feasible to gain some insights into this fascinating problem. Chapters 4 and 5 address this issue.

Kudoh and Basu (2008) and Nakamura and Li (2008) have recently presented three-dimensional non-ideal MHD simulations which included turbulence and can shed light onto the initial conditions with which to start such a collapse simulation. Under consideration of simplified grain physics, Kunz and Mouschovias (2009, 2010) studied the axisymmetric collapse problem in the (r, z) plane with two non-ideal MHD effects: ambipolar diffusion and Ohmic dissipation. They also included radiative transfer as a grey flux-limited diffusion prescription, but did not include rotation, and terminated their calculation shortly after the formation of the first core. Chapter 5 of this Thesis uses the approach of Kunz and Mouschovias (2009) in a model similar to Tassis and Mouschovias (2007), and carries the calculations all the way to protostellar densities in order to see whether a centrifugal disk can form. This work is another step towards answering the question regarding the interplay of the angular momentum and magnetic flux problems. The coming years may finally see the simultaneous resolution to these long-standing issues, as well as the problem of catastrophic magnetic braking.

1.3.3 Accretion rates

A very important quantity in understanding the physics of star formation is the *mass accretion rate* since it influences most of the evolution of a forming star. The termination of accretion sets the star's final mass, which, along with the chemical composition, fixes the evolutionary track of a star after hydrogen burning begins. The *initial mass function* (IMF) describes the distribution of stars as a function of their mass as they enter onto the main sequence.

In order to understand star formation on a theoretical basis, astronomers in the 1950s looked for an explanation in terms of what they already understood fairly well. In this case, this was stellar structure and so the first theoretical models assumed a quasi-hydrostatic contraction of the parent clouds to form stars (e.g., Henyey et al., 1955). Stars are quasi-hydrostatic objects, and so seemed interstellar clouds. In the 1960s it was suggested that the early evolution of a molecular cloud towards a star involved dynamical free-fall collapse (e.g., Hayashi and Nakano, 1965), which was only then followed by a quasi-hydrostatic contraction of the already-formed star onto the main sequence. Hayashi (1966) arrived at a maximum radius for protostars of $\approx 50 R_{\odot}$ in homologous collapse, and calculated that a star with a mass comparable to that of the Sun would be assembled from its parent cloud in ≈ 1 yr (see the description in Shu, 1992). Soon, however, various numerical simulations (e.g., Bodenheimer and Sweigart, 1968; Larson, 1969) showed that the collapse of a molecular cloud really was not homologous at all but rather non-uniform (this was also backed by some self-similar analytical solutions, Penston, 1969). In the so-called Larson-Penston (LP) model, a central hydrostatic core forms quickly, but the subsequent accretion process from the cloud onto that protostar is very slow. The time it takes to assemble a star in this initially disputed model lies around 10^5 yr and at the end of the evolution its radius is $2 R_{\odot}$ rather than $50 R_{\odot}$.

Indeed, if one solves the hydrodynamic equations in the highly simplified case of a non-rotating, nonmagnetic SIS, starting out from equilibrium (Shu, 1977), one finds a mass accretion rate of

$$\begin{aligned}\dot{M} &= 0.975 \ c_s^3 / G \\ &\approx 2 \times 10^{-6} \ M_{\odot} \ \text{yr}^{-1}\end{aligned}$$

for an isothermal sound speed at the fiducial temperature of 10 K. According to Shu's so-called *inside-out collapse model*, it takes about 5×10^5 yrs to build a $1 M_{\odot}$ star.

The LP model assumes dynamical collapse from the onset, and thus is distinctly different from Shu's SIS collapse model. In fact, its material is not at rest at the time

of the formation of the protostar, but falls inward at 3.28 times the sound speed. Its density is 4.43 times higher than in the SIS model (cf. Larson, 2003) and so it is not surprising that its mass accretion rate (as calculated by Hunter, 1977) is almost 50 times higher than in the SIS model. Later, more detailed simulations showed that the collapse initially tends to be more similar to the LP model than to the inside-out collapse solution in the central region, with an initially very high mass accretion rate which subsequently drops to values closer to Shu's solution (see the review by Larson, 2003).

Accretion rates cannot be measured directly by observational means. They have to be determined indirectly, for instance by measuring outflow masses and velocities. High accretion rates are envisioned to be accompanied by strong outflows, blowing off about 1/3 of the accreted gaseous matter (e.g., Shu et al., 2000). The detailed effects of disk winds, outflows, and jets onto the accretion rate (and vice versa) are still uncertain (see, e.g., the review by Ray et al., 2007).

Over time, various refinements over the early simple star formation models have been proposed, made necessary because it was realized that other physical phenomena significantly impact the accretion history during the assemblage of a star. Rotation causes the formation of centrifugally supported disks and effectively creates a barrier to mass transport from the envelope to the star (e.g., Vorobyov and Basu, 2006). At this stage of evolution, the central protostar has reached only a mass of typically around $0.007 M_{\odot}$ (Shu et al., 1987). There must exist a mechanism that allows for efficient transport of angular momentum outwards (see Section 1.3.1) and associated mass transport inwards. Another issue is an increasing radiation pressure. Even a modest mass accretion rate of $\dot{M} = 10^{-6} M_{\odot} \text{ yr}^{-1}$ onto a small YSO with mass $0.01 M_{\odot}$ and a radius of R_{\odot} produces a luminosity of $0.3 L_{\odot}$ by the approximate formula $L \approx GM_{\star}\dot{M}/R_{\star}$ (where the subscript \star refers to quantities pertaining to the protostar). The larger the mass of the YSO, and the higher the mass accretion rate, the greater the amount of radiation that has to escape. Obviously, this is a significant problem for massive star formation where the accretion luminosities are expected to reach $10^4 L_{\odot}$ and more. It can be mitigated by channeling the material through an accretion disk (see the review by Beuther et al., 2007) instead of requiring spherical accretion (Bondi, 1952).

None of the models discussed so far helps to answer the question why accretion stops at some point and so sets a star's mass. This can only be achieved by limiting the total mass available to the protostar. If the mass reservoir is finite, accretion will eventually decline to very low values as the envelope runs out of matter (see Fig. 1.2). This problem is closely related to another long-standing open question in star formation research, the low *star formation efficiency* (SFE). Only a small percentage of the total gas available

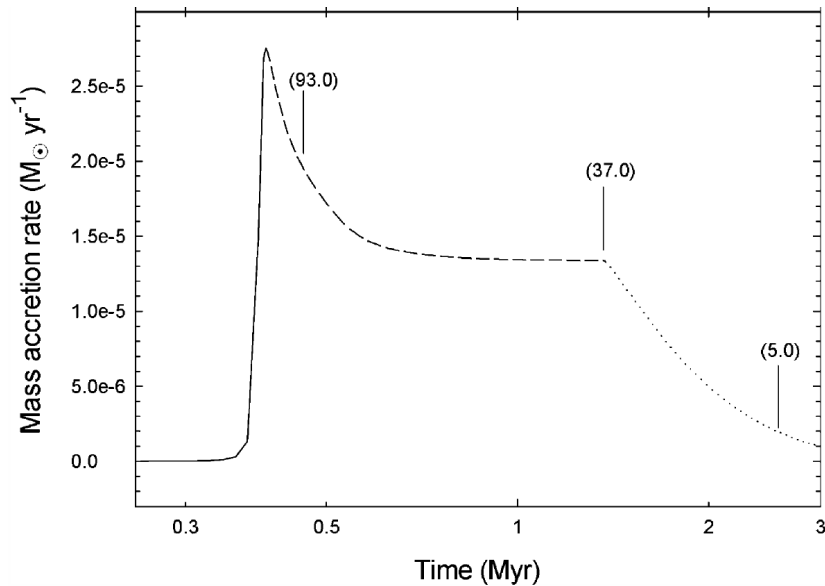


Figure 1.2: Time evolution of the accretion rate in the spherically-symmetric model from Vorobyov and Basu (2005). The accretion rate is very high at first when material moving at supersonic velocity falls onto the protostar, but then settles into a static accretion phase. During this phase, the accretion rate behaves according to $\dot{M} \propto c_s^3 G^{-1}$, even though it is still higher than the SIS model prediction. As a result of the finite reservoir of mass the accretion rate drops terminally. The numbers in brackets indicate the percentage of mass left in the envelope at the given time.

in molecular clouds is converted into stars during a free-fall time, both on the level of individual clouds and on galactic scales (see, e.g., Basu et al., 2009a). It remains unclear what keeps the rest of the gas from participating in star formation. Again, a currently-unknown self-regulation mechanism may be at work.

Several physical mechanisms are being discussed in the literature for imposing a limit on accretion on the core level. The simplest one is isolation. Bok globules (e.g., Alves et al., 2001) are small isolated dark clouds surrounded by a hot tenuous medium. The final mass of a star forming in one of these globules is constrained by the total mass in the cloud. However, star formation typically occurs in deeply embedded cores within GMCs rather than in isolated clouds.

Competitive accretion (see the review by Bonnell et al., 2007) is a more refined approach. It invokes the picture that stars forming simultaneously in a cluster-forming region “compete” for the total amount of gas. In this paradigm more massive stars form closer to the center of a clump as an effect of the deeper gravitational well. This funnels more gas into the central regions, to the disadvantage of less-massive stars towards the periphery of the clump (e.g., Bate and Bonnell, 2005), as this gas is no longer available for accretion there. In addition, many-body interactions cause some YSOs to be ejected

from the cluster prematurely, before being able to accumulate a lot of mass. Finally, after a few million years, the first massive star undergoes a supernova and disperses most of the remaining gas, revealing a gas-free young open cluster with a certain IMF. Problems with this picture lie in the velocity distribution of field stars (Brown Dwarfs are predicted to move ballistically through the Galaxy) and the observed spatial mass and age distributions in cluster-forming regions (for instance, the most massive stars are expected to be near the center of the cluster). Also, Elmegreen (2000) notes that stars most likely form close to the sites where their native cores became unstable, which would also rule out an IMF significantly influenced by interactions. Finally, competitive accretion fails to explain why some clouds are exclusively forming low-mass stars, and none of their high-mass siblings. Other mechanisms must be at work in more quiescent regions such as the Taurus molecular cloud.

Other authors propose high levels of ambient turbulence caused by feedback and intrinsic large-scale velocities (e.g., Mac Low et al., 1998; Padoan and Nordlund, 2002; Ballesteros-Paredes et al., 2003; Mac Low and Klessen, 2004, see also Section 1.2.1) as a mechanism for controlling accretion. One possibility could be colliding gas flows that disperse the gas remaining of the core envelope. This would effectively limit the mass available to protostars forming in the center of the core.

Mouschovias (1976) proposed that strong magnetic fields could hold up the envelope while the inner core collapses (see Sections 1.2.1 and 1.3.2). This idea is backed by observations that show the low-density regions of molecular clouds to have strong magnetic fields and a low mass-to-flux ratio (Cortes et al., 2005; Heyer et al., 2008). Another argument for magnetic domination of the low-density regions is their higher ionization fraction due to the penetration of ionizing UV radiation (McKee, 1989). The very dense regions can only be reached by cosmic rays.

Aside from the issue how accretion is terminated, another question arises. Once sufficient material has fallen onto an accretion disk, it needs to get to the central protostar. Assuming the disk is centrifugally-supported and near-Keplerian, it is stable, and gas will remain in orbit unless there is a mechanism for angular momentum redistribution at this stage as well (cf. Section 1.3.1). The literature suggests similar candidates as in the previous discussion. The magneto-rotational instability (MRI) and its resulting effective accretion rates are usually studied in shearing-box simulations (e.g., Gammie, 2001; Sano and Stone, 2002; Balsara et al., 2009; see also the review by Balbus and Hawley, 1998) where the MRI is often parametrized using α -viscosity (e.g., Hartmann, 1998). For a significant α , this approach leads to a smooth disk without much azimuthal structure (Vorobyov and Basu, 2007) and will also produce a smooth accretion rate. In fact, the

concept of α -viscosity was originally introduced to mimic an accretion rate empirically required to assemble stars in a reasonable amount of time. However, Vorobyov and Basu (2006) showed in their global disk simulations that non-axisymmetries, specifically the formation of clumps and “protoplanets” in disks, can lead to an effective transport of angular momentum by gravitational torques and subsequent accretion of entire dense clumps onto the central star. This will cause a vigorous burst in luminosity and accretion rate, while they are much smaller rate in between bursts and in the absence of artificial viscous effects. Vorobyov and Basu (2006) argue that these bursts resemble observed FU Ori bursts in strength, frequency, and duration. They suggest that most of the stellar mass may, in fact, accrete in this episodic non-continuous manner instead of in the traditional, more smooth way.

This problem, as the ones previously discussed, will be solved using high-resolution, long-term, physically-accurate and complete, self-consistent numerical simulations. This should ideally happen as part of a larger three-dimensional collapse simulation including all effects: rotation, “turbulence” in the core envelope, magnetic fields, and radiative transfer in both envelope and centrifugal disk, as well as their feedback effects onto the surroundings. However, in absence of these all-encompassing simulations, it seems prudent to use simplified models and approaches, reduced in dimensionality and physics, in order to gain some insights into which effects must be considered and which can be neglected. These simulations, however, must allow for long-term integration. Great progress has been made in the past on these problems already, but the future promises many more achievements using the new technology of hardware and computational facilities to run these simulations. Maybe the next decade will finally see the resolution of some of the great outstanding problems in star formation.

Bibliography

- Allen, A., Li, Z., and Shu, F. H.: 2003, *ApJ* **599**, 363
- Alves, J. F., Lada, C. J., and Lada, E. A.: 2001, *Nature* **409**, 159
- André, P., Basu, S., and Inutsuka, S.: 2009, in Chabrier, G. (ed.), *Structure Formation in Astrophysics*, pp 254–+, Cambridge University Press
- Arons, J. and Max, C. E.: 1975, *ApJ* **196**, L77+
- Bacmann, A., André, P., Puget, J.-L., Abergel, A., Bontemps, S., and Ward-Thompson, D.: 2000, *A&A* **361**, 555

- Balbus, S. A. and Hawley, J. F.: 1991, *ApJ* **376**, 214
- Balbus, S. A. and Hawley, J. F.: 1998, *Reviews of Modern Physics* **70**, 1
- Ballesteros-Paredes, J., Klessen, R. S., and Vázquez-Semadeni, E.: 2003, *ApJ* **592**, 188
- Balsara, D. S.: 1996, *ApJ* **465**, 775
- Balsara, D. S., Crutcher, R. M., and Pouquet, A.: 2001, *ApJ* **557**, 451
- Balsara, D. S., Tilley, D. A., Rettig, T., and Brittain, S. D.: 2009, *MNRAS* **397**, 24
- Basu, S.: 1998, *ApJ* **509**, 229
- Basu, S.: 2005, in A. Chalabaev, T. Montmerle, and H. J. Tran-Thanh-Van, (The Gioi Publishers (eds.), *Young Local Universe, Proceedings of XXXIXth Rencontres de Moriond*, 191, Proceedings article available online from <http://www.astro.uwo.ca/basu/docs/ylu-basu.pdf>
- Basu, S. and Ciolek, G. E.: 2004, *ApJ* **607**, L39
- Basu, S., Ciolek, G. E., Dapp, W. B., and Wurster, J.: 2009a, *New A* **14**, 483
- Basu, S., Ciolek, G. E., and Wurster, J.: 2009b, *New A* **14**, 221
- Basu, S. and Mouschovias, T. C.: 1994, *ApJ* **432**, 720
- Basu, S. and Mouschovias, T. C.: 1995a, *ApJ* **452**, 386
- Basu, S. and Mouschovias, T. C.: 1995b, *ApJ* **453**, 271
- Bate, M. R.: 1998, *ApJ* **508**, L95
- Bate, M. R. and Bonnell, I. A.: 2005, *MNRAS* **356**, 1201
- Beuther, H., Churchwell, E. B., McKee, C. F., and Tan, J. C.: 2007, *Protostars and Planets V* pp 165–180
- Bodenheimer, P.: 1981, in D. Sugimoto, D. Q. Lamb, & D. N. Schramm (ed.), *Fundamental Problems in the Theory of Stellar Evolution*, Vol. 93 of *IAU Symposium*, pp 5–24
- Bodenheimer, P. and Sweigart, A.: 1968, *ApJ* **152**, 515
- Bondi, H.: 1952, *MNRAS* **112**, 195

- Bonnell, I. A., Clark, P., and Bate, M. R.: 2008, *MNRAS* **389**, 1556
- Bonnell, I. A., Larson, R. B., and Zinnecker, H.: 2007, *Protostars and Planets V* pp 149–164
- Borra, E. F. and Landstreet, J. D.: 1978, *ApJ* **222**, 226
- Cami, J., Bernard-Salas, J., Peeters, E., and Malek, S. E.: 2010, *Science* **329**, 1180
- Caselli, P., Benson, P. J., Myers, P. C., and Tafalla, M.: 2002, *ApJ* **572**, 238
- Chen, F. F.: 1984, *Introduction to Plasma Physics and controlled fusion, 2nd edition*, Springer, New York, LLC
- Ciolek, G. E. and Basu, S.: 2006, *ApJ* **652**, 442
- Ciolek, G. E. and Königl, A.: 1998, *ApJ* **504**, 257
- Ciolek, G. E. and Mouschovias, T. C.: 1993, *ApJ* **418**, 774
- Ciolek, G. E. and Mouschovias, T. C.: 1994, *ApJ* **425**, 142
- Contopoulos, I., Ciolek, G. E., and Königl, A.: 1998, *ApJ* **504**, 247
- Cortes, P. and Crutcher, R. M.: 2006, *ApJ* **639**, 965
- Cortes, P. C., Crutcher, R. M., and Watson, W. D.: 2005, *ApJ* **628**, 780
- Crutcher, R. M.: 1999, *ApJ* **520**, 706
- Crutcher, R. M. and Troland, T. H.: 2007, in B. G. Elmegreen & J. Palous (ed.), *IAU Symposium*, Vol. 237 of *IAU Symposium*, pp 141–147
- Dapp, W. B. and Basu, S.: 2010, *A&A* **521**, L56+
- Durisen, R. H., Gingold, R. A., Tohline, J. E., and Boss, A. P.: 1986, *ApJ* **305**, 281
- Elmegreen, B. G.: 2000, *ApJ* **530**, 277
- Elmegreen, B. G.: 2007, *ApJ* **668**, 1064
- Fiedler, R. A. and Mouschovias, T. C.: 1993, *ApJ* **415**, 680

- Fukagawa, M., Hayashi, M., Tamura, M., Itoh, Y., Hayashi, S. S., Oasa, Y., Takeuchi, T., Morino, J., Murakawa, K., Oya, S., Yamashita, T., Suto, H., Mayama, S., Naoi, T., Ishii, M., Pyo, T., Nishikawa, T., Takato, N., Usuda, T., Ando, H., Iye, M., Miyama, S. M., and Kaifu, N.: 2004, *ApJ* **605**, L53
- Galli, D. and Shu, F. H.: 1993, *ApJ* **417**, 220
- Galli, D., Walmsley, M., and Gonçalves, J.: 2002, *A&A* **394**, 275
- Gammie, C. F.: 2001, *ApJ* **553**, 174
- Goldsmith, P. F. and Arquilla, R.: 1985, in D. C. Black & M. S. Matthews (ed.), *Protostars and Planets II*, pp 137–149
- Goldsmith, P. F., Heyer, M., Narayanan, G., Snell, R., Li, D., and Brunt, C.: 2008, *ApJ* **680**, 428
- Goodman, A. A., Benson, P. J., Fuller, G. A., and Myers, P. C.: 1993, *ApJ* **406**, 528
- Güdel, M. and Nazé, Y.: 2009, *A&A Rev.* **17**, 309
- Han, J. L. and Zhang, J. S.: 2007, *A&A* **464**, 609
- Hartmann, L.: 1998, *Accretion Processes in Star Formation*, Accretion processes in star formation / Lee Hartmann. Cambridge, UK ; New York : Cambridge University Press, 1998. (Cambridge astrophysics series ; 32) ISBN 0521435072.
- Hartmann, L.: 2001, *AJ* **121**, 1030
- Hartmann, L., Ballesteros-Paredes, J., and Bergin, E. A.: 2001, *ApJ* **562**, 852
- Hayashi, C.: 1966, *ARA&A* **4**, 171
- Hayashi, C. and Nakano, T.: 1965, *Progress of Theoretical Physics* **34**, 754
- Hayashi, C., Narita, S., and Miyama, S. M.: 1982, *Progress of Theoretical Physics* **68**, 1949
- Heitsch, F. and Hartmann, L.: 2008, *ApJ* **689**, 290
- Heitsch, F., Zweibel, E. G., Slyz, A. D., and Devriendt, J. E. G.: 2004, *ApJ* **603**, 165
- Hennebelle, P. and Ciardi, A.: 2009, *A&A* **506**, L29

- Hennebelle, P. and Fromang, S.: 2008, *A&A* **477**, 9
- Heneyey, L. G., Lelevier, R., and Levée, R. D.: 1955, *PASP* **67**, 154
- Herbig, G. H.: 1962, *Advances in Astronomy and Astrophysics* **1**, 47
- Heyer, M., Gong, H., Ostriker, E., and Brunt, C.: 2008, *ApJ* **680**, 420
- Heyer, M. H. and Brunt, C.: 2007, in B. G. Elmegreen & J. Palous (ed.), *IAU Symposium*, Vol. 237 of *IAU Symposium*, pp 9–16
- Hezareh, T., Houde, M., McCoey, C., Vastel, C., and Peng, R.: 2008, *ApJ* **684**, 1221
- Huff, E. M. and Stahler, S. W.: 2006, *ApJ* **644**, 355
- Hunter, C.: 1977, *ApJ* **218**, 834
- Keto, E. and Wood, K.: 2006, *ApJ* **637**, 850
- Kirk, H., Johnstone, D., and Basu, S.: 2009, *ApJ* **699**, 1433
- Klessen, R. S., Ballesteros-Paredes, J., Vázquez-Semadeni, E., and Durán-Rojas, C.: 2005, *ApJ* **620**, 786
- Krumholz, M. R., Klein, R. I., and McKee, C. F.: 2007, *ApJ* **656**, 959
- Kudoh, T. and Basu, S.: 2008, *ApJ* **679**, L97
- Kunz, M. W. and Mouschovias, T. C.: 2009, *ApJ* **693**, 1895
- Kunz, M. W. and Mouschovias, T. C.: 2010, *MNRAS* **408**, 322
- Lada, C. J.: 2006, *ApJ* **640**, L63
- Larson, R. B.: 1969, *MNRAS* **145**, 271
- Larson, R. B.: 1972, *MNRAS* **156**, 437
- Larson, R. B.: 1981, *MNRAS* **194**, 809
- Larson, R. B.: 1984, *MNRAS* **206**, 197
- Larson, R. B.: 2003, *Reports of Progress in Physics* **66**, 1651
- Li, H. and Houde, M.: 2008, *ApJ* **677**, 1151

- Li, Z. and McKee, C. F.: 1996, *ApJ* **464**, 373
- Li, Z. and Nakamura, F.: 2004, *ApJ* **609**, L83
- Lin, D. N. C. and Pringle, J. E.: 1987, *MNRAS* **225**, 607
- Lizano, S. and Shu, F. H.: 1989, *ApJ* **342**, 834
- Lynden-Bell, D. and Pringle, J. E.: 1974, *MNRAS* **168**, 603
- Mac Low, M.: 1999, *ApJ* **524**, 169
- Mac Low, M. and Klessen, R. S.: 2004, *Reviews of Modern Physics* **76**, 125
- Mac Low, M., Klessen, R. S., Burkert, A., and Smith, M. D.: 1998, *Physical Review Letters* **80**, 2754
- Machida, M. N., Inutsuka, S., and Matsumoto, T.: 2006, *ApJ* **647**, L151
- Masunaga, H. and Inutsuka, S.: 2000, *ApJ* **531**, 350
- McKee, C. F.: 1989, *ApJ* **345**, 782
- McKee, C. F. and Ostriker, E. C.: 2007, *ARA&A* **45**, 565
- Mellon, R. R. and Li, Z.: 2008, *ApJ* **681**, 1356
- Mellon, R. R. and Li, Z.: 2009, *ApJ* **698**, 922
- Mestel, L.: 1965, *QJRAS* **6**, 265
- Mestel, L.: 1999, *Stellar magnetism*, Oxford Science Publications : Clarendon, 1999. (International series of monographs on physics ; 99)
- Mestel, L. and Spitzer, Jr., L.: 1956, *MNRAS* **116**, 503
- Mohanty, S., Basri, G., Shu, F., Allard, F., and Chabrier, G.: 2002, *ApJ* **571**, 469
- Motte, F., Bontemps, S., Schilke, P., Schneider, N., Menten, K. M., and Brogière, D.: 2007, *A&A* **476**, 1243
- Motte, F., Zavagno, A., Bontemps, S., Schneider, N., Hennemann, M., di Francesco, J., André, P., Saraceno, P., Griffin, M., Marston, A., Ward-Thompson, D., White, G., Minier, V., Men'shchikov, A., Hill, T., Abergel, A., Anderson, L. D., Aussel, H., Balog, Z., Baluteau, J., Bernard, J., Cox, P., Csengeri, T., Deharveng, L., Didelon,

- P., di Giorgio, A., Hargrave, P., Huang, M., Kirk, J., Leeks, S., Li, J. Z., Martin, P., Molinari, S., Nguyen-Luong, Q., Olofsson, G., Persi, P., Peretto, N., Pezzuto, S., Roussel, H., Russeil, D., Sadavoy, S., Sauvage, M., Sibthorpe, B., Spinoglio, L., Testi, L., Teyssier, D., Vavrek, R., Wilson, C. D., and Woodcraft, A.: 2010, *A&A* **518**, L77+
- Mouschovias, T. C.: 1974, *ApJ* **192**, 37
- Mouschovias, T. C.: 1976, *ApJ* **207**, 141
- Mouschovias, T. C.: 1977, *ApJ* **211**, 147
- Mouschovias, T. C.: 1979, *ApJ* **228**, 475
- Mouschovias, T. C.: 1991, *ApJ* **373**, 169
- Mouschovias, T. C. and Morton, S. A.: 1991, *ApJ* **371**, 296
- Mouschovias, T. C., Tassis, K., and Kunz, M. W.: 2006, *ApJ* **646**, 1043
- Myers, P. C.: 1983, *ApJ* **270**, 105
- Nakamura, F. and Li, Z.: 2005, *ApJ* **631**, 411
- Nakamura, F. and Li, Z.: 2008, *ApJ* **687**, 354
- Nakano, T.: 1979, *PASJ* **31**, 697
- Nakano, T.: 1984, *Fund. Cosmic Phys.* **9**, 139
- Nakano, T. and Nakamura, T.: 1978, *PASJ* **30**, 671
- Nakano, T., Nishi, R., and Umebayashi, T.: 2002, *ApJ* **573**, 199
- Nakano, T. and Umebayashi, T.: 1986, *MNRAS* **218**, 663
- Narita, S., Hayashi, C., and Miyama, S. M.: 1984, *Progress of Theoretical Physics* **72**, 1118
- Narita, S., Nakano, T., and Hayashi, C.: 1970, *Progress of Theoretical Physics* **43**, 942
- Norman, M. L., Wilson, J. R., and Barton, R. T.: 1980, *ApJ* **239**, 968
- Onishi, T., Mizuno, A., Kawamura, A., Tachihara, K., and Fukui, Y.: 2002, *ApJ* **575**, 950

- Osterbrock, D. E.: 1961, *ApJ* **134**, 270
- Ostriker, E. C., Stone, J. M., and Gammie, C. F.: 2001, *ApJ* **546**, 980
- Padoan, P. and Nordlund, Å.: 2002, *ApJ* **576**, 870
- Palla, F. and Stahler, S. W.: 2000, *ApJ* **540**, 255
- Parker, E. N.: 1966, *ApJ* **145**, 811
- Penston, M. V.: 1969, *MNRAS* **144**, 425
- Pudritz, R. E. and Norman, C. A.: 1983, *ApJ* **274**, 677
- Puget, J. L. and Léger, A.: 1989, *ARA&A* **27**, 161
- Ray, T., Dougados, C., Bacciotti, F., Eisloffel, J., and Chrysostomou, A.: 2007, *Protostars and Planets V* pp 231–244
- Saigo, K. and Hanawa, T.: 1998, *ApJ* **493**, 342
- Sano, T. and Stone, J. M.: 2002, *ApJ* **570**, 314
- Shakura, N. I. and Sunyaev, R. A.: 1973, *A&A* **24**, 337
- Shu, F. H.: 1977, *ApJ* **214**, 488
- Shu, F. H.: 1992, *Physics of Astrophysics, Vol. II*, Physics of Astrophysics, Vol. II, by Frank H. Shu. Published by University Science Books, ISBN 0-935702-65-2, 476pp, 1992.
- Shu, F. H., Adams, F. C., and Lizano, S.: 1987, *ARA&A* **25**, 23
- Shu, F. H., Galli, D., Lizano, S., and Cai, M.: 2006, *ApJ* **647**, 382
- Shu, F. H., Najita, J. R., Shang, H., and Li, Z.: 2000, *Protostars and Planets IV* pp 789–+
- Smith, M. D. and Mac Low, M.: 1998, *Ap&SS* **261**, 191
- Solomon, P. M., Rivolo, A. R., Barrett, J., and Yahil, A.: 1987, *ApJ* **319**, 730
- Stahler, S. W. and Palla, F.: 2005, *The Formation of Stars*, The Formation of Stars, by Steven W. Stahler, Francesco Palla, pp. 865. ISBN 3-527-40559-3. Wiley-VCH , January 2005.

- Stamatellos, D., Whitworth, A. P., Bisbas, T., and Goodwin, S.: 2007, *A&A* **475**, 37
- Stone, J. M., Ostriker, E. C., and Gammie, C. F.: 1998, *ApJ* **508**, L99
- Tafalla, M., Mardones, D., Myers, P. C., Caselli, P., Bachiller, R., and Benson, P. J.: 1998, *ApJ* **504**, 900
- Tassis, K. and Mouschovias, T. C.: 2005, *ApJ* **618**, 783
- Tassis, K. and Mouschovias, T. C.: 2007, *ApJ* **660**, 370
- Terebey, S., Shu, F. H., and Cassen, P.: 1984, *ApJ* **286**, 529
- Tielens, A. G. G. M.: 2008, *ARA&A* **46**, 289
- Tilley, D. A. and Balsara, D. S.: 2010, *MNRAS* **406**, 1201
- Tohline, J. E.: 1982, *Fund. Cosmic Phys.* **8**, 1
- Toomre, A.: 1981, in S. M. Fall & D. Lynden-Bell (ed.), *Structure and Evolution of Normal Galaxies*, pp 111–136
- Toomre, A.: 1982, *ApJ* **259**, 535
- Troland, T. H., Crutcher, R. M., Goodman, A. A., Heiles, C., Kazes, I., and Myers, P. C.: 1996, *ApJ* **471**, 302
- Vorobyov, E. I. and Basu, S.: 2005, *MNRAS* **360**, 675
- Vorobyov, E. I. and Basu, S.: 2006, *ApJ* **650**, 956
- Vorobyov, E. I. and Basu, S.: 2007, *MNRAS* **381**, 1009
- Walsh, A. J., Bourke, T. L., and Myers, P. C.: 2006, *ApJ* **637**, 860
- Williams, J. P. and McKee, C. F.: 1997, *ApJ* **476**, 166
- Winkler, K. and Newman, M. J.: 1980a, *ApJ* **236**, 201
- Winkler, K. and Newman, M. J.: 1980b, *ApJ* **238**, 311
- Zuckerman, B. and Evans, II, N. J.: 1974, *ApJ* **192**, L149
- Zuckerman, B. and Palmer, P.: 1974, *ARA&A* **12**, 279

Chapter 2

Long-lived Magnetic-Tension-Driven Modes in a Molecular Cloud

2.1 Introduction

Nonthermal linewidths are ubiquitous in molecular clouds (Solomon et al., 1987) and are interpreted to represent highly supersonic random internal motions (see McKee and Ostriker, 2007, for a recent review). Principal component analysis (Heyer and Brunt, 2007) reveals that most of the energy is contained in modes that span the largest scale of the cloud.

Numerical simulations of molecular cloud turbulence using a three-dimensional simulation cube with periodic boundary conditions have revealed that supersonic MHD turbulence decays away rapidly, on about a sound crossing time of the driving scale (Stone et al., 1998; Mac Low et al., 1998; Mac Low, 1999; Ostriker et al., 2001). Periodic box simulations represent a “local” patch of uniform background density that is embedded within a larger cloud, and are equivalent to studying an infinite uniform medium. Furthermore, a 1.5-dimensional model that included vertical stratification (Kudoh and Basu, 2003, 2006) found that turbulent decay could be delayed, but only mildly, by some conversion of energy to large scale modes along the magnetic field direction. The rapid turbulence dissipation in all of these models is due to the presence of shocks and takes place under the assumption of magnetic flux freezing, without any contribution from magnetic field dissipation, e.g., by ambipolar diffusion.

In a recent paper, Basu et al. (2009a) carried out an extensive parameter survey of fragmentation initiated by nonlinear turbulent flows, employing the magnetic thin-sheet

¹A version of this chapter has been published as Basu, Shantanu & Dapp, Wolf B. 2010, ApJ, 716, 427

approximation and also including the effect of ambipolar diffusion (see also Basu and Ciolek, 2004; Li and Nakamura, 2004; Nakamura and Li, 2005; Ciolek and Basu, 2006; Basu et al., 2009b). In this approximation, the sheet interacts at its upper and lower surfaces with an external magnetic field, and can be considered a “global” model in the z -direction (parallel to the mean background magnetic field), although it is a periodic (“local”) model in the x - and y -directions. Basu et al. (2009a) found that initial turbulent fluctuations decayed away quite rapidly in all models with supercritical mass-to-flux ratio, as well as for subcritical models that included the effect of ambipolar diffusion. However, a surprising result was that subcritical clouds evolving under flux-freezing were able to maintain a substantial portion of their initial kinetic energy to indefinitely large times.

In this paper, we analyze this unique instance of a turbulent MHD simulation that yields long-lived nonlinear motions. We perform a suite of numerical simulations to test its generality, and also establish the analytic explanation for this very interesting result.

2.2 Method

The thin-sheet equations, formulation of our model, and numerical methods are described in several papers (Ciolek and Basu, 2006; Basu et al., 2009b,a). The background state has a uniform (in the x - and y - directions) neutral surface density $\sigma_{n,0}$ and a uniform vertical (z -direction) magnetic field B_{ref} . We input nonlinear velocity fluctuations with spectrum $v_k^2 \propto k^{-4}$ in Fourier space, where $k = (k_x^2 + k_y^2)^{1/2}$, and modes are damped at a fixed (small) scale that is independent of the box size or the number of grid zones used in a simulation. The evolution equations for the magnetized thin sheet include the effects of magnetic tension due to the external magnetic field $\mathbf{B}(x, y, z)$. It is calculated as a potential field, with the vertical magnetic field in the equatorial plane, $B_{z,\text{eq}}(x, y)$, acting as a source for $\mathbf{B}(x, y, z) - B_{\text{ref}}\hat{z}$, much as $\sigma_n(x, y)$ acts as a source for the gravitational field (see details in Ciolek and Basu, 2006).

The gas is isothermal with sound speed c_s , and partial ionization is mainly due to cosmic rays. This introduces the dimensionless free parameter $\tilde{\tau}_{\text{ni},0} \equiv \tau_{\text{ni},0}/t_0$, where $\tau_{\text{ni},0}$ is the initial neutral-ion collision time, and $t_0 = c_s/2\pi G\sigma_{n,0}$ is a characteristic time in the problem. The flux-freezing limit, used extensively in this paper, corresponds to $\tilde{\tau}_{\text{ni},0} = 0$. Another important parameter is the initial dimensionless mass-to-flux ratio $\mu_0 \equiv 2\pi G^{1/2}\sigma_{n,0}/B_{\text{ref}}$, i.e., $\mu_0 > 1$ yields a supercritical cloud in which fragmentation occurs dynamically and $\mu_0 < 1$ yields a subcritical cloud in which fragmentation is driven on a longer time scale by ambipolar diffusion (see Ciolek and Basu, 2006). Turbulent initial conditions introduce the dimensionless parameter v_a/c_s , where v_a is the root mean

square (rms) amplitude of the initial velocity fluctuations in each direction. Finally, we also vary the ratio L/L_0 (where L is the box width in each direction, and $L_0 = c_s^2/2\pi G\sigma_{n,0}$ is a characteristic length scale of the system), and N , the number of grid zones in each direction. An additional parameter, the dimensionless external pressure $\tilde{P}_{\text{ext}} = 2P_{\text{ext}}/\pi G\sigma_{n,0}^2$, is kept fixed at 0.1 in all models, and does not play an important role in the dynamics.

2.3 Results

2.3.1 Canonical models

Two models illustrate the key result for subcritical clouds with turbulent initial conditions. Figure 2.1 shows the time evolution of total kinetic energy for a model which allows for neutral-ion drift ($\tilde{\tau}_{\text{ni},0} = 0.2$), and another model which has flux freezing ($\tilde{\tau}_{\text{ni},0} = 0$). The value $\tilde{\tau}_{\text{ni},0} = 0.2$ corresponds to the canonical ionization fraction implied by primarily cosmic ray ionization: $\chi_i \simeq 10^{-7}(n_n/10^4 \text{ cm}^{-3})^{-1/2}$ (see Basu et al., 2009b,a), where n_n is the number density of neutrals. Both models are characterized by $\mu_0 = 0.5$, $v_a = 2c_s$, $L = 32\pi L_0$. The flux-frozen run has $N = 512$ while the ambipolar diffusion run has $N = 1024$. The evolution of the ambipolar diffusion model terminates at time $t = 45.4 t_0$, when the highest column density in the simulation reaches $100 \sigma_{n,0}$ — a useful proxy for runaway collapse of the first core. At this time, the kinetic energy has decayed away substantially, and appears to still be declining. In contrast, the flux-frozen model has, after an initial loss of some kinetic energy, stabilized to executing oscillations about a mean value $E_{\text{kin}} \approx 0.7 E_{\text{kin},0}$. We have run simulations with flux freezing up to $t \approx 35,000 t_0$ with no change in this behavior.

Figure 2.2 shows color images of the column density for models that are equivalent to the ones described above, but with $N = 256$. The ambipolar diffusion model is shown at its end time $t = 43.5 t_0$, and the flux-frozen model is shown at the same time, although it continues to evolve indefinitely. The ambipolar diffusion model shows evidence of monolithic collapse towards one or more density peaks, while the flux-frozen model shows a more wispy character and gives no indication of impending collapse in any region, neither visually nor quantitatively. Figure 2.3 shows a model snapshot of the flux-frozen model but viewed from a three-dimensional perspective, with the external field lines illustrated in the region above the sheet. Since this is a subcritical model, the field lines are not significantly deformed. The pitch angle of the magnetic field relative to the vertical direction, measured at the sheet surface, maintains an average value that is

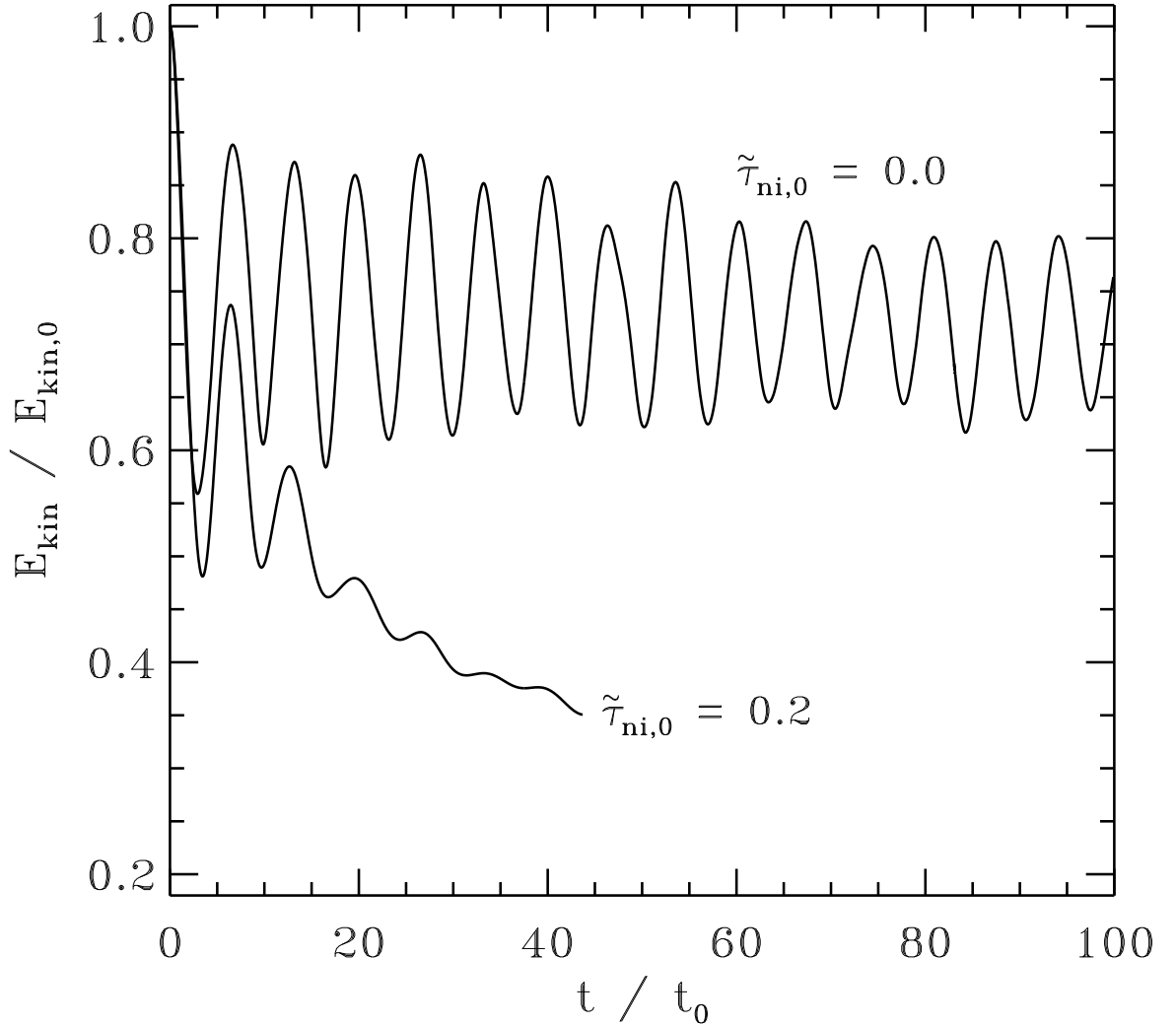


Figure 2.1: Kinetic energy E_{kin} normalized to its initial value $E_{\text{kin},0}$, for two models. Each model has $\mu_0 = 0.5$, $v_a = 2c_s$, and $L/L_0 = 32\pi$. One model evolves with flux freezing, $\tilde{\tau}_{\text{ni},0} = 0$, and is run with $N = 512$. The other model has partial coupling of neutrals and ions characterized by $\tilde{\tau}_{\text{ni},0} = 0.2$, and is run with $N = 1024$.

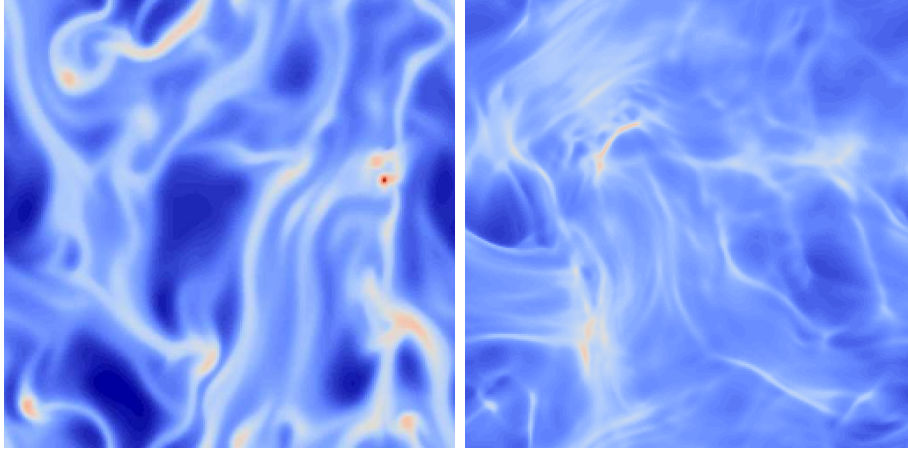


Figure 2.2: Images of gas column density $\sigma_n(x, y)/\sigma_{n,0}$ for models with ambipolar diffusion (top) and flux freezing (bottom), shown in identical color schemes that are proportional to the logarithm of the column density. Both models have $\mu_0 = 0.5$, initial turbulence with $v_a = 2c_s$ and spectrum $v_k^2 \propto k^{-4}$, and are run with $N = 256$. The ambipolar diffusion model terminates at time $t = 43.5 t_0$ in this realization due to the eventual runaway collapse of a core (in the upper right of the image). The flux-frozen model is shown at the same time, but continues to evolve to indefinitely large times without collapse. It shows a more wispy column density structure, with no evidence of monolithic collapse toward any density peaks. An animation of the evolution of each model is available online.

a little less than 10° . For a comparison of field line curvature for models with a range of μ_0 , see Basu et al. (2009b) and Basu et al. (2009a). Animations of both Figure 2.2 and Figure 2.3, with the latter also showing external field line evolution, are available online.

2.3.2 Connection to Linear Analysis

To gain insight into the long-lived mode for the flux-freezing model, we revisit the modal analysis of a partially ionized magnetized sheet. Equations (32a) -(32d) of Ciolek and Basu (2006) can be combined to yield the dispersion relation

$$\begin{aligned} (\omega + i\theta) [\omega^2 - C_{\text{eff}}^2 k^2 + 2\pi G \sigma_{n,0} |k|] \\ = \omega [V_{A,0}^2 k^2 + 2\pi G \sigma_{n,0} \mu_0^{-2} |k|], \end{aligned} \quad (2.1)$$

where

$$\theta = 2\pi \tau_{\text{ni},0} [V_{A,0}^2 k^2 + 2\pi G \sigma_{n,0} \mu_0^{-2} |k|] \quad (2.2)$$

contains the effect of ambipolar diffusion. In the above equations, we have introduced the Alfvén speed $V_{A,0}$ for physical clarity of the magnetic-pressure-driven terms proportional to k^2 , while retaining μ_0 for physical clarity of the magnetic-tension-driven terms propor-

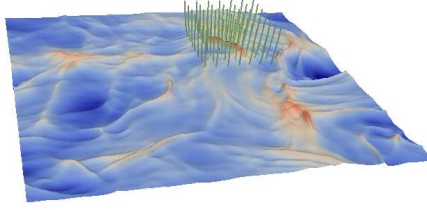


Figure 2.3: Surface map of gas column density $\sigma_n(x, y)/\sigma_{n,0}$ for the flux-frozen model shown in Fig. 2.2. The elevation and color of the surface is proportional to the logarithm of the local column density. The sheet is viewed from a non-face-on viewing angle. The external magnetic field above the sheet is also represented by field lines, in a region near a density peak. An animation of the evolution of the model, including field line evolution, is available online.

tional to k . The two parameters are actually related: $V_{A,0}^2 \equiv B_{\text{ref}}^2/4\pi\rho_{n,0} = 2\pi G\sigma_{n,0}\mu_0^{-2}Z_0$, where the sheet half-thickness $Z_0 = \sigma_{n,0}/2\rho_{n,0}$ and $\rho_{n,0}$ is its mass volume density. The quantity C_{eff} is a effective sound speed that takes into account the restoring force due to an external pressure P_{ext} (see Ciolek and Basu, 2006). In the flux-freezing limit, Equation (2.1) becomes

$$\omega^2 = (V_{A,0}^2 + C_{\text{eff}}^2)k^2 + 2\pi G\sigma_{n,0}(\mu_0^{-2} - 1)|k|. \quad (2.3)$$

In the case of subcritical clouds ($\mu_0 < 1$), the second term on the right hand side becomes a stabilizing term rather than a destabilizing term associated with gravitational instability. However, the full dispersion relation (Equation (2.1)) does contain destabilizing terms due to ambipolar diffusion; the effect on a subcritical cloud is a “slow” instability leading to collapse on an ambipolar diffusion time scale rather than a dynamical time. Equation (42) of Ciolek and Basu (2006) yields a good approximation to the ambipolar diffusion growth time for significantly subcritical clouds.

Equation (2.3) shows that long-wavelength modes evolving under flux freezing have a phase speed

$$V_{\text{MT},0} \equiv \frac{\omega}{k} = \sqrt{(\mu_0^{-2} - 1)G\sigma_{n,0}\lambda}, \quad (2.4)$$

where $\lambda = 2\pi/k$. These modes are driven by the restoring force of the magnetic tension of inclined field lines that connect the sheet to the external medium. These magnetic-tension-driven modes should not be confused with the traditional MHD wave modes. Within the thin sheet, in the short-wavelength limit, magnetic pressure drives the magnetosound mode with phase speed $V_{\text{MS},0} = (V_{A,0}^2 + C_{\text{eff}}^2)^{1/2}$.

Since $V_{\text{MT},0} \propto \sqrt{\lambda}$, it achieves significant values (much larger than $V_{\text{MS},0}$), for $\mu_0 = 0.5$ and the wavelengths equal to the box sizes we consider: $L = 16\pi L_0 - 128\pi L_0$. The values are in the range $4.9 c_s - 13.9 c_s$ and typical values of input parameters would

correspond to dimensional box sizes $\approx 2 \text{ pc} - 16 \text{ pc}$ (see Basu et al., 2009b,a, for scaling of units). Since the restoring force is provided by the external potential field that can adjust instantaneously as the sheet evolves, the modes found in this linear analysis cannot be applied to arbitrarily large wavelengths. In reality, there must be time for readjustment of the external field. The magnetic potential $\Psi_M(x, y, z)$ above and below the sheet decays as $\exp(-k|z|)$ (see Ciolek and Basu, 2006; Basu et al., 2009b), so that a characteristic height of deformation of the field lines is k^{-1} . The ratio ϵ of the Alfvén crossing time across this distance divided by the wave period must be well below unity in order for the potential field approximation to be valid. While the Alfvén crossing time grows more rapidly ($\propto \lambda$) with increasing wavelength than does the wave period ($\propto \sqrt{\lambda}$), we find that $\epsilon \leq 0.26$ for modes of even our largest box size, if the external density $\rho_{\text{ext}} \leq 0.1 \rho_{\text{n},0}$. The nature of a low-density medium external to clouds or clumps is discussed in Section 2.4.

An interesting analogy can be made between the magnetic-tension-driven modes and gravity-driven waves in deep water. There, the undulations of wavenumber k on a water surface can be felt down to a characteristic depth k^{-1} . Velocities below the surface are determined from a velocity potential solution of Laplace’s equation. This is partly due to the incompressible fluid approximation in which the water pressure can adjust instantaneously. A clearer mathematical analogy also occurs in the following manner. Since the vertical gravitational field above and below a uniform thin sheet has magnitude $|g_z| = 2\pi G\sigma_{\text{n},0}$, Equation (2.4) may be rewritten as

$$V_{\text{MT},0} = \sqrt{(\mu_0^{-2} - 1)|g_z|/k}, \quad (2.5)$$

in analogy to the phase speed $v = \sqrt{g/k}$ for deep water waves in a constant gravitational field g .

2.3.3 Further modeling

The implication of the high values of $V_{\text{MT},0}$ for the magnetic-tension-driven modes is that waves with nonlinear particle motions (in comparison to the sound speed c_s or magnetosound speed $V_{\text{MS},0}$) may still act as linear waves since their material motions are much slower than $V_{\text{MT},0}$. They will then evolve (in the flux-freezing limit) without any nonlinear distortion and dissipation. All models do lose significant kinetic energy in an early phase, due to shocks and compression that leads to significant losses in an isothermal gas. Small-scale modes are prone to such decay; for them the relevant signal speed is $V_{\text{MS},0}$, which equals $2.9 c_s$ for the models presented in Section 2.3.1. However, the $v_k^2 \propto k^{-4}$ spectrum means that most of the energy is in the largest scale mode, which can

survive indefinitely, as long as the velocity amplitude is significantly less than $V_{\text{MT},0}$, either initially or after some nonlinear decay. In the magnetic-tension-driven mode, energy is stored and released by the magnetic field, without losses due to ambipolar diffusion (in the $\tilde{\tau}_{\text{ni},0} = 0$ models) or other forms of magnetic field dissipation. Furthermore, the isothermal assumption does not rob any net energy at this stage. In symmetric oscillations, energy is lost during wave compressions and an equal amount gained back during wave expansions.

Figure 2.4 explores the effect of different initial conditions on the decay and residual amount of turbulence in several flux-frozen ($\tilde{\tau}_{\text{ni},0} = 0$) models. The top panel shows a comparison of models with v_k^2 proportional to k^{-4} , k^{-2} , and k^0 , respectively, but all having the same initial rms speed. The spectrum with the greatest amount of energy on the largest scale retains the most energy, as it is the largest scale mode that has the greatest phase speed and is most likely to survive with significant amplitude. The bottom panel shows that models with fixed spectrum $v_k^2 \propto k^{-4}$ but differing v_a will lose different proportions of their initial turbulent energy. The phase speed of the largest mode in these simulation boxes is $V_{\text{MT},0} = 4.9 c_s$, and increasing v_a leads to greater proportionate loss of initial kinetic energy. However, there is a weak trend toward retaining a greater *absolute* amount of energy, as a tabulation of v_{rms} , the one-dimensional rms speed at $t \approx 100 t_0$ in each simulation, reveals. Table 2.1 lists v_{rms} for many models that have flux-freezing, $\mu_0 = 0.5$, and $v_k^2 \propto k^{-4}$ initially. Supersonic motions remain in all models, and the residual amplitude rises with increasing box size as well as initial velocity amplitude v_a . The values of v_{rms} appear to saturate however, so that they remain a reasonably small fraction (14%-56%) of $V_{\text{MT},0}$ for each model.

Oscillations of the kinetic energy are clearly visible in the models that retain a large part of their initial energy, so that the values of v_{rms} in Table 2.1 are varying by up to 10%. The dominance of the largest mode in the initial conditions and the preferential nonlinear damping of smaller modes implies that the period of the largest mode is a reasonable approximation to these observed periods P . We determine P by an average over many peak-to-peak oscillations in each model. The kinetic energy should oscillate with half the period of the velocity eigenfunction, so its expected period is

$$P = \frac{1}{2} \frac{L}{V_{\text{MT},0}} = \frac{1}{2} \left[\frac{L}{(\mu_0^{-2} - 1)G\sigma_{\text{n},0}} \right]^{1/2}, \quad (2.6)$$

where we have used $\lambda = L$. In terms of the dimensionless box size L/L_0 and t_0 , we can

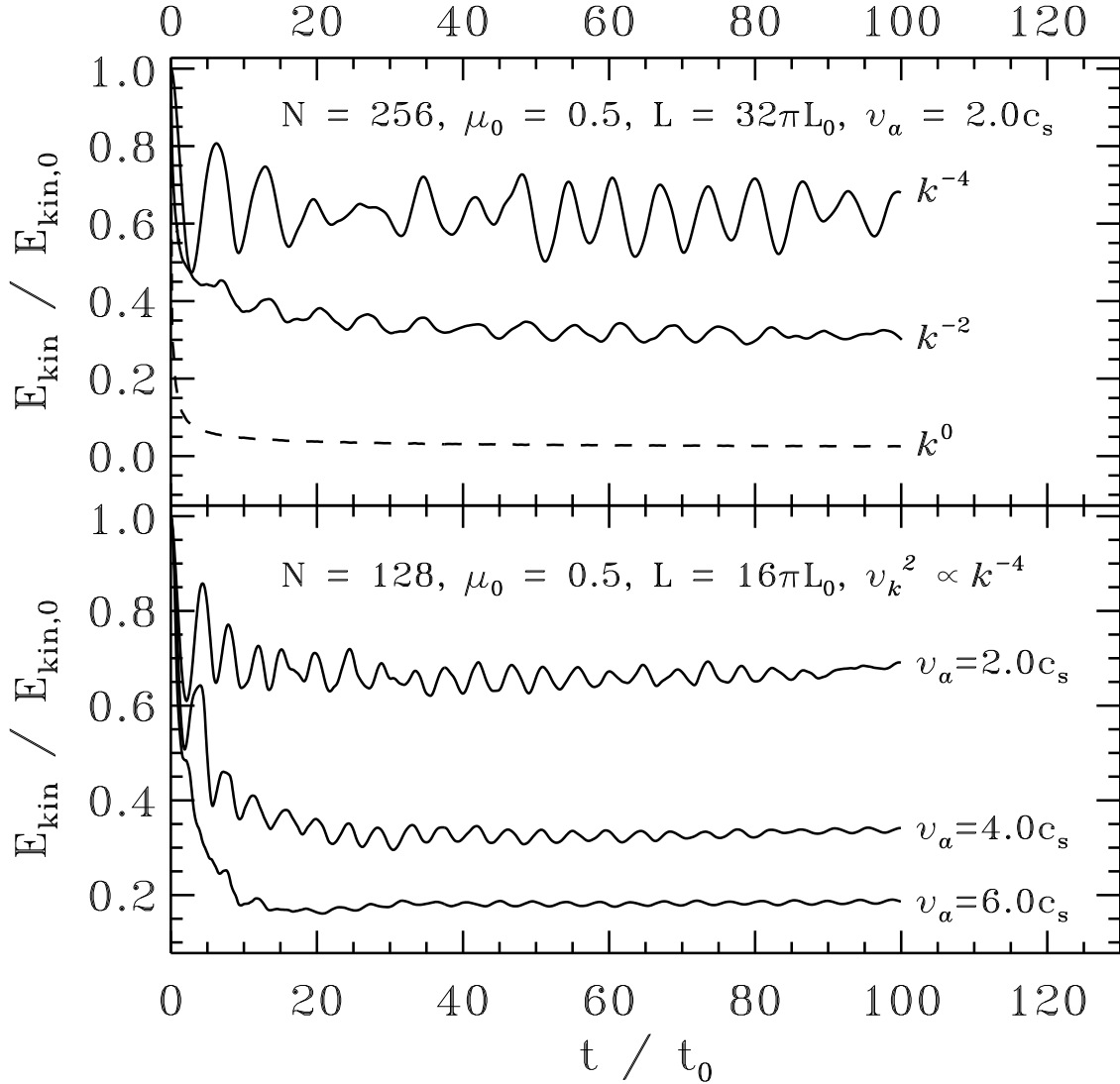


Figure 2.4: Effect of different power spectra and turbulent velocity amplitudes on kinetic energy decay. All models evolve with flux freezing ($\tilde{\tau}_{\text{ni},0} = 0$). Top panel: three models with fixed v_a and other parameters (as labeled) but differing power spectra of initial turbulence, as labeled next to each curve. The model with the most energy on the largest scale retains the greatest part of its energy. Bottom panel: three models with differing v_a but all other parameters including the power spectrum kept fixed, as labeled. Models with greater v_a lose a greater proportion of their initial kinetic energy, although they retain a slightly greater absolute amount of kinetic energy (see Table 2.1).

Table 2.1: Velocity amplitude results for selected models.

N	L/L_0	$V_{\text{MT},0}/c_s$	v_a/c_s	v_{rms}/c_s	$v_{\text{rms}}/V_{\text{MT},0}$
128	16π	4.9	2	1.7	0.35
128	16π	4.9	4	2.4	0.48
128	16π	4.9	6	2.6	0.53
256	32π	6.9	2	1.6	0.23
256	32π	6.9	4	3.4	0.49
256	32π	6.9	6	3.9	0.56
512	32π	6.9	2	1.7	0.25
512	64π	9.8	2	1.9	0.19
512	64π	9.8	3	2.7	0.28
512	64π	9.8	4	2.9	0.29
1024	128π	13.9	2	1.9	0.14
1024	128π	13.9	4	3.4	0.25
1024	128π	13.9	6	5.0	0.36

All models above have $\mu_0 = 0.5$, $\tilde{\tau}_{\text{ni},0} = 0$, and initial turbulent spectrum $v_k^2 \propto k^{-4}$. The one-dimensional velocity dispersion v_{rms} is measured at $t \approx 100 t_0$, and is present indefinitely with variability of up to 10%.

write this as

$$P = \frac{1}{2} \left[\frac{2\pi(L/L_0)}{\mu_0^{-2} - 1} \right]^{1/2} t_0. \quad (2.7)$$

Figure 2.5 shows the predicted dependence in solid lines, for $\mu_0 = (0.25, 0.5, 0.7)$. Different symbols as described in in the figure caption represent the empirical determinations of P from various models. The agreement is remarkably good, and improves for the largest box sizes, where the long-wavelength approximation made in Equation (2.4) holds particularly well.

2.4 Discussion

The study of the decay of MHD turbulence has generally been based on the modeling of Alfvén, slow MHD, and fast MHD modes in media that have a uniform background. The study of more complex global MHD (including magnetogravitational) modes for molecular clouds remains to be explored. It has been suggested that nonthermal motions in molecular clouds can be attributed to long-wavelength MHD waves (Mouschovias, 1987). In this paper, we have analyzed turbulent decay in a magnetically subcritical

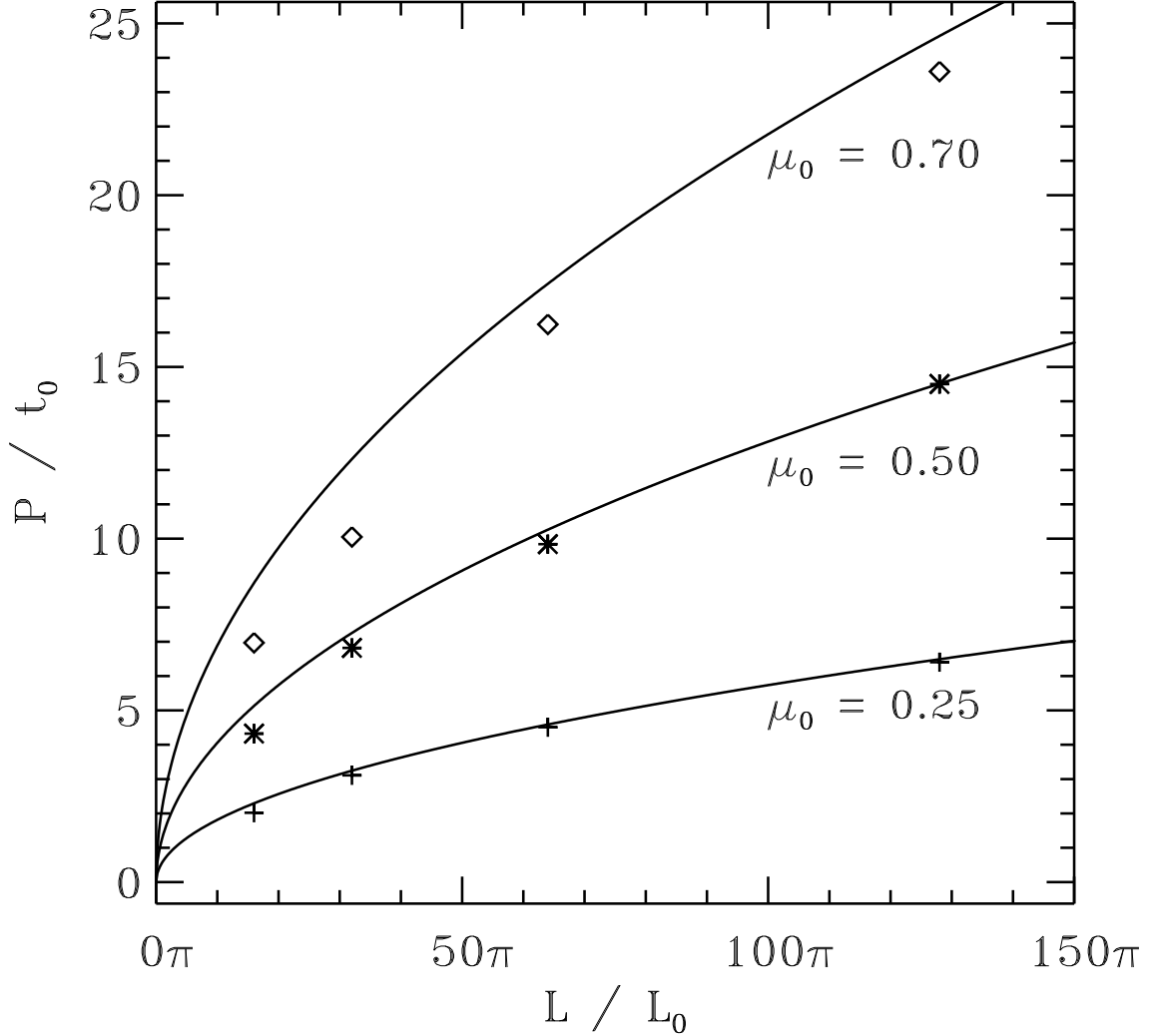


Figure 2.5: Comparison of analytically predicted periods of kinetic energy oscillation with results of simulations. Solid lines are the predicted periods from the linear theory of large-scale flux-frozen modes driven by magnetic tension, for three different values of the dimensionless mass-to-flux ratio $\mu_0 = (0.25, 0.5, 0.7)$. Open diamonds represent average periods of oscillation for four models of differing box size L and fixed $\mu_0 = 0.7$. Asterisks and plus signs represent the same but for fixed $\mu_0 = 0.5$ and $\mu_0 = 0.25$, respectively. The agreement between the solid lines and symbols is remarkably good, and best for the largest box sizes, since the analytic prediction is made in the long-wavelength limit.

sheet-like cloud. It is an idealized model of a molecular cloud that is tied to a magnetic field anchored in the interstellar medium. A large fraction of the initial input kinetic energy is retained by the deformed magnetic field, and then persists in the cloud as large scale oscillations. These represent linear waves of large extent which are nevertheless supersonic since the phase speed of the magnetic-tension-driven modes is up to ≈ 10 times the sound speed for typical cloud sizes.

Our model may approximate the realistic situation of molecular clouds that are embedded in a low-density warm HI halo, or even the case of molecular cloud clumps that may be embedded in a matrix of HI gas (see Hennebelle and Inutsuka, 2006). Flux freezing is a good approximation for molecular cloud envelopes (as opposed to dense cores), due to significant photoionization by background starlight (McKee, 1989; Ciolek and Mouschovias, 1995). Observations also reveal that the low-column-density molecular cloud envelopes actually contain most of the cloud mass (Kirk et al., 2006; Goldsmith et al., 2008). These envelopes may have a subcritical mass-to-flux ratio, as implied by their lack of star formation (Kirk et al., 2006), velocity data (e.g., in Taurus, Heyer et al., 2008), and the subcritical state of the HI clouds (Heiles and Troland, 2005) from which molecular clouds are presumably assembled.

Continuous driving of turbulent motions in molecular clouds is often invoked because the canonical numerical result of decay in a crossing time (e.g., Stone et al., 1998; Mac Low, 1999) is inconsistent with estimated cloud lifetimes that are at least a few crossing times (Williams and McKee, 1997). Basu and Murali (2001) have argued that continuous driving of turbulence is consistent with observational constraints only if the driving occurs on the largest scale in the cloud, i.e., most of the energy is contained on that scale. Furthermore, continuous driving may not even be required if the decay time of the large scale modes is greater than or equal to the estimated cloud lifetimes. Our models suggest that large-scale modes that are coupled to the external magnetic field can persist for very long times, thus reducing the need for continuous driving in order to explain observations. These modes preferentially span the largest scales in the model cloud, in agreement with analysis of observed cloud turbulence (Heyer and Brunt, 2007). Future spectral line modeling of the large-scale cloud oscillations in our model cloud may make for useful comparison with observations, as has been done in a previous study of motions in the vicinity of dense cores (Kirk et al., 2009).

A counter-effect to the maintenance of large-scale modes is the loss of energy to the external medium by the propagation of MHD waves along the magnetic field. This is a possible energy loss mechanism for all molecular clouds, although one may also argue that a clump embedded in a larger complex may reach a steady state in which it gains

as much energy from its exterior as it loses. In any case, the study of the propagation of waves outside the cloud remains outside the scope of our model. Future three-dimensional global MHD models of molecular clouds, which include the effect of an external medium, can address this point.

2.5 Summary

We have demonstrated that MHD modes driven by the tension of inclined magnetic field lines have a large phase speed for subcritical clouds, which increases in proportion to the square root of the wavelength. Numerical simulations show that nonlinear motions (in comparison to the sound speed) persist indefinitely for thin-sheet evolution in the limit of magnetic flux-freezing. These are the first of any variety of MHD turbulence simulations that show long-lived nonlinear motions. For the broad set of models that we study, the residual one-dimensional rms material motions are in the range of $\approx 2 c_s - 5 c_s$ for cloud sizes in the range of $\approx 2 \text{ pc} - 16 \text{ pc}$. We find that runaway collapse toward isolated density peaks occurs when partial ionization due to (primarily) cosmic rays and ambipolar diffusion is included. However, the flux-freezing results can be relevant to understanding the low-column-density molecular cloud envelopes, which are photoionized to the level of effective flux-freezing, and contain most of the mass in a molecular cloud. While our model of a magnetized sheet is an idealized representation of a molecular cloud, the existence of wave modes driven by a magnetic field that threads the cloud and is connected to an external medium must have some counterpart in real molecular clouds. Long-wavelength modes such as the ones we study may provide at least part of the explanation for widely observed supersonic motions in molecular clouds.

Acknowledgements

SB acknowledges the hospitality of the Isaac Newton Institute for Mathematical Sciences at Cambridge University during the writing of this paper. SB was supported by a Discovery Grant from NSERC. WBD was supported by an Alexander Graham Bell Canada Graduate Scholarship from NSERC.

Bibliography

Basu, S. and Ciolek, G. E.: 2004, *ApJ* **607**, L39

- Basu, S., Ciolek, G. E., Dapp, W. B., and Wurster, J.: 2009a, *New A* **14**, 483
- Basu, S., Ciolek, G. E., and Wurster, J.: 2009b, *New A* **14**, 221
- Basu, S. and Murali, C.: 2001, *ApJ* **551**, 743
- Ciolek, G. E. and Basu, S.: 2006, *ApJ* **652**, 442
- Ciolek, G. E. and Mouschovias, T. C.: 1995, *ApJ* **454**, 194
- Goldsmith, P. F., Heyer, M., Narayanan, G., Snell, R., Li, D., and Brunt, C.: 2008, *ApJ* **680**, 428
- Heiles, C. and Troland, T. H.: 2005, *ApJ* **624**, 773
- Hennebelle, P. and Inutsuka, S.: 2006, *ApJ* **647**, 404
- Heyer, M., Gong, H., Ostriker, E., and Brunt, C.: 2008, *ApJ* **680**, 420
- Heyer, M. H. and Brunt, C.: 2007, in B. G. Elmegreen & J. Palous (ed.), *IAU Symposium*, Vol. 237 of *IAU Symposium*, pp 9–16
- Kirk, H., Johnstone, D., and Basu, S.: 2009, *ApJ* **699**, 1433
- Kirk, H., Johnstone, D., and Di Francesco, J.: 2006, *ApJ* **646**, 1009
- Kudoh, T. and Basu, S.: 2003, *ApJ* **595**, 842
- Kudoh, T. and Basu, S.: 2006, *ApJ* **642**, 270
- Li, Z. and Nakamura, F.: 2004, *ApJ* **609**, L83
- Mac Low, M.: 1999, *ApJ* **524**, 169
- Mac Low, M., Klessen, R. S., Burkert, A., and Smith, M. D.: 1998, *Physical Review Letters* **80**, 2754
- McKee, C. F.: 1989, *ApJ* **345**, 782
- McKee, C. F. and Ostriker, E. C.: 2007, *ARA&A* **45**, 565
- Mouschovias, T. C.: 1987, in G. E. Morfill & M. Scholer (ed.), *NATO ASIC Proc. 210: Physical Processes in Interstellar Clouds*, pp 453–489
- Nakamura, F. and Li, Z.: 2005, *ApJ* **631**, 411

Ostriker, E. C., Stone, J. M., and Gammie, C. F.: 2001, *ApJ* **546**, 980

Solomon, P. M., Rivolo, A. R., Barrett, J., and Yahil, A.: 1987, *ApJ* **319**, 730

Stone, J. M., Ostriker, E. C., and Gammie, C. F.: 1998, *ApJ* **508**, L99

Williams, J. P. and McKee, C. F.: 1997, *ApJ* **476**, 166

Chapter 3

An analytic column density profile to fit prestellar cores

3.1 Introduction

In recent years, observational advances have made it possible to measure column density profiles in prestellar cores. Various methods are being used in the literature. Ward-Thompson et al. (1999) measured mm continuum emission, while Bacmann et al. (2000) utilized mid-IR absorption, and Alves et al. (2001) measured dust extinction and reddening of the light of background stars in the near-IR. A fourth method is to use flux measurements in optically thin lines (Tafalla et al., 2002). Most of the column density profiles measured in these ways show certain prominent common features: a central flat region, followed by a power-law decline. Some cores additionally exhibit signatures of steepening of the profile, while some show a more-or-less smooth merger to some background value of the column density (Bacmann et al., 2000).

One model often used to fit to such cores (e.g., Evans et al., 2001; Teixeira et al., 2005) is the *Bonnor-Ebert sphere* (hereafter BE sphere). This model assumes an isothermal sphere in equilibrium, acted upon only by gravity and thermal pressure, and bound by some external pressure (Bonnor, 1956; Ebert, 1955). In the central region its density profile is flat with density $\approx \rho_c \equiv \rho(r=0)$. The size of this region is proportional to the Jeans length, $R_J \propto c_s/\sqrt{G\rho_c}$. It transitions into a power-law decline that approaches the *Singular Isothermal Sphere* (SIS) with $\rho_{\text{SIS}} = c_s^2(2\pi Gr^2)^{-1}$ for large radii (Shu, 1977). The cloud is finally cut off at some finite radius, where external pressure forces match the internal forces. The BE model invokes the dimensionless radius parameter

¹A version of this chapter has been published as Dapp, Wolf B. & Basu, Shantanu 2009, MNRAS, 395, 1092

$\xi \equiv r\sqrt{4\pi G\rho_c}/c_s$. The value $\xi_{\text{crit}} = 6.45$ marks a dividing line such that clouds truncated at dimensionless radius $\xi_s > \xi_{\text{crit}}$ are in an unstable equilibrium, and clouds with $\xi_s < \xi_{\text{crit}}$ are stable.

The column density profile of the BE sphere, obtained by integrating the volume density numerically along a line of sight, matches well with some observations (B68; Alves et al., 2001). Depending on the parameters, the power-law decline $\propto r^{-1}$ in column density can be more or less pronounced, or even almost completely absent. The profile steepens at the edge because the line of sight through the sphere becomes shorter. This is a geometric effect which is present in all truncated models, unless the density *increases* sufficiently fast with radius.

While physically motivated and reproducing features of several observed column density profiles, the BE model has shortcomings. The most important is the key assumption of equilibrium. In fact, most fits are found to be supercritical (Teixeira et al., 2005), representing unstable equilibria. These states are not expected to exist in reality, as any perturbation will send them to immediate collapse. On a more practical side, the procedure of fitting the BE model to observations is quite involved. The volume density is only available as a numerical solution, which then needs to be integrated (again numerically) to calculate the column density. Sometimes the fit demands temperatures *well above* those measured for the centres of prestellar cores (Bacmann et al., 2000; André et al., 2003; Kirk et al., 2005), and predicted by detailed models of the thermodynamics within the core (Galli et al., 2002). Finally, most of the observed cores are deeply embedded within their parent clouds, and the source of a bounding external pressure is not obvious. The often-cited example B68 (Alves et al., 2001) is an exception, as it is thought to lie within a hot HII region.

We stress that the generic features of the BE density profile are not unique to equilibrium situations (see Kandori et al., 2005). The flat region with adjacent r^{-2} density profile appears also in solutions of the hydrodynamic equations for gravitationally collapsing objects (Larson, 1969), as long as pressure is not completely negligible (Shu et al., 1987). The pressure gradient then establishes a region where it nearly balances gravity. Here, the density is nearly constant on the scale of the local Jeans length, shrinking in size over time as the density increases. Inverted, this requires that $\rho \propto r^{-2}$ in the outer profile that is left behind outside the central region (see Basu, 1997).

There is no reason why the above two features (flat region with size of Jeans length and adjacent r^{-2} density profile) should be present in a non-self-gravitating cloud. However, Ballesteros-Paredes et al. (2003) find that convergent turbulent flows, with and even without self-gravity (which are expected to have very different volume density profiles),

nevertheless yield column density profiles that resemble those of a BE sphere. There are three reasons for this seemingly surprising result. The first one is the effect of smoothing the data, by angle-averaging, and also by integration along the line of sight. Secondly, the BE sphere leaves the modeller the freedom to fit the size of the central flat region by varying the temperature. Indeed, Ballesteros-Paredes et al. (2003) fit their simulated cores with BE temperatures in the range of 5 – 60 K, despite their models being strictly isothermal at $T = 11.3$ K. Finally, the position of the outer radius cutoff is somewhat arbitrary. This often leaves large parts of profiles unfitted. In this paper, we argue that fitting a prestellar core profile at a *set* temperature *does* still allow one to distinguish between different models of internal structure.

We propose an analytic density profile reproducing the characteristics of not only isothermal equilibria (Bonnor, 1956; Ebert, 1955), but also non-equilibrium collapse solutions (e.g., Larson, 1969), and many observed profiles (Bacmann et al., 2000). Within the margins of uncertainty it fits the observations as well as the BE model does. However, it possesses a closed-form expression for the column density, and is therefore very easy to fit. Furthermore, the temperature can be an input parameter instead of a fitting parameter, so that the model avoids some of the possible inconsistencies of fitting the BE model to either observations or simulation results. We can use our model to make some inference about the dynamical state of the core.

This paper is organized the following way: Section 3.2 describes the spherical model and its parameters, while Section 3.3 presents a corresponding model for intrinsically flattened objects. In Section 3.4, we apply our model to B68 and L1689B, and we summarize our results in Section 3.5.

3.2 Spherical Geometry

3.2.1 Basic model

The characteristics found in observed column density profiles and theoretically both in equilibrium and collapse solutions can be parametrized by a volume density more generic than the BE sphere. We propose using the profile

$$\varrho(r) = \begin{cases} \varrho_c a^2 / (r^2 + a^2) & r \leq R, \\ 0 & r > R, \end{cases} \quad (3.1)$$

characterized by a central volume density ρ_c and truncated at some radius R . The parameter a fits the size of the flat region in terms of the Jeans length, and is given by

$$a = k \frac{c_s}{\sqrt{G\rho_c}}, \quad (3.2)$$

where G is the gravitational constant and k is a constant of proportionality. This profile is also mentioned in King (1962) and Tafalla et al. (2002). The temperature T , which can be constrained observationally, is *not* used as a fitting parameter. It enters through the value of the isothermal sound speed $c_s = \sqrt{k_B T / \mu}$. The Boltzmann constant is denoted by k_B , and $\mu = 2.33 m_H$ is the mean mass of a particle, where m_H is the mass of a hydrogen atom. We assume a 10% number fraction of helium.

The column density is derived by integrating the volume density along a line of sight through the sphere:

$$\begin{aligned} \Sigma(x) &= 2 \int_0^{\sqrt{R^2-x^2}} \rho(s) ds \\ &= 2 \int_x^R \frac{\rho(r) r dr}{\sqrt{r^2-x^2}} \end{aligned} \quad (3.3)$$

where we have used the transformation $s = \sqrt{r^2-x^2}$ and hence $ds = r dr / \sqrt{r^2-x^2}$. Fig. 3.1 defines the quantities appearing in this derivation.

Inserting equation (3.1) into equation (3.3), we find that the integral is analytically tractable. The closed-form expression for the column density is then

$$\Sigma(x) = \frac{2a^2 \rho_c}{\sqrt{x^2+a^2}} \arctan \left(\frac{\sqrt{R^2-x^2}}{\sqrt{x^2+a^2}} \right). \quad (3.4)$$

This can be re-written in terms of the central column density by introducing the ratio $c \equiv R/a$, called the concentration in King (1962). With $\Sigma(x=0) \equiv \Sigma_c = 2a\rho_c \arctan(c)$ we find

$$\begin{aligned} \Sigma(x) &= \frac{\Sigma_c}{\sqrt{1+(x/a)^2}} \\ &\times \left[\arctan \left(\sqrt{\frac{c^2-(x/a)^2}{1+(x/a)^2}} \right) / \arctan(c) \right]. \end{aligned} \quad (3.5)$$

Fig. 3.2 demonstrates that this profile possesses generic features that it shares with observations, collapse solutions, and with the BE model: a flat central region, a power-

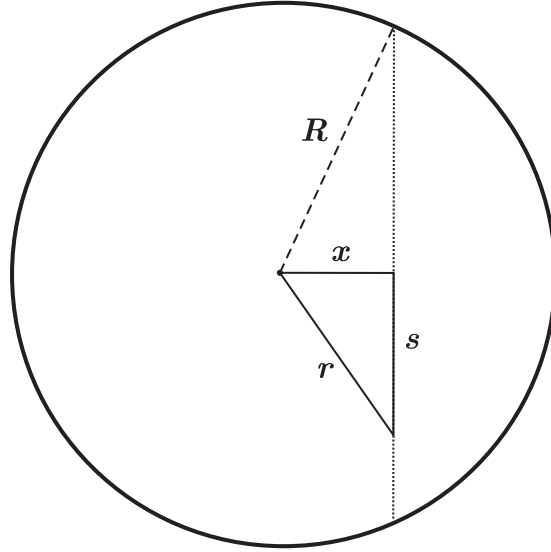


Figure 3.1: Schematic illustration of a cut through a spherical cloud of radius R . The observer is positioned along the direction of the coordinate s , and measures an integrated column density Σ as a function of the offset x .

law decline, and steepening at the edge. We note that the effect of the boundary is exclusively contained in the factor in square brackets.

The quantity c determines the size of the region described by the power-law. If it is large, there is a pronounced power-law, whereas if c approaches unity, the cut-off already dominates near the flat region and inhibits the power-law.

The three parameters to fit are (i) the outer radius R , (ii) the central column density Σ_c , and (iii) the size of the flat region a . The latter contains the product of k and \sqrt{T} , as shown in equation (3.2). If the temperature is pre-determined, a only depends on the value of k . This then allows for a stability assessment, as demonstrated in the following section.

3.2.2 Model parameters

The pressure in an isothermal system is given by $P = c_s^2 \rho$, and hence the pressure gradient for the spherically symmetric volume density profile of equation (3.1) is

$$\frac{dP}{dr} = c_s^2 \frac{d\rho}{dr} = \frac{-2c_s^2 \rho_c r}{a^2 [1 + (r/a)^2]^2}. \quad (3.6)$$

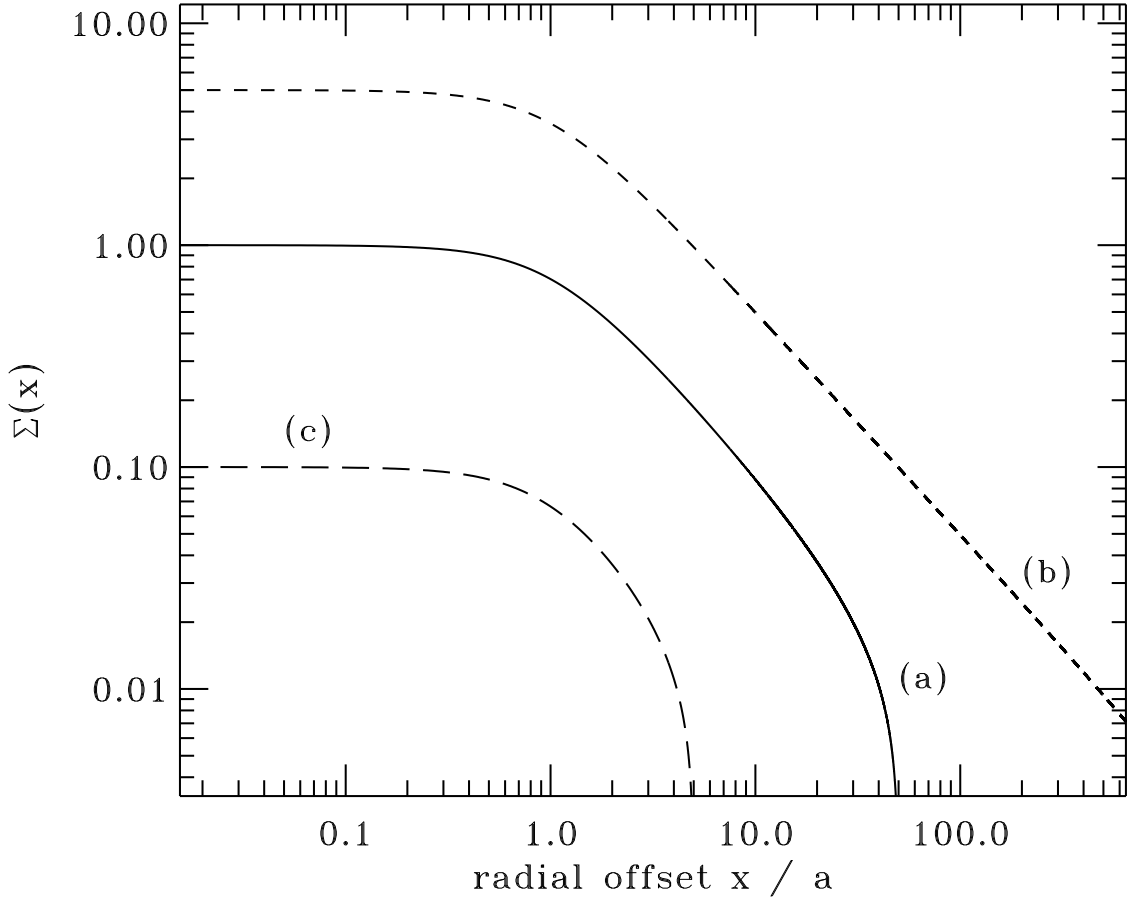


Figure 3.2: Plots of equation (3.5) for varying $c \equiv R/a$. All cases have identical values for a . The central column densities are chosen to be different in order for the plots not to overlap. The solid line illustrates the three major characteristics of this function: the flat region in the centre of size a , the adjacent power-law decline $\propto x^{-1}$, a steepening at the edge for geometric reasons (see text), out to the cut-off radius R . In this case, $c = 50$. The dashed-line shows a model dominated by the power-law regime, with $c > 1000$. R is chosen so that the influence of the cut-off is negligible. The long-dashed line finally demonstrates that the power-law can be suppressed entirely if $R \gtrsim a$. In this case, $c = 5$.

In the inner regions, where $r \ll a$,

$$\frac{dP}{dr}\Big|_{r \ll a} = \frac{-2c_s^2 \varrho_c r}{a^2}. \quad (3.7)$$

This demonstrates a simple point: the larger the flat region a , the smaller the pressure gradient in that region. The minimal value for a is reached in an equilibrium situation. A larger a would result in a smaller pressure gradient, gravity would win out, and collapse would ensue. Conversely, for a smaller than its equilibrium value the pressure force would dominate, causing expansion. However, that case is not probable since a profile with $\varrho \propto r^{-2}$ mandates a strong gravitational influence.

Another well-known model besides the SIS is the so-called Larson-Penston solution (LP solution), a self-similar spherical collapse solution, assuming a homogeneous initial density distribution (Larson, 1969; Penston, 1969). This highly dynamical model does not assume equilibrium, and asymptotically reaches a density profile for which

$$\varrho_{\text{LP}} = 4.4 \varrho_{\text{SIS}} \quad (3.8)$$

everywhere. We now want to find an expression for the parameter a in the SIS and the LP models. In the outer regions, equation (3.1) becomes

$$\varrho(r \gg a) \approx \frac{\varrho_c a^2}{r^2} = \frac{\tilde{k} c_s^2}{2\pi G r^2}, \quad (3.9)$$

where $\tilde{k} \equiv 2\pi k^2 = 1$ for the SIS (equilibrium) and $\tilde{k} = 4.4$ for the asymptotic LP collapse solution. Therefore

$$k \equiv \sqrt{\frac{\tilde{k}}{2\pi}} = \begin{cases} 0.399 & \text{for SIS,} \\ 0.837 & \text{for LP.} \end{cases} \quad (3.10)$$

This has a direct application to observed prestellar cores. If an estimate for the core temperature is available, equation (3.5) can be fit to the column density profile, with k as a fitting parameter. If $k \approx 0.4$, the system can be considered to be in equilibrium. If k is significantly larger than 0.4, and closer to 1, the cloud under scrutiny is collapsing.

Fig. 3.3 shows our model with a chosen to converge to either the SIS or the asymptotic LP solution. We also plot the equilibrium BE model. In order to avoid boundary effects, the outer radius was moved to $\approx 10^2 c_s / \sqrt{G \varrho_c}$. The BE profile does not join onto the SIS profile right away. It overshoots, then steepens and asymptotically approaches the SIS profile at large radii.

We may ask which value of k is most appropriate to model a critical BE sphere. The

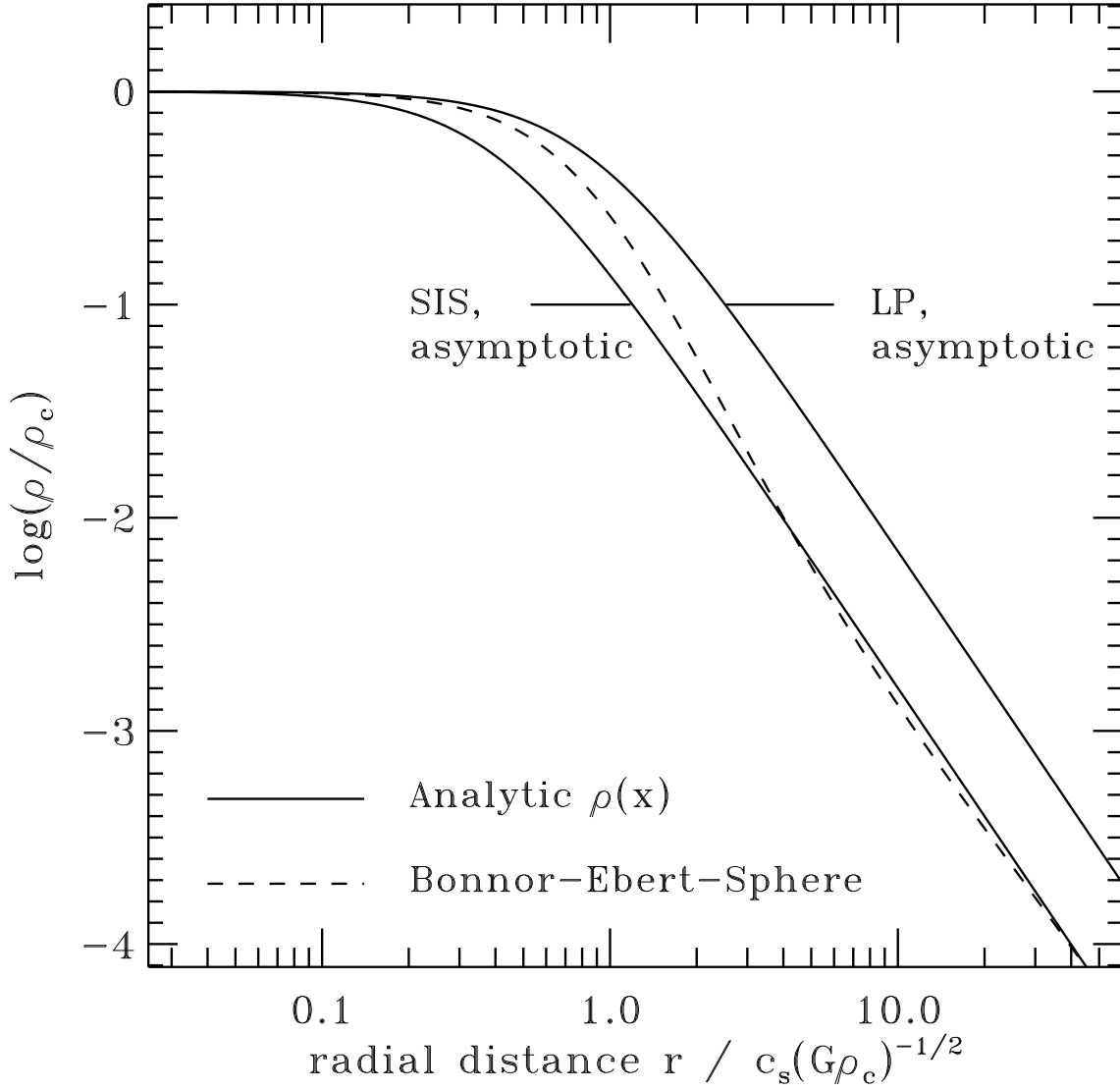


Figure 3.3: Comparison between the BE sphere (dashed line) and our model (solid lines) for identical central temperature and cut-off radius. The top line is our model with $k = 0.837$, for which the profile approaches the asymptotic LP solution. The lower line shows $k = 0.399$, for which the SIS profile is reached. The dashed line represents the BE model, which also asymptotically approaches the SIS.

overshoot effectively produces a larger flat region if the solution is truncated at $\xi_s = \xi_{\text{crit}}$. The resultant a has to be larger than for the SIS. Having fixed the temperature this can only be achieved by increasing k , as we show in Fig. 3.4. Profile (a) shows a subcritical BE sphere, i.e. a stable equilibrium solution. In this case, there is no discernible power-law region and the central flat region makes up a significant portion of the total radius. The cut-off becomes dominant just outside the flat region, and the best-fit dimensionless dynamics parameter is $k = 0.63$. Note that the density contrast is less than an e -folding, which means a mean column density enhancement of $< 40\%$ over the background. Such an object would not be observationally characterized as a prestellar core (André et al., 2009).

Profile (c) in Fig. 3.4 shows the opposite situation, where the power-law portion of the profile is fit, and $k = 0.46$ is closer to the equilibrium value. As shown in Fig. 3.3, the BE model initially has a power-law index steeper than -2 . This is the reason why the profiles do not match up as well as for the other cases. Profile (b) finally shows a critical BE sphere. A density contrast greater than $\rho_c/\rho_s = 14.0$ would characterize an unstable equilibrium, initiating collapse upon the smallest of perturbations. The two profiles are very similar, only minor deviations are discernible. In order to fit our model to the overshoot of the BE profile over the SIS, a has to be larger, which can only be achieved by $k = 0.54$. We demonstrate this effect on the examples of B68 and L1689B in Sections 3.4.1 and 3.4.2: as a consistency check, we insert the derived BE temperatures into our model, and indeed find $k = 0.57$ and $k = 0.56$ respectively. Note that the BE model *is* a valid model in absence of any effects other than gravity and thermal pressure, and thus we conclude that in this case, not the asymptotic value of $k = 0.4$ but rather the critical BE value of $k = 0.54$ is relevant for the stability assessment. We stress that if k is significantly larger than that, it is strongly indicative of collapse.

Since the BE model effectively has $k \approx 0.5$ and collapsing clouds have $k \approx 1.0$, trying to force a BE model fit to such a cloud results in spurious higher temperatures. This can be seen in Bacmann et al. (2000). A factor of 2 in the dimensionless dynamics parameter k needs to be compensated by a factor of 4 in temperature when fitting a BE equilibrium state.

3.2.3 Total mass

Both our model and the BE sphere have a well-defined outer radius, and the total mass depends on it. For the profile of equation (3.1), the total mass has a closed-form expres-

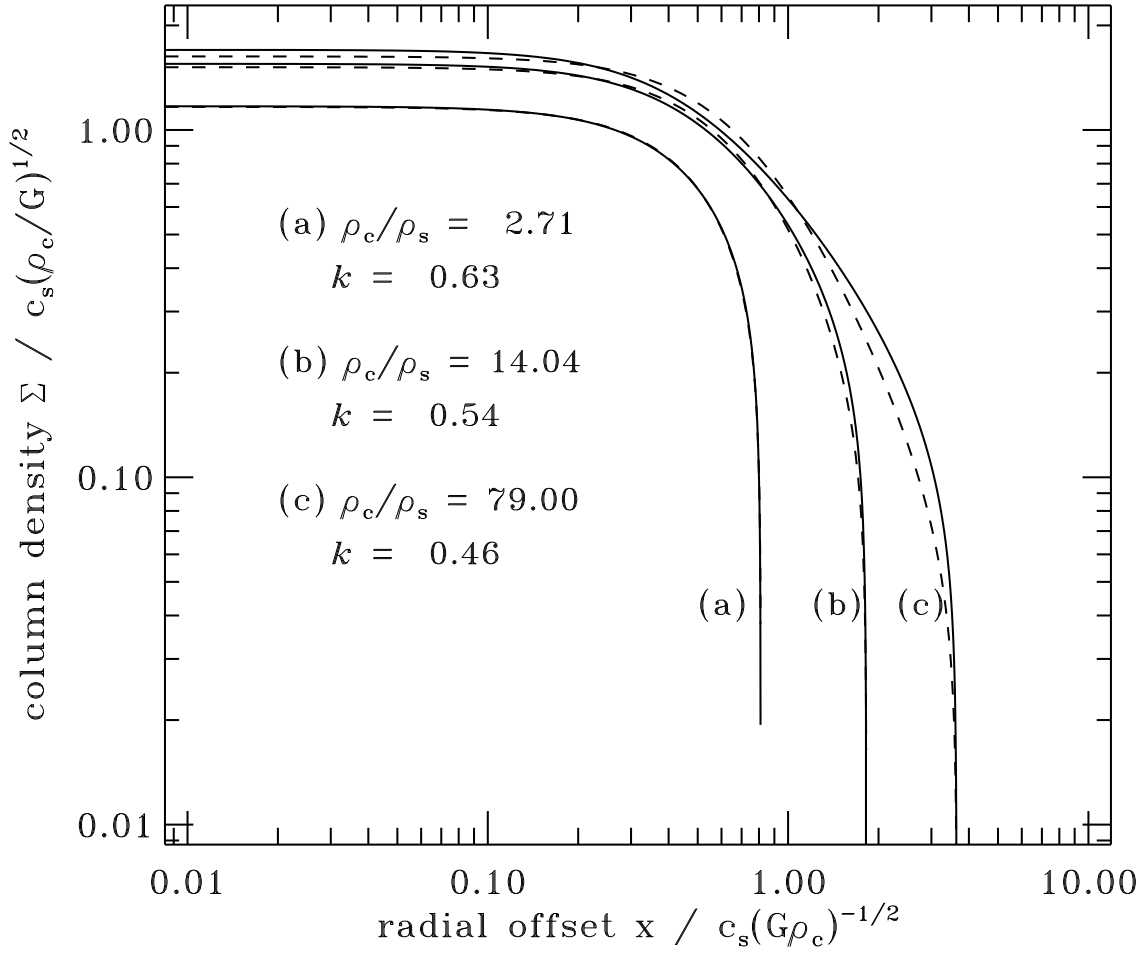


Figure 3.4: Fit of the integrated column density of various BE spheres (dashed lines) with our model (solid lines). (a) is a subcritical (stable) model, while (b) shows a critical BE sphere. In that case, $k = 0.54$ (see text for explanation). (c) presents a fit to a highly supercritical (unstable) BE model.

sion. Evaluating $\int_0^R 4\pi r^2 \varrho(r) dr$ yields

$$M = 4\pi \varrho_c a^3 \left[\frac{R}{a} - \arctan\left(\frac{R}{a}\right) \right]. \quad (3.11)$$

There is evidence for some power-law behaviour in most observed profiles (e.g., Bacmann et al., 2000). In such a situation, the value of R/a must be at least $\gtrsim 10$ (cf. Fig. 3.2). Then, the contribution of $\arctan(c)$ is quite close to its limiting value of $\pi/2$, and the total mass is given by

$$M \approx 4\pi \varrho_c a^2 R = 4\pi k^2 R c_s^2 / G \quad (3.12)$$

with $< 15\%$ error. The equivalent expression for the BE model is (derived assuming an SIS profile at large radii)

$$M_{\text{BE}} \approx 2R c_s^2 / G. \quad (3.13)$$

Both expressions for the masses are linearly dependent on the unknown radius R . For a given (measured) temperature, our model additionally invokes the dimensionless dynamics parameter k , which is well constrained by the size of the flat region. The BE mass instead depends on the temperature of the fit, which we show in Sections 3.2.2 and 3.4.2 to potentially be a very poor value, and prone to overestimation by as much as a factor of 4.

3.3 Disc geometry

3.3.1 Basic model

Most observed cores do not appear circular in projection. A corresponding analysis as in Section 3.2.2 can be done for a disc-like geometry as well. Here, a generic face-on column density profile is

$$\sigma(r) = \begin{cases} \sigma_c / \sqrt{1 + (r/a)^2} & r \leq R, \\ 0 & r > R. \end{cases} \quad (3.14)$$

This profile provides a good fit to the column density of collapsing flattened clouds (Basu, 1997), even though the models in that paper are not truncated.

Assuming vertical hydrostatic equilibrium and ignoring the effect of external pressure, the volume density is proportional to the square of the column density

$$c_s^2 \varrho = \frac{\pi}{2} G \sigma^2, \quad (3.15)$$

and the density accordingly is given by

$$\varrho(r) = \frac{\pi G}{2c_s^2} \frac{\sigma_c^2}{1 + (r/a)^2}. \quad (3.16)$$

The assumption of vertical hydrostatic equilibrium is well justified by simulations when some source of flattening is present, such as rotation (Narita et al., 1984), or magnetic fields (Fiedler and Mouschovias, 1993). Abbreviating $\pi G \sigma_c^2 / (2c_s^2) = \varrho_c$, the volume density profile has exactly the same form as for the spherical case (with a different constant).

3.3.2 Model parameters

Integrating $\varrho(r)$ through the disc viewed edge-on, the column density versus the offset x has the same functional form as derived above for the spherical case in equation (3.5). The only difference is that the central column density is now given by $\Sigma_c = \pi k \sigma_c \arctan(c)$, since for a thin disc, the relation between a and the Jeans length is

$$a = k \frac{c_s^2}{G \sigma_c}. \quad (3.17)$$

This similarity means that both a flattened and a spherical object (see Section 3.2) can be fit with the same formula. Note that $\sigma(r)$ is the face-on column density, whereas $\Sigma(x)$ is its edge-on counterpart.

We can compare the (face-on) generic column density profile to one of an equilibrium solution, in order to get the minimal value for a , as done for the spherical case above. Here, the appropriate profile is the singular isothermal disc, characterized by

$$\sigma_{\text{SID}} = \frac{c_s^2}{2\pi G r}. \quad (3.18)$$

Following the same steps as in Section 3.2.2, the large-radius asymptote of equation (3.14) is

$$\sigma(r \gg a) \approx \frac{\sigma_c a}{r}, \quad (3.19)$$

yielding $a = c_s^2 / (2\pi G \sigma_c)$. Comparing this expression to equation (3.17), we find $k = 1/2\pi = 0.160$ for equilibrium.

Saigo and Hanawa (1998) show that for an isothermal disc-like cloud during runaway collapse, the self-similar column density profile is given by $3.61 \sigma_{\text{SID}}$, analogous to how the LP solution is over-dense compared to the SIS. This provides a good estimate for

the value of the dimensionless dynamics parameter for a dynamically collapsing disc-like cloud, $k = 0.57$. Flattened cloud cores best fit with values for the dimensionless dynamics parameter $k \approx 0.2$ are therefore close to equilibrium, while $k \approx 0.6$ is strongly indicative of dynamical collapse.

Effect of magnetic fields

Inclusion of magnetic fields into a spherical model poses a problem: the magnetic field lines cannot be arranged in a spherically symmetric way. There has to be a preferred direction. However, in disc-like geometry, the axis perpendicular to the disc is preferred already, and can be chosen as the axis of orientation of a large-scale magnetic field. Starting with initially straight field lines through a collapsing astrophysical gas sphere, flattening ensues along this preferred direction. Matter can contract significantly along the field lines, but the Lorentz force will impede motions perpendicular to the field (Mouschovias, 1976).

In the limit of a magnetic field much stronger than the field of the ambient cloud, Basu (1997), Nakamura and Hanawa (1997) and Shu and Li (1997) showed that the contribution of the magnetic field can be folded into a force calculation of the collapse of a magnetized disc by magnetic pressure modifying the effective sound speed, and magnetic tension changing the effective gravitational constant. Then we can write (see Basu, 1998)

$$a = k \frac{c_s^2 (1 + 2\mu^{-2})}{G\sigma_c (1 - \mu^{-2})}. \quad (3.20)$$

We use the standard definition of the mass-to-flux ratio in units of the critical value (Nakano and Nakamura, 1978):

$$\mu = \frac{\sigma(r)}{B_z(r)} 2\pi\sqrt{G}. \quad (3.21)$$

Collapse requires $\mu > 1$, otherwise the magnetic forces will dominate over gravity and stabilize the cloud, and evolution can only happen on long time scales by ambipolar diffusion (see, e.g., Shu et al., 1987).

We can absorb the modification into an effective k , writing it as $k_{\text{eff}} = k (1 + 2\mu^{-2}) (1 - \mu^{-2})^{-1}$. The value $k = 0.160$ as derived for the non-magnetic case remains the minimal value, while k_{eff} can exceed it by a factor of 1.1 to 2 for $\mu \approx 2 - 5$, which is a reasonable estimate for supercritical cores (Ciolek and Mouschovias, 1994; Basu and Mouschovias, 1994). This means $k_{\text{eff}} \lesssim 0.3$, which leaves it still a factor of 2 smaller than the value for the dimensionless dynamics parameter for dynamical collapse ($k \approx 0.6$, as shown above),

and thus clearly distinguishable.

Effect of rotation

Similar to the problem for magnetic fields, rotation cannot be considered in strict spherical symmetry. In fact, rotation can be the cause of disc-like geometry, as a collapsing rotating spherical cloud will flatten along the rotation axis before contracting in the radial direction.

There exist self-similar solutions for the collapse of a rotating thin disc (Narita et al., 1984; Saigo and Hanawa, 1998). Following the discussion in Basu (1997), one can express the additional effect of rotation as an effective acceleration $a_{\text{eff}} = a_{\text{T}} (1 + a_{\text{C}}/a_{\text{T}})$, where a_{T} is the thermal acceleration, while a_{C} denotes the centrifugal acceleration. Assuming the column density profile of equation (3.14) and proportionality between the specific angular momentum and enclosed mass, this leads to

$$a_{\text{C}}/a_{\text{T}} \approx 3 \times 10^{-3}. \quad (3.22)$$

This number is computed for a background rotation rate of the molecular cloud $\Omega_{\text{c}} = 10^{-14} \text{ rad s}^{-1}$, a central column number density $N_{\text{c}} = 10^{21} \text{ cm}^{-2}$, and a temperature $T = 10 \text{ K}$. Hence, we find that the effective radial acceleration opposing gravity exceeds the thermal acceleration by less than 1%. This shows that, unlike magnetic forces, rotation does not significantly modify the size of the flat region and hence the dimensionless dynamics parameter k .

3.4 Applications

We fit both the BE model and our model to observational data by determining the best-fitting parameters using a standard Levenberg-Marquardt least-squares minimization algorithm based on MINPACK.

3.4.1 B68

We fit our model to B68, the prime example in the literature for an extraordinarily good fit of the BE model to a (angular-averaged) column density profile measured in near-IR dust extinction (Alves et al., 2001). B68 is an isolated Bok globule, a small dark cloud which has been studied extensively. Alves et al. (2001) assume a distance of 125 pc and quote a BE mass of $2.1 M_{\odot}$, a temperature of $T = 16 \text{ K}$, an outer radius of 12,500 au,

and a dimensionless outer radius $\xi_s = 6.9 \pm 0.2$. Hotzel et al. (2002) and Lai et al. (2003) more recently updated some of these values by measuring the temperature to be $T = 10 \pm 1.2$ K and $T = 11 \pm 0.9$ K, respectively, and estimated the cloud to be closer by about 25 pc, placing it at the near side of the Ophiuchus complex. This reduces the outer radius and decreases the BE mass to $\approx 1 M_\odot$, but does not change the value for ξ_s , as that is determined by the shape of the profile.

We perform a similar analysis as Alves et al. (2001). We calculate a BE sphere, vary the temperature, the dimensionless and physical outer radii ξ_s and R , and fit the line-of-sight integral to the observational data, assuming a distance of 100 pc. This procedure yields a BE mass of $M = 1.17 M_\odot$, a BE model temperature of $T = 11.1$ K, and a central number density of $n_c = 2.3 \times 10^5 \text{ cm}^{-3}$. The outer radius of the best BE fit is 10,680 au, and the dimensionless outer radius $\xi_s = 7.0$. The best fit of our model to the same data yields a total mass of $M = 1.2 M_\odot$, $R = 10,420$ au, and $n_c = 2.7 \times 10^5 \text{ cm}^{-3}$. The size of the flat region is $a = 2,830$ au. Assuming a temperature of $T = 11$ K, as in the observations mentioned above, this corresponds to $k = 0.57$. We showed in Section 3.2.2 that a critical BE sphere is fit with $k = 0.54$, and we conclude that the internal structure of B68 may indeed very closely resemble a critical BE sphere. Fig. 3.5 shows that the best fits to B68 of the BE sphere and our model differ by very little over the whole range of data.

The BE analysis is much more involved and computationally expensive than our model. It necessitates a numerical solution of the Lane-Emden equation. This ordinary differential equation (ODE) underlies the BE model, and does not have a general analytical solution. The numerical solution is truncated at the dimensionless radius ξ_s and converted into physical units. Only then can one integrate along lines of sight through the solution numerically, yielding the column density to be compared with observational data. In contrast, fitting our model to a dataset requires less than a dozen lines of code.

3.4.2 L1689B

Another prestellar core to which we apply our model is L1689B. Its central column density is much greater and it is more extended than B68. Furthermore, it is not isolated, but rather embedded within the larger complex of the Ophiuchus molecular cloud. Its profile was measured by Bacmann et al. (2000) using mid-IR absorption observations and updated by André et al. (2003). We use the East-West profile, which shows evidence of steepening in the outer regions.

The BE fit to the data in Fig. 3.6 yields $\xi_s = 11.2$ (supercritical, unstable core) and

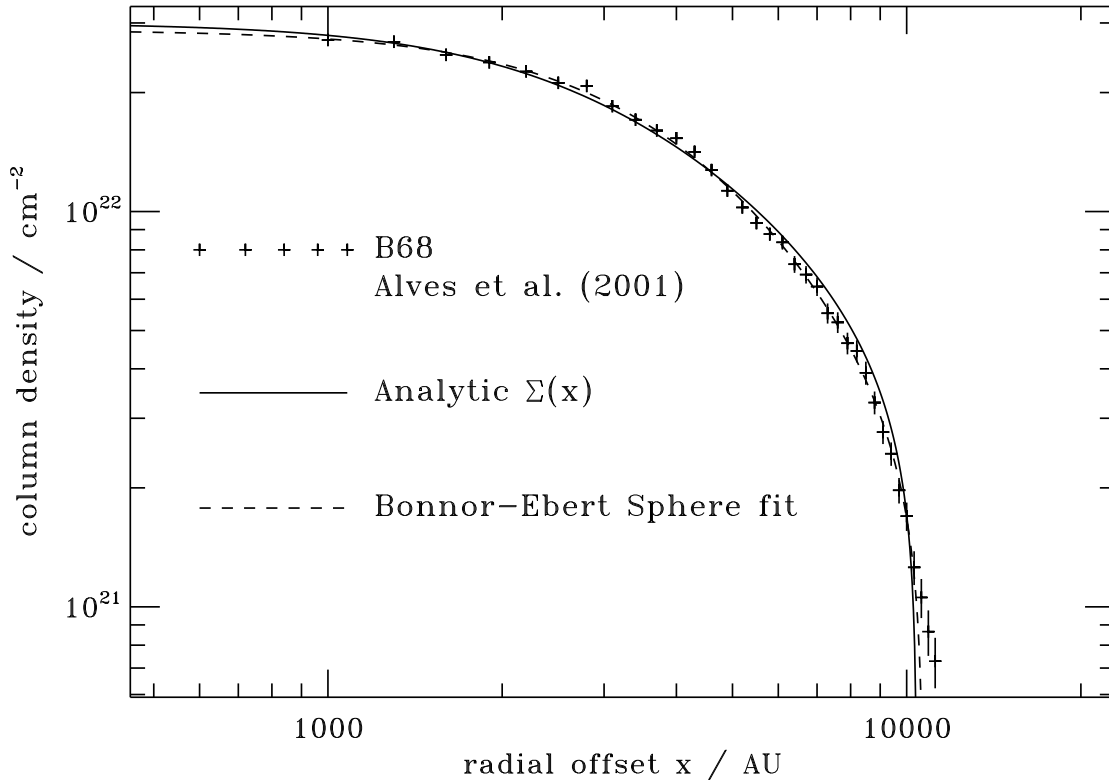


Figure 3.5: Best fit of the BE model (dashed line) and our model (solid line) to the column density of B68 (Alves et al., 2001). Both fits follow the data points extremely closely and yield very similar results for the total mass (see text). Like the BE model, our model fit is consistent with an equilibrium cloud. The symbols reflect the r.m.s. dispersion of the extinction measurement in each averaging annulus.

a mass of $M = 9.3 M_{\odot}$, similar to what André et al. (2003) found. Fitting our model results in $M = 9.1 M_{\odot}$. However, in contrast to the case of B68, the temperatures of the two fits are vastly different. The BE model requires a temperature $T = 40$ K, whereas our model can achieve the same quality of fit with a temperature $T = 10$ K. We fit the size of the flat region $a = 3,600$ au which is a combination of the temperature and k . A temperature of $T = 10$ K mandates $k = 1.1$, which is very far from the value required for equilibrium, and even surpasses the value $k = 0.837$ achieved in the highly dynamical asymptotic LP solution. As discussed in Section 3.2.2, this is a strong indication that L1689B cannot be in equilibrium, but must instead be collapsing.

Again, our model fits this dynamically evolving object just as well as it fit the presumably almost static B68. It can do so without introducing inconsistent temperatures, and with much less computational and coding effort.

3.5 Summary and conclusions

We have introduced an analytic profile for the integrated line-of-sight column density of an isothermal spherical or flattened cloud. This cloud can either be in equilibrium or in a state of dynamical collapse. Our model is very simple to calculate compared to the BE model, and a few lines of code suffice to find a best-fit set of parameters. Another advantage lies in its ability to also encompass non-equilibrium states. The dimensionless dynamics parameter k allows one to assess whether a cloud is near equilibrium or vigorously collapsing. At the same time, our model does not produce inconsistencies like the BE model regarding the object's temperature (which can be treated as a constrained quantity and not a free parameter).

Our model can be applied both to spherical and to flattened clouds, and in both cases yields the same functional form for the column density $\Sigma(x)$. It fits the size of the central flat region and allows the modeller to adjust either k or the temperature to match it.

Results of fitting our model to B68 show that it is indeed a near-equilibrium cloud, with parameters very similar to the best-fit BE model. For L1689B, our model avoids the need for a high temperature (the BE model requires $T = 40$ K) since it can be interpreted as having a temperature of $T = 10$ K but being in a state of dynamical collapse. This finding is confirmed by the detection of infall motions for L1689B by means of the shape of the line profiles in optically-thick molecular transitions (Bacmann et al., 2000; Lee et al., 2004). In the future, our model can be applied to many other prestellar cores.

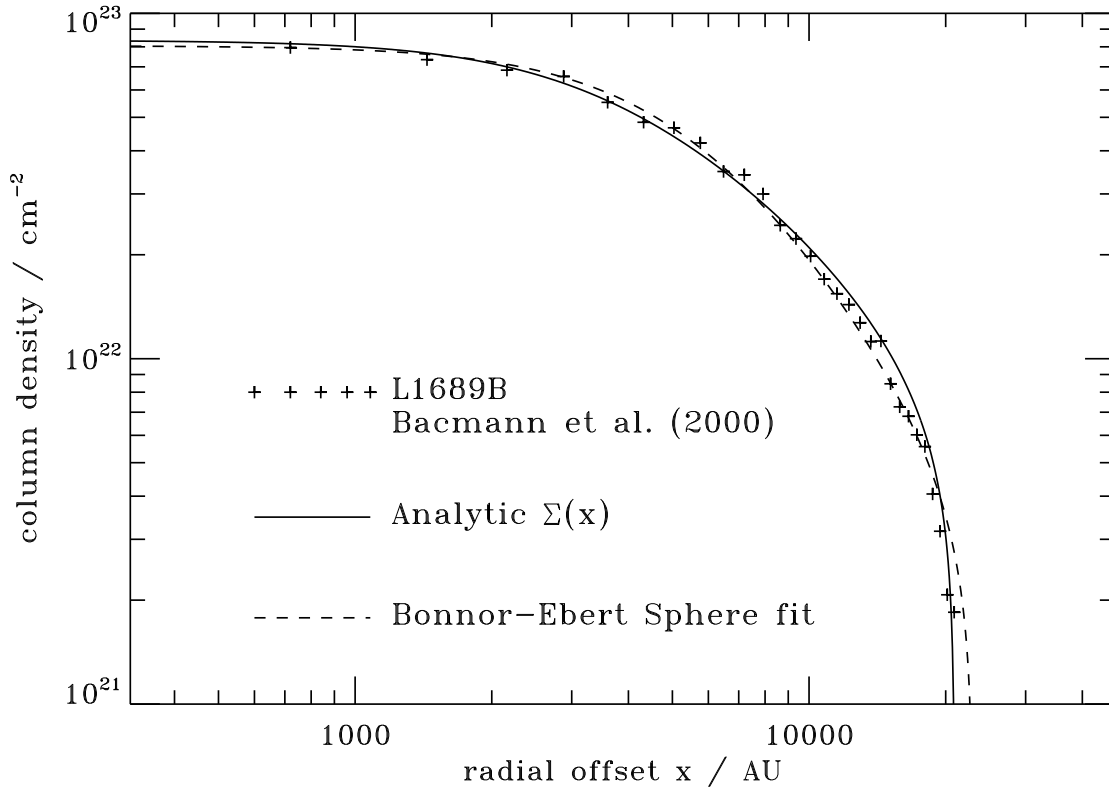


Figure 3.6: Best fit of the BE model (dashed line) and our model (solid line) to the column density of L1689B, as measured by Bacmann et al. (2000) and later updated by André et al. (2003) (symbols). Here, the symbols do not indicate errors bars. Again, both fits are very similar and yield observationally almost indistinguishable results. However, the BE model requires a relatively high temperature of $T = 40$ K, while our model can fit the data with $T = 10$ K. The dimensionless dynamics parameter $k = 1.1$, which means that the cloud is collapsing.

Acknowledgements

We thank Joao Alves for giving access to his data on B68. We also thank Philippe André for his data on L1689B and for his comments on the manuscript. SB was supported by a research grant from NSERC.

Bibliography

- Alves, J. F., Lada, C. J., and Lada, E. A.: 2001, *Nature* **409**, 159
- André, P., Basu, S., and Inutsuka, S.: 2009, in Chabrier, G. (ed.), *Structure Formation in Astrophysics*, pp 254–+, Cambridge University Press
- André, P., Bouwman, J., Belloche, A., and Hennebelle, P.: 2003, in C. L. Curry & M. Fich (ed.), *SFChem 2002: Chemistry as a Diagnostic of Star Formation*, pp 127–+
- Bacmann, A., André, P., Puget, J.-L., Abergel, A., Bontemps, S., and Ward-Thompson, D.: 2000, *A&A* **361**, 555
- Ballesteros-Paredes, J., Klessen, R. S., and Vázquez-Semadeni, E.: 2003, *ApJ* **592**, 188
- Basu, S.: 1997, *ApJ* **485**, 240
- Basu, S.: 1998, *ApJ* **509**, 229
- Basu, S. and Mouschovias, T. C.: 1994, *ApJ* **432**, 720
- Bonnor, W. B.: 1956, *MNRAS* **116**, 351
- Ciolek, G. E. and Mouschovias, T. C.: 1994, *ApJ* **425**, 142
- Ebert, R.: 1955, *Zeitschrift fur Astrophysik* **37**, 217
- Evans, II, N. J., Rawlings, J. M. C., Shirley, Y. L., and Mundy, L. G.: 2001, *ApJ* **557**, 193
- Fiedler, R. A. and Mouschovias, T. C.: 1993, *ApJ* **415**, 680
- Galli, D., Walmsley, M., and Gonçalves, J.: 2002, *A&A* **394**, 275
- Hotzel, S., Harju, J., and Juvela, M.: 2002, *A&A* **395**, L5

- Kandori, R., Nakajima, Y., Tamura, M., Tatematsu, K., Aikawa, Y., Naoi, T., Sugitani, K., Nakaya, H., Nagayama, T., Nagata, T., Kurita, M., Kato, D., Nagashima, C., and Sato, S.: 2005, *AJ* **130**, 2166
- King, I.: 1962, *AJ* **67**, 471
- Kirk, J. M., Ward-Thompson, D., and André, P.: 2005, *MNRAS* **360**, 1506
- Lai, S., Velusamy, T., Langer, W. D., and Kuiper, T. B. H.: 2003, *AJ* **126**, 311
- Larson, R. B.: 1969, *MNRAS* **145**, 271
- Lee, C. W., Myers, P. C., and Plume, R.: 2004, *ApJS* **153**, 523
- Mouschovias, T. C.: 1976, *ApJ* **207**, 141
- Nakamura, F. and Hanawa, T.: 1997, *ApJ* **480**, 701
- Nakano, T. and Nakamura, T.: 1978, *PASJ* **30**, 671
- Narita, S., Hayashi, C., and Miyama, S. M.: 1984, *Progress of Theoretical Physics* **72**, 1118
- Penston, M. V.: 1969, *MNRAS* **144**, 425
- Saigo, K. and Hanawa, T.: 1998, *ApJ* **493**, 342
- Shu, F. H.: 1977, *ApJ* **214**, 488
- Shu, F. H., Adams, F. C., and Lizano, S.: 1987, *ARA&A* **25**, 23
- Shu, F. H. and Li, Z.: 1997, *ApJ* **475**, 251
- Tafalla, M., Myers, P. C., Caselli, P., Walmsley, C. M., and Comito, C.: 2002, *ApJ* **569**, 815
- Teixeira, P. S., Lada, C. J., and Alves, J. F.: 2005, *ApJ* **629**, 276
- Ward-Thompson, D., Motte, F., and Andre, P.: 1999, *MNRAS* **305**, 143

Chapter 4

Averting the magnetic braking catastrophe on small scales: disk formation due to Ohmic dissipation

4.1 Introduction

Understanding how protostellar and protoplanetary disks form is of fundamental importance to theories of star- and planet formation. Observations show their ubiquity around Class II objects (e.g., Andrews and Williams, 2005). In recent years, doubt was cast on their accepted formation mechanism, when it was shown that for flux freezing *magnetic braking* is so effective in removing angular momentum from the parent core that large-scale ($\approx 10^2$ AU) disks are suppressed entirely (Allen et al., 2003; Mellon and Li, 2008; Hennebelle and Fromang, 2008). This scenario held true even when a simplified version of ambipolar diffusion (Mellon and Li, 2009) was included in the model, and has been referred to as the *magnetic braking catastrophe*. Recently, Hennebelle and Ciardi (2009) demonstrated that inclination effects can modify the efficiency of magnetic braking, but a supercritical mass-to-flux ratio by a factor $> 3 - 5$ (i.e., a weak magnetic field) was still required to form a large-scale disk. Duffin and Pudritz (2009) performed three-dimensional simulations with ambipolar diffusion, but only resolved the first core, and did not find Keplerian motion.

Runaway collapse of a prestellar core can effectively trap the magnetic flux in the prestellar phase (e.g., Basu and Mouschovias, 1994). If the evolution continued to proceed under flux-freezing, a big magnetic flux problem would remain, since the emerging

¹A version of this chapter has been published as Dapp, Wolf B. & Basu, Shantanu 2010, A&A, 521L, 56

star would hold $10^3 - 10^5$ times more magnetic flux than observed in T Tauri stars. At densities $\lesssim 10^{12} \text{ cm}^{-3}$, ambipolar diffusion causes flux leakage, while at even higher densities, matter decouples entirely from the magnetic field, and *Ohmic dissipation* becomes dominant (e.g., Nakano et al., 2002). Both effects are revitalized after the formation of a central star (Li and McKee, 1996; Contopoulos et al., 1998). Recently, Krasnopolsky et al. (2010) have shown that for an isothermal core without self-gravity, only an ‘anomalous’ resistivity—a factor of 100 larger than the canonical level—allows disks of size 10^2 AU to form during the Class 0 phase. However, their simulations are dominated by numerical reconnection events that make precise statements about the efficacy of magnetic braking difficult.

Currently, there is no evidence for the presence of centrifugal disks larger than ≈ 50 AU around Class 0 or Class I objects (e.g., Maury et al., 2010). However, there are outflows observed even at these early ages. It is therefore reasonable to assume that disks form at a small scale and only subsequently grow to the larger sizes observed in the Class II phase. We demonstrate the first part explicitly by using a canonical level of Ohmic dissipation alone, and speculate that the combined effects of ambipolar diffusion and Ohmic dissipation will allow for the second part. Additionally, an initially small disk could expand significantly if angular momentum transport is regulated by internal processes (e.g., Basu, 1998; Vorobyov and Basu, 2007).

Machida et al. (2007) performed three-dimensional simulations of resistive MHD on a nested grid, following the evolution to stellar densities, but were only able to integrate until a few days after stellar core formation. We extend their calculations in a dimensionally-simplified model in order to simultaneously address the magnetic flux problem, integrate further in time, and study the formation of a centrifugal disk. We show that catastrophic magnetic braking can be avoided, and that a small disk forms in a very early phase of evolution.

4.2 Method

We solve the normalized MHD equations in axisymmetric thin-disk geometry (see Ciolek and Mouschovias, 1993; Basu and Mouschovias, 1994), assuming vertical hydrostatic equilibrium in a vertical one-zone approximation. An integral method for calculating the self-gravity of an infinitesimally-thin disk is used (detailed in Ciolek and Mouschovias, 1993), with modifications for the finite extent and finite thickness of the flattened core.

In our model, the magnetic field points solely in the vertical direction inside the disk, but also possesses radial and azimuthal components (B_r and B_ϕ) at the disk surfaces and

above. B_r is determined from a potential field assuming force-free and current-free conditions in the external medium. We calculate B_ϕ and implement magnetic braking using a steady-state approximation to the transport of Alfvén waves in the external medium, as in Basu and Mouschovias (1994). Owing to numerical complexity, a calibration of this method with results of three-dimensional MHD wave propagation through a stratified compressible medium has not been done to date. We modify the ideal-MHD induction equation to include Ohmic dissipation:

$$\frac{\partial B_{z,\text{eq}}}{\partial t} + \frac{1}{r} \frac{\partial}{\partial r} (r B_{z,\text{eq}} v_r) = \frac{1}{r} \frac{\partial}{\partial r} \left(\eta r \frac{\partial B_{z,\text{eq}}}{\partial r} \right). \quad (4.1)$$

Here, $B_{z,\text{eq}}$ denotes the z -component of the magnetic field at the midplane of the disk, and v_r is the radial component of the neutral velocity.

We use the parametrization of Machida et al. (2007) for the resistivity calculated by Nakano et al. (2002), with a dimensionless scaling parameter $\tilde{\eta}_0$ whose standard value is unity. The resistivity is then

$$\eta = \tilde{\eta}_0 1.3 \times 10^{18} \left(\frac{n}{10^{12} \text{ cm}^{-3}} \right) \left(\frac{T}{10 \text{ K}} \right)^{1/2} \left[1 - \tanh \left(\frac{n}{10^{15} \text{ cm}^{-3}} \right) \right] \text{ cm}^2 \text{ s}^{-1}, \quad (4.2)$$

where n is the volume number density, and the term in square brackets is a cutoff representing the restoration of flux freezing at high densities. The uncertainties in $\tilde{\eta}_0$ hinge largely on the grain properties (e.g., Machida et al., 2007). Different from Machida et al. (2007), we do not (inconsistently) pull the resistivity outside all spatial derivatives.

For simplicity, we replace the detailed energy equation by a barotropic relation. The temperature-density relation of Masunaga and Inutsuka (2000) is transformed into a pressure-density relation using the ideal gas law $P = nk_{\text{B}}T$, where P is the pressure, k_{B} is Boltzmann’s constant, and T is the temperature. We calculate the midplane pressure self-consistently, including the effects of the weight of the gas column, constant external pressure ($P_{\text{ext}} = 0.1 \pi G \Sigma_0^2 / 2$), magnetic pressure, and the extra squeezing added by a central star (once present).

The MHD equations are solved with the method of lines (e.g., Schiesser, 1991) using a finite volume approach on an adaptive grid with up to 1024 radial cells in logarithmic spacing. The smallest cell is initially 10^{-2} AU and as small as $0.02 R_\odot$ at the highest refinement. We use the second-order van-Leer TVD advection scheme (van Leer, 1977), and calculate all derivatives to second-order accuracy on the nonuniform grid. The code will be described in detail in a forthcoming paper.

4.3 Initial conditions and normalization

We assume that our initial state was reached by core contraction preferentially along magnetic field lines (e.g., Fiedler and Mouschovias, 1993) and rotational flattening, and start with initial profiles for the column density and angular velocity given by

$$\Sigma(r) = \frac{\Sigma_0}{\sqrt{1 + (r/R)^2}}, \quad \Omega(r) = \frac{2\Omega_c}{\sqrt{1 + (r/R)^2 + 1}}. \quad (4.3)$$

Here, $R \approx 1,500$ AU approximately equals the Jeans length at the core's initial central density (see below). The column density profile is representative of the early stage of collapse (e.g., Basu, 1997; Dapp and Basu, 2009), and the angular velocity profile reflects that the specific angular momentum of any parcel is proportional to the enclosed mass.

We assume an initial profile for $B_{z,\text{eq}}$ in a way that the normalized mass-to-flux ratio $\mu = \Sigma/B_{z,\text{eq}} 2\pi\sqrt{G} = 2$ everywhere, which is the approximate starting point of runaway collapse (e.g., Basu and Mouschovias, 1994). The radial velocity is initially zero. The initial state is not far from equilibrium, because the pressure gradient and magnetic and centrifugal forces add up to $\approx 82\%$ of the gravitational force. Our results do not depend strongly on the choice of initial state as long as gravity remains dominant.

The initial central column density and number density are $\Sigma_0 = 0.23 \text{ g cm}^{-2}$ and $n_c = 4.4 \times 10^6 \text{ cm}^{-3}$, respectively. The total mass and radius of the core are $2.5 M_\odot$ and 1.2×10^4 AU, respectively. The initial central magnetic field strength is $B_{z,\text{eq}} \approx 200 \mu\text{G}$. We choose the external density in a way that $n_c/n_{\text{ext}} = 500$, (i.e., $n_{\text{ext}} \approx 10^3 \text{ cm}^{-3}$), and the central angular velocity Ω_c so that the cloud's edge rotates at a rate of $1 \text{ km s}^{-1} \text{ pc}^{-1}$, consistent with observations of molecular cloud cores (Goodman et al., 1993; Caselli et al., 2002).

4.4 Results

4.4.1 Prestellar phase and formation of the second core

During the prestellar phase (for number densities $n < 10^{11} \text{ cm}^{-3}$) the collapse proceeds in a nearly self-similar fashion. We find that—insensitive to initial conditions—the column density is approximately $\propto r^{-1}$ for three orders of magnitude of central enhancement, which corresponds to the volume density being $\propto r^{-2}$ for a central enhancement of $\approx 10^6$. This profile is characteristic of a collapsing prestellar core (e.g., Larson, 1969). The collapse proceeds dynamically, and to a good approximation under isothermality,

flux-freezing, and without significant magnetic braking (Basu and Mouschovias, 1994).

Once the density reaches $\approx 10^{11} \text{ cm}^{-3}$, the central region becomes opaque and traps the energy released by the collapse, which previously could escape freely as radiation. This region heats up (Larson, 1969; Masunaga and Inutsuka, 2000) and its thermal pressure gradient temporarily stabilizes it against further collapse. This is the *first core*. Its density and temperature increase with continued accretion, while its size stays almost constant at \approx a few AU, bounded by an accretion shock. The external gravitational potential of this object closely resembles that of a point mass, and an expansion wave develops and moves outward at nearly the sound speed (Shu, 1977). Material within this region moves at near free-fall speed.

When the temperature in the first core reaches $\approx 2000 \text{ K}$, for $n \gtrsim 10^{15} \text{ cm}^{-3}$, hydrogen molecules are collisionally dissociated. This process provides an energy sink, so that the temperature rise stagnates, and the collapse reinitiates. As the temperature rises yet further, hydrogen is ionized sufficiently that flux freezing is re-established. Collapse is then finally halted, and sufficiently high densities are reached that electron degeneracy becomes important (Masunaga and Inutsuka, 2000). A protostellar core (the *second core*) forms with a radius \approx a few R_{\odot} (e.g., Larson, 1969). This Class 0 object initially only has a mass of a few $\times 10^{-3} M_{\odot}$. The gravitational potential resembles that of a point mass outside the second core, and an expansion wave once again moves outward from the accretion shock, eventually consuming the entire region of the previous first core.

Figure 4.1 shows the profiles of column density, mass-to-flux ratio and angular velocity shortly after the second core forms ($\approx 4.8 \times 10^4 \text{ yr}$ into the simulation). For $n \gtrsim 10^{12} \text{ cm}^{-3}$, Ohmic dissipation becomes dynamically important (Nakano et al., 2002), because all charge carriers decouple from the magnetic field, and flux is dissipated. While the density in the first core increases, we find the magnetic field strength remains stagnant. A *magnetic wall* (Li and McKee, 1996; Contopoulos et al., 1998) forms at $\approx 10 \text{ AU}$, visible as a sharp transition in column density in the resistive model ($\tilde{\eta}_0 = 1$, top panel). Here, infalling neutrals within the expansion wave are temporarily slowed down by the relatively well-coupled magnetic field that is expelled from the first core with a radius $\approx 1 \text{ AU}$. Further inward, the neutrals resume near-free-fall motion, but with enhanced magnetic support and at a greater column density than for flux-freezing ($\tilde{\eta}_0 = 0$, dotted line). Under angular momentum conservation (no magnetic braking), the additional rotational support stabilizes the first core against further collapse (top panel, dash-dotted line), consistent with previous findings (e.g., Saigo and Tomisaka, 2006).

Because of magnetic flux dissipation, the mass-to-flux ratio increases by two orders of magnitude in the first core region for $\tilde{\eta}_0 = 1$, but by a factor of 15 even for $\tilde{\eta}_0$ as

low as 0.01 (Fig. 4.1, middle panel). The torque on the cloud caused by magnetic braking scales linearly with the amount of enclosed flux (Basu and Mouschovias, 1994). Ohmic dissipation therefore allows spin-up to proceed, even though the rotation rate is still reduced by a factor of a few outside the first core, compared with the case without magnetic braking (Fig. 4.1, bottom panel, dash-dotted line). In the flux-freezing case, the comparatively slow evolution of the first core allows enough time for magnetic braking to spin down the first core region, and ‘catastrophically’ brake it (Fig. 4.1, bottom panel, dotted line).

4.4.2 Evolution after second core formation

When the second core forms, the thin-disk formulation breaks down, because the object is now truly hydrostatic and spherical. Presumably, dynamo processes within the fully convective protostar will also take over, and the magnetic field will mostly decouple from that of its parent core (Mestel and Landstreet, 2005). Therefore, we switch off magnetic braking in the second core, and introduce a sink cell with a size of $3 R_{\odot}$, slightly larger than the second core. The processes within it are beyond the scope of our model, but are not expected to significantly influence the surroundings. This is not necessarily the case with a sink cell of size ≈ 10 AU, as is the more common approach (e.g., Vorobyov and Basu, 2007; Mellon and Li, 2008, 2009).

Figure 4.2 shows the profiles of column density, infall velocity, and the ratio of centrifugal to gravitational acceleration about a year after the introduction of the sink cell. Centrifugal balance is achieved in a small region ($\approx 10 R_{\odot}$) close to the center (bottom panel) in the resistive model. This is a necessary and sufficient condition for the formation of a centrifugally-supported disk. At the same time all infall is halted there and the radial velocity plummets (middle panel). After a few years of evolution, a Toomre instability develops, and the rotationally-supported structure breaks up into a ring (top panel). At this point, we stop the simulation, because more physics would be required to follow the further evolution of the disk. Our model allows a clear distinction between a magnetic pseudo-disk, a flattened (disk-like) prestellar core, and a centrifugal (nearly Keplerian) disk. This distinction is not clear in profiles from three-dimensional simulations (Machida et al., 2007; Duffin and Pudritz, 2009).

Figure 4.3 shows the magnetic field line topology above and below the disk on two scales (10 AU and 100 AU), for both flux-freezing and resistive models. They are calculated immediately after the formation of the second core, assuming force-free and current-free conditions above a thin disk (Mestel and Ray, 1985). The split monopole of

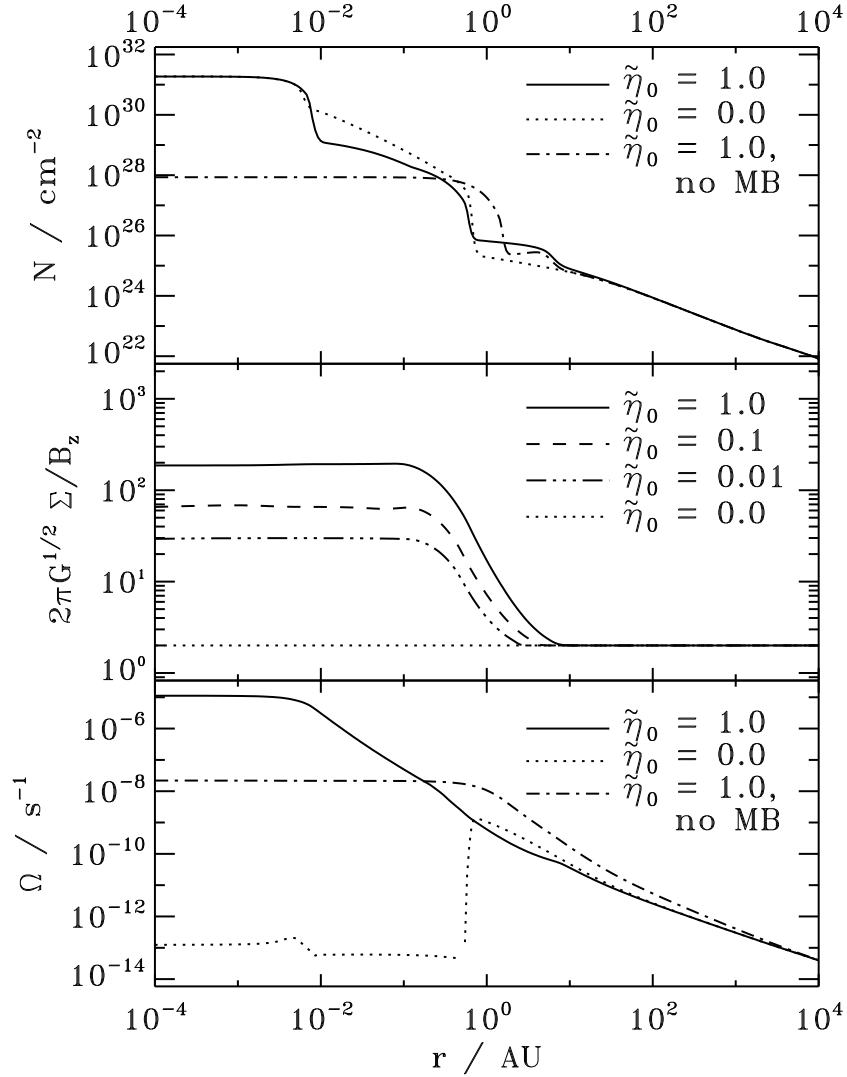


Figure 4.1: Spatial profiles of various quantities after the second collapse (after $\approx 4.8 \times 10^4$ yr). **Top:** The first and second core and their accretion shocks are at radii ≈ 1 AU and $\approx 5 \times 10^{-3}$ AU $\approx 1 R_{\odot}$, respectively. Within the expansion wave outside the first core, the column density profile assumes that of free-fall collapse in the flux-freezing case ($\tilde{\eta}_0 = 0$), and shows a magnetic wall in the resistive case. Beyond ≈ 20 AU, the prestellar infall profile remains unchanged. Without magnetic braking (dash-dotted line), the first core is larger and rotation prevents further collapse. **Middle:** The mass-to-flux ratio is increased by (even weak) Ohmic dissipation by a factor between 15 and 100. The influence is significant even well outside the boundary of the first core (at a few AU). **Bottom:** For flux-freezing, catastrophic magnetic braking spins down the first core to nearly the background rotation rate. In the resistive case (solid line), the rotation rate outside the first core is reduced only slightly compared with the case without magnetic braking (dash-dotted line).

the $\tilde{\eta}_0 = 0$ model (dashed lines) is created as field lines are dragged in by the freely falling material within the expansion wave front at ≈ 20 AU. This is replaced by a much more relaxed field line structure in the resistive case (solid lines). The extreme flaring of field lines in the $\tilde{\eta}_0 = 0$ model is a fundamental cause of the magnetic braking catastrophe. Galli et al. (2009) presented similar field configurations resulting from a simplified model for resistive collapse.

4.5 Discussion and conclusions

We demonstrate the formation of a centrifugally-supported disk despite the presence of magnetic braking. The magnetic braking catastrophe is averted by including the canonical level of Ohmic dissipation, which removes large amounts of magnetic flux from the high-density region of the first core. In the absence of Ohmic dissipation, this region would be spun down tremendously prior to the second collapse. We emphasize that disk formation happens very shortly after the second collapse in a region very close to the central object, while it is still very small ($< 10^{-2} M_\odot$). This is consistent with the observational evidence of outflows at a very young age.

Our simulations yield $\approx 0.1 - 1$ kG magnetic fields, comparable to those observed in T Tauri stars (e.g., Johns-Krull, 2007), in a central object of mass $\approx 10^{-2} M_\odot$. This is achieved by non-ideal MHD effects reducing the field strength by $\approx 10^2$ compared to a flux-freezing model. Our model does not have the capability of including outflows or jets, even though those are launched very close to the stellar surface.

There is presently no evidence for centrifugal disks $\gtrsim 50$ AU around Class 0 objects (e.g., André et al., 2004; Maury et al., 2010). ALMA will allow observers to improve on this, and to probe for disks down to ≈ 10 AU. We anticipate that the centrifugal disk that forms in our simulations *can* grow over time into disks of size ≈ 100 AU observed around Class II objects. Recent work (Machida et al., 2010) shows that magnetic braking can be cut off at late times as the envelope is accreted, and the existing disk can also grow by internal angular momentum redistribution processes (e.g., Vorobyov and Basu, 2007). Furthermore, we speculate that ambipolar diffusion (e.g., Kunz and Mouschovias, 2010) has the potential to dissipate enough flux outside the first core (an area not significantly affected by Ohmic dissipation) to reduce braking and to allow the disk to form there as well. We will present results of a study including both non-ideal MHD effects and grain physics in an upcoming paper.

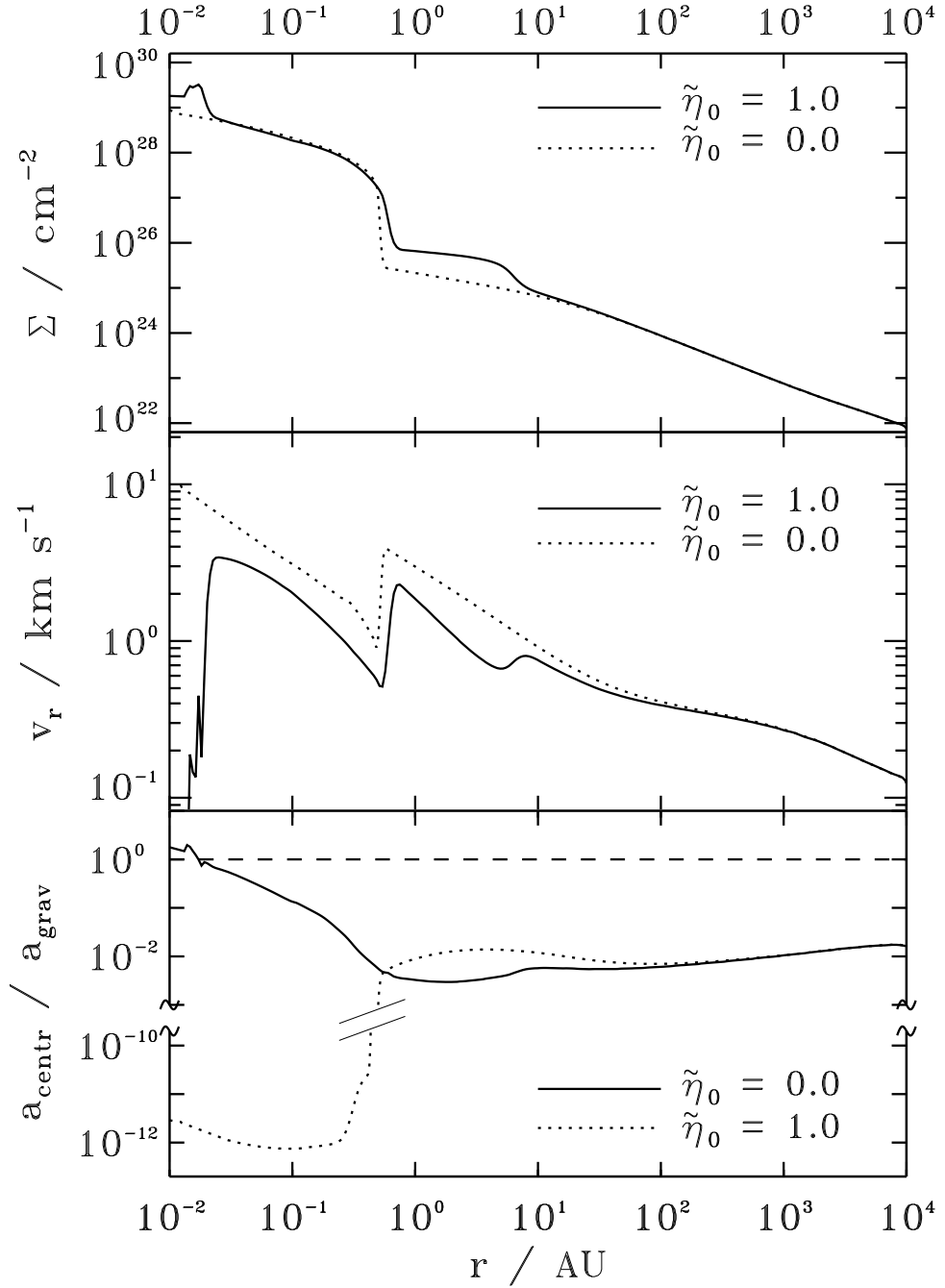


Figure 4.2: Spatial profiles of various quantities ≈ 1 yr after the introduction of a sink cell of size $\approx 3 R_{\odot}$. **Top:** The Toomre-unstable centrifugally-supported disk breaks up into a ring. **Middle:** Infall is halted after the formation of a centrifugal disk at $\approx 5 \times 10^{-2}$ AU $\approx 10 R_{\odot}$ in the resistive case ($\tilde{\eta}_0 = 1$), while for flux-freezing ($\tilde{\eta}_0 = 0$), infall continues. **Bottom:** Ratio between centrifugal and gravitational accelerations. The dashed line indicates rotational balance, achieved within $\approx 10 R_{\odot}$ with Ohmic dissipation. For flux-freezing, rotational support is negligible in the first core region owing to the magnetic braking catastrophe.

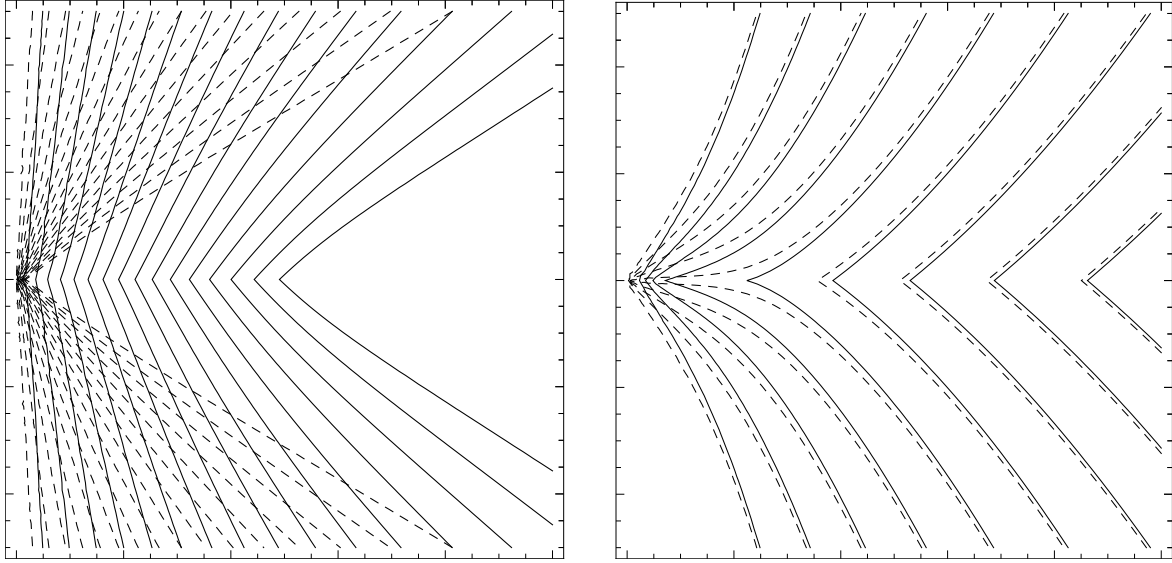


Figure 4.3: Magnetic field lines. The box on the left has dimensions 10 AU on each side, while the box on the right has dimensions 100 AU. The dashed lines represent the flux-freezing model ($\tilde{\eta}_0 = 0$), while the solid lines show the same field lines for the resistive model ($\tilde{\eta}_0 = 1$). The second core has just formed and is on the left axis midplane.

Acknowledgments

The authors thank the participants of the CC2YSO conference for engaging and illuminating discussions. W.B.D. was supported by an NSERC Alexander Graham Bell Canada Graduate Scholarship, and S.B. by an NSERC Discovery Grant.

Bibliography

- Allen, A., Li, Z., and Shu, F. H.: 2003, *ApJ* **599**, 363
- André, P., Bouwman, J., Belloche, A., and Hennebelle, P.: 2004, *Ap&SS* **292**, 325
- Andrews, S. M. and Williams, J. P.: 2005, *ApJ* **631**, 1134
- Basu, S.: 1997, *ApJ* **485**, 240
- Basu, S.: 1998, *ApJ* **509**, 229
- Basu, S. and Mouschovias, T. C.: 1994, *ApJ* **432**, 720
- Caselli, P., Benson, P. J., Myers, P. C., and Tafalla, M.: 2002, *ApJ* **572**, 238
- Ciolek, G. E. and Mouschovias, T. C.: 1993, *ApJ* **418**, 774

- Contopoulos, I., Ciolek, G. E., and Königl, A.: 1998, *ApJ* **504**, 247
- Dapp, W. B. and Basu, S.: 2009, *MNRAS* **395**, 1092
- Duffin, D. F. and Pudritz, R. E.: 2009, *ApJ* **706**, L46
- Fiedler, R. A. and Mouschovias, T. C.: 1993, *ApJ* **415**, 680
- Galli, D., Cai, M., Lizano, S., and Shu, F. H.: 2009, in *Revista Mexicana de Astronomia y Astrofisica Conference Series*, Vol. 36 of *Revista Mexicana de Astronomia y Astrofisica Conference Series*, pp 143–148
- Goodman, A. A., Benson, P. J., Fuller, G. A., and Myers, P. C.: 1993, *ApJ* **406**, 528
- Hennebelle, P. and Ciardi, A.: 2009, *A&A* **506**, L29
- Hennebelle, P. and Fromang, S.: 2008, *A&A* **477**, 9
- Johns-Krull, C. M.: 2007, *ApJ* **664**, 975
- Krasnopolsky, R., Li, Z., and Shang, H.: 2010, *ApJ* **716**, 1541
- Kunz, M. W. and Mouschovias, T. C.: 2010, *MNRAS* **408**, 322
- Larson, R. B.: 1969, *MNRAS* **145**, 271
- Li, Z. and McKee, C. F.: 1996, *ApJ* **464**, 373
- Machida, M. N., Inutsuka, S., and Matsumoto, T.: 2007, *ApJ* **670**, 1198
- Machida, M. N., Inutsuka, S., and Matsumoto, T.: 2010, *ArXiv e-prints*
- Masunaga, H. and Inutsuka, S.: 2000, *ApJ* **531**, 350
- Maury, A. J., André, P., Hennebelle, P., Motte, F., Stamatellos, D., Bate, M., Belloche, A., Duchêne, G., and Whitworth, A.: 2010, *A&A* **512**, A40+
- Mellon, R. R. and Li, Z.: 2008, *ApJ* **681**, 1356
- Mellon, R. R. and Li, Z.: 2009, *ApJ* **698**, 922
- Mestel, L. and Landstreet, J. D.: 2005, in R. Wielebinski & R. Beck (ed.), *Cosmic Magnetic Fields*, Vol. 664 of *Lecture Notes in Physics*, Berlin Springer Verlag, pp 183–+

- Mestel, L. and Ray, T. P.: 1985, *MNRAS* **212**, 275
- Nakano, T., Nishi, R., and Umebayashi, T.: 2002, *ApJ* **573**, 199
- Saigo, K. and Tomisaka, K.: 2006, *ApJ* **645**, 381
- Schiesser, W. E.: 1991, *The Numerical Method of Lines: Integration of Partial Differential Equations*, Academic Press, 1991. 326 p.
- Shu, F. H.: 1977, *ApJ* **214**, 488
- van Leer, B.: 1977, *Journal of Computational Physics* **23**, 276
- Vorobyov, E. I. and Basu, S.: 2007, *MNRAS* **381**, 1009

Chapter 5

Bridging the gap: intermediate-scale disk formation with ambipolar diffusion and Ohmic dissipation

5.1 Introduction

At the beginning of the star formation process, prestellar cores are observed to be rotating (e.g., Goldsmith and Arquilla, 1985; Goodman et al., 1993; Caselli et al., 2002). At the end of the process, observations show nearly all Class II objects to be surrounded by rotating disks of size $\gtrsim 100$ AU (e.g., Andrews and Williams, 2005), likely in centrifugal balance. The amount of observational data available about what happens in between those two snapshots is not as abundant. Currently, there is no evidence for the presence of centrifugal disks larger than ≈ 50 AU around Class 0 or Class I objects (e.g., Maury et al., 2010). However, there are outflows observed around these young objects, commonly linked to disk accretion. Disks must therefore form with a small size and grow over time. The dearth of observational data at smaller scales will be remedied by ALMA. In the meantime, the evolution of angular momentum and the formation of a centrifugal disk have to be studied theoretically and numerically.

It was shown long ago that there is a so-called *angular momentum problem*, in that the lion's share of angular momentum has to be removed from the gas in order to arrive at rotation rates observed in main sequence stars. This feat was credited to *magnetic braking*, which acts during the contraction and collapse by linking the core with its envelope and transfers angular momentum from one to the other. Recently the converse problem appeared (e.g., Allen et al., 2003; Mellon and Li, 2008; Hennebelle and Fromang, 2008),

when it was shown that cores may experience *catastrophic magnetic braking*, in that so much angular momentum might be removed as to leave insufficient angular momentum for the observed large-scale disks to form in models. This remained the case when the assumption of flux freezing was abandoned (Mellon and Li, 2009), and ambipolar diffusion was introduced.

In a previous paper (Dapp and Basu, 2010), we followed the evolution of a collapsing molecular cloud core in axisymmetric thin-disk geometry all the way to protostellar densities. We found that Ohmic dissipation alone (in a simplified form, see Machida et al. 2006, 2007) reduces the magnetic field strength sufficiently to inactivate magnetic braking within the first core. It was shown that a centrifugal disk can indeed form around the second core (the protostar). In this paper, we improve on the implementation of non-ideal MHD (magnetohydrodynamical) effects. We use the method presented in Kunz and Mouschovias (2009, 2010) to calculate both Ohmic dissipation and ambipolar diffusion simultaneously (and the Hall effect, in principle, even though that is not applicable for the geometry chosen in this paper). Both effects are revitalized after the formation of a central star (e.g., Li and McKee, 1996; Contopoulos et al., 1998), and cannot be studied with a sink cell of ≈ 10 AU, which is what some simulations use. We follow the evolution of the core to stellar sizes, in a 7-fluid model including inelastic collisions between gas-phase species and grains, and we study the effect of different grain sizes.

We demonstrate that a more realistic calculation of Ohmic dissipation and the addition of ambipolar diffusion reduces the efficacy of magnetic braking in the inner regions further. We show that catastrophic magnetic braking can be avoided, and that a small disk forms in a very early phase of evolution. We propose a disk formation scenario in which the disk forms at size ≈ 1 AU, and subsequently expands significantly (Basu, 1998) due to internal angular momentum transport mechanisms such as MRI or gravitational torques (e.g., Balbus and Hawley, 1991; Vorobyov and Basu, 2007).

This paper is structured the following way. In Section 5.2 we formulate the problem, and describe the method of solution and the numerical code. Section 5.3 discusses the implementation of magnetic braking, while Section 5.4 outlines the derivation of the induction equation. Section 5.5 details the chemical model used to calculate the abundances of each species. Section 5.6 contains the description of our initial condition and normalizations used, and we present our results in Section 5.7. Those are then discussed in Section 5.8, and we summarize our findings in Section 5.9.

5.2 Method

We solve the normalized equations of non-ideal MHD for a rotating, axisymmetric thin disk (Basu and Mouschovias, 1994) made of partially-ionized gas. In the thin-disk approximation all quantities are assumed uniform over one scale height of the disk. It is applicable as long as the half-thickness of the disk remains small compared to the radius of the disk. Fiedler and Mouschovias (1993) showed that an initially cylindrical cloud quickly flattens parallel to the magnetic field before any significant collapse in radial direction occurs, and a disk is formed that can be described by the thin-disk approximation (see also Basu and Mouschovias, 1994).

We solve the following system of equations

$$\frac{\partial \Sigma_n}{\partial t} = -\frac{1}{r} \frac{\partial}{\partial r} (r \Sigma_n v_r), \quad (5.1a)$$

$$\frac{\partial (\Sigma_n v_r)}{\partial t} = -\frac{1}{r} \frac{\partial}{\partial r} (r \Sigma_n v_r v_r) + f_p + f_g + f_m + f_r, \quad (5.1b)$$

$$\frac{\partial L}{\partial t} = -\frac{1}{r} \frac{\partial}{\partial r} (r L v_r) + \frac{1}{2\pi} r B_{z,\text{eq}} B_{\varphi,Z}, \quad (5.1c)$$

$$\begin{aligned} \frac{\partial B_{z,\text{eq}}}{\partial t} = & -\frac{1}{r} \frac{\partial}{\partial r} (r B_{z,\text{eq}} v_r) \\ & + \frac{1}{r} \frac{\partial}{\partial r} \left(r \eta_{\text{eff}} \frac{\partial B_{z,\text{eq}}}{\partial r} \right), \end{aligned} \quad (5.1d)$$

$$P = P(\varrho_n). \quad (5.1e)$$

Here, Σ_n is the mass column density, v_r is the radial velocity, while $L \equiv \Sigma_n \Omega r^2$ is the angular momentum per unit area. The mass volume density is denoted by ϱ_n , and the forces f and the magnetic field components ($B_{z,\text{eq}}$, $B_{r,Z}$, and $B_{\varphi,Z}$) are discussed below. We do not include a separate continuity equation for the grains since no significant change of the dust-to-gas ratio occurs beyond a density of $n_c \approx 10^6 \text{ cm}^{-3}$ (Kunz and Mouschovias, 2010).

We include the effect of both ambipolar diffusion (e.g., Mestel and Spitzer, 1956; Mouschovias, 1991) *and* Ohmic dissipation (e.g., Nakano et al., 2002) in an effective resistivity η_{eff} (Kunz and Mouschovias, 2009, 2010), as derived from microphysical considerations in Section 5.4. Because of the chosen field geometry, there is no contribution of the Hall effect (e.g., Wardle, 2007), even though it would be straightforward to add it in the same formulation in a higher-dimensional study (e.g., Kunz and Mouschovias, 2010). Note that we do not assume the resistivity to be spatially constant by pulling it outside all spatial derivatives, which is different from Machida et al. (2007).

For computational ease, we use the barotropic relation Eq.(5.1e) instead of a detailed

energy equation. The resulting mid-plane temperatures are very similar to those arrived at in an axisymmetric (r, z) simulation with explicit radiative transfer added (Kunz and Mouschovias, 2010). We transform the temperature-density relation of Masunaga and Inutsuka (2000) into a pressure-density relation using the ideal gas law $P = nk_{\text{B}}T$. Here, P is the thermal pressure, k_{B} is Boltzmann's constant, and T is the mid-plane temperature, while n is the volume number density¹. We calculate the thermal mid-plane pressure of the neutrals in our thin disk self-consistently, including the effects of the weight of the gas column, external pressure, magnetic pressure, and the extra squeezing added by a central star (once present, with mass M_{\star}). The latter weight is

$$W_{\star} = 2 GM_{\star}\varrho \int_0^Z \frac{zdz}{(r^2 + z^2)^{3/2}}, \quad (5.2)$$

where Z is the disk's half-thickness, and ϱ is the mass density. This is solved iteratively, as $\varrho \equiv \varrho(Z)$ itself. The external pressure is fixed at $P_{\text{ext}} = 0.1 \pi G \Sigma_0^2 / 2$, where G is Newton's constant and Σ_0 is the initial central column density. The mass density corresponding to a given pressure is then interpolated from a table. This also fixes the mid-plane temperature of our disk, as well as the scale height (i.e., the half-thickness of the thin disk).

The forces per unit area appearing in the momentum equation Eq.(5.1b) are given by

$$f_{\text{p}} = -\frac{\partial}{\partial r} [Z\pi G \Sigma_{\text{n}}^2] \quad (5.3a)$$

$$f_{\text{g}} = \Sigma_{\text{n}} g_r \quad (5.3b)$$

$$f_{\text{m}} = \frac{B_{z,\text{eq}}}{2\pi} \left(B_{r,Z} - Z \frac{\partial B_{z,\text{eq}}}{\partial r} \right) + \frac{1}{4\pi} \frac{dZ}{dr} (B_{r,Z}^2 + B_{\varphi,Z}^2) \quad (5.3c)$$

$$f_{\text{r}} = \frac{L^2}{\Sigma_{\text{n}} r^3} \quad (5.3d)$$

Note that the effects of external pressure, magnetic pressure, and the protostar's squeezing enter the pressure force through the half-thickness Z .

We calculate the gravitational potential Ψ and the radial gravitational acceleration g_r with the integral method for infinitesimally-thin disks employed in Ciolek and

¹Note that during hydrogen dissociation the mass per particle is reduced from $2.3 m_{\text{H}}$ (which is calculated assuming 10% helium in number) to $1.3 m_{\text{H}}$, and then finally to $0.6 m_{\text{H}}$ after the gas is fully ionized. m_{H} is the mass of a hydrogen atom. The effect of changing mass per particle was not considered by Machida et al. (2006, 2007).

Mouschovias (1993) and Morton et al. (1994), and correct for the fact that this produces a diverging field at the disk edge. We also correct for the finite thickness of the flattened core so as not to overestimate the field strength (see Basu and Mouschovias, 1994).

In our model, the magnetic field points solely in the vertical direction inside the disk, but also possesses radial and azimuthal components ($B_{r,Z}$ and $B_{\varphi,Z}$) at the disk surfaces and beyond. $B_{r,Z}$ is determined from a potential field assuming force-free and current-free conditions in the external medium, using the same integral kernel $\mathcal{M}(r, r')$ as for the gravitational field. We calculate $B_{\varphi,Z}$ and implement magnetic braking as in Basu and Mouschovias (1994) (for details see Section 5.3).

Therefore, the remaining constituting equations are

$$B_{r,Z} = - \int_0^\infty dr' r' (B_{z,\text{eq}} - B_{\text{ref}}) \mathcal{M}(r, r') \quad (5.4a)$$

$$B_{\varphi,Z} = -2 \frac{\sqrt{4\pi \varrho_{\text{ext}}}}{B_{\text{ref}}} \frac{\Phi}{r} (\Omega - \Omega_{\text{ref}}) \quad (5.4b)$$

$$\Phi = \int_0^r dr' r' B_{z,\text{eq}} \quad (5.4c)$$

$$g_r(r) = 2\pi G \int_0^\infty dr' r' \Sigma_n(r') \mathcal{M}(r, r') \quad (5.4d)$$

$$\mathcal{M}(r, r') = \frac{2}{\pi} \frac{d}{dr} \frac{1}{r_{>}} K \left(\frac{r_{<}}{r_{>}} \right) \quad (5.4e)$$

$$Z = \frac{\Sigma_n}{2\varrho_n}. \quad (5.4f)$$

Here, Φ is the magnetic flux, B_{ref} is the assumed uniform background magnetic field of the surrounding medium with density ϱ_{ext} , and Ω_{ref} is the background rotation rate (for detailed parameter choice and initial conditions see Section 5.6). Lastly, K is the Complete Elliptic Integral of the First Kind, and the symbols $r_{<}$ and $r_{>}$ denote the smaller and larger of r and r' , respectively.

We use the method of lines (e.g., Schiesser, 1991) together with a finite volume approach on an adaptive grid with up to 1024 radial cells in logarithmic spacing to solve the equations described above. Hereby, only the spatial part of the equations is discretized, and the resultant set of ordinary differential equations (ODEs) is solved with LSODE (Radhakrishnan and Hindmarsh, 1993). This implicit ODE solver uses the adaptive backward-difference method due to Gear (1971) and is up to 12th order in time. The smallest cell is initially 10^{-2} AU and as small as $0.02 R_\odot$ at the highest refinement. The advection step is done using a second-order van-Leer TVD advection scheme (van Leer, 1977), and we calculate all derivatives to second-order accuracy on our nonuniform grid

(see Ciolek and Mouschovias, 1993). We employ the method of Norman et al. (1980) to advect angular momentum, which avoids angular momentum diffusion and associated spurious ring formation.

Our adaptive code refines to a higher resolution (each step by a factor of 3), whenever the column density increases by a factor of 50. This allows us to satisfy the Truelove criterion (Truelove et al., 1997), in that the Jeans length (Jeans, 1902, 1928) is resolved at all times by a minimum of 10 cells, even with our minimum resolution of 256 radial cells, highest refinement (smallest cell size $0.02 R_{\odot}$), and our maximal central density ($n_c \approx 10^{22} \text{ cm}^{-3}$). In higher-resolution runs (up to 1024 radial cells), and at lower densities, the Jeans length is resolved even better.

Our boundary conditions are as follows. Besides the axial symmetry (independence of φ), we have reflection symmetry at the mid-plane, as well as at the origin. Finally, at the edge, we have constant-volume boundary conditions, with an external medium with low density ρ_{ext} , external pressure P_{ext} , and high temperature, so that it is force-free. We assume the column density to go to zero at the edge, and the magnetic field to go to its constant external value B_{ref} .

5.3 Magnetic braking

We calculate magnetic braking with the same technique as presented in Basu and Mouschovias (1994), namely an analytical approximation to steady-state Alfvén wave transport from the disk to an external medium above and below. Owing to numerical complexity, a calibration of this method with results of three-dimensional MHD wave propagation through a stratified compressible medium, and the associated transport of angular momentum has not been done to date.

In order to derive the relevant equations for magnetic braking, we consider the transport of angular momentum through the flux tubes from the disk to the surrounding tenuous medium. The transport occurs at Alfvén speed, because it is driven by transversal Alfvén waves of the magnetic field. The definitions of angular momentum and Alfvén speed in the external medium are

$$J = m\Omega r^2 \quad \text{and} \quad v_{\text{A,ext}}^2 = \frac{B_{\text{ref}}^2}{4\pi\rho_{\text{ext}}}. \quad (5\text{a,b})$$

If the timescale for the Alfvén waves to reach the background medium far away from the disk is much smaller than the dynamical evolution timescale of the disk, then the rate of angular momentum flux (a loss if $(\Omega - \Omega_{\text{ref}}) > 0$, hence the minus sign) per unit

radian through an annulus at radius r_{ref} of thickness dr_{ref} is

$$\frac{dJ}{dt} = -\varrho_{\text{ext}} r_{\text{ref}}^2 (\Omega - \Omega_{\text{ref}}) v_{\text{A,ext}} r_{\text{ref}} dr_{\text{ref}}. \quad (5.6)$$

In this expression r_{ref} denotes the distance from the rotation axis of the disk, but far above the disk, where the magnetic field has reached its homogeneous background state. r_{ref} corresponds to radius r in the disk threaded by the same field line. Eq.(5.6) considers the angular momentum that a volume of gas of mass far away from the disk can take on. Angular momentum flux is given by multiplying the angular momentum density $\varrho\Omega r^2$ with the transport velocity $v_{\text{A,ext}}$ (which is constant far from the disk). The external medium has the mass density ϱ_{ext} and rotates at the angular frequency Ω_{ref} .

We perform transformations to express Eq.(5.6) in terms of quantities at the disk's surface instead of the external medium. First, we replace the external density by the Alfvén speed in Eq.(5.5). Another assumption is that magnetic flux Φ , defined by Eq.(5.4c), is conserved above the disk (flux freezing). Then, we can equate the flux in equatorial plane of the disk $\Phi(r)$ with its value far above the disk, where the magnetic field B_{ref} is constant. The footpoint r in the disk maps to a radius r_{ref} above, since the two are connected by a flux tube. We have $r_{\text{ref}} > r$ because the field lines are extending (diverging) above the disk (see Fig. 4.3). This means

$$\Phi(r) = \frac{1}{2} B_{\text{ref}} r_{\text{ref}}^2, \quad (5.7a)$$

$$d\Phi = B_{\text{ref}} r_{\text{ref}} dr_{\text{ref}} = B_{z,\text{eq}} r dr. \quad (5.7b)$$

Using these relations, we can rewrite Eq.(5.6) to yield the angular momentum flux

$$\frac{dJ}{dt} = -\frac{\Phi}{2\pi v_{\text{A,ext}}} (\Omega - \Omega_{\text{ref}}) B_{z,\text{eq}} r dr. \quad (5.8)$$

Finally, taking into account the flux in both directions, above and below the disk (yielding a factor of 2), and change to specific angular momentum $L \equiv \Sigma_n \Omega r^2 = J/r dr$, i.e. angular momentum per cell, we arrive at an expression for N_{cl} , the torque acting on the cloud

$$\frac{dL}{dt} \equiv N_{\text{cl}} = -\frac{\Phi}{\pi v_{\text{A,ext}}} (\Omega - \Omega_{\text{ref}}) B_{z,\text{eq}}. \quad (5.9)$$

At the same time, the stress-energy tensor yields the change in angular momentum to be equal to $r B_{z,\text{eq}} B_{\varphi,Z} / 2\pi$, which allows us to calculate the φ -component of the magnetic

field at the upper surface of the disk as

$$\begin{aligned} B_{\varphi,Z} &= -\frac{2\Phi}{v_{A,\text{ext}}} \frac{(\Omega - \Omega_{\text{ref}})}{r}, \\ &= -2\frac{\sqrt{4\pi\rho_{\text{ext}}}\Phi}{B_{\text{ref}}} \frac{1}{r} (\Omega - \Omega_{\text{ref}}). \end{aligned} \quad (5.10)$$

5.4 Non-ideal MHD treatment

We derive a version of the Induction equation that contains all non-ideal MHD effects, *ambipolar diffusion*, *Ohmic dissipation*, and the *Hall effect*. For brevity and clarity, we only present the instructional derivation of the resistivities in absence of inelastic collisions. However, we include their effect in our code, and refer the interested reader to the detailed exposition in Appendix B.1 in Kunz and Mouschovias (2009) where all terms are included.

We start with Faraday's law in cgs units

$$\frac{\partial \mathbf{B}}{\partial t} = -c\nabla \times \mathbf{E}, \quad (5.11)$$

where \mathbf{B} and \mathbf{E} are the magnetic and electric fields in the lab frame, respectively. In the frame of the neutrals the electric field is

$$\mathbf{E}_n = \mathbf{E} + \frac{\mathbf{v}_n}{c} \times \mathbf{B}, \quad (5.12)$$

so that Eq.(5.11) becomes

$$\frac{\partial \mathbf{B}}{\partial t} = c\nabla \times \left(\frac{\mathbf{v}_n}{c} \times \mathbf{B} - \mathbf{E}_n \right). \quad (5.13)$$

In ideal MHD, $\mathbf{E}_n \equiv 0$ by definition, as the conductivity is infinite, and all local electric fields (in the neutral frame) are shorted by currents immediately. This is not the case in non-ideal MHD, where $\mathbf{E}_n \neq 0$. We therefore seek an expression for \mathbf{E}_n in the general case.

We take the force equations for all charged species (denoted by s , where in our discussion $s = (i, e, g^+, g^-)$, but others would be possible), assuming force balance between the Lorentz force and collisions with neutrals. Inertial forces and collisions with other charged particles are neglected, as we are working under the assumption of a weakly-

ionized plasma (with an ionization fraction $\chi \approx 10^{-8}$). Then we have

$$0 = n_s q_s \left(\mathbf{E} + \frac{\mathbf{v}_s}{c} \times \mathbf{B} \right) - \frac{\rho_s}{\tau_{sn}} (\mathbf{v}_s - \mathbf{v}_n). \quad (5.14)$$

Subscript ‘ s ’ means pertaining to species s . The time scale for collisions between species s and neutrals is given by τ_{sn} . The mass density of the charged species is ρ_s , while q_s is their charge number. Note that the latter carries a minus sign if the charge is negative (e.g. for electrons).

We can transform this to the reference frame of the neutrals, introducing the *drift velocity* $\mathbf{w}_s = (\mathbf{v}_s - \mathbf{v}_n)$, and the *cyclotron frequency* (in cgs units)

$$\omega_s \equiv \frac{q_s B}{m_s c}, \quad (5.15)$$

where m_s is the mass of the charged particle, and $B \equiv |\mathbf{B}|$ is the magnetic field strength. Also using Eq.(5.12), and noting that $\rho_s \equiv m_s n_s$ where n_s is the number density of the charged species s , we find

$$0 = \omega_s \tau_{sn} \left(\frac{c}{B} \mathbf{E}_n + \mathbf{w}_s \times \mathbf{b} \right) - \mathbf{w}_s, \quad (5.16)$$

where $\mathbf{b} \equiv \mathbf{B}/B$ is the normalized magnetic field vector. Eq.(5.16) is an equation for the drift velocity \mathbf{w}_s .

To make further progress, we write down the *electric current density* due to all charged species

$$\begin{aligned} \mathbf{j} &= \sum_s n_s q_s \mathbf{v}_s = \sum_s n_s q_s \left(\overbrace{\mathbf{v}_s - \mathbf{v}_n}^{\equiv \mathbf{w}_s} + \mathbf{v}_n \right), \\ &= \sum_s n_s q_s \mathbf{w}_s + \underbrace{\sum_s n_s q_s \mathbf{v}_n}_{\equiv 0}. \end{aligned}$$

In the last step, overall charge neutrality was used to eliminate the second term. We are left with

$$\mathbf{j} = \sum_s n_s q_s \mathbf{w}_s. \quad (5.17)$$

Before we insert \mathbf{w}_s , we simplify our expressions further. Consider the cross product (5.16) $\times \mathbf{b}$.

$$\mathbf{w}_s \times \mathbf{b} = \omega_s \tau_{sn} \left(\frac{c}{B} \mathbf{E}_n \times \mathbf{b} - \mathbf{w}_{s,\perp} \right). \quad (5.18)$$

This can now be inserted back into Eq.(5.16), and yields

$$\mathbf{w}_s = \omega_s \tau_{sn} \left(\frac{c}{B} \mathbf{E}_n + \omega_s \tau_{sn} \frac{c}{B} \mathbf{E}_n \times \mathbf{b} - \omega_s \tau_{sn} \mathbf{w}_{s,\perp} \right). \quad (5.19)$$

First, we look at the component parallel to \mathbf{b} :

$$\mathbf{w}_{s,\parallel} = \omega_s \tau_{sn} \frac{c}{B} \mathbf{E}_{n,\parallel} \quad (5.20)$$

Using Eq.(5.17), we arrive at a generalized Ohm's law for the parallel component

$$\begin{aligned} \mathbf{j}_{\parallel} &= \sum_s n_s q_s \omega_s \tau_{sn} \frac{c}{B} \mathbf{E}_{n,\parallel} \\ &= \sum_s \frac{n_s q_s^2 \tau_{sn}}{m_s} \mathbf{E}_{n,\parallel} \\ &= \sum_s \sigma_s \mathbf{E}_{n,\parallel}, \end{aligned} \quad (5.21)$$

where

$$\sigma_s \equiv n_s q_s^2 \tau_{sn} / m_s \quad (5.22)$$

is the conductivity due to species s , and we have replaced ω_s by Eq.(5.15). Lastly, we define $\sigma_{\parallel} = \sum_s \sigma_s$ as well as $\eta_{\parallel} = 1/\sigma_{\parallel}$ and invert Eq.(5.21) to get

$$\mathbf{E}_{n,\parallel} = \frac{1}{\sigma_{\parallel}} \mathbf{j}_{\parallel} = \eta_{\parallel} \mathbf{j}_{\parallel}. \quad (5.23)$$

Similarly, we seek a relation between the perpendicular components of electric current density and electric field. Again, we start from Eq.(5.19), and this time look at the other component

$$\mathbf{w}_{s,\perp} = \left(\frac{\omega_s \tau_{sn}}{1 + \omega_s^2 \tau_{sn}^2} \frac{c}{B} \right) \mathbf{E}_{n,\perp} + \left(\frac{\omega_s^2 \tau_{sn}^2}{1 + \omega_s^2 \tau_{sn}^2} \frac{c}{B} \right) \mathbf{E}_n \times \mathbf{b}. \quad (5.24)$$

Again, we want to insert this into Eq.(5.17), so we multiply by $n_s q_s$, and once more use $\omega_s = q_s B / m_s c$. Lastly, we identify $\sigma_s \equiv n_s q_s^2 \tau_{sn} / m_s$, and sum the result over all s , to get

$$\begin{aligned} \mathbf{j}_{\perp} &= \sum_s \left(\frac{\sigma_s}{1 + \omega_s^2 \tau_{sn}^2} \right) \mathbf{E}_{n,\perp} \\ &+ \sum_s \left(\frac{\sigma_s \omega_s \tau_{sn}}{1 + \omega_s^2 \tau_{sn}^2} \right) \mathbf{E}_n \times \mathbf{b}. \end{aligned} \quad (5.25)$$

Defining

$$\sigma_{\perp} = \sum_s \left(\frac{\sigma_s}{1 + \omega_s^2 \tau_{sn}^2} \right) \quad \text{and} \quad \sigma_H = - \sum_s \left(\frac{\sigma_s \omega_s \tau_{sn}}{1 + \omega_s^2 \tau_{sn}^2} \right),$$

Ohm's law for the perpendicular component is

$$\mathbf{j}_{\perp} = \sigma_{\perp} \mathbf{E}_{n,\perp} - \sigma_H \mathbf{E}_n \times \mathbf{b}. \quad (5.26)$$

Combining both parallel and perpendicular components, we can write the overall generalized Ohm's law in tensor form.

$$\mathbf{j} = \begin{pmatrix} \sigma_{\perp} & -\sigma_H & 0 \\ \sigma_H & \sigma_{\perp} & 0 \\ 0 & 0 & \sigma_{\parallel} \end{pmatrix} \mathbf{E}_n \quad (5.27)$$

Note that the magnetic field introduces asymmetry, and thus off-diagonal components and makes a tensor expression necessary. Finally, we invert the matrix to get an expression for the electric field in the reference frame of the neutrals.

$$\mathbf{E}_n = \begin{pmatrix} \eta_{\perp} & \eta_H & 0 \\ -\eta_H & \eta_{\perp} & 0 \\ 0 & 0 & \eta_{\parallel} \end{pmatrix} \mathbf{j} \quad (5.28)$$

where

$$\eta_{\perp} \equiv \frac{\sigma_{\perp}}{\sigma_{\perp}^2 + \sigma_H^2}, \quad \eta_H \equiv \frac{\sigma_H}{\sigma_{\perp}^2 + \sigma_H^2}, \quad \text{and} \quad \eta_{\parallel} = \frac{1}{\sigma_{\parallel}}.$$

In the thin disk in our application, the magnetic field is purely poloidal in nature, and is generated by an azimuthal current. This means that there is no component of the electric current density parallel to the field (and neither in radial direction). Hence we are only interested in the perpendicular component of the electric field, and for convenience quote its expression:

$$\begin{aligned} \mathbf{E}_{n,\perp} &= \eta_{\perp} \mathbf{j}_{\perp} + \eta_H \mathbf{j} \times \mathbf{b}, \\ &= \underbrace{\eta_{\parallel} \mathbf{j}_{\perp}}_{\text{OD}} + \underbrace{(\eta_{\perp} - \eta_{\parallel}) \mathbf{j}_{\perp}}_{\text{AD}} + \underbrace{\eta_H \mathbf{j} \times \mathbf{b}}_{\text{Hall}}. \end{aligned} \quad (5.29)$$

Note that the quantity η_{\perp} contains the effects of both ambipolar diffusion and Ohmic dissipation. In Eq.(5.29), the contributions of each of the three non-ideal MHD effects Ohmic dissipation ('OD'), ambipolar diffusion ('AD'), and the Hall effect ('Hall') are highlighted. We point out that due to the purely azimuthal current, the Hall term

vanishes also. The reason lies in the fact that the curl operator that is applied to the electric field in Faraday's law given in Eq.(5.11) points in radial direction, but so does the Hall term.

Summarizing the above derivation, we can write Eq.(5.13) as follows (all but the radial component vanish)

$$\begin{aligned} \frac{\partial B_{z,\text{eq}}}{\partial t} + \frac{1}{r} \frac{\partial}{\partial r} (r B_{z,\text{eq}} v_r) \\ &= -c \frac{1}{r} \frac{\partial}{\partial r} (r E_{n,\varphi}) = -c \frac{1}{r} \frac{\partial}{\partial r} (r \eta_{\perp} j_{\varphi}), \\ &= \frac{1}{r} \frac{\partial}{\partial r} \left(r \eta_{\text{eff}} \frac{\partial B_{z,\text{eq}}}{\partial r} \right), \end{aligned} \quad (5.30)$$

where the relation $\mathbf{j} = c/4\pi \nabla \times \mathbf{B}$ has been used, and $\eta_{\text{eff}} \equiv c^2/4\pi\eta_{\perp}$ was introduced.

5.5 Chemistry

In this section, we develop the chemical model used to calculate the ionization fraction, fractional abundances, and resistivities for seven species. We consider neutral matter (one helium atom per five H_2 molecules), atomic and molecular ions (such as Mg^+ or HCO^+), electrons, as well as grains (positively-charged, neutral, and negatively-charged). Multiply-charged species are neglected, because the capture rate by a charged grain of a particle with the same charge q is reduced by a factor $\exp(-q^2/ak_{\text{B}}T)$ (Spitzer, 1941), where a is the particle's radius. It is thus far more likely that the grain is neutralized by capturing a particle of opposite charge than that it acquires a second (or even higher) charge. For example, Nakano et al. (2002) show that the abundance of doubly-charged grains is 5 orders of magnitude less than that of singly-charged ones.

5.5.1 Ionization rate

We consider four sources of ionization, and will describe them each in turn.

- UV ionization,
- cosmic ray ionization,
- ionization due to radiation liberated in radioactive decay,
- thermal ionization through collision.

UV ionization is only important where $A_V \lesssim 10$ (Ciolek and Mouschovias, 1995). This is the case for a column density $N_{\text{H}_2} \lesssim 2 \times 10^{22} \text{ cm}^{-2}$. The part of the cloud relevant to this work is much denser (in fact, everything within 10^4 AU from the center is denser) and, to good approximation, UV ionization would not need to be considered. However, for completeness, we still include its contribution in parametrized form, by adding $467.64 n_{\text{H}_2}^{-2} \text{ cm}^{-3}$ (see Fiedler and Mouschovias, 1992) to the electron and ion number densities. This has the effect to maintain an ionization fraction of $\approx 3 \times 10^{-5}$ in the outermost envelope of the core, and keep it flux-frozen, but does not affect the dynamical evolution of higher-density regions.

In the higher-density regions (where $10^4 \text{ cm}^{-3} \lesssim n_{\text{H}_2} \lesssim 10^{12} \text{ cm}^{-3}$), we assume the ionization to be mainly due to cosmic rays. Their ionization rate is calculated by

$$\zeta_{\text{CR}} = \zeta_0 \exp[-\Sigma_{\text{H}_2}/96 \text{ g cm}^2], \quad (5.31)$$

(Umebayashi and Nakano, 1980), where $\zeta_0 = 5 \times 10^{-17} \text{ s}^{-1}$ is the canonical unshielded cosmic-ray ionization rate (Spitzer, 1978).

Beyond $n_{\text{H}_2} \gtrsim 10^{12} \text{ cm}^{-3}$, even cosmic rays are shielded and cannot penetrate deep. Here, radioactivity, mainly due to ^{40}K , still provides a background level of ionization. Their ionization rate is $\zeta_{40} = 2.43 \times 10^{-23} \text{ s}^{-1}$ (Kunz and Mouschovias, 2009). Other radionuclides (such as ^{26}Al) are not considered, due to their low abundance, their short half-life time, their low ionization rate, or a combination thereof.

Finally, when the temperature reaches $\gtrsim 1000$ K, collisions are energetic enough to cause thermal ionization of some atoms with low ionization potential (predominantly potassium). As the temperature rises further, collisions becomes the dominant source of ionization. We parametrize this as an additional source term in the ion equilibrium equation (see Section 5.5.2) with the value (see Pneuman and Mitchell, 1965)

$$\begin{aligned} \frac{dn_{\text{A}^+}}{dt} &= 2.9 \times 10^{-16} \text{ cm}^3 \text{ s}^{-1} n_{\text{H}_2} n_{\text{A}^0} (T/1000 \text{ K})^{1/2} \\ &\times \exp(-5.03 \times 10^4 \text{ K}/T), \end{aligned} \quad (5.32)$$

where n_{A^0} is the fractional abundance of the relevant neutral atomic particles (see Kunz and Mouschovias, 2009). The fact that potassium only makes up $\approx 1/14$ of all metals has been considered in the numeric factor in front.

Beyond $n_{\text{H}_2} \gtrsim 10^{18} \text{ cm}^{-3}$, at a temperature of $\gtrsim 1500$ K, we assume the grains to be destroyed, and the stored charges to be released into the gas. The gas becomes highly ionized, and we thus revert back to flux freezing (Pneuman and Mitchell, 1965). Note that

the resistivity has already decreased significantly at this temperature as a consequence of thermal ionization.

5.5.2 Fractional abundances

We calculate the fractional abundances of the species relevant for the determination of the resistivity (see Section 5.4) using a chemical equilibrium network. This approach assumes the time for the chemical and collisional reactions to occur to be shorter than the local dynamical time.

The molecular ion equation describes the production of molecular ions (such as HCO^+) by radiative ionization, as well as their destruction through charge-exchange reactions with neutral atoms and grains, as well as recombination reactions with electrons.

$$\begin{aligned} \zeta n_{\text{H}_2} = & n_{\text{m}^+} n_{\text{A}^0} \beta + n_{\text{m}^+} n_{\text{e}} \alpha_{\text{dr}} \\ & + n_{\text{m}^+} n_{\text{g}^-} \alpha_{\text{m}^+ \text{g}^-} + n_{\text{m}^+} n_{\text{g}^0} \alpha_{\text{m}^+ \text{g}^0}, \end{aligned} \quad (5.33)$$

where α_{dr} is the dissociative recombination rate (collisions with electrons). Cosmic rays will ionize molecular hydrogen, forming H_3^+ almost instantaneously; this in turn is highly reactive and will strip away an electron from any (non- H_2) molecule A^0 it encounters, for instance CO , and form HCO^+ and H_2 . This is why cosmic rays act on H_2 in the first term of this equation; it is very unlikely that a cosmic ray will hit any molecule other than H_2 due to their sheer abundance.

Atomic ions (e.g., Na^+), on the other hand are produced by charge exchange reactions with neutral atoms, as well as thermal ionization, while they are destroyed by radiative recombinations with electrons, and by the collision with grains.

$$\begin{aligned} n_{\text{m}^+} n_{\text{A}^0} \beta + n_{\text{A}^0} n_{\text{H}_2} \alpha_{\text{A}^0 \text{H}_2} = & n_{\text{A}^+} n_{\text{e}} \alpha_{\text{rr}} \\ & + n_{\text{A}^+} n_{\text{g}^-} \alpha_{\text{A}^+ \text{g}^-} + n_{\text{A}^+} n_{\text{g}^0} \alpha_{\text{A}^+ \text{g}^0}, \end{aligned} \quad (5.34)$$

where α_{rr} is the radiative recombination rate, and the second term on the right represents thermal ionization (see Section 5.5.1).

The equation for positively-charged grains balances the deposition of charge from atomic and molecular ions with the capture of electrons and neutralization with negatively-charged grains. The charge exchange between positively-charged and neutral grains is in

steady-state, and so their contribution appears on both sides of the equation and cancels.

$$\begin{aligned} n_{\text{m}^+}n_{\text{g}^0}\alpha_{\text{m}^+\text{g}^0} + n_{\text{A}^+}n_{\text{g}^0}\alpha_{\text{A}^+\text{g}^0} \\ = n_{\text{e}}n_{\text{g}^+}\alpha_{\text{eg}^+} + n_{\text{g}^+}n_{\text{g}^-}\alpha_{\text{g}^+\text{g}^-}, \end{aligned} \quad (5.35)$$

Similarly, negatively-charged grains form by capture of an electron by a neutral grain, and are neutralized by charge exchange during collisions with molecular and atomic ions as well as positively-charged grains. Again, the charge exchange between negatively-charged and neutral grains is in steady-state, and so does not appear.

$$\begin{aligned} n_{\text{e}}n_{\text{g}^0}\alpha_{\text{eg}^0} = n_{\text{m}^+}n_{\text{g}^-}\alpha_{\text{m}^+\text{g}^-} + n_{\text{A}^+}n_{\text{g}^-}\alpha_{\text{A}^+\text{g}^-} \\ + n_{\text{g}^+}n_{\text{g}^-}\alpha_{\text{g}^+\text{g}^-}, \end{aligned} \quad (5.36)$$

Finally, to close the system, we add equations for the total number of atoms and grains

$$n_{\text{A}^0} + n_{\text{A}^+} = n_{\text{A}} \quad (5.37)$$

$$n_{\text{g}^0} + n_{\text{g}^+} + n_{\text{g}^-} = n_{\text{g}}, \quad (5.38)$$

as well as overall charge neutrality

$$n_{\text{m}^+} + n_{\text{A}^+} + n_{\text{g}^+} - n_{\text{g}^-} - n_{\text{e}} = 0. \quad (5.39)$$

The various rate coefficients α and β depend on temperature and grain properties, and are described in Appendix A (see also Kunz and Mouschovias, 2009).

Equations (5.33)-(5.39) form the non-linear system to be solved for the fractional abundances; we do this iteratively in each time step for each grid point by solving the matrix equation directly, using a LU-decomposition package. We assume a mean mass of the molecular and atomic species to be $m_{\text{m}^+} = 29 m_{\text{p}}$ and $m_{\text{A}^+} = 23.5 m_{\text{p}}$, respectively, where m_{p} is the proton mass. Those values are the masses of HCO^+ and the average of atomic magnesium and sodium, respectively, which are good representatives of the broader range of species present.

5.6 Initial Conditions and Normalization

We assume that our initial state was reached by core contraction preferentially along magnetic field lines (e.g., Fiedler and Mouschovias, 1993) and rotational flattening, and

prescribe initial profiles for column density and angular velocity given by

$$\Sigma(r) = \frac{\Sigma_0}{\sqrt{1 + (r/R)^2}}, \quad \Omega(r) = \frac{2\Omega_c}{\sqrt{1 + (r/R)^2 + 1}}. \quad (5.40)$$

Here, $R \approx 1,500$ AU approximately equals the Jeans length at the core's initial central density (see below). The column density profile is representative of the early stage of collapse (e.g., Basu, 1997; Dapp and Basu, 2009), and the angular velocity profile reflects that the specific angular momentum of any parcel is proportional to the enclosed mass.

We assume an initial profile for $B_{z,\text{eq}}$ such that the normalized mass-to-flux ratio $\mu = 2\pi\sqrt{G}\Sigma/B_{z,\text{eq}} = 2$ everywhere, which is the approximate starting point of runaway collapse (e.g., Basu and Mouschovias, 1994; Kunz and Mouschovias, 2010). The radial velocity is initially zero. The initial state is not far from equilibrium, as the pressure gradient and magnetic and centrifugal forces add up to $\approx 82\%$ of the gravitational force. Our results do not depend strongly on the choice of initial state, as long as gravity remains dominant.

The initial central column density, and the unit of column density for normalization purposes, is set to $\Sigma_0 = 2 \times 10^{-2}$ g cm $^{-2}$. The isothermal sound speed at $T = 10$ K is $c_{s,0} = 1.88 \times 10^4$ cm s $^{-1}$ and serves as the unit of velocity. Third, we choose $2\pi G\Sigma_0$ as the unit of acceleration. The total mass and radius of the core are $28.5 M_\odot$ and 0.6 pc, respectively. The initial central number density and magnetic field strength are $n_c = 3.3 \times 10^4$ cm $^{-3}$ and $B_{z,\text{eq}} \approx 200 \mu G$, respectively. The magnetic field is normalized using $2\pi\sqrt{G}\Sigma_0$ as a unit. This last unit is chosen purely out of convenience, and would not strictly be necessary; the other three quantities already allow to uniquely form a complete system of units. It allows, however, to drop some factors of 2π from the equations. We choose the external density to be $n_{\text{ext}} = 100$ cm $^{-3}$, and the central angular velocity Ω_c such that the cloud's edge rotates at a speed of 0.1 km s $^{-1}$ pc $^{-1}$.

Transient adjustments occur if the simulation is started from an initial non-equilibrium state that is at rest. The chemistry calculations are quite sensitive to fluctuations in density, which can cause problems. We therefore let the system evolve from an initial state with the above-mentioned profiles and characteristics, but initially without non-ideal MHD effects. Once the cloud has settled into a steady infall (at a central density of approximately $n_c \approx 10^6$ cm $^{-3}$) the full MHD equations Eqs. (5.1a) to (5.1e) are solved. The state at which we switch on the detailed treatment of chemistry corresponds very closely to the initial state of the previous paper (Dapp and Basu, 2010, see also Chapter 4), so that comparisons are possible. The rotation rate by then has increased to 1 km s $^{-1}$ pc $^{-1}$, consistent with observations of large molecular cloud cores (Goodman

Table 5.1: Simulation model overview.

Model Number	$a_{\text{gr}}/\mu\text{m}$	
1	0.019	—
2	0.038	—
3	0.075	—
4	0.113	—
5	0.150	—
6	0.038	no resistivity
7	0.038	no magnetic braking
8	—	OD alone (as in DB10)

^a All models above start from the same initial conditions, comparable to those described in Dapp and Basu (2010). For details, see Section 5.6.

et al., 1993; Caselli et al., 2002). In the plots in this paper, we show only the region of the core within 0.05 pc, again consistent with Dapp and Basu (2010). Note that the nature of the collapse is very dynamical and happens under flux freezing to a very good approximation between $n_c = 10^4 - 10^{10} \text{ cm}^{-3}$ (see Kunz and Mouschovias, 2010). Therefore, we assert that this initial state is justified.

We fix the dust-to-gas ratio at 1%, which is consistent with observations (Spitzer, 1978), and keep it constant everywhere and at all times. This means that a different mean grain size will result in differing total numbers of grains available, by a factor of a^{-3} , with a total surface area $\propto a^{-1}$.

5.7 Results

5.7.1 Collapse phase

We ran multiple models with different (constant) grain sizes. The models are summarized in Table 5.1.

Figure 5.1 shows the column number density profile versus radius at different times for the resistive model with $a_{\text{gr}} = 0.038 \mu\text{m}$. Several features are identifiable via their associated breaks in the profile. From the outside in, those are:

1. Prestellar infall profile with $N \propto r^{-1}$. This corresponds to a volume number density profile of $n \propto r^{-2}$, typical for collapsing cores dominated by gravity (see, e.g.,

Larson, 1969, and also Chapter 3). The vertical hydrostatic condition mandates $n \propto N^2$.

2. At ≈ 10 AU, there is a hint of a *magnetic wall* (Li and McKee, 1996; Contopoulos et al., 1998), where the relatively well-coupled, bunched-up magnetic field expelled from the first core decelerates material temporarily. Behind it, the infall continues.
3. Expansion wave profile with $N \propto r^{-1/2}$ outside the first core. Once this reaches the outer boundary of the natal cloud core, accretion terminates. The power law can be motivated analytically (see Shu, 1992, for the spherical case). Energy conservation requires the infall speed from large distances towards a point mass (i.e., the first core) with mass M to scale as $\sqrt{GM/r} \propto r^{-1/2}$. At the same time it can be argued that the infall onto the point mass is essentially a steady-state process, and thus $\dot{M} \equiv 2\pi r \Sigma v_r = \text{const}$, close to the border of the first core. Together, those two relations imply $\Sigma \propto r^{-1/2}$.
4. First core at 1 AU. Here, the density is sufficiently high that the gravitational energy released in the collapse cannot escape as radiation anymore. The temperature rises, and thermal pressure gradient stabilizes the object. The first core is nearly in hydrostatic equilibrium, and its radial and vertical extent are approximately equal.
5. Infall profile onto the second core with $N \propto r^{-1}$. After the first core has reached $\approx 1,000$ K, hydrogen is being dissociated. This process provides a heat sink, and the temperature does not increase sufficiently any longer for thermal pressure to balance gravity. The core starts to collapse again.
6. Beginning expansion wave profile with $N \propto r^{-1/2}$ outside the second core, for the same reasons as outside the first core. Once this rarefaction reaches the boundary of the first core, the material comprising the first core will fall in to a region of stellar dimensions, unless it forms a centrifugal disk.
7. Second core at $\approx 1 R_\odot$. After hydrogen dissociation (and ionization) has concluded, the temperature rises again, and a truly hydrostatic object, the YSO, is formed. It is also partly supported by electron degeneracy pressure (Masunaga and Inutsuka, 2000).

Figure 5.3 shows the evolution of the effective diffusion coefficient versus the central density for the various grain sizes, as well as the parametrized resistivity used in Machida et al. (2006) and Dapp and Basu (2010). At low densities, electrons and ions are the

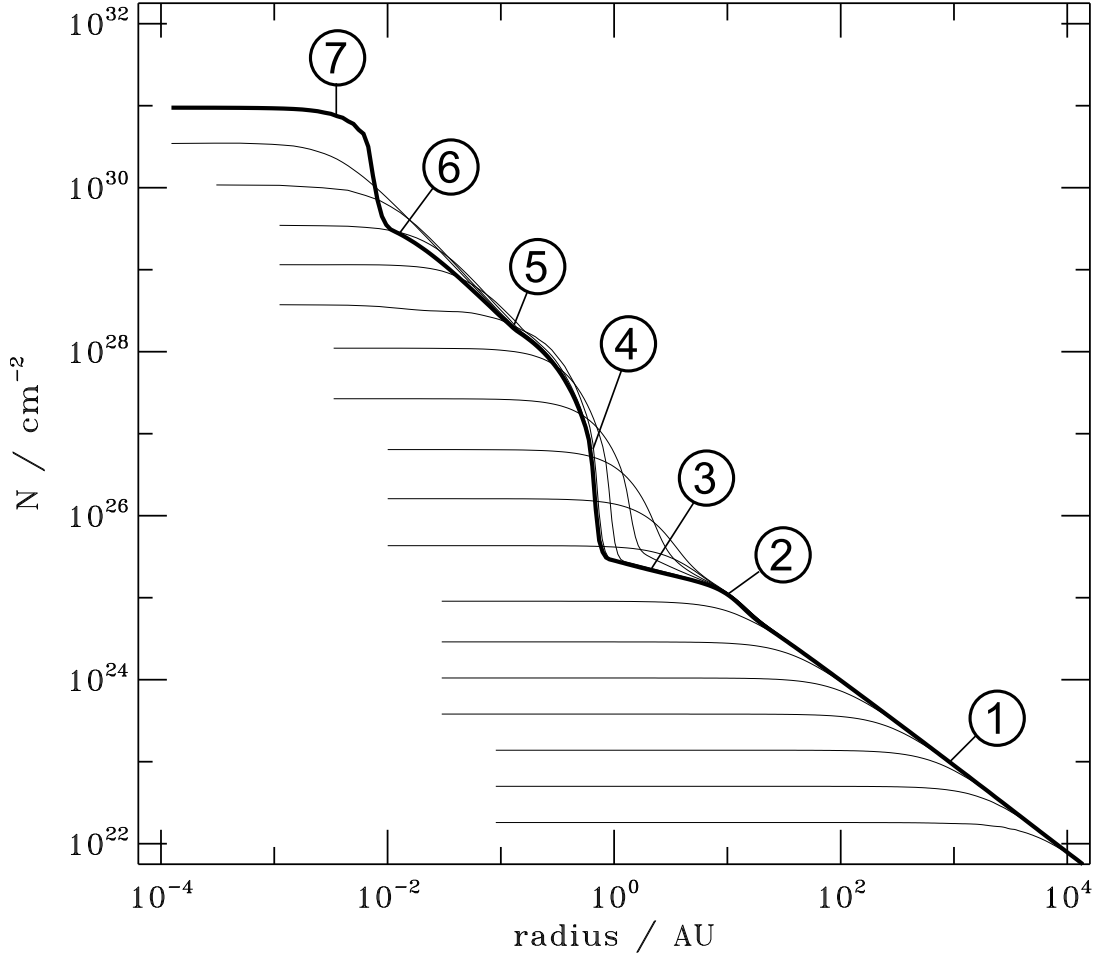


Figure 5.1: Column number density profile versus radius. The thin lines (in ascending order) are plots at the times listed in Table 5.2, for the fiducial grain radius of $a_{\text{gr}} = 0.038 \mu\text{m}$. Several features are identifiable via their associated breaks in the profile. From the outside in: (1) Prestellar infall profile with $N \propto r^{-1}$. (2) At ≈ 10 AU, there is a hint of a magnetic wall, where the bunched-up field lines decelerate material before it continues the infall. (3) Expansion wave profile with $N \propto r^{-1/2}$ outside the first core. Once this rarefaction wave reaches the outer boundary of the natal cloud core, accretion terminates. (4) First core at 1 AU. (5) Infall profile onto the second core with $N \propto r^{-1}$. After the first core has reached $\approx 1,000$ K, it starts to collapse, as H_2 is dissociated. (6) Expansion wave profile with $N \propto r^{-1/2}$ outside the second core. (7) Second core at $\approx 1 R_{\odot}$.

Table 5.2: Output times^a in the evolution plots.

Line number ^b	output time / 10 ³ yr
1	0.0
2	14.338
3	19.303
4	21.063
5	21.692
6	21.944
7	22.045
8	22.085
9	22.105
10	22.116
11	22.139
12	22.1508
13	22.15137
14	22.15149
15	22.15153
16	22.15154
17	22.15156

^a Time is counted from when chemistry and non-ideal MHD effects are is switched on (see Section 5.6).

^b Lines count from bottom up.

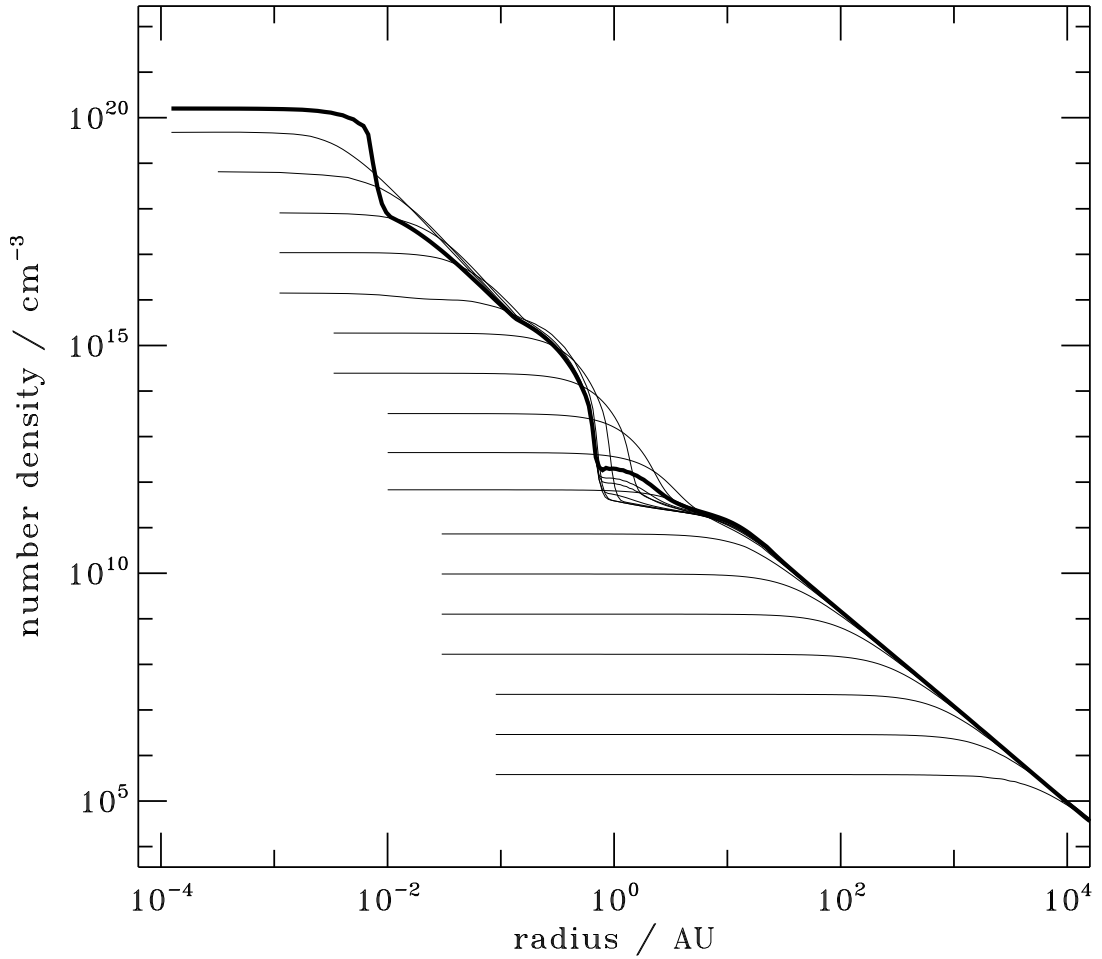


Figure 5.2: Volume number density versus radius over time. The features identifiable in Fig. 5.1 are visible here, too. Especially the magnetic wall is more pronounced. The thin lines are plots at the times listed in Table 5.2, for the fiducial grain radius of $a_{\text{gr}} = 0.038 \mu\text{m}$.

dominant but not exclusive contributors to the conductivity. Smaller grains are fairly well coupled to the magnetic field because of their smaller gyro-radius and a smaller collisional cross section, so their contribution to the effective resistivity is lower than that of larger grains. However, there is a competing effect: smaller grains have an increased capability to absorb gas-phase charge carriers because of their larger total surface area. For grains with radius $a_{\text{gr}} = 0.075 \mu\text{m}$ (dot-dashed line) and larger the trend reverses, and the conductivity increases (and the resistivity conversely decreases) with larger grain radius, as expected from an increased ionization fraction. At intermediate densities the resistivity rises sharply, as a consequence of a combination of the grains soaking up gas-phase charges and getting decoupled from the magnetic field. Additionally, the conductivity drops because at high column density cosmic rays are shielded increasingly, according to Eq.(5.31). At $n_c \approx 10^{13} \text{ cm}^{-3}$ the only remaining source of ionization is radioactivity, which provides a floor ionization rate (see Section 5.5.1). At this stage, clearly distinguished by a break in the profile, the resistivity is almost exclusively due to grains, i.e., their collisions with neutrals. Inserting Eq.(A.10) of Appendix A.2 into Eq.(5.22), we see that conductivity scales as a^{-2} in this phase. The resistivity is the inverse of the conductivity, and hence it *increases* with larger grains as a consequence of their lower gyro-frequency and greater collision cross section. This is despite the smaller number and reduced total surface area of the grains as they increase in size. As the temperature approaches 1,000 K, collisions become violent enough that thermal ionization occurs, described by Eq.(5.32). The conductivity recovers, and the resistivity hence drops again. Finally, during the second collapse, as temperatures of 1500 K are reached, grains are destroyed, and all locked-up charges released. Electrons and ions flood the gas, the ionization fraction skyrockets, and flux-freezing is restored (see Section 5.5.1). We point out that the simple parametrization used in Machida et al. (2006, 2007); Dapp and Basu (2010, the dotted line in Fig. 5.3) yields values for the resistivity consistently lower by at least a factor of 10.

In Figure 5.5 we present the evolution of the ionization fraction versus central density for the various grain sizes. At low densities the plot reveals that the smaller the grains, the lower the ionization fraction. The reason is that in that case, the grains are small and highly abundant and thus have a large surface area to which electrons and ions can stick. A mounting density causes the ionization fraction to diminish with a slope slightly steeper than the canonical relation $\propto n_n^{-1/2}$ for cosmic-ray-dominated ionization. At intermediate densities the ionization fractions levels off, starting with the smallest grains and continuing to successively larger grain radius. This is caused by the electrons adsorbing to the grains. Due to the electrons' high thermal speed, their collision rate with

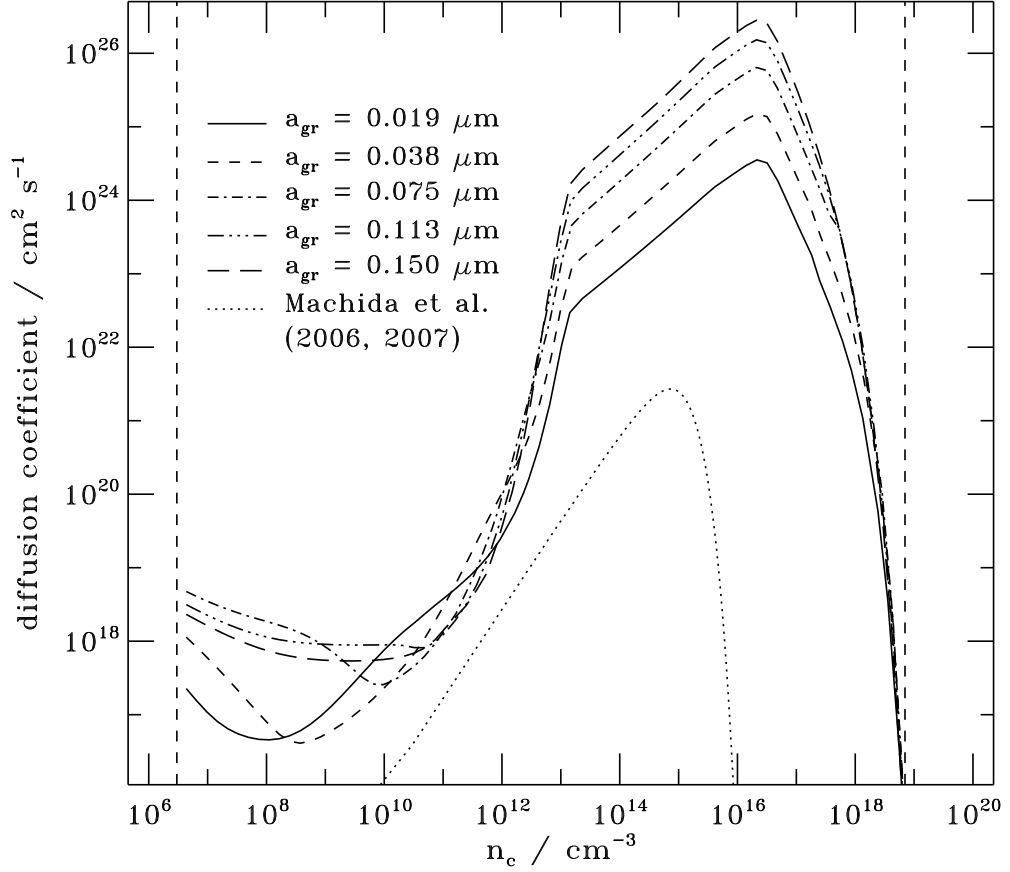


Figure 5.3: Diffusion coefficient vs. central density for different grain sizes. The vertical line indicates the density at which the detailed chemistry and non-ideal MHD treatment is switched on. Beyond $n_c \approx 10^{18} \text{ cm}^{-3}$ the resistivity drops, after having declined steadily for a bit due to thermal ionization. This is where we switch the chemistry calculations off again. Due to grain destruction, flux-freezing is restored there.

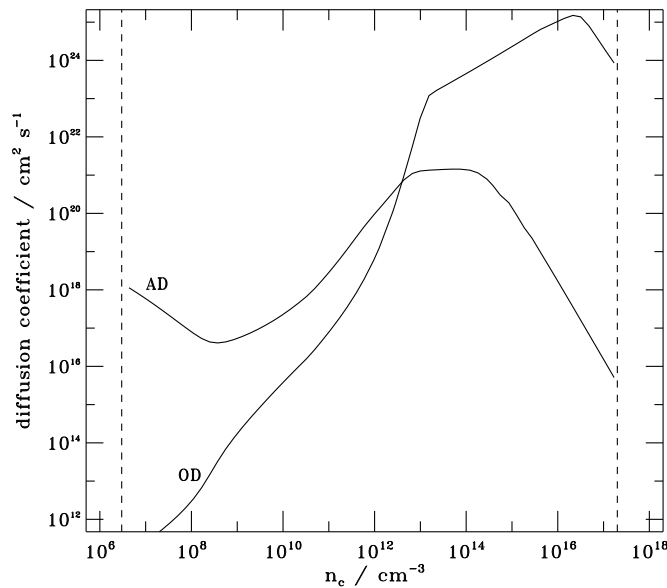


Figure 5.4: Contributions due to ambipolar diffusion (AD) and Ohmic dissipation (OD) to the effective resistivity in the standard model ($a_{\text{gr}} = 0.038 \mu\text{m}$). Ohmic dissipation only dominates ambipolar diffusion beyond $n_c \gtrsim 10^{12} \text{ cm}^{-3}$.

grains is much higher than the ions’. The separation of the electron abundance from the ions abundance accompanied by a strong increase in neutral grains is evidence for that. The ions also stick to the grains, and the abundance of positively-charged grains increases greatly during this phase as well. This increase seems even more dramatic because of the low initial abundance of positive grains, but their abundance remains lower than that of the neutral grains by nearly two orders of magnitude. This phenomenon occurs at later stages with increasing grain size, as Figs. 5.6 and 5.7 show, for the reason of the lower overall grain abundance (scaling as a_{gr}^{-3}), which cannot be compensated by a larger collision rate (see Eq.(A.7) in Appendix A). Beyond $n_c \gtrsim 10^{12} \text{ cm}^{-3}$, the ionization fraction drops precipitously for all grain sizes, as cosmic rays become shielded due to high column densities. The evolution at still higher densities is determined by radioactivity, until finally thermal ionization kicks in at $n_c \approx 10^{16} \text{ cm}^{-3}$. Potassium is one of the first species to be ionized, but as the temperature increases further, grain evaporation also releases charges into the gas.

Figure 5.8 compares the mass-to-flux ratio normalized to the critical value for the various models at the time thermal ionization reestablishes flux freezing, when $n_c \gtrsim 10^{19} \text{ cm}^{-3}$, shortly before the formation of a central protostar. For comparison, we also show the mass-to-flux ratio for a model with flux-freezing throughout, and the model with only the simple prescription for Ohmic dissipation used in Dapp and Basu (2010).

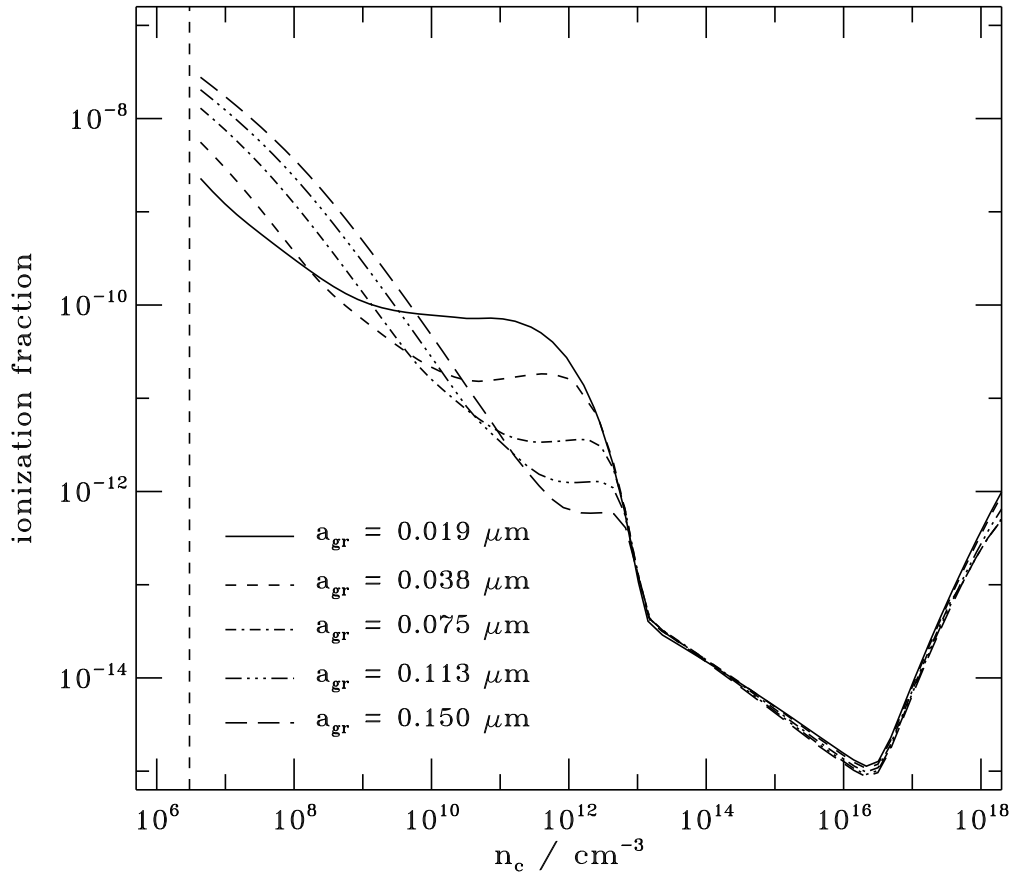


Figure 5.5: Total ionization fraction versus central density for different grain sizes. The vertical line indicates the density at which the detailed chemistry and non-ideal MHD treatment is switched on, and at which it is switched off again, due to grain destruction, and restoring of flux-freezing, respectively.

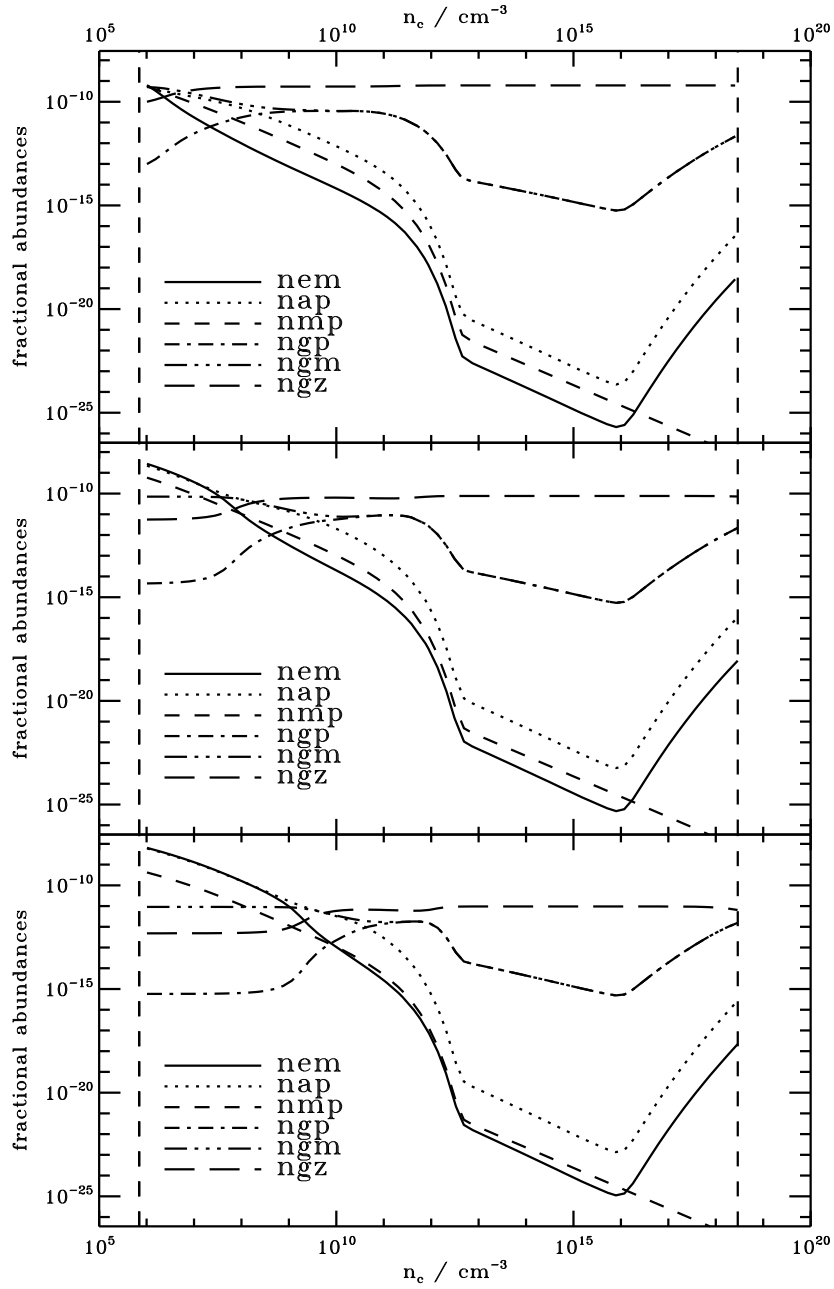


Figure 5.6: Fractional abundances of species (normalized to the neutral density) for the three smaller grain sizes. **Top:** $a_{\text{gr}} = 0.019 \mu\text{m}$, **Middle:** $a_{\text{gr}} = 0.038 \mu\text{m}$, **Bottom:** $a_{\text{gr}} = 0.075 \mu\text{m}$. The convergence of the abundances of positively- and negatively-charged grains is pushed to higher densities with increasing grain radius. The decoupling of electron and ion abundance also happens at higher densities with decreasing grain surface area. The vertical lines indicate the density at which the chemistry and non-ideal MHD treatment is switched on, and at which it is switched off again, respectively, due to grain destruction, and restoring of flux-freezing.

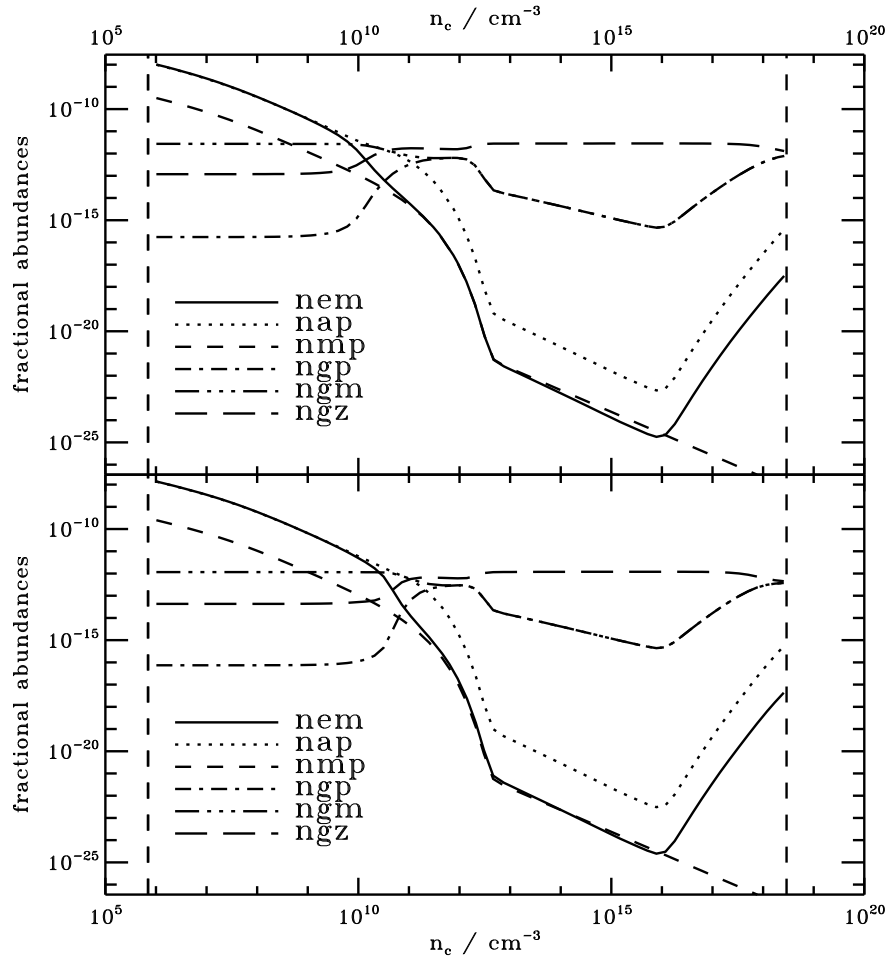


Figure 5.7: Fractional abundances of species (normalized to the neutral density) for the two larger grain sizes. **Top:** $a_{\text{gr}} = 0.113 \mu\text{m}$, **Bottom:** $a_{\text{gr}} = 0.150 \mu\text{m}$. Since the grain radius increases only by a factor of 4/3, the effect on the abundances is less pronounced than it was for the smaller grains.

It is evident that the inclusion of ambipolar diffusion, and the more realistic treatment of the microphysics leads to a further weakening of the magnetic field, both in the first core (by a factor of $\approx 10^2$), and in the region outside (by a factor of ≈ 2). It also extends out slightly further, also by a factor of ≈ 2 . This is caused by the higher effective value of the resistivity, and the earlier onset of its efficacy. The mass-to-flux ratio increases by a factor of $\approx 10^4$ over the course of the evolution, to a final value of $\approx 20,000$ times the critical value.

We expect the centrifugal disk to be able to form at slightly greater sizes (a least a few AU) than in the case with only Ohmic dissipation. We believe it will grow beyond that size by internal processes of angular momentum redistribution, bridging the gap to the extended disks of size ≈ 100 AU seen around Class II objects.

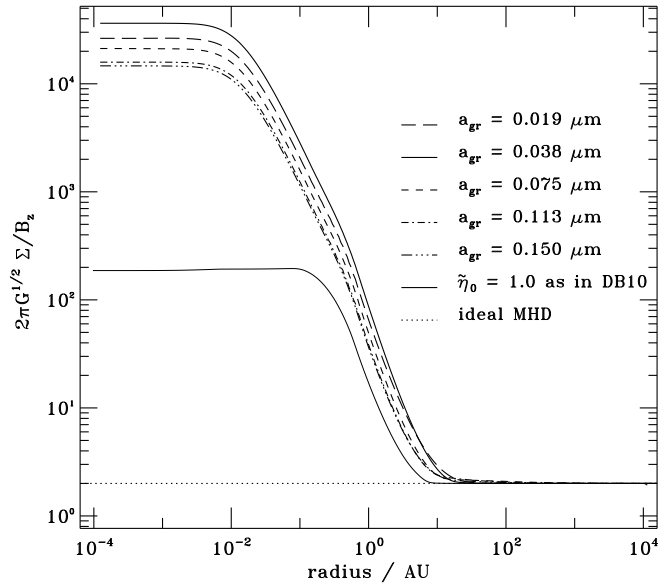


Figure 5.8: Mass-to-flux ratio μ versus radius for different grain sizes at the time of the formation of the second core. For comparison, the thin solid line shows the case with only the simplified version of Ohmic dissipation, as used in Dapp and Basu (2010). In the center, the difference is a factor of $\approx 10^2$, but further out it is still $2\times$ higher, and also shows a greater extent by about this factor. The reason is twofold: firstly, the effective resistivity is important at lower densities, and secondly it is larger everywhere than the parametrization used in Dapp and Basu (2010) (cf. Fig. 5.3).

Figures 5.9 and 5.10 show the evolution of the radial profiles of the vertical and radial components of the magnetic field, with the latter at the top surface of the disk. At low densities, they increase with near flux freezing. Ambipolar diffusion is present and active, but too slow to be dynamically important. Dramatic flux loss occurs once grains

become the dominant charge carriers at $n_c \approx 10^{11} \text{ cm}^{-3}$ and the field evolution slows. This can be seen in the bunching-up of the thin lines that are snapshots at different times (at constant increments of number density, at times given in Table 5.2). The small fluctuations near the interface of the first core are due to the extreme gradient of the density at the core boundary causing problems for the chemistry routine. To make matters worse, the resistivity increases steeply in this density regime, exacerbating the sensitivity of the magnetic field to perturbations. Higher resolution at the interface can remedy this (the data shown is at a resolution of 256 radial cells).

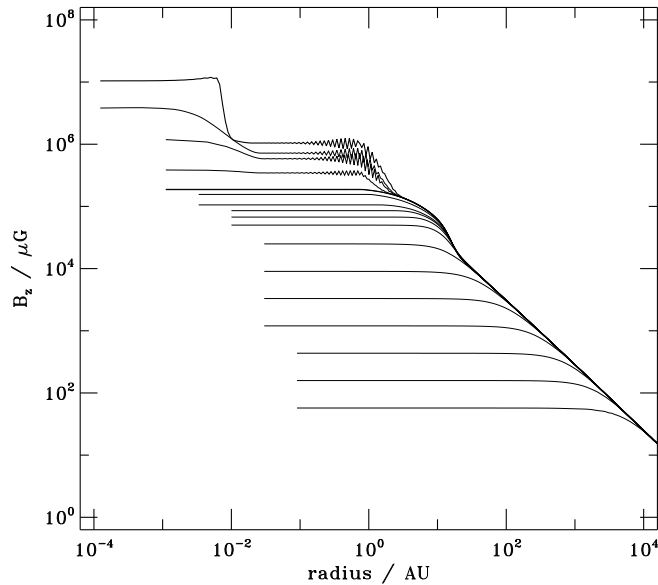


Figure 5.9: Evolution of B_z versus radius over time. The thin lines are plots at the times listed in Table 5.2, for the fiducial grain radius of $a_{\text{gr}} = 0.038 \mu\text{m}$.

In Figs. 5.11 and 5.12, the profiles at different times of the angular and radial (infall) velocities are shown, respectively. The angular velocity Ω behaves the same way as the column density profile ($\Omega \propto r^{-1}$, cf. Fig. 5.1), because the evolution happens at near angular momentum conservation. The specific angular momentum is then proportional to the enclosed mass, and thus $\propto \Sigma$ in thin disk geometry. Inside the expansion wave, there is a break in the angular velocity profile, as expected (e.g., Saigo and Hanawa, 1998). The enclosed mass in that region is essentially that of the first core, and approximately constant. Then $j \equiv \Omega r^2 \propto M_{\text{encl}} \approx \text{const}$, and therefore $\Omega \propto r^{-2}$.

The radial velocity shows the first and second cores very clearly. At their edges (at $\approx 1 \text{ AU}$, and $\approx 10^{-2} \text{ AU} = 2 R_{\odot}$, respectively), accretion shocks develop, and the velocity drops precipitously. Outside the cores, in the expansion wave, the velocity follows a power

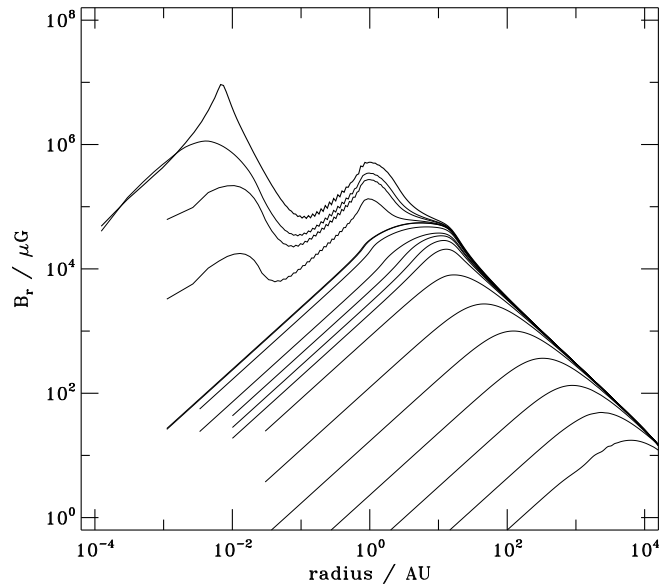


Figure 5.10: Evolution of B_r versus radius over time. The thin lines are plots at the times listed in Table 5.2, for the fiducial grain radius of $a_{\text{gr}} = 0.038 \mu\text{m}$.

law $\propto r^{-1/2}$, as explained above. At ≈ 10 AU, a slight bump in the infall velocity hints at the magnetic wall. The fluctuations within the first and second cores stem from the fact that we plot absolute values in a log-log plot: in nearly-stable conditions as prevalent there, the velocity can be positive or negative, but remains small.

5.7.2 Disk formation

In Fig. 5.13 we present evidence for the formation of a centrifugal disk. The figure shows the profiles of column density, infall velocity, and the ratio of centrifugal to gravitational acceleration shortly after the introduction of a sink cell. This is done for a model with resistivity and a grain size $a_{\text{gr}} = 0.038 \mu\text{m}$, and for a model without resistivity. In the resistive model, centrifugal balance is achieved in a small region ($\approx 10 R_{\odot}$) close to the center (bottom panel), while the flux-freezing model is braked “catastrophically”, and the support drops to minuscule values. Centrifugal balance is a necessary and sufficient condition for the formation of a centrifugally-supported disk. At the same time all infall is halted there and the radial velocity plummets (middle panel), while in the flux-freezing model, infall continues unhampered. After a few more months of evolution, a Toomre instability develops, and the rotationally-supported structure breaks up into a ring (top panel, solid line). At this point, we stop the simulation, because more physics would be required to follow the further evolution of the disk.

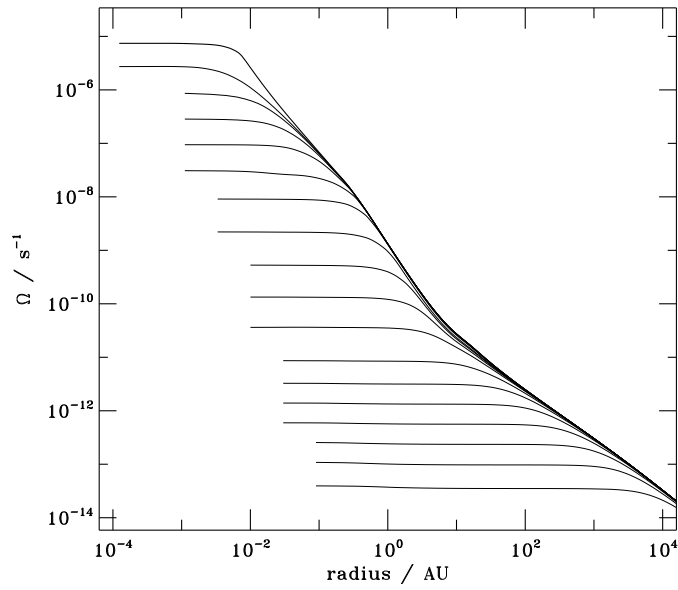


Figure 5.11: Evolution of the angular velocity Ω versus radius over time. The thin lines are plots at the times listed in Table 5.2, for the fiducial grain radius of $a_{\text{gr}} = 0.038 \mu\text{m}$.

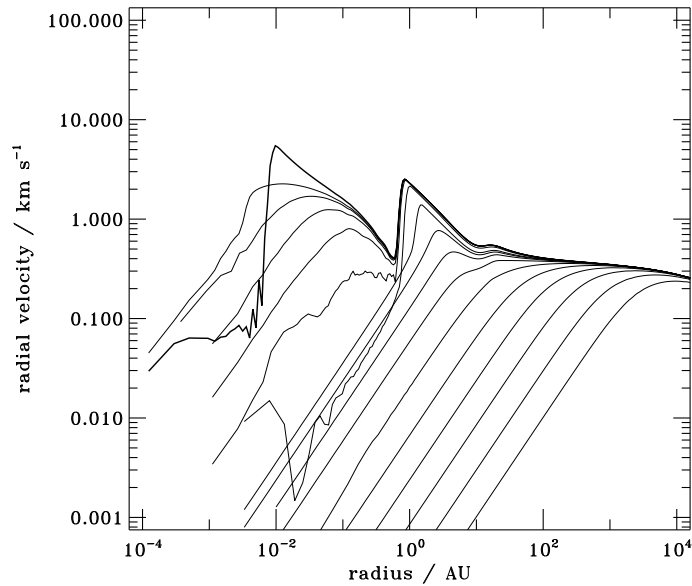


Figure 5.12: Evolution of the infall velocity velocity $|v_r|$ versus radius over time. The thin lines are plots at the times listed in Table 5.2, for the fiducial grain radius of $a_{\text{gr}} = 0.038 \mu\text{m}$. In the first and second cores material is moving about inwards and outwards with small speeds. This causes spikes when absolute values are plotted on double-logarithmic axes.

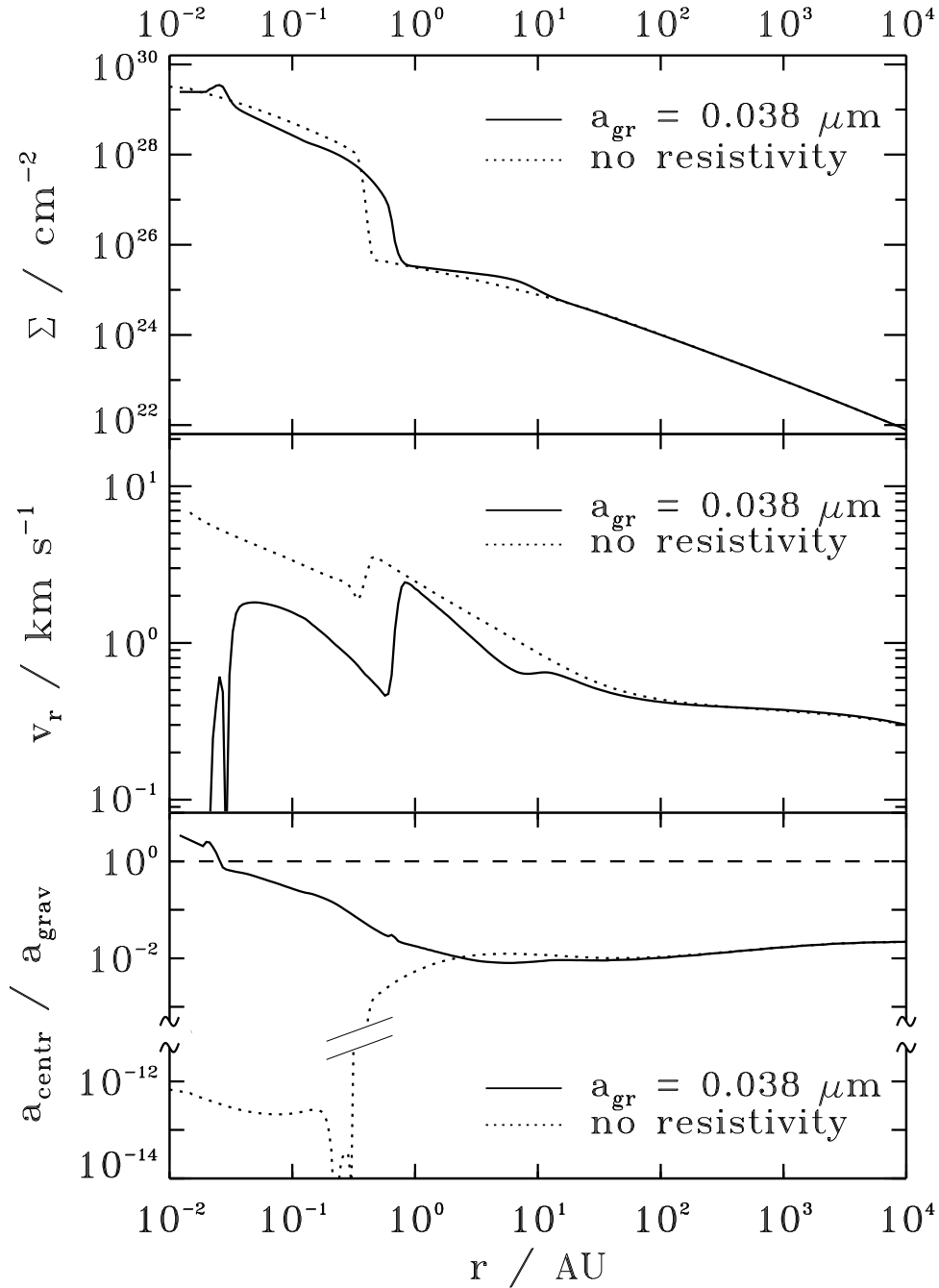


Figure 5.13: Evidence for disk formation. **Top panel:** column density profile. The system is Toomre-unstable, and breaks up into a ring in the resistive model (solid line), while no such occurrence is visible in case of flux freezing (dotted line). **Middle panel:** infall profile. As expected, infall is stopped where a centrifugal disk forms (see also, e.g., Vorobyov and Basu, 2007). **Bottom panel:** ratio of centrifugal over gravitational acceleration. In the resistive case, centrifugal balance is achieved. In contrast, catastrophic magnetic braking happens for flux freezing, and the centrifugal support drops to negligible values as the first core is spun down drastically.

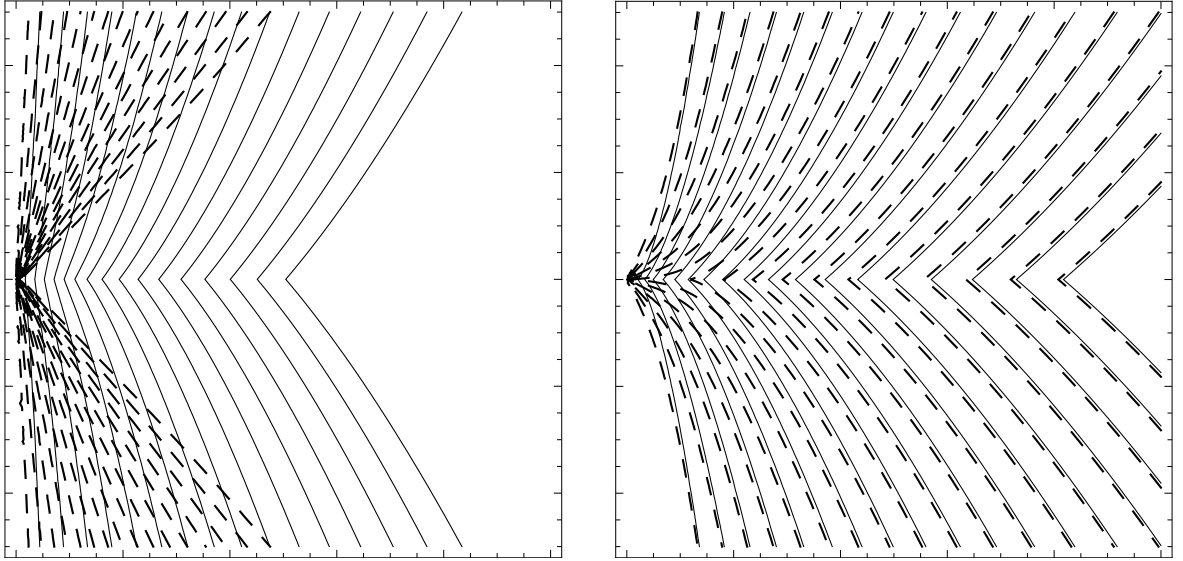


Figure 5.14: Magnetic field lines. The box on the left has dimensions 10 AU on each side, while the box on the right has dimensions 100 AU. The dashed lines represent the flux-freezing model, while the solid lines show *the same* field lines for the model including non-ideal MHD effects for a grain size $a_{\text{gr}} = 0.038 \mu\text{m}$. In both cases, the second core has just formed and is on the left axis mid-plane. The field lines straighten out significantly on small scales in the non-ideal model compared to the flux-frozen model.

5.8 Discussion

Figure 5.14 shows the magnetic field line topology above and below the disk on two scales (10 AU and 100 AU), for both flux-freezing and non-ideal MHD models. The field lines are calculated immediately after the formation of the second core, assuming force-free and current-free conditions above a finite thin disk (Mestel and Ray, 1985) (for details on the field line calculation see Appendix C.6). The split monopole of the flux-frozen model (dashed lines) is created as field lines are dragged in by the freely falling material within the expansion wave front at ≈ 15 AU. This is replaced by a more relaxed field line structure in the non-ideal case (solid lines), for which the field is almost straight in the center. Galli et al. (2009) presented similar field configurations resulting from a simplified model for Ohmic dissipation during the collapse. The extreme flaring of field lines in the flux-freezing model is a fundamental cause of the magnetic braking catastrophe.

We can estimate how efficient magnetic braking is, by comparing its instantaneous timescale with that of the dynamical evolution of the core. This yields

$$\frac{\tau_{\text{MB}}}{\tau_{\text{dyn}}} \approx \frac{L/N_{\text{cl}}}{c_{\text{s}}/G\Sigma}, \quad (5.41)$$

where $L = \Sigma\Omega r^2$ is the angular momentum per unit area, $N_{\text{cl}} = 2\pi r B_\phi B_z$ is the torque per unit area acting on the cloud, and $\tau_{\text{dyn}} = c_s/G\Sigma$ is the dynamical time for a thin disk. Figure 5.15 shows the magnetic braking condition for our cloud after the first core has formed. It is satisfied only for a small region outside the first core at ≈ 1 AU, namely where the expansion wave is moving out. In the region of dynamical collapse further out, and within the first core, where the magnetic field has been weakened by diffusive effects, magnetic braking is ineffective, and the cloud evolves under approximate angular momentum conservation.

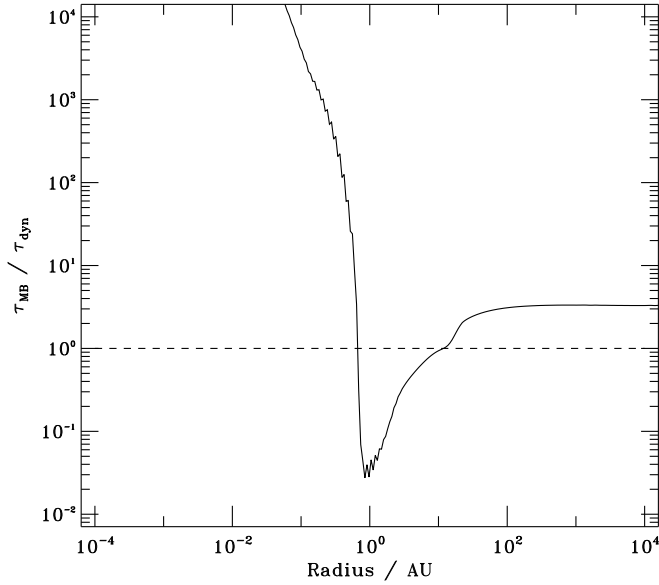


Figure 5.15: Plot of the magnetic braking condition $\tau_{\text{MB}}/\tau_{\text{dyn}}$. In the region of the expansion wave, the magnetic braking time is smaller than the dynamical evolution time, and thus material experiences magnetic braking there. In the region of dynamical collapse further out, and within the first core, where the magnetic field has been weakened by magnetic diffusion, magnetic braking is ineffective.

The specific centrifugal radius of a mass shell can be estimated according to

$$r_{\text{cf}} = j^2/GM, \quad (5.42)$$

where $j = \Omega r^2$ is the specific angular momentum, and M is the mass in the central object. While no YSO is present, we take that to be the cumulative mass enclosed within a location (i.e., assuming all enclosed mass will fall onto a protostar). The result shown in Fig. 5.16. This estimation is flawed within the first core, but outside it gives a fair approximation, to within factors of unity, since the first core's gravitational potential

looks like that of a point mass. Within the region of the expansion wave, the centrifugal radius is constant at ≈ 0.1 AU, and then increases linearly with radius, to $r_{\text{cf}} \approx 10$ AU at a distance of 100 AU from the center, and $r_{\text{cf}} \approx 100$ AU at 1,000 AU.

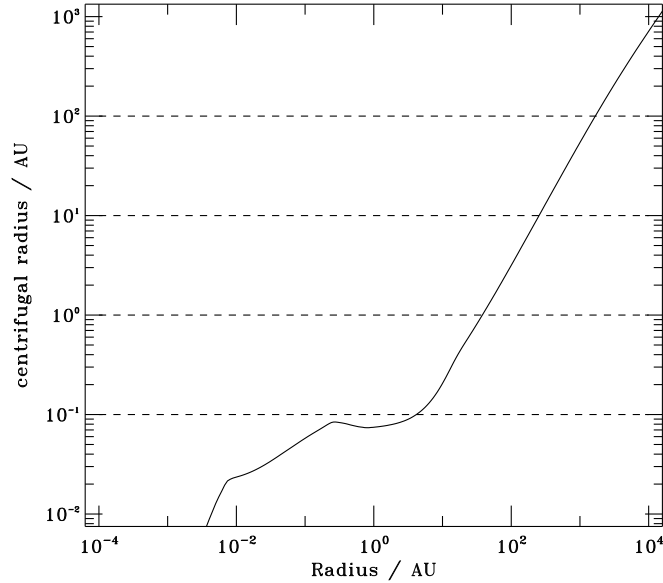


Figure 5.16: Estimated specific centrifugal radius of each mass shell. Beyond ≈ 10 AU, the centrifugal radius increases linearly.

Our results lead us to propose the following scenario of disk formation and evolution in low-mass stars:

- A small disk forms, initially $\ll 1$ AU, but eventually encompasses the entire first core with ≈ 1 AU, since magnetic diffusion is very efficient there, and inactivates magnetic braking. The disk will have a few tenths of M_{\odot} for a typical low-mass star.
- Figure 5.16 shows that the estimated centrifugal radius of a mass shell $\lesssim 10^3$ AU out lies within ≈ 10 AU. That means that the matter can fall to this radius without hitting a rotational barrier.
- At the same time, Fig. 5.15 shows that magnetic braking is active within the expansion wave, while it is dormant in the region of dynamical infall further out. Any material within the expansion wave (that slowly moves out) will lose part of its angular momentum by magnetic braking, and have its centrifugal barrier moved further in. This allows the material to accumulate onto the existing (small) accretion disk at ≈ 1 AU.

- The material in the disk will be subjected to internal mechanisms of angular momentum redistribution, e.g., the MRI (Balbus and Hawley, 1991), or gravitational torques (e.g., Vorobyov and Basu, 2007). It is a fair assumption that the disk self-regulates to $Q \approx 1$ by such processes (e.g., Lin and Pringle, 1987; Vorobyov and Basu, 2007). The parameter $Q = c_s \Omega / (\pi G \Sigma)$ approximately determines whether a rotating disk is unstable to fragmentation (Toomre, 1981). The exact critical value depends on the geometry and the equation of state, but generally spirals and clumps will form if $Q \lesssim 1$, while a situation with $Q \gtrsim 1$ is stable.
- The redistribution allows material in the inner disk to lose its angular momentum, and be funneled onto the star, while material further gains the excess angular momentum, and expands its orbit. Basu (1998) showed that disk's radius follows

$$r_{\text{final}} \simeq r_{\text{initial}} \left(\frac{M_{\star}}{M_{\text{disk}}} \right)^2, \quad (5.43)$$

where M_{disk} and M_{\star} are the disk's and star's mass, respectively. This means that the disk has expanded by a factor of 10^2 by the time 90% of its mass have accreted onto the central object.

- By the time the central object has accreted a significant amount of the available material, a tenuous disk of several hundred AU will be present, consistent with observations (e.g., Andrews and Williams, 2005).

5.9 Summary and conclusions

We present a new axisymmetric code using the thin-disk approximation to calculate the collapse of rotating magnetized prestellar cores. We follow the evolution all the way to stellar sizes and near-stellar densities. We determine the abundances of seven different species, and consider inelastic collisions. We calculate an effective resistivity that includes the effect of ambipolar diffusion and Ohmic dissipation for five different grain sizes. In a future paper, we will extend the model to use the standard “MRN” distribution for the grain sizes (which is named after its authors, Mathis, Rumpl, and Nordsieck; see Mathis et al., 1977).

We demonstrate the formation of a centrifugally-supported disk despite the presence of magnetic braking. The so-called “magnetic braking catastrophe” is averted by extensive magnetic flux loss from the high-density region of the first core. This weakens the magnetic field, and prevents it from spinning down the material in that region. The

mass-to-flux ratio is reduced by a factor of 10^4 . Shortly after the second collapse, disk formation happens very close to the central object, while it is still very small ($< 10^{-2} M_{\odot}$). This is consistent with the observational evidence of outflows at a very young age and the simultaneous non-detection of disks $\gtrsim 50$ AU around Class 0 objects. ALMA will allow observers to improve on this, and to probe for disks down to ≈ 10 AU.

We propose a disk formation scenario in which centrifugal disks form on small scales but are initially massive. We calculate the centrifugal radius and demonstrate that material can reach the expansion wave, which is moving outward at the local sound speed. Magnetic braking is still effective in that region and can presumably remove enough angular momentum such that the gas can form a small disk of size ≈ 1 AU. The small disk grows over time by continued accretion but more so by internal angular momentum redistribution, and may reach the size ≈ 100 AU observed around Class II objects.

Acknowledgements

The authors thank Jan Cami for providing computational facilities to run some of the models. W.B.D. was supported by an NSERC Alexander Graham Bell Canada Graduate Scholarship. S.B. was supported by an NSERC Discovery Grant. M.W.K. was supported by a STFC Grant.

Bibliography

- Allen, A., Li, Z., and Shu, F. H.: 2003, *ApJ* **599**, 363
- Andrews, S. M. and Williams, J. P.: 2005, *ApJ* **631**, 1134
- Balbus, S. A. and Hawley, J. F.: 1991, *ApJ* **376**, 214
- Basu, S.: 1997, *ApJ* **485**, 240
- Basu, S.: 1998, *ApJ* **509**, 229
- Basu, S. and Mouschovias, T. C.: 1994, *ApJ* **432**, 720
- Caselli, P., Benson, P. J., Myers, P. C., and Tafalla, M.: 2002, *ApJ* **572**, 238
- Ciolek, G. E. and Mouschovias, T. C.: 1993, *ApJ* **418**, 774
- Ciolek, G. E. and Mouschovias, T. C.: 1995, *ApJ* **454**, 194

- Contopoulos, I., Ciolek, G. E., and Königl, A.: 1998, *ApJ* **504**, 247
- Dapp, W. B. and Basu, S.: 2009, *MNRAS* **395**, 1092
- Dapp, W. B. and Basu, S.: 2010, *A&A* **521**, L56+
- Fiedler, R. A. and Mouschovias, T. C.: 1992, *ApJ* **391**, 199
- Fiedler, R. A. and Mouschovias, T. C.: 1993, *ApJ* **415**, 680
- Galli, D., Cai, M., Lizano, S., and Shu, F. H.: 2009, in *Revista Mexicana de Astronomia y Astrofisica Conference Series*, Vol. 36 of *Revista Mexicana de Astronomia y Astrofisica Conference Series*, pp 143–148
- Gear, C. W.: 1971, *Numerical initial value problems in ordinary differential equations*, Prentice-Hall, 1971
- Goldsmith, P. F. and Arquilla, R.: 1985, in D. C. Black & M. S. Matthews (ed.), *Protostars and Planets II*, pp 137–149
- Goodman, A. A., Benson, P. J., Fuller, G. A., and Myers, P. C.: 1993, *ApJ* **406**, 528
- Hennebelle, P. and Fromang, S.: 2008, *A&A* **477**, 9
- J Jeans, J. H.: 1902, *Philosophical Transactions of the Royal Society of London. Series A, Containing Papers of a Mathematical or Physical Character* **199**, 1
- J Jeans, J. H.: 1928, *Astronomy and cosmogony*, Cambridge [Eng.] The University press, 1928.
- Kunz, M. W. and Mouschovias, T. C.: 2009, *ApJ* **693**, 1895
- Kunz, M. W. and Mouschovias, T. C.: 2010, *MNRAS* **408**, 322
- Larson, R. B.: 1969, *MNRAS* **145**, 271
- Li, Z. and McKee, C. F.: 1996, *ApJ* **464**, 373
- Lin, D. N. C. and Pringle, J. E.: 1987, *MNRAS* **225**, 607
- Machida, M. N., Inutsuka, S., and Matsumoto, T.: 2006, *ApJ* **647**, L151
- Machida, M. N., Inutsuka, S., and Matsumoto, T.: 2007, *ApJ* **670**, 1198
- Masunaga, H. and Inutsuka, S.: 2000, *ApJ* **531**, 350

- Mathis, J. S., Rumpl, W., and Nordsieck, K. H.: 1977, *ApJ* **217**, 425
- Maury, A. J., André, P., Hennebelle, P., Motte, F., Stamatellos, D., Bate, M., Belloche, A., Duchêne, G., and Whitworth, A.: 2010, *A&A* **512**, A40+
- Mellon, R. R. and Li, Z.: 2008, *ApJ* **681**, 1356
- Mellon, R. R. and Li, Z.: 2009, *ApJ* **698**, 922
- Mestel, L. and Ray, T. P.: 1985, *MNRAS* **212**, 275
- Mestel, L. and Spitzer, Jr., L.: 1956, *MNRAS* **116**, 503
- Morton, S. A., Mouschovias, T. C., and Ciolek, G. E.: 1994, *ApJ* **421**, 561
- Mouschovias, T. C.: 1991, *ApJ* **373**, 169
- Nakano, T., Nishi, R., and Umebayashi, T.: 2002, *ApJ* **573**, 199
- Norman, M. L., Wilson, J. R., and Barton, R. T.: 1980, *ApJ* **239**, 968
- Pneuman, G. W. and Mitchell, T. P.: 1965, *Icarus* **4**, 494
- Radhakrishnan, K. and Hindmarsh, A. C.: 1993, *Description and Use of LSODE, the Livermore Solver for Ordinary Differential Equations*, Technical report, Lawrence Livermore National Laboratory
- Saigo, K. and Hanawa, T.: 1998, *ApJ* **493**, 342
- Schiesser, W. E.: 1991, *The Numerical Method of Lines: Integration of Partial Differential Equations*, Academic Press, 1991. 326 p.
- Shu, F. H.: 1992, *Physics of Astrophysics, Vol. II*, Physics of Astrophysics, Vol. II, by Frank H. Shu. Published by University Science Books, ISBN 0-935702-65-2, 476pp, 1992.
- Spitzer, Jr., L.: 1941, *ApJ* **93**, 369
- Spitzer, Jr., L.: 1978, *Physical processes in the interstellar medium*, New York Wiley-Interscience, 1978. 333 p.
- Toomre, A.: 1981, in S. M. Fall & D. Lynden-Bell (ed.), *Structure and Evolution of Normal Galaxies*, pp 111–136

Truelove, J. K., Klein, R. I., McKee, C. F., Holliman, II, J. H., Howell, L. H., and Greenough, J. A.: 1997, *ApJ* **489**, L179+

Umebayashi, T. and Nakano, T.: 1980, *PASJ* **32**, 405

van Leer, B.: 1977, *Journal of Computational Physics* **23**, 276

Vorobyov, E. I. and Basu, S.: 2007, *MNRAS* **381**, 1009

Wardle, M.: 2007, *Ap&SS* **311**, 35

Chapter 6

Summary and outlook

In this Thesis we have highlighted the influence of magnetic diffusion (both ambipolar diffusion and Ohmic dissipation) on the star formation process on various scales. In Chapter 2 we studied and gave an analytical description of turbulence-induced waves that are present in clouds on large scales and damped within a crossing time if ambipolar diffusion is present. On a more general note, we demonstrated that noteworthy phenomena (in our case persistent waves) can appear if clouds are investigated in at least partly global models and not in local models that only consider a small patch in the deep interior of a cloud and assume periodic boundary conditions.

In Chapter 3 we introduced an empirical analytic model for the description of the internal structure of prestellar cores. It is intended to replace the venerable Bonnor-Ebert model, which despite being a nice closed-form theory (derived in detail in Appendix D), is severely limited in its applicability. Its equilibrium assumption restricts the fitting temperature and sometimes produces fits that are unrealistic. Our empirically-motivated model rejects this assumption and provides observers with a way to judge the dynamical state of a core with observationally-constrained fitting parameters only. Many simulations show that it approximates a numerical solution much better than the Bonnor-Ebert model. The model has already been used successfully to fit observations (e.g., Kauffmann et al., 2010a,b; Pineda et al., 2010).

In Chapters 4 and 5, we used the thin-disk approximation to follow the evolution of a rotating magnetized prestellar core during its collapse all the way to a protostar and to near-stellar densities. We showed that magnetic diffusion disables magnetic braking in a crucial central region and allows a centrifugal disk to form. Other modelers had been puzzled by the realization that magnetic braking might not allow the (direct) formation of larger-scale disks as observed around many Class II objects. Our simulations extended into regions much smaller than what is often modeled, and found a resolution to the

problem there. In Chapter 5, we used a more realistic description of the magnetic diffusion process, calculating the chemistry of a seven-species fluid including inelastic collisions, and all relevant sources of ionization. However, we still kept other simplifications, such as the barotropic pressure-density relation instead of a detailed energy equation. We showed that the region where magnetic braking is ineffective has an extent greater by a factor of ≈ 2 compared with the parametrization of only Ohmic dissipation, with the result that a forming disk can be larger. The so-called “magnetic braking catastrophe” is averted by extensive magnetic flux loss from the high-density region of the first core. We proposed a disk formation scenario in which centrifugal disks form small but initially massive, and grow over time by internal angular momentum redistribution to reach the size ≈ 100 AU observed around Class II objects.

Of course, the approximations used in this Thesis do not hold everywhere. For instance, the thin disk model is not applicable anymore when the second core forms. Also, after formation of the second core, and at the very latest time when deuterium burning sets in, a detailed treatment of radiative effects is necessary and the simple barotropic energy equation is no longer applicable. If one wants to explore the evolution of the centrifugal disk in detail it is unavoidable to further give up the assumption of axisymmetry in order to capture gravitational torques. In fact, one may even be forced to study the system in all three dimensions, because the magnetic field is inherently three-dimensional and so are phenomena such as the MRI in the disk, accretion flows from the disk to the protostar, or the launching of a jet. We believe that instead of studying patches of the accretion disk in shearing-box simulations, a “global” model is desirable here.

Three-dimensional MHD codes, such as RAMSES (Teyssier, 2002; Fromang et al., 2006) can shed light on issues surrounding the fragmentation of molecular clouds into filaments and cores, and their evolution. It is essential to approach this problem in global models, for instance by embedding a slab of gas into a hot tenuous medium, in which an external magnetic field is anchored. The interplay of gravity, magnetic fields, turbulence, and feedback processes from star formation determines the lifetime of clouds, the initial conditions of star formation, and holds the answer to why it is such an inefficient process. Such simulations can also help to study in detail the propagation of MHD waves in a three-dimensional stratified medium and investigate the associated energy and angular momentum transport.

Furthermore, models may help to remedy a fundamental problem of the study of astrophysical magnetic fields. As a consequence of their relative weakness it is hard to ascertain their magnitude and thus their dynamical importance. After over three decades of observations, only around two dozen confirmed measurements are available (e.g., those

collected in Crutcher, 1999). We are far away from being able to map the field across prestellar cores. This would be desirable in order to constrain models of their formation and to judge whether the magnetic field could be responsible for a low star formation efficiency. Despite auspicious new instruments such as ALMA and the Square Kilometer Array (SKA), it seems prudent to find additional ways to determine the mass-to-flux ratio. One possibility lies in the curvature of magnetic field lines. It is much easier to find the local orientation of the magnetic field by following the linear polarization caused by grain alignment with the local magnetic field, than to measure the field strength. It may be possible to quantify the mass-to-flux ratio by fitting the mapped polarization angles with predictions from magnetic simulations.

We live in exciting times for numerical astrophysical research. The computing power will soon reach the level where large three-dimensional simulations become feasible that resolve all physical scales of interest with AMR, while including most necessary physics. GPGPU computing also promises a great improvement in efficiency. At the same time, the tools of the trade get more and more sophisticated. There are high-level programming languages such as IDL and Python available that combine programming ease, fantastic visualization, and data-analysis capabilities with the fast execution speed of an underlying low-level language, and facilitate the use of computer clusters.

Nevertheless, it is our strong belief that there will remain a place and even the necessity for focused studies of one aspect or another – be it in dimensionally-reduced system such as ours, or concentrating one single physical effect, such as disk formation. Hydrodynamics alone is not fully understood, and when one throws Maxwell’s equations into the mix to create MHD, a plethora of new discoveries can be made, and effects are waiting to be understood in detail, not the least of which is interstellar (magneto-gravitational) turbulence.

As already indicated in the introduction to this Thesis, a “realistic” simulation of the star formation process should solve the three-dimensional equations of RMHD, and include non-ideal MHD effects. The simulation should include full wavelength-dependent radiative transfer and incorporate a sophisticated chemical model as well as grain physics. However, it will still be years until all these effects can be included in a single self-consistent simulation. The main reason is the huge range of scales involved, and the confluence of so many highly nonlinear effects. But we are already getting closer (at least when it comes to physics) to answering the age-old fundamental question how Earth and the Heavens come to exist, and where they are going.

Bibliography

Crutcher, R. M.: 1999, *ApJ* **520**, 706

Fromang, S., Hennebelle, P., and Teyssier, R.: 2006, *A&A* **457**, 371

Kauffmann, J., Pillai, T., Shetty, R., Myers, P. C., and Goodman, A. A.: 2010a, *ApJ* **712**, 1137

Kauffmann, J., Pillai, T., Shetty, R., Myers, P. C., and Goodman, A. A.: 2010b, *ApJ* **716**, 433

Pineda, J. L., Goldsmith, P. F., Chapman, N., Snell, R. L., Li, D., Cambrésy, L., and Brunt, C.: 2010, *ApJ* **721**, 686

Teyssier, R.: 2002, *A&A* **385**, 337

Appendix A

Rate Coefficients and Collision time scales

A.1 Rate Coefficients

For convenience, we reproduce here the rate coefficients used in this work. They can also be found in Appendix A of Kunz and Mouschovias (2009). For radiative recombination of atomic ions and electrons, and for the dissociative recombination of electrons and HCO^+ ions, we respectively adopt the values (Umebayashi and Nakano, 1990)

$$\alpha_{\text{rr}} = 2.8 \times 10^{-12} (300 \text{ K}/T)^{0.86} \text{ cm}^3 \text{ s}^{-1}, \quad (\text{A.1})$$

$$\alpha_{\text{dr}} = 2.0 \times 10^{-7} (300 \text{ K}/T)^{0.75} \text{ cm}^3 \text{ s}^{-1}. \quad (\text{A.2})$$

For charge-exchange reactions between atomic and molecular ions, we use the value from Watson (1976)

$$\beta = 2.5 \times 10^{-9} \text{ cm}^3 \text{ s}^{-1}. \quad (\text{A.3})$$

The rate coefficients pertaining to ions (both molecular and atomic, both indicated with subscript ‘i’) and electrons (subscript ‘e’) on the one hand and grains on the other are taken from Spitzer (1941, 1948), with refinements made by Draine and Sutin (1987)

to account for the polarization of grains:

$$\alpha_{\text{eg}^0} = \pi a^2 \left(\frac{8k_{\text{B}}T}{\pi m_{\text{e}}} \right)^{1/2} \left[1 + \left(\frac{\pi e^2}{2ak_{\text{B}}T} \right)^{1/2} \right] \mathcal{P}_{\text{e}}, \quad (\text{A.4})$$

$$\alpha_{\text{ig}^0} = \pi a^2 \left(\frac{8k_{\text{B}}T}{\pi m_{\text{i}}} \right)^{1/2} \left[1 + \left(\frac{\pi e^2}{2ak_{\text{B}}T} \right)^{1/2} \right] \mathcal{P}_{\text{i}}, \quad (\text{A.5})$$

$$\alpha_{\text{eg}^+} = \pi a^2 \left(\frac{8k_{\text{B}}T}{\pi m_{\text{e}}} \right)^{1/2} \left[1 + \left(\frac{e^2}{ak_{\text{B}}T} \right) \right] \left[1 + \left(\frac{2e^2}{2e^2 + ak_{\text{B}}T} \right)^{1/2} \right] \mathcal{P}_{\text{e}}, \quad (\text{A.6})$$

$$\alpha_{\text{ig}^-} = \pi a^2 \left(\frac{8k_{\text{B}}T}{\pi m_{\text{i}}} \right)^{1/2} \left[1 + \left(\frac{e^2}{ak_{\text{B}}T} \right) \right] \left[1 + \left(\frac{2e^2}{2e^2 + ak_{\text{B}}T} \right)^{1/2} \right] \mathcal{P}_{\text{i}}. \quad (\text{A.7})$$

For the sticking probabilities of electrons or ions onto grains, we take the values from Umebayashi (1983), $\mathcal{P}_{\text{e}} = 0.6$ and $\mathcal{P}_{\text{i}} = 1.0$. In these equations, a is the adopted grain radius, while other quantities have their usual meanings. Lastly, the rate coefficients for charge transfer during collisions between grains are of the same form as the ones above, just with modified masses.

$$\alpha_{\text{g}^+\text{g}^-} = 16\pi a^2 \left(\frac{k_{\text{B}}T}{\pi m_{\text{g}}} \right)^{1/2} \left[1 + \left(\frac{2e^2}{ak_{\text{B}}T} \right) \right] \left[1 + \left(\frac{e^2}{e^2 + ak_{\text{B}}T} \right)^{1/2} \right], \quad (\text{A.8})$$

$$\alpha_{\text{g}^\pm\text{g}^0} = 16\pi a^2 \left(\frac{k_{\text{B}}T}{\pi m_{\text{g}}} \right)^{1/2} \left[1 + \left(\frac{\pi e^2}{ak_{\text{B}}T} \right)^{1/2} \right] \mathcal{P}_{\text{gg}}. \quad (\text{A.9})$$

Here, m_{g} is the average grain mass (assumed constant), and $\mathcal{P}_{\text{gg}} \equiv 1/2$ is the probability of charge exchange between neutral and charged grains (both positive and negative). The probability of neutralization in Eq. (A.8) is assumed unity.

A.2 Collision time scales

As in Kunz (2009), we compute the collision times between the different species s and neutrals according to the formula

$$\tau_{\text{sn}} = k_{s,\text{He}} \frac{m_s + m_{\text{H}_2}}{\rho_{\text{n}} \langle \sigma w \rangle_{s\text{H}_2}}. \quad (\text{A.10})$$

The quantity $k_{s,\text{He}}$ is a correction factor entering the equation due to the fact that the gas also contains helium. The above expression hence calculates the collision time for charged species with *all* neutrals. Helium contributes only a small correction factor due

to its low polarizability compared with H_2 (see Spitzer, 1978). Mouschovias (1996) gives these correction factors as

$$k_{s,\text{He}} = \begin{cases} 1.23, & \text{if } s = i, \\ 1.21, & \text{if } s = e, \\ 1.09, & \text{if } s = g_+, g_0, \text{ or } g_-. \end{cases} \quad (\text{A.11})$$

The values for the rate constant $\langle\sigma w\rangle_{s\text{H}_2}$ are taken from McDaniel and Mason (1973), Mott and Massey (1965), and Ciolek and Mouschovias (1993), respectively:

$$\langle\sigma w\rangle_{s\text{H}_2} = \begin{cases} 1.69 \times 10^{-9} \text{ cm}^3 \text{ s}^{-1}, & \text{if } s = i, \\ 1.3 \times 10^{-9} \text{ cm}^3 \text{ s}^{-1}, & \text{if } s = e, \\ \pi a^2 (8k_{\text{B}}T / \pi m_{\text{H}_2})^{1/2}, & \text{if } s = g_+, g_0, \text{ or } g_-. \end{cases} \quad (\text{A.12})$$

Bibliography

Ciolek, G. E. and Mouschovias, T. C.: 1993, *ApJ* **418**, 774

Draine, B. T. and Sutin, B.: 1987, *ApJ* **320**, 803

Kunz, M. W.: 2009, *Ph.D. thesis*, University of Illinois at Urbana-Champaign

Kunz, M. W. and Mouschovias, T. C.: 2009, *ApJ* **693**, 1895

McDaniel, E. W. and Mason, E. A.: 1973, *Mobility and Diffusion of Ions in Gases (Wiley series in plasma physics)*, John Wiley & Sons (May 1973)

Mott, N. F. and Massey, H. S. W.: 1965, *The theory of atomic collisions / by N.F. Mott and H.S.W. Massey*, Clarendon Press, Oxford :, 3rd ed. edition

Mouschovias, T. C.: 1996, in K. C. Tsinganos (ed.), *Solar and Astrophysical Magnetohydrodynamic Flows*, pp 505–538

Spitzer, Jr., L.: 1941, *ApJ* **93**, 369

Spitzer, Jr., L.: 1948, *ApJ* **107**, 6

Spitzer, Jr., L.: 1978, *Physical processes in the interstellar medium*, New York Wiley-Interscience, 1978. 333 p.

Umebayashi, T.: 1983, *Progress of Theoretical Physics* **69**, 480

Umebayashi, T. and Nakano, T.: 1990, *MNRAS* **243**, 103

Watson, W. D.: 1976, *Reviews of Modern Physics* **48**, 513

Appendix B

Derivation of the thin-disk equations

In this section, we shall derive the equations of hydrodynamics for a infinitely thin disk. This assumption is relaxed for the gravitational field later.

B.1 Applicability

Fiedler and Mouschovias (1992, 1993) showed that a subcritical molecular cloud core threaded by straight-parallel magnetic field lines initially contracts along the field lines, and will form a thin disk. Only then, when approximate vertical force balance is achieved, will collapse perpendicular to the field lines occur. The reason is that the parallel component of the “magnetic pressure” – while being isotropic – is cancelled by terms of magnetic tension. This can be shown when considering the direction of the general expression for the magnetic force $F_{\text{mag}} = 1/4\pi (\nabla \times \mathbf{B}) \times \mathbf{B}$, which has no components parallel to the magnetic field.

$$\begin{aligned} \frac{1}{4\pi} (\nabla \times \mathbf{B}) \times \mathbf{B} &= \frac{1}{4\pi} (\mathbf{B} \cdot \nabla) \mathbf{B} - \nabla \left(\frac{B^2}{8\pi} \right), \\ &= \frac{1}{4\pi} (\mathbf{B} \cdot \nabla) \mathbf{B} - \nabla_{\perp} \left(\frac{B^2}{8\pi} \right) - \nabla_{\parallel} \left(\frac{B^2}{8\pi} \right). \end{aligned} \quad (\text{B.1})$$

The first term (the “magnetic tension”) can be written as

$$\frac{1}{4\pi} (\mathbf{B} \cdot \nabla) \mathbf{B} = \frac{B}{4\pi} \frac{\partial}{\partial s} (\hat{\mathbf{s}} B), \quad (\text{B.2a})$$

$$= \frac{B^2}{4\pi} \frac{\partial \hat{\mathbf{s}}}{\partial s} + \hat{\mathbf{s}} \frac{B}{4\pi} \frac{\partial B}{\partial s} \quad (\text{B.2b})$$

where $\hat{\mathbf{s}}$ is the unit vector parallel to the magnetic field. The first term is related to the change of direction of the instantaneous unit vector parallel to the field, i.e., the radius of curvature, by

$$\partial \hat{\mathbf{s}} / \partial s = \hat{\mathbf{n}} R_c^{-1}, \quad (\text{B.3})$$

where $\hat{\mathbf{n}}$ is the unit vector normal to the field.

The second term in Eq.(B.2b) can be identified as the portion of the gradient parallel to the magnetic field, and therefore cancels that part from the “magnetic pressure”.

We are left with only components perpendicular to the field

$$F_{\text{mag}} = \frac{B^2}{4\pi R_c} \hat{\mathbf{n}} - \nabla_{\perp} \left(\frac{B^2}{8\pi} \right). \quad (\text{B.4})$$

Therefore, while there is support perpendicular to the field (that in the subcritical case can only be overcome with the help of ambipolar diffusion), there is none in parallel direction. Figure (B.1), reproduced from Fiedler and Mouschovias (1993), demonstrates that indeed a flattened structure.

This flattening – possibly further aggravated by the effect of rotation if the rotation axis is aligned with the direction of the mean magnetic field – justifies the use of the *thin disk approximation* for the phase after this dynamical flattening has concluded. The applicability condition is that radial variations in any quantity remain smaller than the local vertical height of the disk (see Ciolek and Mouschovias, 1993):

$$\frac{f(r)}{|\partial f / \partial r|} \geq Z(r). \quad (\text{B.5})$$

While this condition is violated in our simulations near extremely strong gradients, such as the accretion discontinuity at the edge of the first core, it remains satisfied over the vast majority of the simulation domain (see Figs. B.2 and B.3).

B.2 Continuity equation in the thin-disk approximation

The continuity equation for a single fluid of mass volume density ϱ is given by

$$\frac{\partial \varrho}{\partial t} + \nabla \cdot (\varrho \mathbf{v}) = 0 \quad (\text{B.6})$$

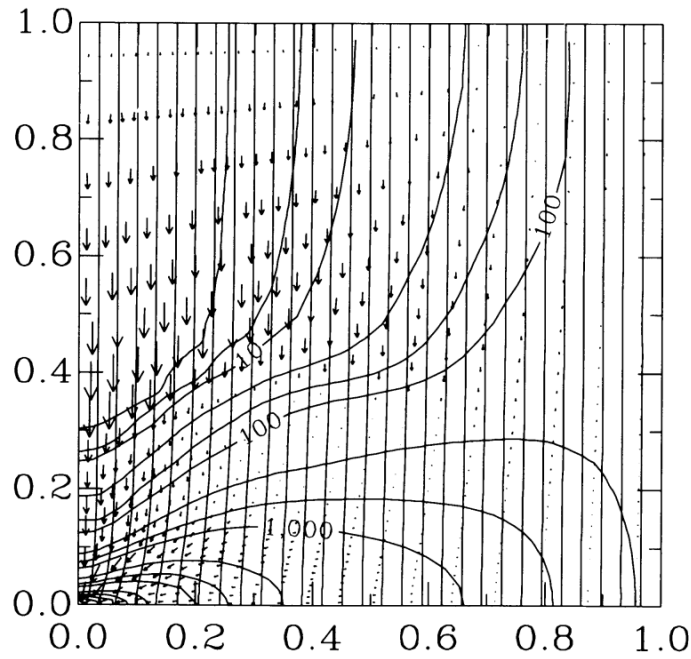


Figure B.1: Flattening of a core along the field lines before radial collapse occurs. In this figure from Fiedler and Mouschovias (1993), the x-axis is r/R , and the y-axis z/R , where R is the total size of the core.

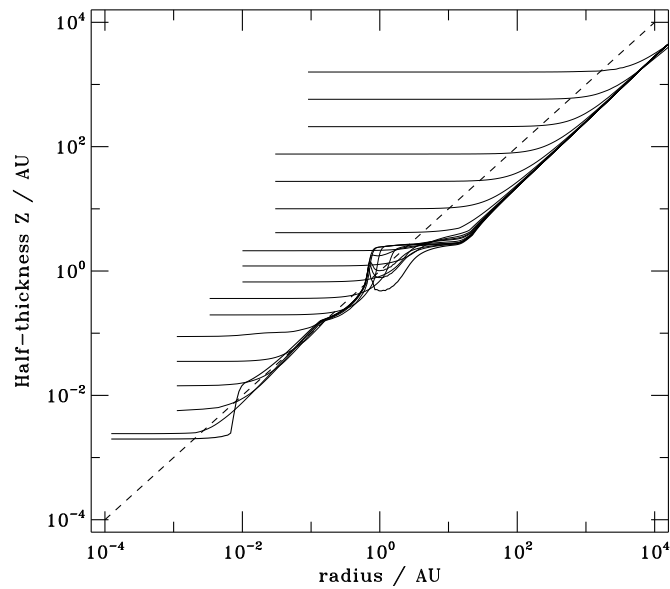


Figure B.2: Evolution of the half-thickness $Z(r)/r$ versus radius over time. The thin lines are plots at the times listed in Table 5.2, for a grain radius of $a_{\text{gr}} = 0.038 \mu\text{m}$.

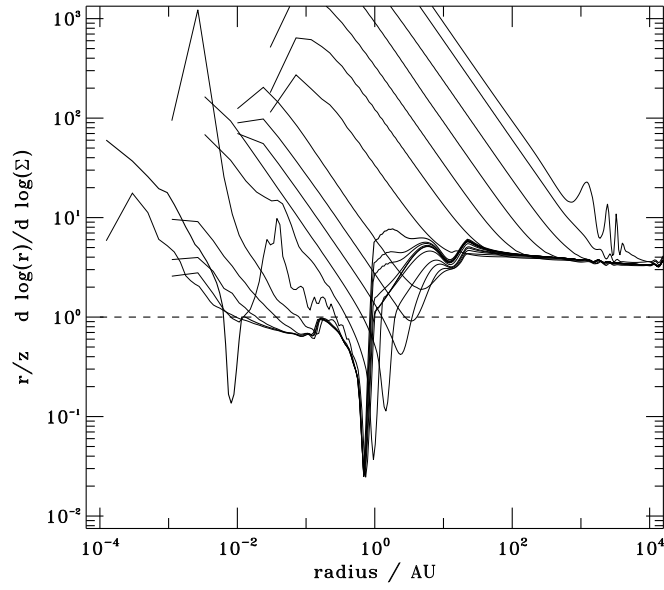


Figure B.3: Evolution of the thin-disk condition for the column density, $\frac{\Sigma(r)}{|\partial\Sigma/\partial r|} Z^{-1}$ (see Eq.(B.5)) plotted versus radius over time. It is satisfied in the outer regions and (nearly) within the first core, but is violated at the interfaces of first and second cores, as expected from the dramatic gradients prevalent there. The thin lines are plots at the times listed in Table 5.2, for a grain radius of $a_{\text{gr}} = 0.038 \mu\text{m}$.

where \mathbf{v} is the bulk fluid velocity. We now want to find a corresponding equation in the thin-disk geometry. To achieve this, we integrate Eq.(B.6) over the (time-dependent, and spatially-varying) thickness of the disk to find

$$\int_{-Z}^{+Z} \frac{\partial \varrho}{\partial t} dz + \int_{-Z}^{+Z} \frac{\partial}{\partial x} (\varrho v_x) dz + \int_{-Z}^{+Z} \frac{\partial}{\partial y} (\varrho v_y) dz + \int_{-Z}^{+Z} \frac{\partial}{\partial z} (\varrho v_z) dz = 0 \quad (\text{B.7})$$

where $Z(x, y, t)$ is the half-thickness. For convenience, we have adapted a Cartesian coordinate system, but any other would do, as well. Later, we will switch to a cylindrical coordinate system.

Leibniz' rule for differentiation under the integral sign states

$$\frac{\partial}{\partial s} \int_{Z_1(s)}^{Z_2(s)} F dz = \int_{Z_1(s)}^{Z_2(s)} \frac{\partial F}{\partial s} dz + F(Z_2, s) \frac{\partial Z_2}{\partial s} - F(Z_1, s) \frac{\partial Z_1}{\partial s}.$$

In our case, $F \equiv \varrho$, $s \equiv t$, $Z_2(s) \equiv Z(t)$, and $Z_1(s) \equiv -Z(t)$. We want to transform the first term on the RHS into the one on the LHS. We find

$$\int_{-Z}^{+Z} \frac{\partial \varrho}{\partial t} dz = \frac{\partial}{\partial t} \int_{-Z}^{+Z} \varrho dz - \varrho(x, y, z = +Z) \frac{\partial Z}{\partial t} - \varrho(x, y, z = -Z) \frac{\partial Z}{\partial t} \quad (\text{B.8a})$$

$$= \frac{\partial \Sigma}{\partial t} - 2\varrho(x, y) \frac{\partial Z}{\partial t} \quad (\text{B.8b})$$

where we have used the definition $\int_{-Z}^{+Z} \varrho dz = \Sigma(x, y)$. Further, the *one-zone approximation* tells us that $\Sigma(x, y) \equiv 2\varrho(x, y) Z(x, y)$, i.e., $\varrho \neq \varrho(z)$. In fact, we assume *all* quantities to be constant in the zone with half-thickness $Z(r)$. Therefore we can replace the integration along z over any function f by

$$\int_{-Z(r)}^{+Z(r)} f(r, z) dz \approx 2f(r) Z(r)$$

and use this as the equatorial value of f in the disk.

Similarly assuming $v_x \neq v_x(z)$ and $v_y \neq v_y(z)$ we get for the next two terms

$$\int_{-Z}^{+Z} \frac{\partial}{\partial x} (\varrho v_x) dz = \frac{\partial}{\partial x} (\Sigma v_x) - 2\varrho(x, y) v_x(x, y) \frac{\partial Z}{\partial x} \quad (\text{B.8c})$$

$$\int_{-Z}^{+Z} \frac{\partial}{\partial y} (\varrho v_y) dz = \frac{\partial}{\partial y} (\Sigma v_y) - 2\varrho(x, y) v_y(x, y) \frac{\partial Z}{\partial y} \quad (\text{B.8d})$$

The last term of Eq.(B.7) can be integrated directly:

$$\int_{-Z}^{+Z} \frac{\partial}{\partial z} (\varrho v_z) dz = 2\varrho v_z \quad (\text{B.8e})$$

since $v_z(z) = -v_z(-z)$ by symmetry. Combining the above results, we find

$$\frac{\partial \Sigma}{\partial t} + \frac{\partial}{\partial x} (\Sigma v_x) + \frac{\partial}{\partial y} (\Sigma v_y) + 2\varrho \left[v_z - \frac{\partial Z}{\partial t} - v_x \frac{\partial Z}{\partial x} - v_y \frac{\partial Z}{\partial y} \right] = 0$$

The last three terms comprise the two-dimensional hydrodynamic derivative

$$\frac{D}{Dt} Z(x, y) = \frac{\partial Z}{\partial t} + v_x \frac{\partial Z}{\partial x} + v_y \frac{\partial Z}{\partial y}$$

and since $v_z \equiv \frac{DZ}{Dt}$ by definition, the term in square brackets vanishes. We arrive at

$$\frac{\partial \Sigma}{\partial t} + \frac{\partial}{\partial x} (\Sigma v_x) + \frac{\partial}{\partial y} (\Sigma v_y) = 0 \quad (\text{B.9a})$$

$$\frac{\partial \Sigma}{\partial t} + \frac{1}{r} \frac{\partial}{\partial r} (r \Sigma v_r) + \frac{1}{r} \frac{\partial}{\partial \varphi} (\Sigma v_\varphi) = 0 \quad (\text{B.9b})$$

which is a continuity equation in two dimensions with the column density $\Sigma(x, y)$ as the dependent variable. Eq.(B.9b) casts this in cylindrical coordinates, assuming the disk to be situated in the $x - y$ plane.

B.3 Equations of motion

The three-dimensional equations of motion for an inviscid fluid of density ϱ , acted upon external forces \mathbf{F} , and with internal pressure P are given by

$$\frac{\partial (\varrho \mathbf{v})}{\partial t} + \nabla \cdot [\varrho (\mathbf{v} \otimes \mathbf{v})] = \frac{\varrho}{m} \mathbf{F} - \nabla P \quad (\text{B.10})$$

where \mathbf{v} is the systematic fluid velocity and \otimes denotes the outer (dyadic) product. We now want to find the corresponding equations for the thin-disk geometry.

First, we split the equation into its three components. We note that the velocity in cylindrical coordinates is $\mathbf{v} \equiv v_r \hat{\mathbf{r}} + v_\varphi \hat{\boldsymbol{\varphi}} + v_z \hat{\mathbf{z}}$. Also, $\varrho (\mathbf{v} \otimes \mathbf{v})$ is a 2-tensor, whose

divergence is given by Morse and Feshbach (1953)

$$\left(\nabla \cdot \overleftarrow{\mathbf{T}}\right)_{\hat{\mathbf{r}}} = \frac{1}{r} \frac{\partial}{\partial r} (rT_{rr}) + \frac{1}{r} \frac{\partial}{\partial \varphi} (T_{\varphi r}) + \frac{\partial}{\partial z} (T_{zr}) - \frac{T_{\varphi\varphi}}{r}, \quad (\text{B.11a})$$

$$\left(\nabla \cdot \overleftarrow{\mathbf{T}}\right)_{\hat{\varphi}} = \frac{1}{r} \frac{\partial}{\partial r} (rT_{r\varphi}) + \frac{1}{r} \frac{\partial}{\partial \varphi} (T_{\varphi\varphi}) + \frac{\partial}{\partial z} (T_{z\varphi}) - \frac{T_{\varphi r}}{r}, \quad (\text{B.11b})$$

$$\left(\nabla \cdot \overleftarrow{\mathbf{T}}\right)_{\hat{\mathbf{z}}} = \frac{1}{r} \frac{\partial}{\partial r} (rT_{rz}) + \frac{1}{r} \frac{\partial}{\partial \varphi} (T_{\varphi z}) + \frac{\partial}{\partial z} (T_{zz}). \quad (\text{B.11c})$$

The extra terms in the $\hat{\mathbf{r}}$ and $\hat{\varphi}$ -components stem from the Christoffel symbols appearing when differentiating curvilinear coordinate systems. With

$$\varrho(\mathbf{v} \otimes \mathbf{v}) = \varrho \begin{pmatrix} v_r v_r & v_r v_\varphi & v_r v_z \\ v_\varphi v_r & v_\varphi v_\varphi & v_\varphi v_z \\ v_z v_r & v_z v_\varphi & v_z v_z \end{pmatrix} \quad (\text{B.12})$$

we find

$$[\nabla \cdot \varrho(\mathbf{v} \otimes \mathbf{v})]_{\hat{\mathbf{r}}} = \frac{1}{r} \frac{\partial}{\partial r} (r\varrho v_r v_r) + \frac{1}{r} \frac{\partial}{\partial \varphi} (\varrho v_r v_\varphi) + \frac{\partial}{\partial z} (\varrho v_r v_z) - \varrho \frac{v_\varphi^2}{r}, \quad (\text{B.13a})$$

$$[\nabla \cdot \varrho(\mathbf{v} \otimes \mathbf{v})]_{\hat{\varphi}} = \frac{1}{r} \frac{\partial}{\partial r} (r\varrho v_\varphi v_r) + \frac{1}{r} \frac{\partial}{\partial \varphi} (\varrho v_\varphi v_\varphi) + \frac{\partial}{\partial z} (\varrho v_\varphi v_z) + \varrho \frac{v_r v_\varphi}{r}, \quad (\text{B.13b})$$

$$[\nabla \cdot \varrho(\mathbf{v} \otimes \mathbf{v})]_{\hat{\mathbf{z}}} = \frac{1}{r} \frac{\partial}{\partial r} (r\varrho v_z v_r) + \frac{1}{r} \frac{\partial}{\partial \varphi} (\varrho v_z v_\varphi) + \frac{\partial}{\partial z} (\varrho v_z v_z). \quad (\text{B.13c})$$

The momentum equations then become

$$\frac{\partial}{\partial t} (\varrho v_r) + \frac{1}{r} \frac{\partial}{\partial r} (r\varrho v_r v_r) + \frac{1}{r} \frac{\partial}{\partial \varphi} (\varrho v_r v_\varphi) + \frac{\partial}{\partial z} (\varrho v_r v_z) - \varrho \frac{v_\varphi^2}{r} = \frac{\varrho}{m} F_r - \frac{\partial P}{\partial r}, \quad (\text{B.14a})$$

$$\frac{\partial}{\partial t} (\varrho v_\varphi) + \frac{1}{r} \frac{\partial}{\partial r} (r\varrho v_\varphi v_r) + \frac{1}{r} \frac{\partial}{\partial \varphi} (\varrho v_\varphi v_\varphi) + \frac{\partial}{\partial z} (\varrho v_\varphi v_z) + \varrho \frac{v_r v_\varphi}{r} = \frac{\varrho}{m} F_\varphi - \frac{1}{r} \frac{\partial P}{\partial \varphi}, \quad (\text{B.14b})$$

$$\frac{\partial}{\partial t} (\varrho v_z) + \frac{1}{r} \frac{\partial}{\partial r} (r\varrho v_z v_r) + \frac{1}{r} \frac{\partial}{\partial \varphi} (\varrho v_z v_\varphi) + \frac{\partial}{\partial z} (\varrho v_z v_z) = \frac{\varrho}{m} F_z - \frac{\partial P}{\partial z}. \quad (\text{B.14c})$$

We now integrate Eqns.(B.14) over z , component-by-component. The vertical component of the momentum equation does not apply in our geometry, so we discard this entirely.

B.3.1 Radial momentum equation in the thin disk model

Next, we consider the radial component. For now, we ignore the RHS, as these terms are treated separately.

$$\begin{aligned} \int_{-Z}^{+Z} \left[\frac{\partial}{\partial t} (\varrho v_r) + \frac{1}{r} \frac{\partial}{\partial r} (r \varrho v_r v_r) + \frac{1}{r} \frac{\partial}{\partial \phi} (\varrho v_r v_\phi) \right] dz + \frac{\partial}{\partial z} (\varrho v_r v_z) dz - \varrho \frac{v_\phi^2}{r} dz \\ = \int_{-Z}^{+Z} \frac{\varrho}{m} F_r dz - \int_{-Z}^{+Z} \frac{\partial P}{\partial r} dz \end{aligned} \quad (\text{B.15})$$

We investigate each term in turn. As with the continuity equation (see Section B.2), Leibniz' rule is used

$$\begin{aligned} \int_{-Z}^{+Z} \frac{\partial}{\partial t} (\varrho v_r) dz &= \frac{\partial}{\partial t} \int_{-Z}^{+Z} (\varrho v_r) dz - \varrho v_r|_{z=+Z} \frac{\partial Z}{\partial t} - \varrho v_r|_{z=-Z} \frac{\partial Z}{\partial t} \\ &= \frac{\partial (\Sigma v_r)}{\partial t} - 2 \varrho v_r \frac{\partial Z}{\partial t} \end{aligned} \quad (\text{B.16})$$

where we have used $\int_{-Z}^{+Z} \varrho dz = \Sigma(x, y)$ and $v_r = v_r(r, \phi)$, i.e. independence of z . We treat the other terms similarly, and find

$$\int_{-Z}^{+Z} \frac{1}{r} \frac{\partial}{\partial r} (r \varrho v_r v_r) dz = \frac{1}{r} \frac{\partial}{\partial r} (r \Sigma v_r v_r) - 2 \varrho v_r v_r \frac{1}{r} \frac{\partial (rZ)}{\partial r}, \quad (\text{B.17a})$$

$$\int_{-Z}^{+Z} \frac{1}{r} \frac{\partial}{\partial \phi} (\varrho v_r v_\phi) dz = \frac{1}{r} \frac{\partial}{\partial \phi} (\Sigma v_r v_\phi) - 2 \varrho v_r v_\phi \frac{1}{r} \frac{\partial Z}{\partial \phi}, \quad (\text{B.17b})$$

$$\int_{-Z}^{+Z} \frac{\partial}{\partial z} (\varrho v_r v_z) dz = [\varrho v_r v_z]_{-Z}^{+Z} = 2 \varrho v_r v_z, \quad (\text{B.17c})$$

$$- \int_{-Z}^{+Z} \varrho \frac{v_\phi^2}{r} dz = - \Sigma \frac{v_\phi^2}{r}. \quad (\text{B.17d})$$

We have used the symmetry conditions $v_z(z) = -v_z(-z)$ in the third term, and pulled v_ϕ^2/r from the integral in the last term, since it does not depend on z in the vertical one-zone approximation. Equation (B.15) becomes

$$\begin{aligned} \frac{\partial (\Sigma v_r)}{\partial t} + \frac{1}{r} \frac{\partial}{\partial r} (r \Sigma v_r v_r) + \frac{1}{r} \frac{\partial}{\partial \phi} (\Sigma v_r v_\phi) - \Sigma \frac{v_\phi^2}{r} \\ + 2 \varrho v_r \left[v_z - \frac{\partial Z}{\partial t} - v_r \frac{1}{r} \frac{\partial (rZ)}{\partial r} - v_\phi \frac{1}{r} \frac{\partial Z}{\partial \phi} \right] \\ = \int_{-Z}^{+Z} \frac{\varrho}{m} F_r dz - \int_{-Z}^{+Z} \frac{\partial P}{\partial r} dz \end{aligned} \quad (\text{B.18})$$

As before in the derivation of the continuity equation, the last three terms are the two-dimensional hydrodynamic derivative, just this time in planar polar coordinates.

$$\frac{D}{Dt}Z(r, \varphi) = \frac{\partial Z}{\partial t} + v_r \frac{1}{r} \frac{\partial (rZ)}{\partial r} + v_\varphi \frac{1}{r} \frac{\partial Z}{\partial \varphi} \quad (\text{B.19})$$

and since $v_z \equiv DZ/Dt$ by definition, the term in square brackets vanishes. We end up with

$$\begin{aligned} \frac{\partial (\Sigma v_r)}{\partial t} + \frac{1}{r} \frac{\partial}{\partial r} (r \Sigma v_r v_r) + \frac{1}{r} \frac{\partial}{\partial \varphi} (\Sigma v_r v_\varphi) - \Sigma \frac{v_\varphi^2}{r} \\ = \int_{-Z}^{+Z} \frac{\rho}{m} F_r dz - \int_{-Z}^{+Z} \frac{\partial P}{\partial r} dz \end{aligned} \quad (\text{B.20})$$

In our axisymmetric thin disk there is no dependence on φ , and the term $\propto \partial/\partial\varphi$ vanishes, leaving us with

$$\frac{\partial (\Sigma v_r)}{\partial t} + \frac{1}{r} \frac{\partial}{\partial r} (r \Sigma v_r v_r) - \Sigma \frac{v_\varphi^2}{r} = \int_{-Z}^{+Z} \frac{\rho}{m} F_r dz - \int_{-Z}^{+Z} \frac{\partial P}{\partial r} dz \quad (\text{B.21})$$

The last term on the LHS can readily be identified with the centrifugal force $L^2/\Sigma r^3$, where $L = \Sigma v_\varphi r$, and we have arrived at the complete *radial momentum equation* for our thin disk. The force due to the pressure gradient is derived in the next section, and the external radial forces due to gravity and the magnetic field are discussed in subsequent sections. Its implementation into the code is discussed in Section C.2.4.

B.3.2 Angular momentum equation in the thin disk model

This procedure is repeated with the φ component. There is no pressure gradient in $\hat{\varphi}$ -direction, as the pressure is azimuthally uniform in an axisymmetric disk, and the only term remaining on the RHS is any azimuthal force. We get

$$\begin{aligned} \int_{-Z}^{+Z} \left[\frac{\partial}{\partial t} (\rho v_\varphi) + \frac{1}{r} \frac{\partial}{\partial r} (r \rho v_\varphi v_r) + \frac{1}{r} \frac{\partial}{\partial \varphi} (r \rho v_\varphi v_\varphi) + \frac{\partial}{\partial z} (r \rho v_\varphi v_z) + \rho \frac{v_r v_\varphi}{r} \right] dz \\ = \int_{-Z}^{+Z} \frac{\rho}{m} F_\varphi dz \end{aligned} \quad (\text{B.22})$$

Carrying out the same steps as before yields

$$\frac{\partial (\Sigma v_\varphi)}{\partial t} + \frac{1}{r} \frac{\partial}{\partial r} (r \Sigma v_\varphi v_r) + \Sigma \frac{v_r v_\varphi}{r} = \int_{-Z}^{+Z} \frac{\rho}{m} F_\varphi dz. \quad (\text{B.23})$$

The latter two terms on the LHS can be combined into one, namely

$$\frac{1}{r^2} \frac{\partial}{\partial r} (r^2 \Sigma v_\varphi v_r) = \frac{1}{r} \frac{\partial}{\partial r} (r \Sigma v_\varphi v_r) + \frac{\Sigma v_\varphi v_r}{r}. \quad (\text{B.24})$$

We multiply the whole equation by r , and define $L = \Sigma \Omega r^2 \equiv \Sigma v_\varphi r$, the angular momentum per unit area. This results in the *angular momentum equation* for our thin disk

$$\frac{\partial L}{\partial t} + \frac{1}{r} \frac{\partial}{\partial r} (r L v_r) = r \int_{-Z}^{+Z} \frac{\rho}{m} F_\varphi dz, \quad (\text{B.25})$$

where we have used that $\partial r / \partial t \equiv 0$. The RHS can be identified with the torque due to magnetic braking

$$r \int_{-Z}^{+Z} \frac{\rho}{m} F_\varphi dz = 2\pi r B_{z,\text{eq}} B_\varphi, \quad (\text{B.26})$$

which is discussed in detail in Section 5.3. The implementation of the angular momentum equation into the code is discussed in Appendix B.

B.4 Forces in the momentum equation

The total force \mathbf{F} exerted on a fluid element is given by integrating its total stress tensor \mathcal{T} over its surface \mathcal{S} .

$$\begin{aligned} dF_i &= \mathcal{T}_{ij} d\mathcal{S}_j \\ \mathbf{F} &= \int \mathcal{T} d\mathcal{S} \end{aligned}$$

The total stress tensor (in absense of effects other than thermal pressure and magnetic forces) is given by combining the thermal pressure and the magnetic contributions

$$\mathcal{T} = - \left(P_n + \frac{B^2}{8\pi} \right) \mathbf{I} + \frac{\mathbf{B}\mathbf{B}}{4\pi}$$

where \mathbf{I} is the identity matrix, indicating that the magnetic pressure and the thermal pressure of the neutrals P_n are both isotropic (but see Section B.1 for a caveat on this).

B.4.1 Normal vector

For the following discussion we need an expression for the normal vector to the surface \mathcal{S} . Fig. B.4 explains the terms used. The quantity $dZ/ds \hat{\mathbf{s}}$ can be identified as the

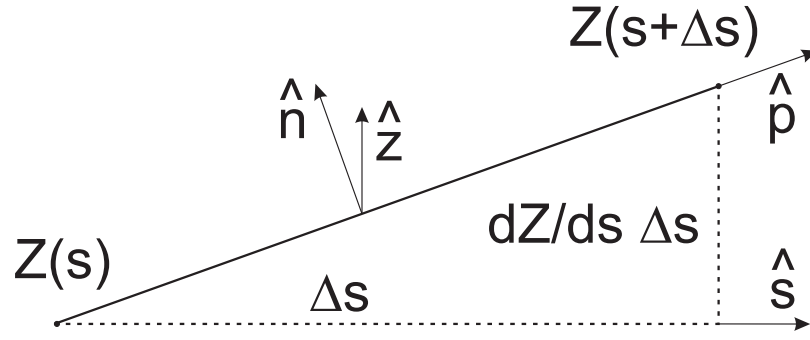


Figure B.4: Definitions for the normal vector.

gradient of the function Z in \hat{s} direction, such that

$$\frac{dZ}{ds} \hat{s} = \nabla_s Z.$$

The vectors $\hat{\mathbf{p}}$ and $\hat{\mathbf{n}}$, parallel and perpendicular to the surface \mathcal{S} , respectively, are given by

$$\begin{aligned} \hat{\mathbf{p}} &= \hat{\mathbf{s}} \Delta s + \frac{dZ}{ds} \Delta s \hat{\mathbf{z}}, \\ \hat{\mathbf{n}} &= \frac{\Delta s}{N} [\hat{\mathbf{z}} - \nabla_s Z]. \end{aligned}$$

Furthermore, the normalization constant N is

$$N = \Delta s \sqrt{1 + (dZ/ds)^2}.$$

Additionally, the surface element is (assuming a Cartesian coordinate system, for simplicity)

$$d\mathcal{S} = \hat{\mathbf{n}} dS = [\hat{\mathbf{z}} - \nabla_s Z] dx dy.$$

At the bottom of the disk, the expression for the normal vector is slightly different:

$$\begin{aligned} \hat{\mathbf{p}}_{\text{bottom}} &= \hat{\mathbf{s}} \Delta s - \frac{dZ}{ds} \Delta s \hat{\mathbf{z}}, \\ \hat{\mathbf{n}}_{\text{bottom}} &= [-\hat{\mathbf{z}} - \nabla_s Z]. \end{aligned}$$

We now have all expressions required to continue with the derivation of the pressure forces.

B.4.2 Thermal pressure

The integral over the contribution of the thermal pressure to the stress tensor is given by

$$\mathbf{F}_P = \int \mathcal{T}_P dS = - \int P \mathbf{I} dS$$

This has to be carried out over the whole surface of the fluid element, consisting of top and bottom surface, plus the circumfering area.

$$\mathbf{F}_P = \mathbf{F}_{P,\text{top}} + \mathbf{F}_{P,\text{bottom}} + \mathbf{F}_{P,\text{side}}$$

At top and bottom, the pressure is equal to the ambient external pressure P_{ext} . This yields

$$\begin{aligned} \mathbf{F}_{P,\text{top}} &= - \int \mathbf{I} P_{\text{ext}} \hat{\mathbf{n}}_{\text{top}} dS \\ &= -P_{\text{ext}} \int [\hat{\mathbf{z}} - \nabla_{\mathbf{s}} Z] dx dy. \\ \mathbf{F}_{P,\text{bottom}} &= -P_{\text{ext}} \int [-\hat{\mathbf{z}} - \nabla_{\mathbf{s}} Z] dx dy. \end{aligned}$$

The contribution of the circumfering area is given by

$$\begin{aligned} \mathbf{F}_{P,\text{side}} &= \oint dl \int_{-Z}^{+Z} \mathcal{T}_P \hat{\mathbf{n}}_{\text{side}} dz, \\ &= - \oint 2Z P_n \hat{\mathbf{n}}_{\text{side}} dl, \\ &= - \int \nabla_{\mathbf{s}} (2Z P_n) dx dy. \end{aligned}$$

where the one-zone approximation was used in the middle step, and Stoke's theorem in the last. Collecting the three contributions and cancelling the terms proportional to Z , we arrive at

$$\mathbf{F}_P = \int -\nabla_{\mathbf{s}} (2Z P_n - 2Z P_{\text{ext}}) dx dy, \quad (\text{B.27a})$$

$$f_{\text{pressure}} = -\nabla_{\mathbf{s}} (2Z P_n - 2Z P_{\text{ext}}). \quad (\text{B.27b})$$

The latter is the expression of the force per unit area due thermal and external pressure gradients. It can be calculated once Z and P_n are known (see Section C.2.3).

B.4.3 Magnetic Force

In order to derive the expression for the magnetic field in the thin-disk approximation, we use the following assumptions (see Ciolek and Mouschovias, 1993):

$$\mathbf{B}(x, y, z, t) = \begin{cases} \widehat{\mathbf{z}}B_{z,\text{eq}}(x, y, t), & |z| \leq Z(x, y, t), \\ \widehat{\mathbf{z}}B_{z,\mathcal{S}}(x, y, t) + \widehat{\mathbf{s}}B_s(x, y, z, t), & |z| > Z(x, y, t), \\ \widehat{\mathbf{z}}B_{\text{ref}}, & |z| \gg R. \end{cases} \quad (\text{B.28})$$

This means that the field inside the disk only points in $\widehat{\mathbf{z}}$ -direction. Above the disk, the magnetic field also has components in other directions, while far away from the disk, the deviation from the constant reference field is negligible. It points in $\widehat{\mathbf{z}}$ -direction again, i.e. perpendicular to the disk. Note that $B_{z,\mathcal{S}}(x, y, t) \neq B_{z,\text{eq}}(x, y, t)$ where the index \mathcal{S} means the value at the surface $z = \pm Z$ of the disk. It is not to be mistaken for the index s which denotes components parallel to the surface. This could be the (x, y) direction in Cartesian coordinates or (r, φ) in polar coordinates. In the following, x and y are used.

Furthermore, we apply the symmetry conditions that

$$B_z(x, y, z) = B_z(x, y, -z) \quad (\text{B.29a})$$

$$B_s(x, y, z) = -B_s(x, y, -z) \quad (\text{B.29b})$$

Using the fact that the normal component of the magnetic field at disk surface is continuous (given by integral form of Gauss' Law, Ampère's Law $\nabla \cdot \mathbf{B} = 0$, see Landau and Lifshitz, 1984), we find the conditions for both the upper and lower surface of the disk

$$\mathbf{B}\left(x, y, \lim_{|z| \rightarrow Z(r)^+} z\right) \widehat{\mathbf{n}} = \mathbf{B}\left(x, y, \lim_{|z| \rightarrow Z(r)^-} z\right) \widehat{\mathbf{n}} \quad (\text{B.30a})$$

$$B_{z,\mathcal{S}}(x, y, \pm Z) \mp B_s(x, y, \pm Z) \frac{dZ}{ds} = B_{z,\text{eq}}(x, y) \quad (\text{B.30b})$$

We can follow the same procedure as for the thermal pressure above,

$$\mathbf{F}_M = \int \mathcal{T}_M d\mathcal{S} = \int \left(\frac{\mathbf{B}\mathbf{B}}{4\pi} - \frac{B^2}{8\pi} \mathbf{I} \right) d\mathcal{S}.$$

Again, we treat top, bottom and circumfering area separately.

$$\begin{aligned}
\mathbf{F}_{M,\text{top}} &= \int \left(\frac{\mathbf{B}\mathbf{B}}{4\pi} - \frac{B^2}{8\pi} \mathbf{I} \right) [\hat{\mathbf{z}} - \nabla_s Z] dx dy, \\
&= \frac{1}{8\pi} \int \left[2B_{z,S}^2 \hat{\mathbf{z}} + 2B_{z,S} B_s \hat{\mathbf{s}} - B^2 \hat{\mathbf{z}} - 2 \left(B_s \frac{dZ}{ds} \right) (B_{z,S} \hat{\mathbf{z}} + B_s \hat{\mathbf{s}}) + B^2 \nabla_s Z \right] dx dy, \\
\mathbf{F}_{M,\text{bottom}} &= \int \left(\frac{\mathbf{B}\mathbf{B}}{4\pi} - \frac{B^2}{8\pi} \mathbf{I} \right) [-\hat{\mathbf{z}} - \nabla_s Z] dx dy, \\
&= \frac{1}{8\pi} \int \left[-2B_{z,S}^2 \hat{\mathbf{z}} + 2B_{z,S} B_s \hat{\mathbf{s}} + B^2 \hat{\mathbf{z}} + 2 \left(B_s \frac{dZ}{ds} \right) (B_{z,S} \hat{\mathbf{z}} - B_s \hat{\mathbf{s}}) + B^2 \nabla_s Z \right] dx dy.
\end{aligned}$$

In both cases, \mathbf{B} was written in terms of its components in $\hat{\mathbf{z}}$ and $\hat{\mathbf{s}}$ -direction.

The contribution of the circumfering area to the force again is a line integral, enclosing an integral over z ,

$$\begin{aligned}
\mathbf{F}_{M,\text{side}} &= \oint dl \int_{-Z}^{+Z} \left(\frac{\mathbf{B}\mathbf{B}}{4\pi} - \frac{B^2}{8\pi} \mathbf{I} \right) \hat{\mathbf{n}}_{\text{side}} dz, \\
&= -\frac{1}{8\pi} \oint dl \int_{-Z}^{+Z} B_{z,\text{eq}}^2 \hat{\mathbf{n}}_{\text{side}} dz, \\
&= -\frac{1}{8\pi} \int \nabla_s (2Z B_{z,\text{eq}}^2) dx dy,
\end{aligned}$$

where we applied that \mathbf{B} only points in $\hat{\mathbf{z}}$ -direction inside the disk. This leaves only one component to the tensor, namely $B_{z,\text{eq}}^2$. Furthermore, we used the one-zone approximation to integrate over z , and Stoke's theorem to transform the line integral.

Summing all three parts, we see that a number of terms cancels from top and bottom

$$\begin{aligned}
\mathbf{F}_M &= \mathbf{F}_{M,\text{top}} + \mathbf{F}_{M,\text{bottom}} + \mathbf{F}_{M,\text{side}} \\
&= \frac{1}{4\pi} \int \left[2B_{z,S} B_s \hat{\mathbf{s}} - 2 \left(B_s \frac{dZ}{ds} \right) B_s \hat{\mathbf{s}} + B^2 \nabla_s Z - \nabla_s Z B_{z,\text{eq}}^2 \right] dx dy. \quad (\text{B.31})
\end{aligned}$$

All terms are expressed in terms of quantities at the top of the disk, but we want to relate it back to the magnetic field in the disk. To this end, the continuity condition for the magnetic field, Eq.(B.30b), yields

$$B_{z,S} = B_{z,\text{eq}} + B_s \frac{dZ}{ds}. \quad (\text{B.32})$$

Using this to replace $B_{z,s}$ in the first term of Eq.(B.31), it simplifies to

$$\mathbf{F}_M = \frac{1}{4\pi} \int [2B_{z,\text{eq}}B_s\hat{\mathbf{s}} + B^2\nabla_s Z - \nabla_s Z B_{z,\text{eq}}^2] dx dy. \quad (\text{B.33})$$

Writing \mathbf{B} in terms of its two components, perpendicular and parallel, we find for its magnitude

$$\begin{aligned} B^2 &= B_{z,s}^2 + B_s^2, \\ &= \left(B_{z,\text{eq}} + B_s \frac{dZ}{ds} \right)^2 + B_s^2, \\ &= B_{z,\text{eq}}^2 + 2B_{z,\text{eq}}B_s \frac{dZ}{ds} + \left(B_s \frac{dZ}{ds} \right)^2 + B_s^2. \end{aligned}$$

Also, the gradient $\nabla_s Z B_{z,\text{eq}}^2$ can be expanded so that Eq.(B.33) becomes

$$\begin{aligned} \mathbf{F}_M &= \frac{1}{4\pi} \int [2B_{z,\text{eq}}B_s\hat{\mathbf{s}} + B^2\nabla_s Z - \nabla_s Z B_{z,\text{eq}}^2] dx dy \\ &= \frac{1}{4\pi} \int \left[2B_{z,\text{eq}}B_s\hat{\mathbf{s}} - Z\nabla_s B_{z,\text{eq}}^2 + \left\{ 2B_{z,\text{eq}}B_s \frac{dZ}{ds} + \left(B_s \frac{dZ}{ds} \right)^2 + B_s^2 \right\} \nabla_s Z \right] dx dy. \end{aligned}$$

Finally, we drop all terms where derivatives of Z appear in higher than first order. Those are but small corrections to the big picture, and we would have to do a higher-order approach in Eq.(B.30b) if we wanted to self-consistently retain them. Further, we switch to cylindrical coordinates, and replace $dx dy = r dr d\varphi$. We subsequently drop all dependences on φ , and take the vector $\hat{\mathbf{s}}$ and its associated gradient ∇_s as pointing in $\hat{\mathbf{r}}$ -direction only. Then we arrive at the expression for the radial force per unit area

$$f_{M,r} = \frac{B_{z,\text{eq}}}{2\pi} \left(B_{r,Z} - Z \frac{\partial}{\partial r} B_{z,\text{eq}} \right) + \frac{1}{4\pi} \frac{dZ}{dr} (B_{r,Z}^2 + B_{\varphi,Z}^2) \quad (\text{B.34})$$

The last term represents the effect that vertical squeezing has on the disk's top and bottom surfaces, them being not perfectly flat but having radial variations. This adds a force in radial direction.

B.4.4 Gravity

We use an integral solver with scaling $\mathcal{O}(n^2)$ (where n is the number of grid cells) to calculate the gravitational force. It is derived in considerable detail in Morton et al. (1994). Here we only present the derivation in broad strokes.

We start with *Poisson's equation* for the gravitational potential Ψ :

$$\nabla^2 \Psi = 4\pi G \rho, \quad (\text{B.35a})$$

$$\frac{1}{r} \frac{\partial}{\partial r} \left(r \frac{\partial}{\partial r} \Psi(r, z) \right) = 4\pi G \Sigma(r) \delta(z), \quad (\text{B.35b})$$

where ρ and Σ are the mass volume and column density, respectively. Equation (B.35b) is Eq.(B.35a) expressed for an axisymmetric infinitely-thin disk. Toomre (1963) studied this equation for flattened galactic disks, and gives its solution for an infinite disk as:

$$\Psi(r, z) = -2\pi G \int_0^\infty dk \int_0^\infty dr' r' \Sigma(r') e^{-k|z|} J_0(kr) J_0(kr'). \quad (\text{B.36})$$

J_0 is the *Bessel functions of the first kind*. This allows us to write for the radial gravitational field

$$g_r(r) = 2\pi G \int_0^\infty dr' r' \Sigma(r') \mathcal{M}(r, r'), \quad (\text{B.37a})$$

$$\mathcal{M}(r, r') = \frac{d}{dr} \int_0^\infty dk J_0(kr) J_0(kr') \quad (\text{B.37b})$$

$$= \frac{2}{\pi} \frac{d}{dr} \frac{1}{r_{>}} K \left(\frac{r_{<}}{r_{>}} \right). \quad (\text{B.37c})$$

Here, $\mathcal{M}(r, r')$ is an integral kernel, and K is the *Complete Elliptic Integral of the first kind*. The identity leading from Eq.(B.37b) to Eq.(B.37c) is found in Gradshteyn et al. (2007, §6.512.1, p. 660). The symbols $r_{<}$ and $r_{>}$ denote the smaller and larger of r and r' , respectively. The implementation of the gravitational acceleration into the code is found in Section C.3.

B.5 Induction equation

Section 5.4 contains a complete discussion of the induction equation and the treatment of non-ideal MHD within. The induction equation as such is not modified by the chosen geometry, because the magnetic field is inherently three-dimensional. However, our choice of magnetic field only pointing in $\hat{\mathbf{z}}$ -direction (see Section B.4.3) mandates that only the z -component of the induction equation is non-zero. Here, we only quote the result

$$\frac{\partial B_{z,\text{eq}}}{\partial t} + \frac{1}{r} \frac{\partial}{\partial r} (r B_{z,\text{eq}} v_r) = \frac{1}{r} \frac{\partial}{\partial r} \left(r \eta_{\text{eff}} \frac{\partial B_{z,\text{eq}}}{\partial r} \right) \quad (\text{B.38})$$

where η_{eff} is the effective resistivity coefficient, and contains the effects of both Ohmic dissipation and ambipolar diffusion (see Section 5.4).

B.6 Radial magnetic field component $B_{r,Z}$

In the previous section, we saw the evolution equation for the (purely vertical) magnetic field $B_{z,\text{eq}}$ within the disk. Furthermore, Eq.(C.531) details its calculation from the evolution array. Similarly, Section 5.3 on magnetic braking contained the derivation of the azimuthal field component $B_{\varphi,Z}$ from the magnetic flux Φ and the angular velocity Ω . This section now completes the derivation of the magnetic field by presenting the corresponding derivation for the radial magnetic field component at the top and bottom surface of the disk, $B_{r,Z}$. This discussion follows the ones in Ciolek and Mouschovias (1993); Basu and Mouschovias (1994).

The magnetic field above and below the disk can be written as a linear combination of the background field and a modification

$$\mathbf{B}(r, z > Z) = \mathbf{B}'(r, z) + B_{\text{ref}} \hat{\mathbf{z}}. \quad (\text{B.39})$$

The boundary condition expressed in Eq.(B.28) for $z \gg Z$ implies that the modification has to vanish for $z \rightarrow \infty$.

We assume the absence of any large-scale electric field, and require that the matter above (and below) the disk is force-free (by requiring an instantaneous adjustment to the constant external pressure P_{ext} , see, e.g., Mouschovias, 1976), and also current-free. Then, Maxwell's equations yield

$$\nabla \times \mathbf{B} = 0 \quad (\text{B.40})$$

$$\quad (\text{B.41})$$

The curl-free property implies the existence of a scalar potential Θ for the magnetic field above the disk, with $\mathbf{B}'(r, z) = -\nabla\Theta$. Together with the assumption of an infinitely-thin axisymmetric disk, this allows to rewrite the continuity condition expressed in Eq.(B.30b) at the top surface of the disk as

$$\lim_{Z \rightarrow 0} \frac{\partial\Theta(r, z)}{\partial z} = -[B_{z,\text{eq}}(r) - B_{\text{ref}}]. \quad (\text{B.42})$$

This is equivalent to the Poisson equation

$$\nabla^2 \Theta(r, z) = - [B_{z,\text{eq}}(r) - B_{\text{ref}}] \delta(z), \quad (\text{B.43})$$

which happens to be exactly the same form as the one for the gravitational field, and whose solution we already know. It is

$$B_{r,z}(r) = - \int_0^\infty dr' r' [B_{z,\text{eq}}(r') - B_{\text{ref}}] \mathcal{M}(r, r'), \quad (\text{B.44a})$$

$$\mathcal{M}(r, r') = \frac{2}{\pi} \frac{d}{dr} \frac{1}{r_>} K \left(\frac{r_<}{r_>} \right). \quad (\text{B.44b})$$

As before, K is the Complete Elliptic Integral of the First Kind. The symbols $r_<$ and $r_>$ denote the smaller and larger of r and r' , respectively.

Bibliography

- Basu, S. and Mouschovias, T. C.: 1994, *ApJ* **432**, 720
- Ciolek, G. E. and Mouschovias, T. C.: 1993, *ApJ* **418**, 774
- Fiedler, R. A. and Mouschovias, T. C.: 1992, *ApJ* **391**, 199
- Fiedler, R. A. and Mouschovias, T. C.: 1993, *ApJ* **415**, 680
- Gradshteyn, I. S., Ryzhik, I. M., Jeffrey, A., and Zwillinger, D.: 2007, *Table of Integrals, Series, and Products*, Academic Press; 7 edition (March 9, 2007)
- Landau, L. D. and Lifshitz, E. M.: 1984, *Electrodynamics of Continuous Media*, Pergamon, New York
- Morse, P. M. and Feshbach, H.: 1953, *Methods of Theoretical Physics*, McGraw-Hill, New York, NY, USA
- Morton, S. A., Mouschovias, T. C., and Ciolek, G. E.: 1994, *ApJ* **421**, 561
- Mouschovias, T. C.: 1976, *ApJ* **206**, 753
- Toomre, A.: 1963, *ApJ* **138**, 385

Appendix C

Implementation into the code

In order to implement our equations into our code, we have to recast them in terms of the conserved quantities in each cell, i.e. mass, momentum, angular momentum, and magnetic flux. This chapter details this.

C.1 Continuity equation and mass conservation

The continuity equation is given by

$$\frac{\partial \Sigma_n}{\partial t} = -\frac{1}{r} \frac{\partial}{\partial r} (r \Sigma_n v_r). \quad (\text{C.1})$$

However, we want an expression for the mass in each cell, not the column density. Therefore, we integrate over the cell (i.e., from r_{i-1} until r_i), to find

$$\int_{r_{i-1}}^{r_i} \frac{\partial \Sigma_n}{\partial t} r dr = - \int_{r_{i-1}}^{r_i} \frac{1}{r} \frac{\partial}{\partial r} (r \Sigma_n v_r) r dr. \quad (\text{C.2})$$

For clarity of presentation, we only kept the subscript i and $i-1$ of the expressions r_i and r_{i-1} , respectively. Because the integral boundaries do not change, the LHS is nothing but the time derivative of the mass in cell i . The RHS is an exact differential, and we can use Stokes' Law and integrate directly. We find for M_i , the mass in cell i

$$\frac{\partial M_i}{\partial t} = - [r \Sigma_n v_r]_{r_{i-1}}^i. \quad (\text{C.3})$$

Obviously, the new RHS is now a flux across the cell interfaces at r_{i-1} until r_i . This flux is calculated using the TVD method due to van Leer (1977).

C.2 Momentum equation

C.2.1 Barotropic energy equation

We adopt a piece-wise barotropic equation as our energy equation. The barotropic index $\gamma \equiv C_P/C_V$ is the ratio between the specific heats for constant pressure and that for constant volume, describes how the pressure changes with density:

$$P = K \varrho^\gamma,$$

where K is a factor of proportionality. Together with an equation of state (the ideal gas law, in our case), this also sets the temperature and the internal energy. In the barotropic index γ , very complicated physical effects are hidden, involving radiative transfer, molecular and granular heating and cooling, and other phenomena. Using a barotropic pressure-density relation instead of a sophisticated energy equation tremendously simplifies the numerical complication by not having to follow the microphysics and radiative processes explicitly. We use the data obtained by Masunaga and Inutsuka (2000) in a detailed spherical radiation hydrodynamical simulation (solid line in Fig. C.1).

C.2.2 Stability

We seek to derive the barotropic index γ for which a cloud is stable against gravitational collapse, i.e., we want to know for which γ pressure scales the same way as gravity does. Several simplifying assumptions are used. First, the cloud is assumed to be spherical and of uniform density, governed by a barotropic pressure-density relation. The pressure gradient then becomes

$$\nabla_r P \approx P/r \propto \varrho^\gamma/r.$$

For hydrostatic equilibrium, the force density due to this pressure gradient has to balance gravity:

$$\begin{aligned} \nabla_r P &= \varrho g_r, \\ &= \varrho \frac{GM}{r^2}. \end{aligned}$$

We write r in terms of the enclosed mass M and the density, and obtain

$$\varrho^{\gamma+1/3} M^{-1/3} = \varrho^{5/3} GM^{1/3},$$

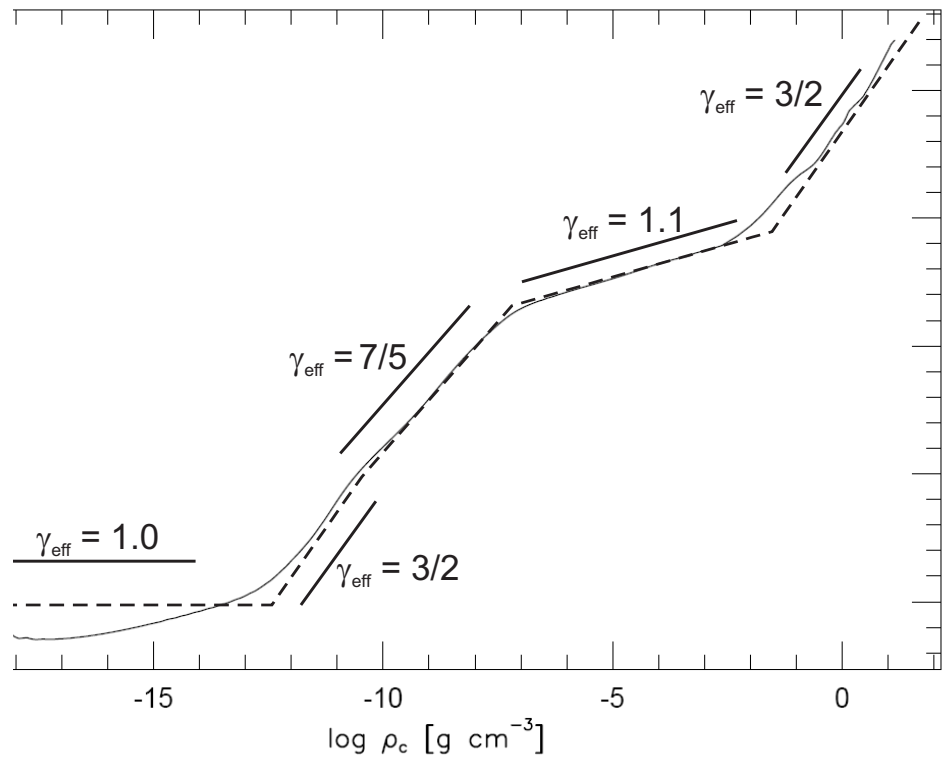


Figure C.1: Change of temperature with density. **Solid line:** data from Masunaga and Inutsuka (2000). **Dashed line:** our fit using γ_{eff}

from which one can immediately deduce that pressure scales the same way as or stronger than gravity if $\gamma \geq 4/3$, thus providing stability.

For a disk, we replace the density with the column density with the usual relation $\varrho = \Sigma/2Z$. If we make the assumption that the scaleheight Z is approximately constant in the region where the density behaves barotropically, the pressure force scales as

$$\nabla_r P \approx P/r \propto \varrho^\gamma/r \propto \Sigma^\gamma/r$$

Furthermore, we assume that gravity still scales inversely quadratic with radius, which is not too bad an oversimplification as long as the density behaves as a power law. Now, we have a different behaviour of the radius with the column density, namely

$$r \propto \Sigma^{-1/2} M^{1/2}$$

and we arrive at

$$\varrho^{\gamma+1/2} M^{-1/2} = \varrho^2 G M^{1/2}$$

to find stability if $\gamma \geq 3/2$. Of course this back-of-the-envelope calculation is extremely crude, but provides a rough guideline.

C.2.3 Implementation of the pressure force

In order to implement the pressure force into the momentum equation, we have to calculate the scale height for a given column density as discussed above. Scale height and column density are related by the volume density, hence we have to get a handle on that first. At any point in the simulation, we can calculate the neutral pressure according to

$$P_n = \frac{\pi}{2} G \Sigma_n^2 + P_{\text{ext}} + \frac{B_r^2}{8\pi} + \frac{B_\varphi^2}{8\pi}, \quad (\text{C.4a})$$

$$\tilde{P}_n = \frac{1}{4} \left[\tilde{\Sigma}_n^2 + \tilde{P}_{\text{ext}} + \tilde{B}_s^2 \right], \quad (\text{C.4b})$$

where Eq.(C.4b) is the normalized version of Eq.(C.4a) (for details on the normalization used, see Section C.7). We assume the equation of state to be that of an ideal gas. Then

$$P = \frac{\varrho k T}{\bar{m}} \quad (\text{C.5})$$

where T is the temperature, k is Boltzmann's constant and \bar{m} is the mean molecular mass of the gas. As numerical value for the latter we choose initially $\bar{m} = 2.3 m_H =$

3.84×10^{-24} g (assuming 90% hydrogen and 10% helium by number). However, this parameter is not constant during the second collapse. During hydrogen dissociation, it changes to $1.3 m_{\text{H}}$ (two helium atoms per 18 hydrogen atoms instead of per 9 H_2 molecules), and then finally to $0.6 m_{\text{H}}$ after the gas is fully ionized. m_{H} is the mass of a hydrogen atom. We assume this change occurs exponentially (such that the change is linear in logarithmic units) between ≈ 2000 K and ≈ 5000 K.

We use the ideal gas law to convert the temperature-density relation due to Masunaga and Inutsuka (2000) (see Fig. C.1) into a pressure-density relation. For any pressure, the corresponding density can then be simply looked up, fixing the temperature. Additionally, the scaleheight is given by

$$Z = \frac{\Sigma_{\text{n}}}{2\rho_{\text{n}}}. \quad (\text{C.6})$$

This approach has the great advantage that it is independent of the detailed energy equation adopted (i.e., what the exact value of γ is). It does not matter if conditions are isothermal or barotropic, as long as a pressure-density relation is given. The mid-plan pressure is a calculable quantity in our code, by Eq.(C.4a), and will then determine ρ , T , and Z . However, this advantage comes at the price of computationally costly interpolation at every timestep.

Knowing both Σ_{n} and Z , we can now calculate the pressure force Eq.(B.27b), reproduced here for convenience

$$f_{\text{pressure}} = -\nabla_{\text{s}} (2ZP_{\text{n}} - 2ZP_{\text{ext}}). \quad (\text{C.7})$$

We insert neutral pressure of Eq.(C.4b) into this expression and calculate the force due to thermal and external pressure gradients. Note that this done sans the magnetic pressure term, because its radial effect is already considered in the magnetic force term. Its effect on the vertical hydrostatic equilibrium still enters through the scaleheight Z . This yields

$$f_{\text{pressure}} = -\frac{\partial}{\partial r} \left(\frac{Z}{2} \Sigma_{\text{n}}^2 \right). \quad (\text{C.8})$$

As we see, the external pressure also only enters through its effect on the scaleheight. As a last step, the pressure force (per unit area) is integrated over each cell to be applied to the momentum equation.

C.2.4 Implemented momentum equation

The overall momentum evolution equation Eq.(B.21) integrated over cell i reads

$$\int_{i-1}^i \frac{\partial(\Sigma v_r)}{\partial t} r dr = - \int_{i-1}^i \frac{1}{r} \frac{\partial}{\partial r} (\Sigma v_r v_r) r dr - \int_{i-1}^i f_{\text{press}} r dr + \int_{i-1}^i \Sigma g_r r dr + \int_{i-1}^i f_{\text{centr}} r dr + \int_{i-1}^i f_{\text{mag}} r dr, \quad (\text{C.9})$$

$$\begin{aligned} \frac{\partial P_i}{\partial t} = & - [r \Sigma v_r v_r]_{i-1}^i - \frac{\partial}{\partial r} \left(\frac{Z}{2} \Sigma_{n,i} \right) A_i + M_i g_{r,i} \\ & + M_i \Omega_i^2 r_i + \Phi_i \left(B_{r,i} - \frac{Z_i}{A_i} \frac{\partial \Phi_i}{\partial r} \right) + \frac{A_i}{2} \frac{\partial Z}{\partial r} (B_{r,i}^2 + B_{\varphi,i}^2). \end{aligned} \quad (\text{C.10})$$

Here, $P \equiv M v_r$ is the radial momentum and $A_i = \int_{i-1}^i r dr$ is the area of cell i ; the other symbols have their usual meanings (see List of Symbols).

C.3 Gravity

In Section B.4.4, we derived the gravitational field as calculated by Morton et al. (1994).

$$g_r(r) = 4G \int_0^r dr' r' \Sigma(r') \frac{d}{dr} \left[\frac{1}{r} K \left(\frac{r'}{r} \right) \right] + 4G \int_r^\infty dr' \Sigma(t, r') \frac{d}{dr} K \left(\frac{r}{r'} \right), \quad (\text{C.11a})$$

$$\begin{aligned} &= -4G \int_0^r \frac{dr' r'}{r^2} \Sigma(r') \left[\frac{E(k)}{1-k^2} \right]_{k=r'/r} \\ &+ 4G \int_r^\infty \frac{dr'}{r} \Sigma(r') \left[\frac{E(k)}{1-k^2} - K(k) \right]_{k=r/r'}, \end{aligned} \quad (\text{C.11b})$$

where $E(k)$ is the *Complete Elliptic Integral of the second kind*. This equation is then discretized, assuming the column density Σ to be constant in each cell. The remaining integrals are analytical, and the resulting expressions depend solely on r and r' . Between grid refinement steps, those are fixed. Thus, the gravitational field is a purely geometric factor calculated only once, and multiplied with Σ at every point, and summed to calculate the force.

$$g_r(\bar{r}_j) = 4G \sum_l \Sigma(\bar{r}_l) I^0(\bar{r}_j, r_l, r_{l-1}), \quad (\text{C.12a})$$

where

$$I^0(\bar{r}_j, r_l, r_{l-1}) = \begin{cases} K\left(\frac{r_{l-1}}{\bar{r}_j}\right) - E\left(\frac{r_{l-1}}{\bar{r}_j}\right) + E\left(\frac{r_l}{\bar{r}_j}\right) - K\left(\frac{r_l}{\bar{r}_j}\right) & \text{for } l < j, \\ K\left(\frac{r_{j-1}}{\bar{r}_j}\right) - E\left(\frac{r_{j-1}}{\bar{r}_j}\right) + \frac{r_j}{\bar{r}_j} \left[E\left(\frac{\bar{r}_j}{r_j}\right) - K\left(\frac{\bar{r}_j}{r_j}\right) \right] & \text{for } l = j, \\ \frac{r_{l-1}}{\bar{r}_j} \left[K\left(\frac{\bar{r}_j}{r_{l-1}}\right) - E\left(\frac{\bar{r}_j}{r_{l-1}}\right) \right] + \frac{r_l}{\bar{r}_j} \left[E\left(\frac{\bar{r}_j}{r_l}\right) - K\left(\frac{\bar{r}_j}{r_l}\right) \right] & \text{for } l > j. \end{cases}$$

We can efficiently approximate the Elliptic Integrals with a logarithmic-polynomial expansion provided in Abramowitz and Stegun (1965)

$$K(k) = \sum_{h=0}^N (a_{K,h} - b_{K,h} \ln q) q^h,$$

$$E(k) = \sum_{h=0}^N (a_{E,h} - b_{E,h} \ln q) q^h,$$

where $q = 1 - k^2$, and $a_{K,h}$, $b_{K,h}$, $a_{E,h}$ and $b_{E,h}$ are coefficients provided in Abramowitz and Stegun (1965). $N = 10$ is sufficient to give an approximation accurate to double precision.

In the implementation of the Elliptic Integrals *Horner's rule* for polynomial notation is employed. Instead of recomputing every power of a variable (for the n th power ($n - 1$) multiplications are needed), only one additional multiplication suffices, if the previous ($n - 1$)th power is just multiplied once more. If m is the order of the polynomial, the naïve method's complexity scales with $\mathcal{O}(m^2)$, Horner's method only with $\mathcal{O}(m)$. Practically, this means

$$a_0 + a_1x + a_2x^2 + a_3x^3 + a_4x^4 + \dots$$

$$= a_0 + x(a_1 + x(a_2 + x(a_3 + x(a_4 + \dots))))).$$

In the first case, in order to compute the Elliptic integrals to the desired precision 142 operations (21 additions and 121 multiplications) are necessary, plus 11 times calculating the logarithm. In the second case, only 42 operations (21 additions and 21 multiplications) plus 1 logarithm evaluation are required.

C.3.1 Gravity correction due to the disk's finite thickness

Our considerations for gravity are technically only valid in for $r > Z$. The fact we calculate gravity all the way to $r = 0$, the center of the cloud, we implicitly assume an infinitesimally-thin sheet. However, for a thin sheet of finite thickness, as we are modelling,

this overestimates the force due to gravity in the central regions. We therefore include a correction term to the radial gravitational force that alleviates this problem.

The vertical Poisson equation reads

$$\frac{d^2\Psi}{dz^2} = 4\pi G \varrho_n(r, z), \quad (\text{C.13})$$

which – applying our one-zone approximation of constancy of any quantity over one scale-height in $\hat{\mathbf{z}}$ -direction – is straightforward to integrate, and yields

$$\Psi = \Psi(r, 0) + 2\pi G \varrho_n(r) z^2. \quad (\text{C.14})$$

There is no contribution linear in z since Ψ is symmetric about the equatorial plane. The term $\Psi(r, 0)$ yields the radial gravitational acceleration in the equatorial plane as it occurs in an infinitesimally thin disk (see derivation in Section B.4.4). The total radial acceleration then is

$$g_r(r, z) \equiv -\frac{\partial\Psi(r, z)}{\partial r} = g_r(r, 0) - 2\pi G \frac{\partial\varrho_n(r)}{\partial r} z^2 \quad (\text{C.15})$$

Since z is a coordinate, its derivative with respect to r vanishes. The mean quantity over the thickness of the cloud is obtained by integrating over the thickness of the disk, hence we get

$$\begin{aligned} \langle g_r \rangle &= \frac{1}{2Z} \int_{-Z}^{+Z} g_r(r, z) dz \\ &= g_r(r, 0) - \frac{1}{2Z} \int_{-Z}^{+Z} 2\pi G \frac{\partial\varrho_n(r)}{\partial r} z^2 dz \\ &= g_r(r, 0) - \frac{2\pi G}{3} \frac{\partial\varrho_n(r)}{\partial r} Z^2 \end{aligned} \quad (\text{C.16})$$

where we again used the one-zone approximation.

For implementation purposes, we normalize Eq.(C.16) (see Section C.7 for details on the normalization), and get

$$\langle g_r \rangle = g_r(r, 0) - \frac{1}{3} \frac{\partial\varrho_n}{\partial r} Z^2. \quad (\text{C.17})$$

We have already calculated the derivative of the mass per cell, but not of ϱ , so we replace

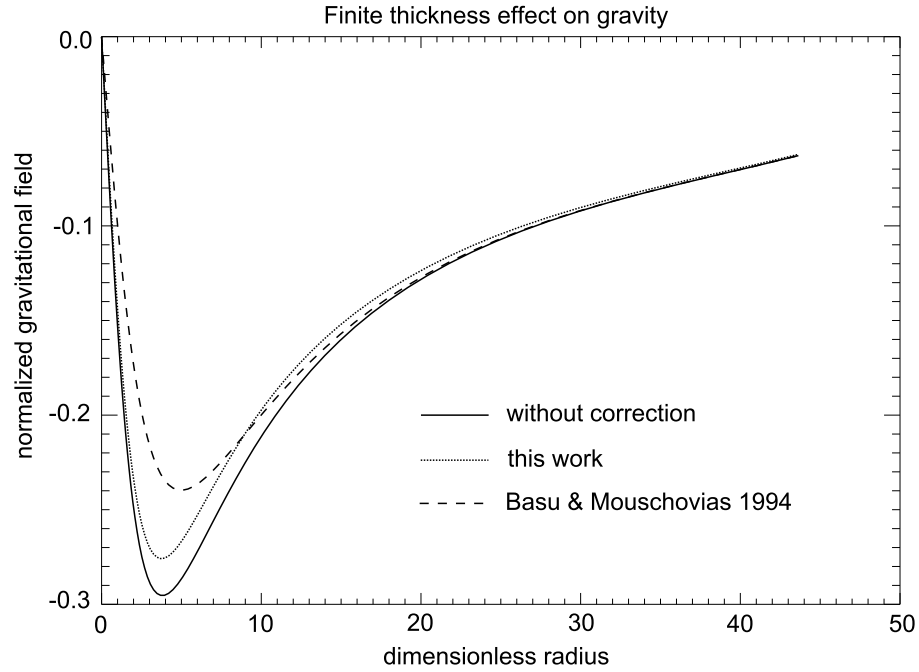


Figure C.2: Gravitational field vs. radius for the initial column density profile in Chapters 4 and 5. The solid line shows the field of an infinitesimally thin disk, the dashed line the calculation adopted by Basu and Mouschovias (1994). The dotted line is the field as we calculate it.

the latter using the definition of the half-thickness, $\varrho_n = \Sigma_n/2Z$.

$$\begin{aligned} \langle g_r \rangle &= g_r(r, 0) - \frac{1}{6} Z^2 \frac{\partial (\Sigma_n/Z)}{\partial r} \\ &= g_r(r, 0) - \frac{1}{6} \left(Z \frac{\partial \Sigma_n}{\partial r} - \Sigma_n \frac{\partial Z}{\partial r} \right) \end{aligned} \quad (\text{C.18})$$

If we multiply the column density with the area of each cell, we recover the mass in that cell, and find

$$\langle g_{r,i} \rangle = g_{r,i} - \frac{1}{6} \frac{\partial M_i}{\partial r} \frac{Z_i}{A_i} + \frac{1}{6} \frac{M_i}{A_i} \frac{\partial Z_i}{\partial r}. \quad (\text{C.19})$$

Figs. C.2 and C.3 show the correction in terms of the dimensionless radius. Gravity would be overestimated by less than 10% everywhere without the correction. Basu and Mouschovias (1994) quoted an overestimation of the field of up to 40%. Note also that the term $\partial Z/\partial r$ term is of considerable importance, as without it, the field would actually be *too small* in the center by a factor of almost 5.

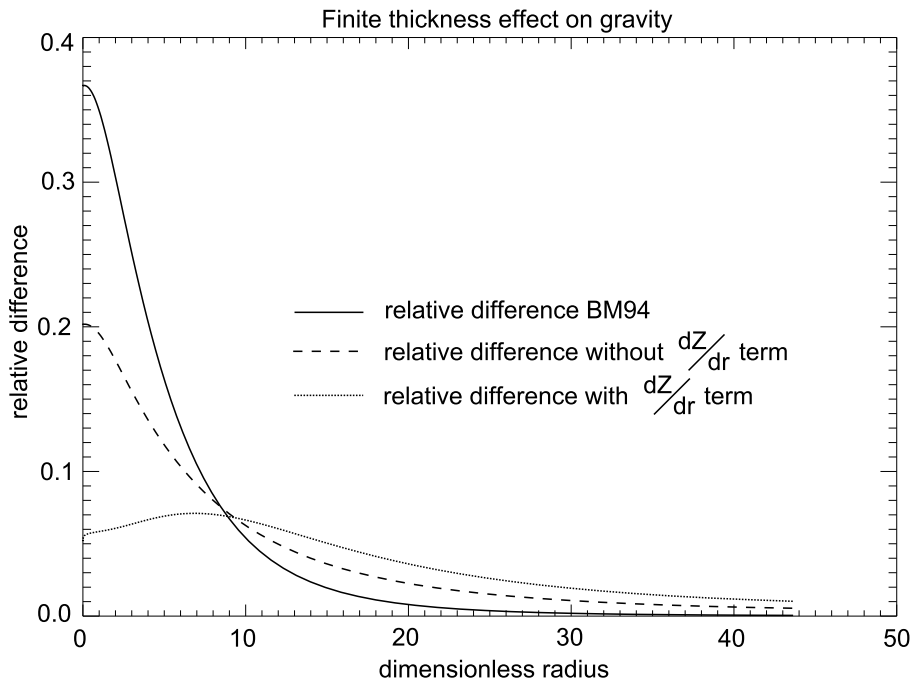


Figure C.3: Relative difference between the gravitational field of an infinitesimally thin disk and that of one with finite thickness. The field is overestimated by less than 10% everywhere, not by almost 40% as noted in Basu and Mouschovias (1994). This also shows the importance of the $\partial Z/\partial r$ term: without it, the field would be underestimated by a factor of 5 in the center.

C.3.2 Gravity correction due to the disk's finite extent

We also have to take into consideration the fact that our computational domain (i.e. the disk) is of finite size. This will cause the gravitational field to diverge at the edge of the cloud. Obviously, this is not a physical effect, since there always is matter outside the cloud that will exert some force there, and therefore will moderate the diverging field. We solve this problem by adding a constant amount of gravitational acceleration that represents the material outside the disk. In practice, we simply add the difference between the field of the finite disk, and that which is analytically-known for an infinite disk. This difference is very small even a short distance away from the edge, but it effectively counteracts the divergence effect at the edge. Since we are not interested in what happens at the outermost edge of the cloud, this does not deteriorate the solution. Furthermore, the dynamical timescale of material near the core's edge is very long compared with that of gas further in. As long as we do not run the code until the entire core has accreted (which is unrealistic for other reasons as well), the effect of the edge is negligible.

C.3.3 Gravity correction for a central point mass

If a central point mass (implemented for instance as a sink cell) is present, there appears another contribution to the pressure force, namely the extra pull towards the center. The radial gravitational pull at height z over the disk is given by

$$g_r = -\frac{GM_\star}{r^2 + z^2}. \quad (\text{C.20})$$

However, the component of gravity we are interested in points in $\hat{\mathbf{z}}$ -direction, since can be expressed as an extra weight W . As illustrated in Fig. C.4, g_z can be calculated by the simple relation

$$\begin{aligned} g_z &= g_r \cos \theta = g_r \frac{z}{\sqrt{r^2 + z^2}} \\ &= -\frac{GM_\star z}{(r^2 + z^2)^{3/2}}. \end{aligned} \quad (\text{C.21})$$

Then, the weight W due to the extra vertical gravity g_z can be calculated by

$$\begin{aligned} W &= 2 \int_0^Z \varrho_n |g_z| dz = 2GM_\star \varrho_n \int_0^Z \frac{z}{(r^2 + z^2)^{3/2}} dz \\ &= \frac{2GM_\star}{r} \varrho_n \left[1 - \frac{1}{\sqrt{1 + (Z/r)^2}} \right], \end{aligned} \quad (\text{C.22})$$

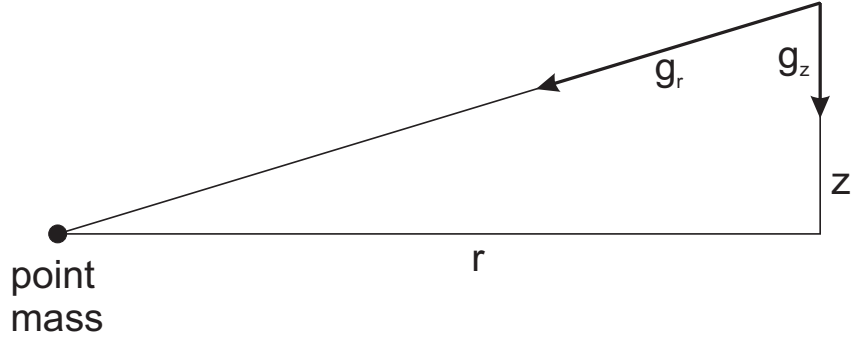


Figure C.4: Illustration of the correction to the pressure force due to consideration of a point mass.

where we used the familiar one-zone approximation. We replace the volume density by the column density, using $Z = \Sigma_n/2\rho_n$. The last expression may suffer from cancellation error, but it can be transformed to avoid that

$$\begin{aligned} W &= \frac{2GM_\star}{r} \rho_n \left[1 - \frac{1}{\sqrt{1 + (\Sigma_n/2\rho_n r)^2}} \right] \\ &= \frac{GM_\star \Sigma_n^2}{2r^3 \rho_n} \left[1 + (\Sigma_n/2\rho_n r)^2 + \sqrt{1 + (\Sigma_n/2\rho_n r)^2} \right]^{-1}. \end{aligned} \quad (\text{C.23})$$

The weight is then added to Eq.(C.4a), the neutral pressure of a magnetic barotropic slab of ideal gas, to get

$$P_n = \frac{\pi}{2} G \Sigma_n^2 + P_{\text{ext}} + \frac{B_r^2}{8\pi} + \frac{B_\varphi^2}{8\pi} + W. \quad (\text{C.24})$$

This, however, poses a problem: we precisely perform the exercise of calculating P_n the way presented in Section C.2.3 in order to avoid having to deal with the density explicitly and then solve a non-linear equation for it. However this is exactly what Eq.(C.24) would require.

The way to get around this is to solve the equation iteratively. First, we assume $W \equiv 0$, and calculate the density and the scale height according to the prescription given in Section C.2.3. With this, we compute a first approximation to the weight W at every point of the cloud, and use this to calculate the neutral pressure again. We repeat the process until W does not change anymore significantly. Only a handful of iterations are usually sufficient. Obviously, the squeezing effect will be much greater for smaller r than for a point near the cloud edge.

C.4 Angular momentum equation

Analogous to the continuity equation and the momentum equation, we integrate the angular momentum equation of our thin disk,

$$\frac{\partial L}{\partial t} + \frac{1}{r} \frac{\partial}{\partial r} (rLv_r) = 2\pi r B_{z,\text{eq}} B_\varphi, \quad (\text{C.25})$$

over each cell. This yields

$$\frac{\partial J_i}{\partial t} = -[rLv_r]_{i-1}^i + rB_\varphi\Phi, \quad (\text{C.26})$$

where $J = M\Omega r^2$ is the angular momentum, $L = \Sigma\Omega r^2$ is its counterpart per unit area, B_φ is the azimuthal component of the magnetic field, and Φ is the magnetic flux.

C.5 Induction Equation

The three-dimensional induction equation reads

$$\frac{\partial}{\partial t} \mathbf{B} + \nabla \times (\mathbf{B} \times \mathbf{v}_n) = -\nabla \times (\eta_{\text{eff}} \nabla \times \mathbf{B}) \quad (\text{C.27})$$

When integrated over the area of each cell $d\mathbf{A}_i$, we get

$$\int_{i-1}^i \frac{\partial}{\partial t} \mathbf{B} \cdot d\mathbf{A}_i + \int_{i-1}^i \nabla \times (\mathbf{B} \times \mathbf{v}_n) \cdot d\mathbf{A}_i = - \int_{i-1}^i \nabla \times (\eta_{\text{eff}} \nabla \times \mathbf{B}) \cdot d\mathbf{A}_i. \quad (\text{C.28})$$

The first term is simply the time derivative of the magnetic flux Φ . The other terms are treated with Stoke's law.

$$\frac{\partial}{\partial t} \Phi + \int_{i-1}^i (\mathbf{B} \times \mathbf{v}_n) \cdot d\mathbf{l}_i = - \int_{i-1}^i (\eta_{\text{eff}} \nabla \times \mathbf{B}) \cdot d\mathbf{l}_i, \quad (\text{C.29})$$

where $d\mathbf{l}_i$ is the line element. Since in our geometry both $(\mathbf{B} \times \mathbf{v}_n) \equiv B_{z,\text{eq}} v_r \hat{\varphi}$ and $(\eta_{\text{eff}} \nabla \times \mathbf{B}) \equiv c^2 \eta / 4\pi \mathbf{j}_\varphi$ point in $\hat{\varphi}$ -direction, so must be the line element. The first of the remaining integral terms (the flux advection term) can be written as (this was shown the component notation above)

$$\int_{i-1}^i (\mathbf{B} \times \mathbf{v}_n) \cdot d\mathbf{l}_i = [rB_{z,\text{eq}}v_r]_{i-1}^i \quad (\text{C.30})$$

so, by analogy, the diffusion term becomes

$$-\int_{i-1}^i (\eta_{\text{eff}} \nabla \times \mathbf{B}) \cdot d\mathbf{l}_i = -\frac{c^2}{4\pi} [r\eta_{\text{eff}} \mathbf{j}_\varphi]_{i-1}^i = \left[r\eta_{\text{eff}} \frac{\partial B_{z,\text{eq}}}{\partial r} \right]_{i-1}^i \quad (\text{C.31})$$

since $\mathbf{j} = c/4\pi \nabla \times \mathbf{B}$ and the $c^2/4\pi$ has been absorbed in the η_{eff} . The same result can also be gleaned from the component notation

$$-\left[\int_{i-1}^i \nabla \times (\eta_{\text{eff}} \nabla \times \mathbf{B}) \cdot d\mathbf{A}_i \right]_z = \int_{i-1}^i \frac{1}{r} \frac{\partial}{\partial r} \left(r\eta_{\text{eff}} \frac{\partial B_{z,\text{eq}}}{\partial r} \right) r dr \quad (\text{C.32})$$

$$= \left[r\eta_{\text{eff}} \frac{\partial B_{z,\text{eq}}}{\partial r} \right]_{i-1}^i \quad (\text{C.33})$$

Here, we used the fact that the z -component of the curl is $r^{-1} \partial (rB_{z,\text{eq}}) / \partial r$, while the φ -component is $-r \partial B_{z,\text{eq}} / \partial r$.

The overall form of the diffusion equation implemented in the code is therefore

$$\frac{\partial \Phi_i}{\partial t} = -[rv_r B_{z,\text{eq}}]_{i-1}^i + \left[r\eta_{\text{eff}} \frac{\partial B_{z,\text{eq}}}{\partial r} \right]_{i-1}^i. \quad (\text{C.34})$$

C.6 Calculation of magnetic field lines

We seek to visualize magnetic field lines above the disk, and use the method described in Mestel and Ray (1985). We follow their derivation closely in the subsequent discussion. They use an expression for a *finite* thin disk (as opposed to Morton et al., 1994 who calculate the field lines assuming an disk with infinite extent).

We want to know the *flux function*, a function constant on individual field lines. Connecting points on which the flux function assumes the same value therefore trace field lines. It is defined by

$$\mathbf{B} \cdot \nabla P = 0. \quad (\text{C.35})$$

It can be shown to be closely related to the magnetic vector potential A , by

$$P(r, z) = rA(r, z), \quad (\text{C.36})$$

in cylindrical coordinates with a poloidal magnetic field, such as in our case.

The magnetic vector potential $\mathbf{A} \equiv \nabla \times \mathbf{B}$ can be expressed in terms of the electric current density \mathbf{j} , by realizing that it is the solution to a Poisson equation. For that, we

take the curl of \mathbf{B}

$$\begin{aligned}
 \nabla \times \mathbf{B} &= \nabla \times (\nabla \times \mathbf{A}), \\
 &= \nabla (\nabla \cdot \mathbf{A}) - \nabla^2 \mathbf{A}, \\
 &= -\nabla^2 \mathbf{A}, \\
 &\equiv \frac{4\pi}{c} \mathbf{j},
 \end{aligned} \tag{C.37}$$

where the Coulomb gauge condition that $\nabla \cdot \mathbf{A} \equiv 0$ was used.

Now, we can write down the general solution for the vector potential

$$\mathbf{A}(\mathbf{r}) = \frac{1}{c} \int \frac{\mathbf{j} dV}{|\mathbf{r} - \mathbf{r}'|}. \tag{C.38}$$

Considering a magnetic field in the (r, z) -plane, the vector potential (and the current) only has a component in $\hat{\varphi}$ -direction, and its solution can be written as

$$A(r, z) = \frac{1}{c} \int_0^R \int_0^{2\pi} \frac{J_\varphi(r') r' dr' \cos \theta d\theta}{[(r - r' \cos \theta)^2 + (r' \sin \theta)^2 + z^2]^{1/2}}, \tag{C.39}$$

where J_φ is the sheet's current density. Finally, realizing that there is a contribution to the flux from an external field with field strength B_{ref} as well, the overall flux function is

$$P(r, z) = \frac{1}{2} B_{\text{ref}} r^2 + \frac{r}{2\pi} \int_0^R B_r(r') r' dr' \int_0^{2\pi} \frac{\cos \theta d\theta}{[r^2 + r'^2 - 2rr' \cos \theta + z^2]^{1/2}}, \tag{C.40}$$

where we have inserted $J_\varphi = B_r c / 2\pi$. This can be derived by using Stoke's theorem on Eq.(C.37) integrated over an area. Furthermore, we have simplified the denominator slightly.

Using the normalizations $x = r/R$ and $x' = r'/R$, the second (angular) part of the integral can be transformed (see Mestel and Ray, 1985) to contain the form

$$\int_0^u \frac{t^2 dt}{\sqrt{(\alpha^2 - t^2)(\beta^2 - t^2)}} = \alpha [F(\eta, t) - E(\eta, t)], \tag{C.41}$$

$$\eta = \arcsin \frac{u}{\beta}, \quad t = \frac{\beta}{\alpha}.$$

The symbols F and E represent the (incomplete) Elliptic integrals of First and Second Kind, and the integral identity is from Gradshteyn et al. (2007, §3.153.5, p. 280).

In our case, $u = \beta$, and the expression becomes

$$\frac{4}{\alpha\beta} \int_0^\beta \frac{t^2 dt}{\sqrt{(\alpha^2 - t^2)(\beta^2 - t^2)}} = \alpha [K(\beta/\alpha) - E(\beta/\alpha)]. \quad (\text{C.42})$$

Here, K and E are the Complete Elliptic integrals for first and second kind, respectively, and α and β are defined as

$$\alpha\beta = xx', \quad \text{and} \quad (\text{C.43a})$$

$$\alpha^2 + \beta^2 = x^2 + x'^2 + z^2. \quad (\text{C.43b})$$

Solving for α and β , we get

$$\alpha^2 = \frac{1}{2} \left[(x^2 + x'^2 + z^2) + \sqrt{(x^2 + x'^2 + z^2)^2 - 4x^2x'^2} \right], \quad (\text{C.44a})$$

$$\begin{aligned} \beta^2 &\equiv x^2x'^2/\alpha^2, \\ &= 2x^2x'^2 / \left[(x^2 + x'^2 + z^2) + \sqrt{(x^2 + x'^2 + z^2)^2 - 4x^2x'^2} \right]. \end{aligned} \quad (\text{C.44b})$$

Note that α and β are symmetric in x and x' , and Eq.(C.42) is symmetric to the exchange of α and β . We choose $\alpha > \beta$, in accordance with Mestel and Ray (1985).

We could compute β using Eq.(C.44a) with a minus sign before the square root, but instead chose the equivalent formulation Eq.(C.43a). This is advantageous for numerical reasons, as it avoids large cancellation errors that can occur if x and/or x' are small and thus the expression under the square root is very close to the expression it's subtracted from.

Finally, we arrive at the following form of the flux function (recall the normalization $x = r/R$)

$$P(x, z) = \frac{1}{2} B_{\text{ref}} x^2 R^2 + \frac{B_{\text{ref}}}{2\pi} R^2 G(x, z), \quad (\text{C.45})$$

where

$$G(x, z) = 4 \int_0^1 B_r(x) \alpha(x, x', z) [K(\beta/\alpha) - E(\beta/\alpha)] dx'. \quad (\text{C.46})$$

A contour plot of the integral that is the flux function (with B_r an output of our simulations) will then yield the field lines. Of course, since B_r is not a closed-form expression, but rather is given by discrete values at each grid point, the integral has to be solved numerically. Two examples are given in Fig. 4.3.

In order to construct a test of the integrator, we identify the derivative $dE(k)/dk =$

$k^{-1} [E(k) - K(k)]$, and can transform the integral to read

$$\begin{aligned} G(x, z) &= -4 \int_0^1 B_r(x) \beta(x, x', z) \frac{dE(\beta/\alpha)}{d(\beta/\alpha)} dx', \\ &= -4 \int_0^1 B_r(x) \beta(x, x', z) \left(\frac{d(\beta/\alpha)}{dx'} \right)^{-1} \frac{dE(\beta/\alpha)}{dx'} dx'. \end{aligned} \quad (\text{C.47})$$

We can now simply choose

$$\begin{aligned} B_r &= \frac{d(\beta/\alpha)}{dx'} \frac{1}{\beta}, \\ &= \frac{x}{\beta\alpha^2} \left(1 - \frac{2x'}{\alpha} \right), \end{aligned} \quad (\text{C.48})$$

where we used the fact that $\beta/a = xx'/\alpha^2$. Note that now $B_r \equiv B_r(x, x', z)$, but since x and z are constants for each evaluation of the integral, that is not a real problem. In this case, we simply get

$$G(x, z) = -4 \int_0^1 \frac{dE(\beta/\alpha)}{dx'} dx' \quad (\text{C.49})$$

$$= -4 [E(\beta/\alpha)]_{x'=0}^{x'=1} = 2\pi - 4E(\beta/\alpha)|_{x'=1}, \quad (\text{C.50})$$

and can use this to test the numerical integrator.

C.7 Normalization and full system of equations

We normalize the MHD equations, Eqs.(5.1a) to (5.1e) in Section 5.2, by the following values

$$\Sigma_0 = 0.02 \text{ g cm}^{-2} \quad \text{as the unit of column density,} \quad (\text{C.51a})$$

$$2\pi G\Sigma_0 = 8.38 \times 10^{-9} \text{ cm s}^{-2} \quad \text{as the unit of acceleration,} \quad (\text{C.51b})$$

$$c_s = 1.88 \times 10^4 \text{ cm s}^{-1} \quad \text{as the unit of velocity, and} \quad (\text{C.51c})$$

$$2\pi\sqrt{G}\Sigma_0 = 32.5 \text{ } \mu\text{G} \quad \text{as the unit of magnetic field.} \quad (\text{C.51d})$$

Eq.(C.51a) is the initial central column density, and Eq.(C.51b) is the vertical gravitational acceleration of an infinite thin sheet of column density Σ_0 . The speed of sound in a gas comprised of hydrogen molecules and 10% helium in number at a temperature of 10 K is the third unit. The unit of magnetic field is chosen purely out of convenience, and would not strictly be necessary, as the other three quantities allow to uniquely form a complete system of units already. It allows, however, to drop some factors of 2π from the equations.

With these normalizations, we can construct our system of units:

$$[t] = \frac{c_s}{2\pi G\Sigma_0} = 2.24 \times 10^{12} \text{ s} \quad \text{as the unit of time,} \quad (\text{C.52a})$$

$$[L] = \frac{c_s^2}{2\pi G\Sigma_0} = 4.23 \times 10^{16} \text{ cm} \quad \text{as the unit of length,} \quad (\text{C.52b})$$

$$[m] = \frac{c_s^4}{(2\pi G)^2 \Sigma_0} = 2.25 \times 10^{32} \text{ g} \quad \text{as the unit of mass, and} \quad (\text{C.52c})$$

$$[\Omega] = \frac{2\pi G\sigma_0}{c_s} = 4.45 \times 10^{-13} \text{ s}^{-1} \quad \text{as the unit of angular velocity.} \quad (\text{C.52d})$$

The normalization is done to eliminate scale dependence, and to work with numbers closer to unity. The former is not really possible for the collapse problem beyond the isothermal phase, as the density at which the molecular gas becomes opaque sets a physical scale. Furthermore, the chemistry calculations work with physical values. However, the latter goal of more manageable numbers is still desirable.

The full system of equations in this unit system then reads

$$\frac{\partial \Sigma_n}{\partial t} = -\frac{1}{r} \frac{\partial}{\partial r} (r \Sigma_n v_r), \quad (\text{C.53a})$$

$$\frac{\partial (\Sigma_n v_r)}{\partial t} = -\frac{1}{r} \frac{\partial}{\partial r} (r \Sigma_n v_r v_r) + f_p + f_g + f_m + f_r, \quad (\text{C.53b})$$

$$\frac{\partial L}{\partial t} = -\frac{1}{r} \frac{\partial}{\partial r} (r L v_r) + r B_{z,\text{eq}} B_{\varphi,Z}, \quad (\text{C.53c})$$

$$\frac{\partial B_{z,\text{eq}}}{\partial t} = -\frac{1}{r} \frac{\partial}{\partial r} (r B_{z,\text{eq}} v_r) + \frac{1}{r} \frac{\partial}{\partial r} \left(r \eta_{\text{eff}} \frac{\partial B_{z,\text{eq}}}{\partial r} \right), \quad (\text{C.53d})$$

$$P = P(\varrho_n), \quad (\text{C.53e})$$

$$f_p = -\frac{\partial}{\partial r} \left[\frac{Z}{2} \Sigma_n^2 \right], \quad (\text{C.53f})$$

$$f_g = \Sigma_n g_r, \quad (\text{C.53g})$$

$$f_m = B_{z,\text{eq}} \left(B_{r,Z} - Z \frac{\partial B_{z,\text{eq}}}{\partial r} \right) + \frac{1}{4\pi} \frac{dZ}{dr} (B_{r,Z}^2 + B_{\varphi,Z}^2), \quad (\text{C.53h})$$

$$f_r = \frac{L^2}{\Sigma_n r^3}, \quad (\text{C.53i})$$

$$B_{r,Z} = -\int_0^\infty dr' r' (B_{z,\text{eq}} - B_{\text{ref}}) \mathcal{M}(r, r'), \quad (\text{C.53j})$$

$$B_{\varphi,Z} = -\frac{\sqrt{8\varrho_{\text{ext}}}}{B_{\text{ref}}} \frac{\Phi}{r} (\Omega - \Omega_{\text{ref}}), \quad (\text{C.53k})$$

$$\Phi = \int_0^r dr' r' B_{z,\text{eq}}, \quad (\text{C.53l})$$

$$g_r = \int_0^\infty dr' r' \Sigma_n(r') \mathcal{M}(r, r'), \quad (\text{C.53m})$$

$$\mathcal{M}(r, r') = \frac{2}{\pi} \frac{d}{dr} \frac{1}{r_{>}} K \left(\frac{r_{<}}{r_{>}} \right), \quad (\text{C.53n})$$

$$Z = \frac{\Sigma_n}{2\varrho_n}. \quad (\text{C.53o})$$

C.8 Numerical Code

C.8.1 Programming Language

The code exists in two versions; one is written in `Fortran90`, the other in `IDL` (ITTTVIS Interactive Data Language). While Fortran offers greater execution speed, we did not need to rely on that. Since we only solve the axisymmetric thin-disk MHD equations, instead of the full three-dimensional problem, each run is fast enough that we almost exclusively use the `IDL` version, and take advantage of higher-level programming, included debugging, and advanced analysis tools that `IDL` offers.

C.8.2 Code description

- The code uses the *finite-volume approach*. Differential forms of conservation laws are evolved, instead of the direct hydrodynamics equations.
- This is being done on a *staggered grid*: one grid holds the dependent variables (mass, momentum, angular momentum, magnetic flux), while the other contains the cell faces where fluxes are calculated with the van-Leer method (van Leer, 1977). This scheme is *TVD* (Total Variation Diminishing) in that it ensures monotonicity in all quantities, thus avoiding spurious maxima and minima. Godunov (1959) showed that it is impossible to solve a PDE with second-order accuracy and not create new extrema.
- This procedure allows to fulfill conservation laws to machine precision, preserve the correct advection speed and avoid dispersion, while also being shock-capturing and resolving discontinuities over only a few cells. The last property removes the need for artificial viscosity which introduces a lot of diffusivity into the code.
- The grids are *logarithmic*; the cell sizes increase by a constant factor from the center to the edge, and allows the computational domain to cover a large size while simultaneously resolving the central region with very high resolution.
- Our system is *axisymmetric*; we assume two-dimensional cylindrical symmetry (only r and z -dependence). Additionally, we assume vertical hydrostatic equilibrium, and thus solve the equations for a thin disk. This reduces the problem to being *radial*-only, with an additional equation for the hydrostatic equilibrium.

The z -dependence is covered in a *one-zone approximation*, and our and the disk is assumed *reflective symmetric* about the equatorial plane.

- The boundary conditions at the center of the core are reflective. At the edge, we impose constant-volume boundary conditions, assuming a high-temperature external medium with negligible density and constant external pressure.
- We use the *method of lines* (Schiesser, 1991): only the spatial part of the PDEs is discretized, the temporal part is left as a differential. Every quantity at every grid point is treated as a separate dependent variable. Hence we are not dealing with PDEs anymore, but rather a large system of coupled ODEs, which is solved using an implicit of-the-shelf ODE solver. We use LSODE (Radhakrishnan and Hindmarsh, 1993), which integrates the equations with the *Gear algorithm* (Gear, 1971) up to 12th order in time and is geared towards stiff ODEs. This approach has the advantage of being *unconditionally stable* and thus not imposing a time step restriction.

C.8.3 Code structure

The structure of the code is illustrated in Figs. C.5, C.6, and C.7. When code execution is started, if it is not a restart run, the normalized staggered logarithmic grid is created. The integral method we used for calculating the gravitational field translates into a matrix multiplication problem, and the coefficient matrix is purely geometrically determined. Therefore it is constant on each refinement level, and is calculated next. Similar considerations hold for the differentiation on a non-uniform grid.

Next, the initial conditions are implemented, and the evolution array is initialized with them. It consists of mass, momentum, angular momentum, and magnetic flux. At this point, the initial state is written to a data file, or, if a previous run was restarted, that run's data file loaded into memory.

Thereafter, LSODE is executed on the discretized spatial part of the equations (see Fig. C.7). All variables such as column density and radial velocity besides the primary quantities mentioned above can be derived from the latter, and are calculated in a subsequent step. This includes the rotation rate and the magnetic field components, as well as the mass-to-flux ratio. The latter are needed to calculate the total mid-plane pressure, which in turn determines the density, temperature, and half-thickness of the disk. This comprises the next step in execution.

The magnetic field components are also involved in the computation of the torque on the core due to magnetic braking. After this, the chemistry module is called. An

equilibrium calculation, independent for each cell, fixes the abundances of the various species. Those are required for the the determination of the resistivity. Next, the forces are calculated, and in a final step, all is put together as the fluxes of mass, momentum, angular momentum, and magnetic flux across the cell faces are evaluated in the van-Leer advection step.

After returning from LSODE, a check is performed whether to refine the grid and increase the central resolution. If this happens, the necessary interpolations are carried out, and all grid-related parameters are computed for the new grid. After this, data is written out and the cycle repeats, if the stop conditions are not met.

Bibliography

- Abramowitz, M. and Stegun, I. A. (eds.): 1965, *Handbook of Mathematical Functions*, Dover Publications, New York
- Basu, S. and Mouschovias, T. C.: 1994, *ApJ* **432**, 720
- Dapp, W. B. and Basu, S.: 2006, *Master's thesis*, The University of Western Ontario
- Gear, C. W.: 1971, *Numerical initial value problems in ordinary differential equations*, Prentice-Hall, 1971
- Godunov, S. K.: 1959, *Math. Sbornik* **47**, 271
- Gradshteyn, I. S., Ryzhik, I. M., Jeffrey, A., and Zwillinger, D.: 2007, *Table of Integrals, Series, and Products*, Academic Press; 7 edition (March 9, 2007)
- Masunaga, H. and Inutsuka, S.: 2000, *ApJ* **531**, 350
- Mestel, L. and Ray, T. P.: 1985, *MNRAS* **212**, 275
- Morton, S. A., Mouschovias, T. C., and Ciolek, G. E.: 1994, *ApJ* **421**, 561
- Radhakrishnan, K. and Hindmarsh, A. C.: 1993, *Description and Use of LSODE, the Livermore Solver for Ordinary Differential Equations*, Technical report, Lawrence Livermore National Laboratory
- Schiesser, W. E.: 1991, *The Numerical Method of Lines: Integration of Partial Differential Equations*, Academic Press, 1991. 326 p.
- van Leer, B.: 1977, *Journal of Computational Physics* **23**, 276

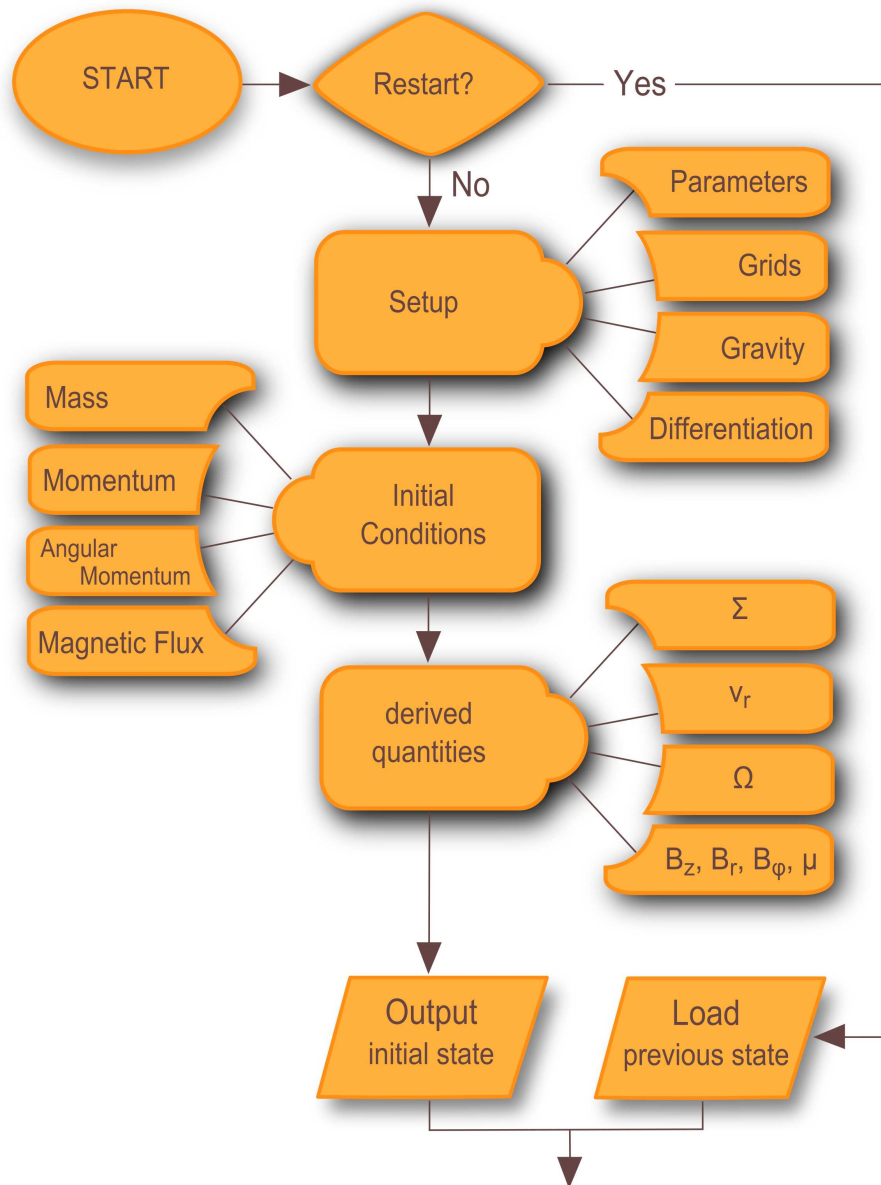


Figure C.5: Flow-chart of code execution: initialization. At the start of a run the staggered grid and associated parameters such as the geometrical factor associated with the adopted integral method for calculating the gravitational field, are initialized. Subsequently, the initial conditions in the primary evolution quantities mass, momentum, angular momentum and magnetic flux are implemented, and the initial state is written out after derived quantities have been calculated.

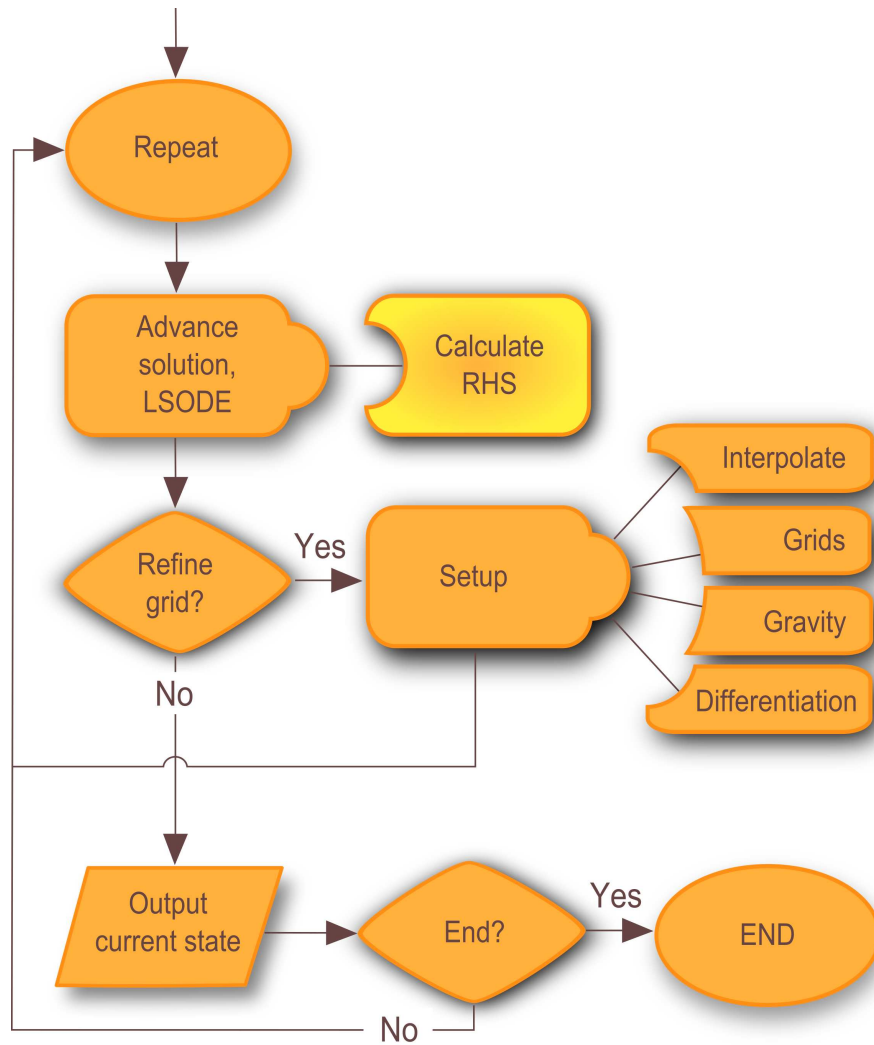


Figure C.6: Flow-chart of code execution: main loop. The ODE solver (LSODE) is executed on the discretized spatial part of the equations. This numerical step is shown separately in Fig. C.7. After returning, a check is performed whether to increase the central resolution, and the necessary interpolations and new initializations are carried out. After this, data is written out and the cycle repeats if the stop conditions are not met.

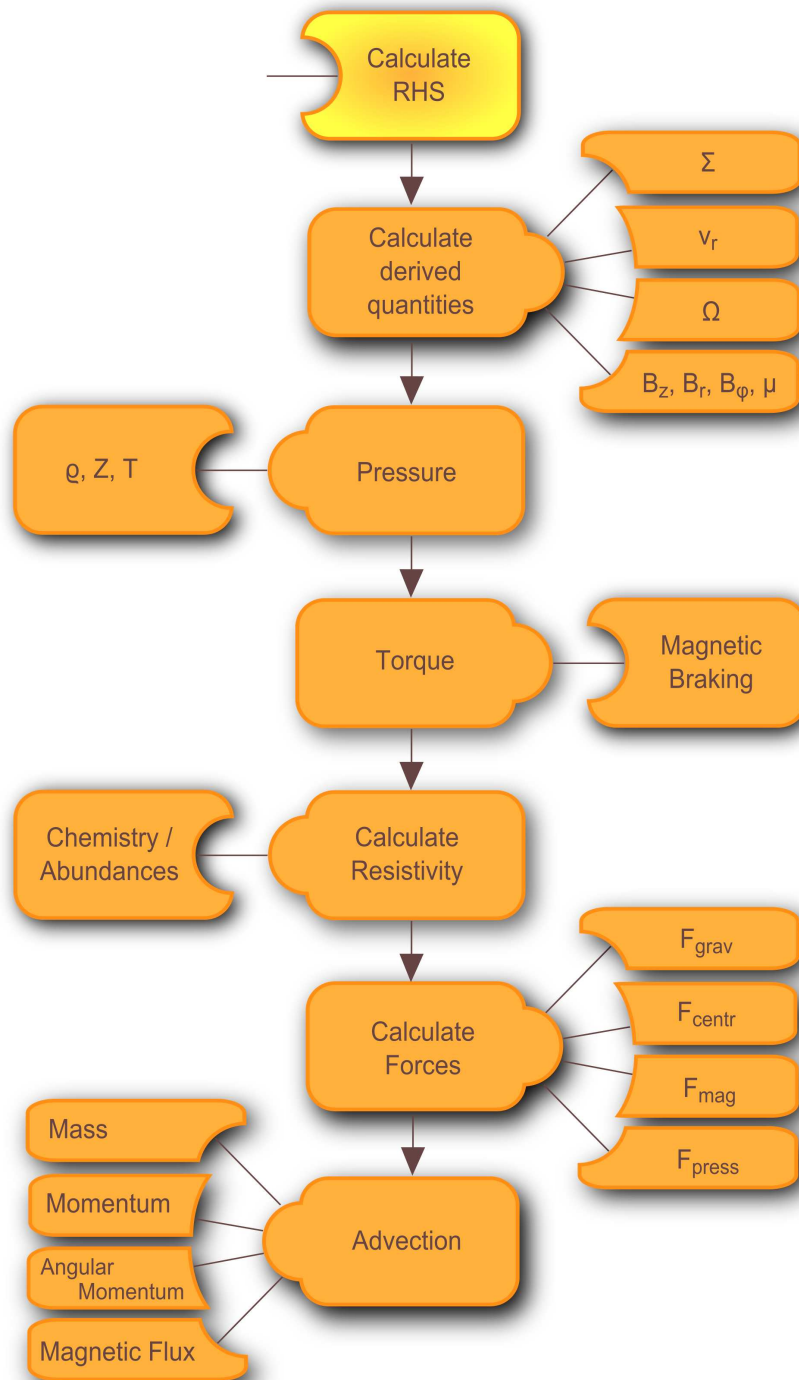


Figure C.7: Flow-chart of code execution: numerical step. The derived quantities are calculated from the evolution array. Next, in the pressure step, the temperature, density and half-thickness are determined, followed by the calculation of the torque on the core due to magnetic braking. After this, the chemistry module computes the abundances of the various species required for the determination of the resistivity. Finally, the forces are calculated, and the fluxes across the cell faces of the various quantities are evaluated in the advection step.

Appendix D

The Bonnor-Ebert Sphere

The Bonnor-Ebert model provides a theoretical approach to the structure of small, isolated, star-forming molecular clouds or prestellar cores for $t < 0$ (i.e., before the formation of a central protostar) confined by some external pressure. Since it is being used extensively in the literature for fitting prestellar cores, and is being compared with in Chapter 3, we include its derivation here. A non-magnetic, non-rotating, hydrostatic, self-gravitating, isothermal gas cloud is described by the following system of equations:

$$\varrho \mathbf{g} - \nabla P = 0 \tag{D.1a}$$

$$\nabla \cdot \mathbf{g} = -4\pi G \varrho \tag{D.1b}$$

$$P = c_s^2 \varrho, \tag{D.1c}$$

where ϱ is the volume mass density, \mathbf{g} is the gravitational acceleration, c_s is the isothermal speed of sound, and G is the gravitational constant. The equation of state is that of an ideal gas. Inserting Eq.(D.1c) into Eq.(D.1a) and taking the gradient yields

$$c_s^2 \nabla^2 \ln \varrho = -4\pi G \varrho,$$

where we have used Eq.(D.1b) to replace $\nabla \cdot \mathbf{g}$. Assuming spherical symmetry, we use the radial form of the Laplacian, and perform a change of variables to $\varrho = \varrho_c e^{-\psi}$ (i.e.,

$\psi = -\ln[\rho/\rho_c]$ and $\xi = r/r_0$, with $r_0^2 = c_s^2/(4\pi G\rho_c)$. Some algebra then results in

$$\frac{1}{\xi^2} \frac{d}{d\xi} \left(\xi^2 \frac{d\psi}{d\xi} \right) = e^{-\psi}, \quad (\text{D.2a})$$

$$\xi = \frac{r}{r_0} = \frac{r}{c_s} \sqrt{4\pi G\rho_c}, \quad (\text{D.2b})$$

$$\psi(\xi) = -\ln\left(\frac{\rho}{\rho_c}\right), \quad (\text{D.2c})$$

which is the *Lane-Emden Equation* together with its defining quantities. It describes a system in isothermal hydrostatic equilibrium in spherical geometry.

In order to solve the Lane-Emden equation numerically, it is first transformed to a system of two first-order differential equations by defining

$$\psi(\xi) = u \quad \text{and} \quad \frac{d\psi(\xi)}{d\xi} = v.$$

Then, Eq.(D.2a) becomes

$$\frac{du}{d\xi} = v \quad \text{and} \quad \frac{dv}{d\xi} = e^{-u} - \frac{2v}{\xi}. \quad (\text{2.3a,b})$$

This *initial value problem* (IVP) in ξ can be solved numerically for the density distribution ψ with any ODE solver with the starting conditions

$$(u)_{\xi=0} = 0, \quad \left(\frac{du}{d\xi}\right)_{\xi=0} = 0, \quad \left(\frac{dv}{d\xi}\right)_{\xi=0} = \frac{1}{3}. \quad (\text{D.4})$$

The initial conditions are obtained by assuming a Taylor expansion for $\psi(\xi) = a_0 + a_1\xi + a_2\xi^2 + a_3\xi^3 + \dots$, for small ξ . The factors a_n can be thought of as the derivatives $\frac{1}{n!} \frac{d^n\psi}{d\xi^n}$. We can re-insert this expansion into Eq.(D.2a) and solve for the coefficients. Since the problem is spherically symmetric, the density must be an even function about the origin at $\xi = 0$, and all odd derivatives vanish. Secondly, since $\psi(\xi) = -\ln(\rho/\rho_c)$, it is obvious that $\psi(0) = 0$, and thus $a_0 \equiv 0$ also. Expanding the exponential on the right hand side and keeping only terms up to fourth order, we find

$$\begin{aligned} \frac{1}{\xi^2} \frac{d}{d\xi} \left(\xi^2 \frac{d\psi}{d\xi} \right) &= e^{-\psi} \\ \frac{1}{\xi^2} \frac{d}{d\xi} \left(\xi^2 [2a_2\xi + 4a_4\xi^3 + 6a_6\xi^5 + \dots] \right) &= 1 - \psi + \psi^2 - \psi^3 + \dots \\ 6a_2 + 20a_4\xi^2 + 42a_6\xi^4 + \dots &= 1 - a_2\xi^2 - a_4\xi^4 + \dots + a_2\xi^4 + \dots \end{aligned}$$

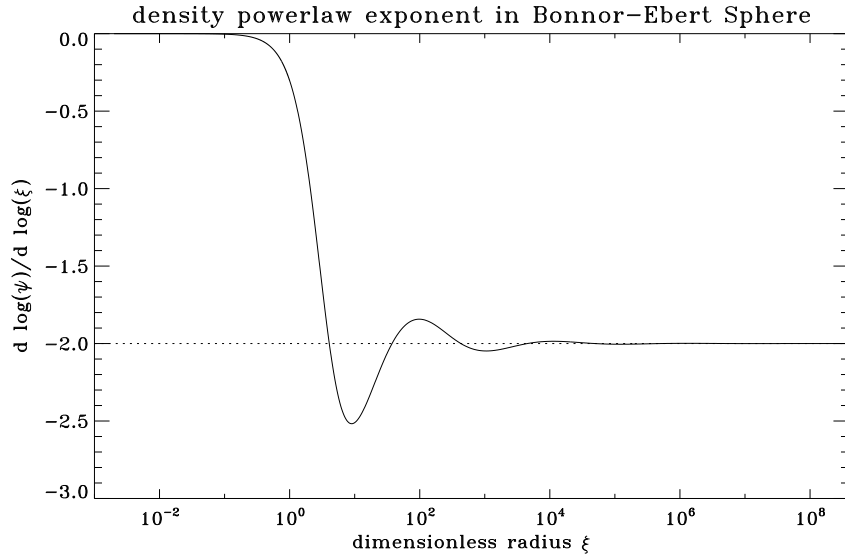


Figure D.1: Exponent k in $\varrho \propto r^{-k}$ for the Lane-Emden equation (solid line). Clearly, ϱ approaches r^{-2} .

By comparison of coefficients, we finally arrive at

$$\psi(\xi) = \frac{1}{6}\xi^2 - \frac{1}{120}\xi^4 + \dots$$

for small ξ . From this, the initial conditions in Eq.(D.4) are then deduced.

The regular solutions of Eq.(D.2a) (which is a special form of Poisson's equation) on an infinite (unbounded) domain have been studied and tabulated by Chandrasekhar (1939a,b). In the limit $\varrho_c \rightarrow \infty$, one can find that the *Singular Isothermal Sphere* (SIS, see Section 1.3) with $\varrho = c_s^2 (2\pi G r^2)^{-1}$ is an exact solution. However, the solution always asymptotically approaches $\varrho \propto r^{-2}$ for any value of ϱ_c (cf. Fig. D.1).

The preceding discussion did not consider boundary conditions, so the solution can be followed to infinite ξ and thus r . However, one can conceptually bound this spherical cloud by external pressure. Then, the cloud is cut off as soon as its internal pressure is equal to the external pressure. This work is due to Bonnor (1956) and Ebert (1955) independently. The cloud is truncated at $r = R$, i.e. $\xi_s = R/r_0$, where the subscript s denotes the value at the surface. Eqs.(D.1a)-(D.1c) then combine to

$$c_s^2 \frac{d}{dr} \ln \varrho = g_r(R). \quad (\text{D.5})$$

Switching once more from r and ϱ to ξ and ψ , respectively, and assuming a spherically-

symmetric mass distribution to simplify the gravitational acceleration, we find

$$\frac{c_s^2}{r_0} \left(\frac{d\psi}{d\xi} \right)_{\xi=\xi_s} = \frac{GM}{R^2}. \quad (\text{D.6})$$

This can be solved to yield for the mass M

$$M = \frac{c_s^3}{G^{3/2} \sqrt{4\pi} \varrho_c} \xi_s^2 \left(\frac{d\psi}{d\xi} \right)_{\xi=\xi_s}. \quad (\text{D.7})$$

Furthermore, we have a condition for the external pressure P_{ext} from Eq.(D.1c):

$$P_{\text{ext}} = c_s^2 \varrho(R) = c_s^2 \frac{\varrho_s}{\varrho_c} \varrho_c = c_s^2 e^{-\psi_s} \varrho_c. \quad (\text{D.8})$$

Solving this for the central density yields

$$\varrho_c = \frac{P_{\text{ext}}}{c_s^2 e^{-\psi_s}}, \quad (\text{D.9})$$

which can be inserted into Eq.(D.7) and, in turn, solved for the external pressure

$$P_{\text{ext}} = \frac{c_s^8}{4\pi G^3 M^2} \xi_s^4 \left(\frac{d\psi}{d\xi} \right)_{\xi=\xi_s}^2 e^{-\psi_s}. \quad (\text{D.10})$$

Virtually any combination of three parameters from physical radius R , external pressure P_{ext} , dimensionless cut-off radius ξ_s , central volume density ϱ_c , temperature T (and thus sound speed c_s), mass M , and density contrast e^{ψ} between center and surface will allow to convert the dimensionless solution derived above into its dimensional form, yielding the full internal structure of the Bonnor-Ebert sphere. Usually, the radius and the temperature are observationally accessible, and thus fitting a third parameter, such as the dimensionless radius ξ_s (related to the shape of the profile) will allow to make statements about the cloud in question.

We plot the mass vs. the density contrast between center and edge e^{ψ_s} , and the external pressure vs. the normalized cutoff radius ξ_s (Figure D.2). Each point on the graph is now an equilibrium state corresponding to a certain outer radius ξ_s of the sphere. The internal structure and the density contrast e^{ψ_s} of these states is known from the numerical solution of the Lane-Emden Equation. As can be seen from the Figure D.2, there are critical states of the system which form a dividing line between stable and unstable equilibria. The critical relative radius is $R = 6.451 r_0$. This is the critical radius for stable equilibrium, and it corresponds to a critical ratio of densities

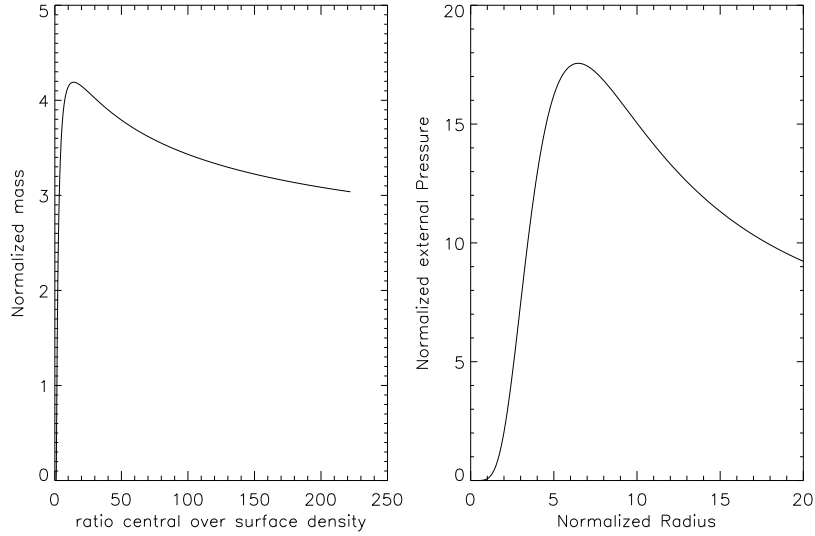


Figure D.2: **Left panel:** Mass vs. $e^\psi = \rho_c/\rho_s$ (central density over surface density) for a Bonnor-Ebert Sphere. The peak marks the dividing line between stable and unstable equilibria. **Right panel:** external pressure vs. dimensionless radius ξ_s . Here (different from the mass graph) the unstable equilibria are located on the left of the maximum, and the stable ones on the right.

of $e^{\psi_s} = 14.043$. Any larger density contrast would be unstable. Critical values for external pressure and mass are easily computed to be $P_{\text{ext,crit}} = 17.564 M^2 4\pi G^3 c_s^{-3}$ and $M_{\text{crit}} = 4.191 \sqrt{4\pi G^3 \rho_c} c_s^{-3}$, respectively.

The column density profile of the BE sphere, obtained by integrating the volume density numerically along a line of sight, matches well with some observations (Alves et al., 2001). Depending on the parameters, the power-law decline $\propto r^{-1}$ in column density can be more or less pronounced, or even almost completely absent. The profile steepens at the edge because the line of sight through the sphere becomes shorter. This is a geometric effect which is present in all truncated models, unless the density *increases* sufficiently fast with radius.

The BE model reproduces features of several observed column density profiles of prestellar cores (such as the flat region and decrease in density described approximately by a powerlaw), and is thus used extensively in the literature to fit those. However, it has several shortcomings, including the key assumption of equilibrium and *imposing* a temperature, instead of using it as an input parameter. Chapter 3 (published in Dapp and Basu, 2009) details an analytic formula to be used instead of the BE model that is not only easier to fit to observed cores, but also does not impose as many assumptions. Furthermore it allows to fit flattened cores as well as cores where magnetic fields and

rotation are important. The effect of rotation and magnetic fields on core collapse are described in Sections 1.3.1 and 1.3.2.

Note that the derivation for a Lane-Emden equation can also be carried out assuming a barotropic pressure-density relation instead of isothermal conditions. This is applicable for conditions in stellar interiors (see, e.g., Kippenhahn and Weigert, 1994), but is beyond the discussion here.

Bibliography

Alves, J. F., Lada, C. J., and Lada, E. A.: 2001, *Nature* **409**, 159

Bonnor, W. B.: 1956, *MNRAS* **116**, 351

Chandrasekhar, S.: 1939a, *An introduction to the study of stellar structure*, Chicago, Ill., The University of Chicago press [1939]

Chandrasekhar, S.: 1939b, *ApJ* **89**, 116

Dapp, W. B. and Basu, S.: 2009, *MNRAS* **395**, 1092

Ebert, R.: 1955, *Zeitschrift fur Astrophysik* **37**, 217

Kippenhahn, R. and Weigert, A.: 1994, *Stellar Structure and Evolution*, Stellar Structure and Evolution, XVI, 468 pp. 192 figs.. Springer-Verlag Berlin Heidelberg New York. Also Astronomy and Astrophysics Library

Curriculum Vitae

Name: Wolfgang Dapp

**Post-Secondary
Education and
Degrees:**

2007 - 2011	Ph.D. Astronomy and Computational Science The University of Western Ontario (UWO) London, ON, Canada
2005 - 2006	M.Sc. Astronomy and Computational Science The University of Western Ontario
2001 - 2007	Diplom Physik Universität Ulm Ulm, Germany
2001 - 2004	Vordiplom Wirtschaftphysik Universität Ulm

**Honours and
Awards:**

2009 - 2011	NSERC Alexander Graham Bell Canada Graduate Scholarship
2009	Ontario Graduate Scholarship (<i>declined</i>)
2007, 2009	Graduate Thesis Research Award, UWO
2006, 2008	Collaborative Graduate Program Scientific Computing Travel Award, UWO
2005	William H. Wehlau Award, Department of Physics and Astronomy, UWO
2005 - 2011	Graduate Research Scholarship, UWO
2004 - 2005	Provincial Scholarship of Baden-Württemberg, Germany

**Related Work
Experience:**

2005 - 2011	Research Assistant, UWO
2004 - 2010	Teaching Assistant, UWO

Publications:

1. **Dapp**, W. B., Basu, S. (2010), “*Averting the magnetic braking catastrophe on small scales: disk formation due to Ohmic dissipation*”, A&A, 521L, 56
2. Basu, S., **Dapp**, W. B. (2010), “*Long-lived Magnetic-Tension-Driven Modes in a Molecular Cloud*”, ApJ, 716, 427
3. Basu, S., Ciolek, G. E., **Dapp**, W. B., Wurster, J. (2009), “*Magnetically-regulated fragmentation induced by nonlinear flows and ambipolar diffusion*”, New Astronomy, 14, 483
4. **Dapp**, W. B., Basu, S. (2009), “*An analytic column density profile to fit prestellar cores*”, MNRAS, 395, 1092

Refereed Conference Proceedings:

1. Basu, S., **Dapp**, W. B. (2010), “*Magnetic Diffusion in Star Formation*”, IAUS 270, Computational Star Formation, J. Alves, B. G. Elmegreen, J. M. Girart, & V. Trimble (eds.), *in press*, arXiv:1011.1051v1 [astro-ph.SR]

Abstracts:

1. Basu, Shantanu, Ciolek, G. E., **Dapp**, W. B., Kudoh, T., Wityk, N. D. (2009) “*Molecular Cloud Fragmentation Driven by Self-Gravity, Magnetic Fields, Ambipolar Diffusion, and Nonlinear Flows*”, American Astronomical Society, AAS Meeting #214, #315.03; Bulletin of the American Astronomical Society, Vol. 41, p.760

Contributed Conference Talks:

1. **Dapp**, W. B., Basu, S. (2010), “*A resolution of the magnetic braking catastrophe during the second collapse*”, CC2YSO, UWO (May 2010)
2. **Dapp**, W. B., Basu, S. (2009), “*A new analytic model to fit prestellar cores*”, CASCA2009, University of Toronto (May 2009)
3. **Dapp**, W. B., Basu, S. (2009), “*A new analytic model to fit prestellar cores*”, Western Research Forum, UWO (February 2009)
4. **Dapp**, W. B., Basu, S. (2008), “*Magnetic field line curvature as indicator of the mass-to-flux ratio*”, Focus Group, EPoS2008, Tegernsee/Germany (July 2008)

5. **Dapp**, W. B., Basu, S. (2008), “*Viability of theoretical models to fit observed column density profiles in prestellar cores*”, Ontario Star Formation Jamboree (OSFJ), Canadian Institute of Theoretical Astrophysics (CITA), Toronto (February 2008)

Posters presented:

1. **Dapp**, W. B., Basu, S. (2010), “*A resolution of the magnetic braking catastrophe during the second collapse*”, IAUS270, Barcelona/Spain (May 2010)
2. **Dapp**, W. B., Basu, S. (2009), “*How turbulence and magnetic fields set the rate of collapse in molecular clouds*”, SFR@50, Spineto/Italy (July 2009)
3. Basu, S., **Dapp**, W. B., Wityk, N., DeSouza, A., (2009), “*Computer Modelling and Visualization of Astrophysical Flows*”, Western Research Showcase 2009, UWO (February 2009)
4. **Dapp**, W. B., Basu, S. (2008), “*New tests of the role of magnetic fields in star forming regions*”, EPoS2008, Tegernsee/Germany (July 2008)
5. **Dapp**, W. B., Basu, S. (2006), “*Axisymmetric simulation of star formation to explain features of IRAM 04191*”, EPoS2006, Tegernsee/Germany (August 2006)